Nadja Heine

Doktorarbeit

Vibrational Spectroscopy of Gaseous Hydrogen-Bonded Clusters: On the Role of Isomer-Specificity and Anharmonicity

Erstellt am Fritz-Haber-Institut
der Max-Planck-Gesellschaft

im Fachbereich Physik der
Freien Universität Berlin eingereichte Dissertation

Berlin, 2014

Erstgutachter	Prof. Dr. Gerard J. M. Meijer Radboud Universiteit Nijmegen Freie Universität Berlin
Zweitgutachter	Prof. Dr. Knut R. Asmis Universität Leipzig Freie Universität Berlin
Disputation	26. September 2014

Zusammenfassung

Schwerpunkt der vorliegenden Arbeit ist die Strukturaufklärung von solvatisierten Clustern in der Gasphase. Gasphasencluster sind ideale Modellsysteme, die es ermöglichen Eigenschaften komplexer Systeme unter wohldefinierten Bedingungen und ohne störenden Wechselwirkungen mit einer Umgebung zu untersuchen. Aber auch die Cluster selbst können in wichtigen Prozessen entscheidend mitwirken. Mikrosolvatisierte Clusteranionen spielen zum Beispiel im Anfangsstadium der Aerosolbildung in unserer Atmosphäre eine zentrale Rolle, die bis heute nicht vollständig aufgeklärt ist. Neue experimentelle Ansätze sind daher notwendig, um einen molekularen Einblick in die Struktur, Energetik, Reaktivität und Dynamik der Cluster zu ermöglichen.

Die Bildung von Mikrosolvathüllen wird spektroskopisch verfolgt, indem einzelne Solvatmoleküle schrittweise an das Zentralion angelagert werden. Die Strukturaufklärung erfolgt dabei mittels Infrarot-Photodissoziationsspektroskopie (IRPD) an den zuvor massenselektierten und thermalisierten Clustern. Der Vergleich von experimentellen Spektren mit quantenmechanischen Elektronenstrukturrechnungen erlaubt die Zuordnung bestimmter Strukturen. Wenn eine eindeutige Zuordnung aufgrund mehrerer Strukturisomere erschwert wird, ermöglicht die IR/IR Doppelresonanzspektroskopie eine Trennung der individuellen Beiträge der Isomere zum IRPD Spektrum. Zur Durchführung solcher Messungen wurde im Rahmen der vorliegenden Doktorarbeit ein Dreifach-Massenspektrometer mit temperaturkontrollierbarer Ionenfalle entwickelt, konstruiert und aufgebaut. Diese Apparatur ermöglicht die Messung isomer-spezifischer Schwingungsspektren als Funktion der Clustergröße, -zusammensetzung und -temperatur.

Die Möglichkeiten des neuen Aufbaus werden am Beispiel des protonierten Wasserhexamers demonstriert. Die spektralen Signaturen der beiden vorhandenen Strukturisomere können erstmals spektroskopisch über nahezu den gesamten Infrarotbereich ($260 - 3900\,\mathrm{cm}^{-1}$) getrennt werden. Der anschließende Vergleich mit *ab initio* Moleküldynamiksimulationen gibt nicht nur Einblick in einen möglichen Mechanismus für die Verbreiterung der charakteristischen IR-Banden des hydratisierten Protons, sondern ermöglicht außerdem die erste experimentelle Identifizierung der Wasserstoffbrücken-Streckschwingungen beider Isomere (im Terahertz-Bereich). Weitere isomer-spezifische Messungen an größeren protonierten Wasserclustern beantworten die Frage, inwiefern die Anzahl der Isomere mit der Größe der Hydrathülle in Zusammenhang steht.

Struktur, Stabilität und Solvatationsverhalten atmosphärisch-relevanter Nitrat-Komplexe sind das Thema des darauffolgenden Kapitels. Diese Experimente verfolgen den Aufbau eines wasserstoffverbrückten Netzwerks, Molekül für Molekül. Die Ergebnisse zeigen unter anderem, dass der kleinste Cluster, Hydrogendinitrat ($O_2NO-\cdots H^+\cdots -ONO_2$), ein überraschend stabiles symmetrisch gebundenes Proton aufweist, das erst bei weiterer Solvatisierung aufgebrochen wird. Die Spektren der größeren Nitrat/Salpetersäure/ Wassercluster konvergieren bereits zu den Spektren der kondensierten Phase und werden insbesondere im Zusammenhang mit dem Auftreten IRMPD "transparenter" Moden diskutiert.

Anharmonische Effekte in den Schwingungsspektren monohydratisierter anorganischer Säuren werden mittels IRPD Spektroskopie in Kombination mit modernsten quanten-chemischen Methoden, wie *ab initio* Moleküldynamiksimulationen und Schwingungskonfigurationswechselwirkungsrechnungen untersucht.

Summary

Gas phase clusters typically serve as model systems for studying properties of more complex systems under well-defined conditions in the absence of perturbing interactions with an environment. However, some clusters themselves play crucial roles in relevant processes. Charged clusters, for example, represent key precursors in the formation of aerosols in the atmosphere. In order to ultimately improve our understanding of atmospheric processes, in general, and climate simulations, in particular, novel experimental techniques yielding molecular-level insight into their structure, energetics, reactivity and dynamics are required.

The studies presented in this thesis aim at shedding new light on the solvation behavior of hydrogen-bonded cluster ions. Gas phase vibrational spectra are measured by means of mass-selective infrared photodissociation (IRPD) spectroscopy and structures are assigned, based on a comparison between experimental and simulated spectra of different isomers derived from electronic structure calculations. Often multiple isomers are present in the experiment. In order to isolate their individual contributions to the IRPD spectrum, IR/IR double-resonance (IR^2MS^2) spectroscopy is performed. To this end a custom ion trap triple mass spectrometer was conceived, designed and constructed, which allows measuring isomer-specific vibrational spectra over nearly the entire IR spectral range as a function of cluster size, composition and internal temperature.

The capabilities of the new instrument are demonstrated by measuring isomer-specific IR^2MS^2 spectra of the Eigen-type and Zundel-type conformers of the protonated water hexamer from 260 to 3900 cm^{-1}. Comparison to *ab initio* molecular dynamics simulations (AIMD) not only provides insight into the mechanism responsible for the characteristically broad IR absorptions of hydrated protons, but also allows for the first experimental identification of hydrogen-bond stretching vibrations in protonated water clusters (in the terahertz region). This study is then extended to larger protonated water clusters $H^+(H_2O)_n$, addressing the question of how the number of isomers evolves with the size of the hydration shell.

The structure, stability and solvation behavior of atmospherically-relevant nitrate-containing anions is studied. These experiments follow how the hydrogen-bonded solvent network evolves, one solvent molecule at a time. Hydrogen dinitrate contains a surprisingly stable equally-shared proton motif ($O_2NO{-}\cdots H^+ \cdots{-}ONO_2$), which is eventually disrupted upon solvation. The spectra of larger nitrate/nitric acid/water complexes already

converge to those of the condensed phase and are furthermore discussed in the context of "IRMPD transparent" bands.

Finally, anharmonic effects in the IRPD spectra of the singly-hydrated complexes are investigated, aided by state-of-the-art AIMD simulations as well as vibrational configuration interaction calculations.

Contents

Abbreviations **xi**

1 Introduction **1**

1.1 Anions in the Atmosphere 3
1.2 Protonated Water Clusters 6
1.3 Outline of the Thesis 8

2 Vibrational Spectroscopy **11**

2.1 Vibrations in Molecules 12
2.2 Infrared Spectroscopy in the Gas Phase 14

3 Experimental Setup and Characterization **23**

3.1 Triple Mass Spectrometer 24
3.2 Vacuum Design 25
3.3 Electrospray Ionization Sources 29
3.4 Radio Frequency Multipoles 34
3.4.1 Octopole Ion Guides 36
3.4.2 Quadrupole Mass Filter 38
3.5 Detection Scheme and Data Extraction 47
3.6 Double-Focusing Reflectron Time-of-Flight Mass Spectrometer 49
3.7 Electronics 55
3.8 Tandem Mass Spectrometer 57
3.9 Infrared Light Sources 59
3.9.1 FELIX 59
3.9.2 OPO/OPA Infrared Laser Systems 61

4 Isomer-Specific Spectroscopy on Protonated Water Clusters **65**

4.1 Introduction 66
4.2 Experimental and Computational Section 70
4.2.1 Experimental Setup 70
4.2.2 Computational Details 72
4.3 Results and Discussion 72
4.3.1 Single-Color IRPD Spectra of $H^+(H_2O)_{5-10}$ 72

4.3.2 Isomer-Selective Detection of Hydrogen-Bond Vibrations
in $H^+(H_2O)_6$ . . . 75
4.3.3 Disentangling Contributions of Multiple Isomers . . 86
4.4 Advantages and Limits of IR^2MS^2 Spectroscopy . . . 95

5 Microsolvation of Nitrate-Nitric Acid Clusters 97
5.1 Introduction . . . 98
5.2 Experimental and Theoretical Methods . . . 100
5.3 Results . . . 101
5.3.1 Trends in the experimental IRMPD spectra . . . 101
5.3.2 Analysis . . . 107
5.4 Discussion . . . 117
5.5 Summary and Conclusions . . . 120

6 Anharmonicity in the IR spectra of Hydrogen-bonded Clusters 121
6.1 Large Amplitude Motion in Monohydrated Dihydrogen Phosphate . . . 122
6.1.1 Introduction . . . 122
6.1.2 Experimental Details . . . 123
6.1.3 Results and Discussion . . . 124
6.1.4 Conclusions: $H_2PO_4^-{\cdot}H_2O$ . . . 132
6.2 Cubic Coupling between High- and Low-Frequency Modes in Nitrate-Water Clusters . . . 133
6.2.1 Introduction . . . 133
6.2.2 Experimental and Computational Details . . . 134
6.2.3 Results and Discussion . . . 137
6.2.4 Conclusions: Nitrate-Water . . . 146

7 Summary and Future Perspectives 147
7.1 Summary . . . 147
7.2 Future Perspectives . . . 149

A Protonated Water Cluster 153

B Microsolvation of Nitrate-Nitric Acid Clusters 157

C Anharmonic Effects in Monohydrated Acid Clusters 165

Bibliography 175

List of Publications **193**

Lebenslauf **195**

Acknowledgements **197**

Abbreviations

AIMD *ab initio* molecular dynamics simulations

CID collision-induced dissociation

DFM difference frequency mixing

DFT density functional theory

dTOF-MS double-focusing time-of-flight mass spectrometer

ESI electrospray ionization

FEL free electron laser

FELIX free electron laser for infrared experiments

FWHM full width half maximum

HB hydrogen bond

HED high energy dynode

HV high voltage

IR infrared

IR^2MS^2 IR/IR double-resonance

IRMPD infrared multiple photon dissociation

IRPD infrared photodissociation

IRVPD infrared vibrational predissociation

IVR internal vibrational redistribution

MCP micro-channel plate

MD molecular dynamics

OPA optical parametric amplifier

OPO optical parametric oscillator

QMS quadrupole mass spectrum

RET ring electrode trap

RF radio frequency

SHG second harmonic generation

TMP turbomolecular pump

TOF time-of-flight

TOF-MS time-of-flight mass spectrometer

VCI vibrational configuration interaction

ZPE zero-point energy

Chapter 1

Introduction

In recent years, the public discourse on climate related topics has significantly changed and the need to pursue a cleaner atmosphere has finally reached a wide range of people. Subjects like “acid rain” or the “ozone hole” are now generally known and accepted problems, which require a fundamental understanding of our complex climate system to be resolved. Great efforts have thus been undertaken to unravel the manifold of chemical processes behind these phenomena [1]. However, one of the largest uncertainty in atmospheric processes to date is related to the influence of aerosols on climate and human health, as they affect, for instance, the air quality or have a cooling effect by intercepting incoming sunlight [2].

Aerosols are stable suspensions of solid and/or liquid particles in the air which can either be emitted from the Earth’s surface or grow through the condensation of organic [3] or inorganic [4] particles directly in the atmosphere. By current estimates, formation of aerosol particles through “nucleation”, meaning clustering of small, and often hydrogen-bonded particles, is likely to be a key element in climate relevant processes [5]. But how can small particles, consisting of one or a few molecules develop into aerosols? To ultimately answer this question it is essential to understand the initial steps of nucleation, starting from a single molecule or molecular ion, and then follow its structural evolution as a function of size.

For probing the properties of growing particles, gas-phase studies have proven to be a powerful technique, as they provide a high degree of control regarding size, composition and charge state of gaseous ions, all in the absence of any perturbing interaction with an environment. In particular, the combination of state-of-the-art ion trapping and mass spectrometric schemes with vibrational spectroscopy has emerged as one of the most generally applicable tools for the structural characterization of hydrogen-bonded ions in the gas phase [6–10, 10–15]. This technique allows for the systematic study of aerosol formation by addition of solvent molecules to a central ion in a stepwise fashion, a process which is also referred to as microsolvation.

Vibrational spectroscopy, and in particular Infrared Photodissociation (IRPD) spectroscopy, on microsolvated clusters is not only important for unraveling the structure of small aerosol particles, but has also proven valuable in providing molecular-scale insights into the physicochemical properties of macroscopic systems, such as protons in liquid water [7]. These can be accessed in a bottom-up approach, using single protonated water molecules as model systems for shedding new light on our understanding of the structural evolution of hydrogen-bonded networks.

There are, however, several aspects that significantly challenge the interpretation of IRPD spectra, for instance, a high internal energy of the ions, population of multiple isomers, and anharmonicity. A high internal temperature of the clusters, for example, often leads to thermal fluctuations, as local molecular environments, in particular of hydrogen-bonded networks, rearrange constantly. This is reflected in diffuse spectral features which are difficult to discern. A low internal temperature is thus crucial, as it allows to quench complex systems into configurations with minimal thermal fluctuations which usually exhibit sharp vibrational bands.

While small clusters, up to a few molecules, typically adopt a single structure, larger systems are prone to populate several nearly iso-energetic isomers. This holds in particular true for hydrogen-bonded clusters. The contribution of several isomers to the vibrational spectrum, despite low internal temperatures, significantly complicates the assignment of the spectrum. Various approaches have been developed to separate isomers mass spectrometrically or spectroscopically. Ion mobility spectrometry, for example, constitutes one of the most powerful mass spectrometric techniques [16–18]. It exploits the fact that the collision cross section depends on the shape of the isomer, which leads to different arrival times after traversing a buffer-gas filled drift tube. A frequently employed spectroscopic method is ion-dip spectroscopy. Here, isomer-specific electronic transitions are excited in order to eliminate or probe individual isomer populations using a combination of ultraviolet and infrared lasers [19–23]. A drawback of the latter method is the requirement of an electronic chromophore or a photodetachable electron. A recently developed variation of this technique is population-labeling IR/IR double resonance spectroscopy (IR^2MS^2) [24–28], which relies entirely on excitations within the vibrational manifold.

One of the central goals of the work presented in this thesis is the design, development and implementation of a novel setup, allowing for isomer-specific measurements on ions with low internal energies. The combination of this apparatus with the widely tunable radiation from an IR free electron laser and with tabletop IR laser systems provides the possibility to explore the potential energy surface of molecular clusters over almost the entire IR spectral range. In particular, these techniques are used to unravel isomer distributions in small protonated water clusters, and to follow the structural evolution of nitrate-containing clusters.

The interpretation of IRPD spectra is accomplished by comparison with electronic structure calculations. These are for hydrogen-bonded clusters often complicated by anharmonic effects in the IR spectra. Therefore, it becomes increasingly evident that sophisticated quantum chemical tools which go beyond the harmonic approximation, are required [29–35]. The interpretation of various anharmonic effects in the IRPD spectra presented in this thesis is achieved in close collaboration with theory groups, employing cutting edge theoretical methods. The following section is aimed at providing general background information on the role of anions in the atmosphere and protons in water.

1.1 Anions in the Atmosphere

Small hydrogen-bonded ionic clusters are ubiquitous throughout all layers of the earth's atmosphere, where they influence manifold chemical and physical processes. They also play a role in new particle formation [36–38], which is, to date, extensively studied and subject to great controversy. Ion-mediated aerosol-formation constitutes one of the largest present uncertainties in the field of atmospheric studies, thus limiting our ability to make accurate projections of the climate [5, 39].

New particle (aerosol) formation is thought to be limited by the initial growth steps [3]. Standard field measurements, however, are not sensitive to particles below a few nanometers [40–42], and therefore information on the seed particles, which fall in the range from single ions/molecules to small nanoparticles, entirely rely on laboratory experiments. Mass spectrometric investigation on the efficiency of the nucleation process, for instance, revealed that small molecular clusters are stabilized by the incorporation of an ion, and that negative ions serve as more effective nucleation sites than positive ions [43–45].

Negative ionic clusters containing nitrate (NO_3^-) and bisulfate (HSO_4^-) are among the most abundant anions in the troposphere and stratosphere, in particular, clusters of these ions with water, and the undissociated acids nitric acid and sulfuric acid [38, 46–48]. Anions were first measured in the upper stratosphere (~35 km) over 35 years ago by Arnold using a

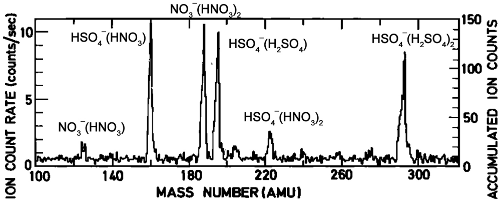

Figure 1.1: One of the first mass spectra of small anionic clusters taken in the upper stratosphere. The figure is adapted from Ref. [46].

balloon-borne mass spectrometer [47]. Figure 1.1 displays one of these mass spectra from 1981 [46], which comprises an almost equal distribution of the aforementioned microsolvated nitrate- and bisulfate ions. These are, typically, directly formed in the atmosphere by gaseous precursor molecules, such as NO_x and SO_2, emitted, for instance, by volcanic eruptions or combustion [49, 50]. The precursors are then oxidized by OH radicals to the neutral acids, and their conjugated bases are formed via interaction with galactic cosmic rays, radioactivity or electric discharges, such as corona or lightning [38]:

$$SO_2 + OH \longrightarrow HSO_3$$
$$HSO_3 + O_2 \longrightarrow SO_3 + HO_2$$
$$SO_3 + H_2O \longrightarrow H_2SO_4 \longrightarrow HSO_4^- + H^+$$

Nucleation of aerosol particles derived from trace vapors in the atmosphere is thought to provide a considerable amount of global cloud condensation nuclei (CCN) [5]. The extent of the contribution of ionic species to CCN formation, however, is still much debated [5, 38, 51]. CCN, in turn, are important precursors for cloud droplets, which are formed in a process known as gas-to-particle conversion. Figure 1.2 shows a scheme of this process, which may be initiated by a single ion or molecule condensing through collisions with neutral molecules to a cluster. At the critical cluster size (Figure 1.3), a nucleation barrier has to be overcome. Here, the ion-induced pathway is energetically favored (red line), since the incorporation of an ion significantly reduces the cluster size and nucleation barrier. Thus, this pathway is mainly limited by the ion production rate and life time. Once the (neutral) cluster has overcome the nucleation barrier, new thermodynamically stable aerosols are formed [45, 52].

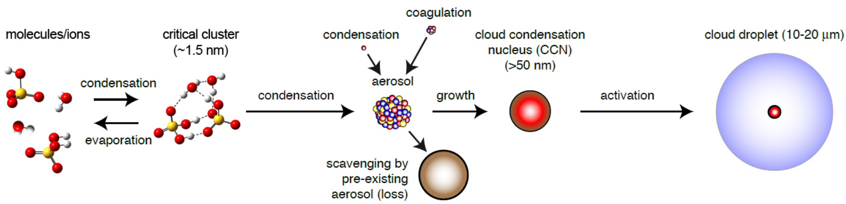

Figure 1.2: Trace gas-to-particle conversion: nucleation of particles in the first step may be ion-induced. Figure taken and adapted from Ref. [53].

However, many aspects of this process are still poorly understood and obtaining direct and detailed information concerning the initial nucleation step is a challenging task [54]. Aerosol chambers such as SAPHIR in Jülich [55] or CLOUD [56] at the CERN facility serve as platforms to study atmospheric-chemical mechanisms. The chambers provide a high degree of control over different parameters, such as temperature, humidity and particle concentration, and therefore allow for their well-defined alteration, concomitant with detection and analysis by a variety of advanced instrumental techniques attached to the chambers. The CLOUD project, for instance, uses a high-energy particle beam, provided by the CERN proton synchrotron, to mimic galactic cosmic rays, which ionize seed particles, and thus provides fundamental insight into the influence of radiation on cloud formation [5, 44]. As a complementary approach, the nucleation

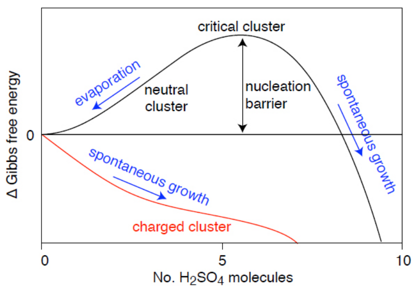

Figure 1.3: Thermodynamic representation of aerosol nucleation. The change of the Gibbs free energy is plotted as a function of cluster size without (upper panel) and with incorporated ion (lower panel). Figure adapted from Ref. [52].

process can also be monitored spectroscopically, in order to get a detailed picture of the structure of the involved clusters. These studies thus provide further molecular-level insight which is necessary for shedding light on the microscopic stability, conformation, reactivity and dynamics from the first individual molecules all the way to bulk aerosols.

The most recent research of our group addressed, for example, the following questions [15, 57–62]: how are ions solvated on a molecular level, *i.e.* is the solvation shell symmetric or asymmetric? How many water molecules are required to complete the first hydration shell and how many to separate an ion pair? Is the pH value still a reliable quantity at a molecular level? Particularly surprising is the answer to the last question. IRPD studies on microsolvated bisulfate/nitric acid (or nitrate/sulfuric acid, respectively) clusters revealed that the charge localization intimately depends on the size and composition of the clusters and cannot be reliably predicted from known gas phase acidities [61]. Further studies on pure bisulfate/sulfuric acid clusters show a recurring triply hydrogen-bound configuration, which can be disrupted by the incorporation of water [63]. As a continuation of these studies, hydrated nitrate/nitric acid and phosphate clusters are presented in Chapters 5 and 6.

1.2 Protonated Water Clusters

Water plays a central role in diverse fields, ranging from atmospheric science to solution chemistry and biology, as it is one of the most abundant molecules on earth [3, 64–66]. It dictates the structure of proteins and DNA, participates as a medium in various chemical reactions, or serves as cloud condensation nucleus in the atmosphere [67].

The properties of water are characterized by its anomalies, which have a critical impact on our ecosystem. It is, for instance, the only molecule on earth that occurs naturally in all three common states of matter, and the fact that it is densest at 4°C, rather than becoming steadily denser with decreasing temperature allows for life in cold aqueous environments [68]. The reason for these properties is connected to strong oriented electrostatic interactions between individual H_2O molecules in water. H_2O itself possesses highly polar covalent bonds, leading to strong dipole-dipole, as well as other short range interactions in-between the electronegative oxygen atom of one water molecule and the hydrogen atoms of the others. The structure of liquid water is in general described as a highly dynamical hydrogen bonded network of water molecules, in which hydrogen bonds are formed and broken on a time scale ranging from 10 fs to 10 ps [69].

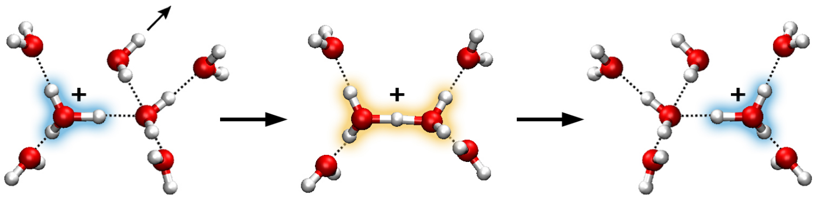

Figure 1.4: Illustration of the Grotthuss mechanism. The excess charge is transferred along a water wire by rearrangement of two limiting binding motifs: the Eigen- (blue) and Zundel-type (yellow).

The rapid rupture and reformation of hydrogen-bonds is a prerequisite for another fundamental and intriguing process occurring in liquid water, namely proton transfer. The anomalously high proton mobility has captivated scientists for more than 200 years [70], but the nature of the excess charge in an aqueous environment remains elusive [71, 72]. A commonly accepted picture involves the transfer of the proton via the Grotthuss mechanism [73–75], wherein the proton is transferred along the hydrogen-bonded network by a structural diffusion process, as depicted in Figure 1.4 [70]. The two limiting structures, in a continuum of intermediate structures, involved in this process have been originally proposed by Eigen [76] and Zundel [77] and consist either of a symmetrically solvated hydronium ion, ${H_9O_4}^+(aq)$, or an equally shared proton, ${H_5O_2}^+(aq)$, respectively. The Zundel structure is thought to be the proton-transferring complex, with a characteristic central antisymmetric O-H stretching mode, also referred to as the shared-proton stretching mode. IR spectra of protons in solution, however, only reveal remarkably diffuse features [78–80].

In this regard, small protonated water clusters, $H^+(H_2O)_n$, are particularly attractive as they represent microscopic models for hydrated protons in the condensed phase, but are amenable to the highest-level quantum chemical methods, as well as gas phase studies.

In the early 70s Fenn studied protonated water clusters mass spectrometrically [81], followed by flow tube dynamics [82], vibrational spectroscopy [29, 83–90] and theory [30, 80, 91–93]. Multiple experimental cluster studies, probing the sequential hydration of the proton in the gas phase, indicate that clusters with $n \leq 5$ only adopt one of the limiting structures that is known from the condensed phase, whereas larger clusters can possess both forms [29, 83, 84, 87, 94–98].

Just recently, the conventional picture of these two limiting structures in the gas phase was challenged based on the results of AIMD simulations [92, 93]. This triggered a lively debate concerning the relative stability of the corresponding binding motifs. On the other hand, new experimental studies, including results presented in Chapter 4, support the original hypothesis [90]. Regardless of which picture is correct, the discussion illustrates how difficult it still is to pinpoint only single characteristics, even at moderate cluster sizes.

1.3 Outline of the Thesis

A key aspect of this thesis is the development of new experimental techniques, combining both mass spectrometric and spectroscopic elements. These techniques are then used to shed new light on the solvation behavior of hydrogen-bonded clusters in the gas phase and to unravel their IRPD spectra by taking different aspects like the internal cluster temperature, contribution of different isomers and anharmonic effects into account.

The following chapter gives a brief introduction to the principles of vibrational spectroscopy, with emphasis on the study of low-density clusters in the gas phase. The concept of single (IRPD) and multiple (IRMPD) photon dissociation spectroscopy is outlined, including a short discussion on IRMPD transparency and the influence of messenger tagging on the structure (Chapter 2).

Chapter 3 describes the new custom triple mass spectrometer that was conceived, designed and constructed as part of this thesis. This setup allows measuring isomer-specific vibrational spectra over nearly the entire IR spectral range as function of cluster size, composition and internal temperature. The individual experimental methods involved in the generation, sampling, thermalization and analysis of microhydrated clusters are explained and the performance of the ion trap is evaluated in terms of maximum ion capacity and lowest achievable internal temperature. Moreover, a new method to measure IR/IR isomer-specific spectra is introduced and described using the example of protonated water clusters.

Isomer-specific measurements of protonated water clusters are then presented in Chapter 4. In particular, the protonated water hexamer is investigated over almost the entire IR spectral range, including the region of water "librational" and "translation" bands in the far-IR. These are assigned by comparison to AIMD simulations. In the second part of this chapter, the contribution of different isomers to the spectra of larger protonated water clusters is unraveled. The chapter ends with a discussion of the advantages and limits of IR^2MS^2-spectroscopy.

Chapter 5 illustrates the early steps of acid solvation as a function of cluster size for nitrate/nitric acid/water clusters. The evolution of the structure is followed as a function of solvent molecules, which are either nitric acid, water or both.

In Chapter 6 several prominent examples for anharmonic effects occurring in hydrogen-bonded clusters are discussed. The first part of this chapter deals with large amplitude motion in $H_2PO_4^- \cdot H_2O$, while the second part illustrates the effects of mode-coupling and Fermi resonances on the IRPD spectrum in monohydrated nitrate clusters. The assignment of spectral features is achieved by comparison to AIMD and vibrational configuration interaction (VCI) calculations.

This thesis concludes with a summary and outlook discussing future possibilities.

Chapter 2

Vibrational Spectroscopy

Gas phase vibrational spectroscopy serves as a powerful and versatile tool to probe the structure of molecular systems. It exploits the fact that molecules exhibit a unique vibrational pattern, typically in the IR spectral region. The vibrational properties of a molecular system are directly connected to the force constants of chemical bonds and hence to the molecular structure. Thus, a rotationally-resolved vibrational spectrum yields a unique and specific fingerprint of a molecule. In the absence of rotational resolution, comparison of the experimental IR spectra to simulated ones from electronic structure calculations offers a generally applicable approach for the structural investigation of such systems.

This chapter aims to give a brief introduction to IR spectroscopy on low-density clusters in the gas phase. First, the basic principle of vibrations in molecules is discussed (Section 2.1). In Section 2.2 the general concepts of IR spectroscopy are outlined and two dissociation pathways are described: 1) Infrared multiple photon dissociation (IRMPD) and 2) Infrared Vibrational Predissociation (IRVPD). The last part of this chapter focuses on those modes that are transparent for the IRMPD mechanism, and on how messenger-tagging affects the cluster structure.

2.1 Vibrations in Molecules

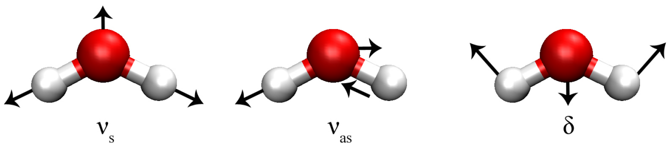

Figure 2.1: Normal modes of the water molecule: symmetric stretching (ν_s), antisymmetric stretching (ν_{as}) and bending (δ) mode.

A non-linear molecule, consisting of N atoms, exhibits $3N$-6 vibrational degrees of freedom ($3N$-5 for linear molecules). These vibrations can be represented as a superposition of $3N$-6 (or $3N$-5) normal modes of the system. For each normal mode, all atoms oscillate in phase with the same frequency, but different amplitudes. This oscillatory motion is described by atomic displacements along a single coordinate, the reduced mass-weighted normal coordinate. As an example, Figure 2.1 represents the three normal modes of the water molecule, the relative displacement of the individual atoms is illustrated by arrows.

The vibrational motion of a system is often described within the harmonic approximation [99]. The harmonic displacement of each atom is then given by the potential energy V, with

$$V = \frac{1}{2}k(r - r_e)^2, \tag{2.1}$$

where k is the force constant and $r - r_e$ the deviation from the equilibrium distance r_e. For each harmonic oscillator the vibrational energy levels, E_n, are given by

$$E_n = h\nu\left(n + \frac{1}{2}\right), n = 0, 1, 2, ... \tag{2.2}$$

where h is the Planck constant, ν the eigen frequency of the normal mode, and n the vibrational quantum number. Within the harmonic approximation the energy levels, E_n, are equally spaced, and for the ground-state the so-called zero-point energy (zpe) $E_0 = \frac{1}{2}h\nu$ is obtained.

A molecular vibration can be probed by the resonant absorption of a photon of energy $h\nu$, which leads to the excitation of that particular vibrational mode. The transition between the $\nu = 0$ (vibrational ground state) and $\nu = 1$ levels is referred to as fundamental transition. Vibrational transitions are only excited (IR-active) if the molecular dipole moment changes during the vibration, and the intensity of the resulting absorption band is proportional to the square of the transition dipole moment. The vibrational frequency, ν, of a mode is given by

$$\nu = \frac{1}{2\pi}\sqrt{\frac{k}{\mu}}, \tag{2.3}$$

where μ is the reduced mass.

The harmonic approximation is typically valid as long as the atomic displacements are small. However, it cannot account for the formation and rupture of molecular bonds. With increasing vibrational energy bonds weaken and are eventually broken, leading to the dissociation of a molecule. An analytical approximation of an anharmonic potential is given by the Morse potential [100]

$$V_m(r) = D_e\left(1 - e^{-a(r-r_e)}\right)^2, \tag{2.4}$$

where r is the relative distance between two atoms, r_e the equilibrium bond distance, and D_e the dissociation energy. Figure 2.1 displays a Morse potential as a function of internuclear separation r. $V_m(r)$ is only approximately harmonic in the vicinity of r_e, whereas for increasing r the potential energy converges towards the dissociation energy D_e. The energy levels, E'_n, of a Morse oscillator are given by

$$E'_n = h\nu\left(n + \frac{1}{2}\right)\left[1 - \chi\left(n + \frac{1}{2}\right)\right], \tag{2.5}$$

where χ is the anharmonicity constant. A positive anharmonicity ($\chi > 0$) leads to a decrease in the spacing of adjacent energy levels with increasing energy.

Anharmonicity also permits IR-active transitions that correspond to changes in quantum number n from ground to higher levels with $\Delta n = \pm 2$, ± 3 ..., so-called overtones. Simultaneous excitation of multiple vibrational modes, commonly referred to as combination bands, becomes possible as well. The intensities of these bands, however, are usually much smaller compared to these of the fundamental transitions.

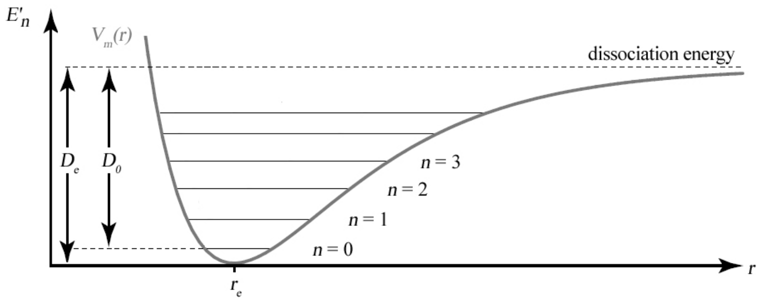

Figure 2.2: Morse potential with vibrational energy levels. D_0 denotes the dissociation energy of the molecule including zpe: $D_0 = D_e$-$\frac{1}{2}h\nu$.

2.2 Infrared Spectroscopy in the Gas Phase

Commonly, IR spectra of molecules are recorded via direct absorption spectroscopy, such as Fourier transform IR spectroscopy. This method detects the attenuation of light by a sample with n molecules/cm^3 and the frequency-dependent absorption cross section $\sigma(\nu)$. The change in light intensity at a frequency ν is given by the Beer-Lambert law [101]

$$I(\nu) = I_0(\nu)e^{-\sigma(\nu)nl}, \tag{2.6}$$

where I_0 denotes the intensity of the incoming light, I the intensity of the transmitted light, and l the optical path length.

A prerequisite for direct absorption spectroscopy is a sufficiently high number density of molecules in the sample of about 10^{10} molecules/cm^3, or, if the concentration is too low, an elongation of the optical beam path, *e.g.* using Cavity Ring-Down Spectroscopy (CDRS). Here, sample concentrations down to $\sim 10^8$ molecules/cm^3 can be measured [102, 103]. The application of direct absorption spectroscopy to gas-phase clusters, however, is rather challenging. Typically, achievable ion densities of mass-selected clusters in the gas phase are on the order of $\leq 10^7$/cm^3, limited by space charge (see Chapter 3.4.2). A change in intensity is thus too small to be detected.

Instead of measuring direct absorption, alternative methods have been developed using the effect of photon absorption on molecular systems. As this method relies on a response of the system to the light, it is also referred to as action spectroscopy. The intensity of light in Equation 2.6 is here replaced by the number density, and the population is detected prior, n_1, and after, n_2, interaction with the light [104]:

$$n_1(\nu) = ne^{-\sigma(\nu)F}, \tag{2.7}$$

$$n_2(\nu) = n(1 - e^{-\sigma(\nu)F}), \tag{2.8}$$

where $F(\nu)$ is the photon fluence in photons/cm^2. Instead of a high number density, this technique relies on a large number of photons, and therefore requires intense light sources.

Different types of actions are conceivable to follow an absorption process: a) change in quantum state, b) emission of photons, c) change in charge, or d) change in mass [104, 105]. One variant of the latter technique is Infrared Photodissociation (IRPD) Spectroscopy which is one of the most common approaches of action spectroscopy today. IRPD spectroscopy detects the photodissociation yield of molecules as a function of the laser frequency, using mass spectrometric schemes. Owing to the high photon fluence dissociation can occur either after the absorption of a single (IRPD) or of multiple (IRMPD) photons. An introduction to both mechanisms is given in the following sections.

Infrared Multiple Photon Dissociation

Dissociation thresholds, D_0, of covalently bound ionic clusters or complexes with strong hydrogen bonds, are typically $\geq 1\,\text{eV}$ ($8000\,\text{cm}^{-1}$), while their fundamental vibrations are found below this limit. Consequently, photodissociation often requires the absorption of multiple IR photons:

$$AB \xrightarrow[1]{h\nu_{IR}} (AB)^* \xrightarrow[2]{h\nu_{IR}} (AB)^* \xrightarrow[\text{n}]{h\nu_{IR}} A + B, \tag{2.9}$$

where n is the number of absorbed photons. Hence, this mechanism is referred to as Infrared Multiple Photon Dissociation (IRMPD).

Mechanism. Dissociation by absorption of many monochromatic photons in a purely coherent process is unrealistic due to the anharmonicity that governs vibrational potentials, the so-called “anharmonic bottleneck”. Figure 2.3 illustrates the mechanism of IRMPD [106–108]. The process can be divided into three overlapping regions: a) resonant absorption, b) absorption in the quasi-continuum region, and c) absorption above the dissociation limit and dissociation.

An absorption event takes place, when the frequency of an IR photon is in resonance with an IR active vibrational transition. In the first region (a in Figure 2.3), photons are resonantly absorbed between discrete ro-vibrational states, *i.e.* the vibrational quantum number within a single vibrational mode is raised by one, upon the absorption of each photon. Small anharmonic shifts between adjacent energy levels can still be compensated for by changes in the rotational quantum number or the bandwidth of the laser, but the internally excited system will eventually reach the "anharmonic bottleneck", where further resonant absorption is unlikely.

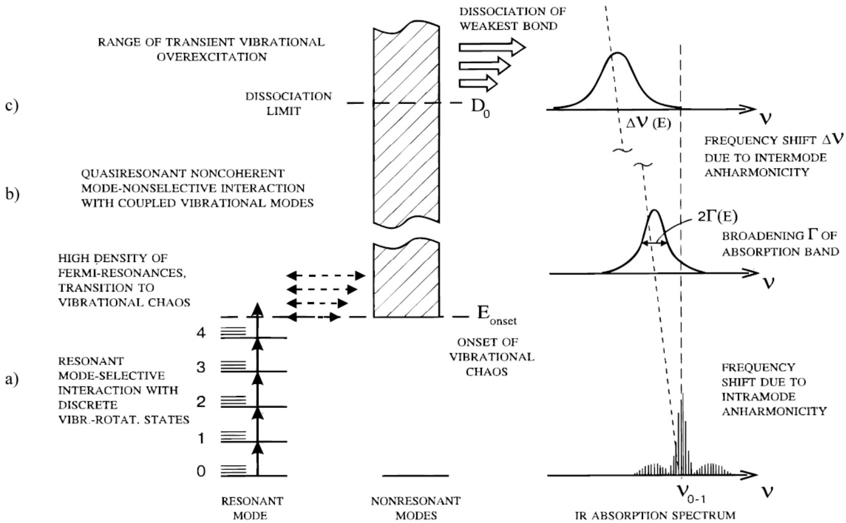

Figure 2.3: Schematic of the infrared multiple photon dissociation mechanism in a polyatomic molecule. Figure adapted from Ref. [109]. See text for details.

With every absorbed photon the internal energy, E_i, increases, and the vibrational density of states, $\rho(E_i)$, rises rapidly. The increase of $\rho(E_i)$ roughly scales with E_i^N, where N is the number of vibrational degrees of freedom [110]. This region is commonly referred to as the *quasi-continuum* region (Figure 2.3 b). In contrast to vibrational ladder climbing, the absorbed energy is quickly dissipated between the vibrational modes, due to anharmonic coupling between bright, absorbing states and dark, background states. This process is referred to as intramolecular vibrational redistribution (IVR) [111]. It allows for a rapid depopulation of the excited energy levels and thus facilitates the absorption of more photons. For large molecules typical timescales for IVR are in the range of $10^{-11} - 10^{-12}$ s.

These short vibrational lifetimes result in a broadening of absorption lines as shown on the right side of Figure 2.3. The transition between the discrete regime and the quasi-continuum depends on the interaction strength between vibrational modes, as well as on the vibrational density of states.

While the *quasi-continuum* is characterized by the semi-resonant absorption of photons close to the original fundamental transition [108, 112], dissociation of the molecule in the *continuum region* readily occurs upon incoherent absorption of IR photons of any wavelength (Figure 2.3 c). This region is only reached at very high internal energies, resulting in a dramatic increase in the density of ro-vibrational states. As a result of strong anharmonic coupling between the quasi-bound states above the dissociation limit, IVR occurs on a time scale much faster than the absorption rate and the vibrational energy is statistically redistributed over all vibrational degrees of freedom [108].

For highly excited molecules two cooling channels are possible, either the emission of photons (radiative cooling) or of particles (evaporative cooling), such as electrons (ionization), atoms or molecular fragments (dissociation). Radiative cooling typically is the only open channel at lower energies, while evaporative cooling prevails at higher internal energies. Dissociation is often favored over ionization, since the lowest energy fragmentation channel lies usually below the first ionization energy [108, 112].

IRMPD Transparency of Vibrational Modes. The efficiency of the IRMPD mechanism depends on the nature of the initially excited vibrational mode. Modes, which are IR-active, but not observed in the IRMPD spectrum are termed IRMPD *transparent*. These modes can be partially or fully recovered by lowering the dissociation limit of the system, *e.g.* by messenger-tagging (see following section). In order to explain the type of these modes, three mechanisms, based on experimental observations, have been proposed [63, 113–115]. These include (a) a change in the fundamental frequency upon heating, (b) a change in the transition dipole moment upon heating and (c) non-statistical mode-specific fragmentation. In the following each mechanism will be discussed in more detail based on selected examples.

(a) Studies on hydrogen-bonded (HB) microsolvated clusters, such as $NO_3^- \cdot H_2O$, $HSO_4^-(H_2O)_n$ or $HSO_4^-(H_2SO_4)_n$ [57, 61, 63, 116], have shown that their IRMPD signatures lack some vibrational features observed in the corresponding IRPD spectra of the messenger-tagged species. Messenger-tagged complexes typically yield spectra close to the linear absorption

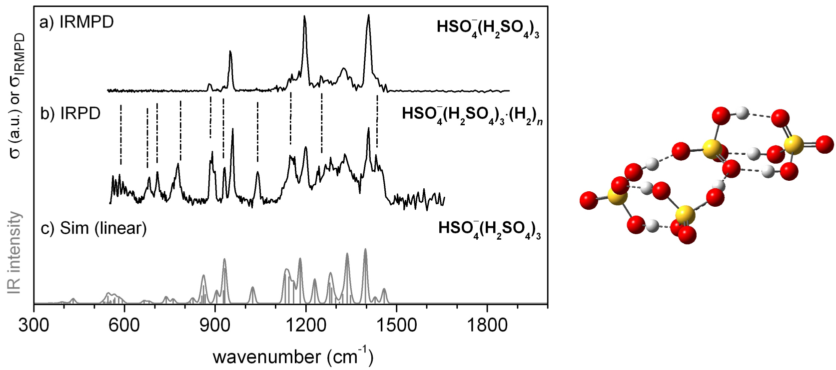

Figure 2.4: Comparison of the IRMPD spectrum of $HSO_4^-(H_2SO_4)_3$ (a) to the IRPD spectrum of the corresponding H_2 messenger-tagged species (b) and the simulated linear absorption spectrum (c). Dashed lines indicate IRMPD *transparent* modes. The figure is adapted from Ref. [63].

regime, and are thus more reliable, when compared to simulated linear absorption spectra. Vibrational modes involving weak HBs are most strongly affected by this mechanism. Absorption of the first or first few photons and subsequent IVR cycles leads to an increase of the internal energy of the cluster, followed by the rupture of one or more HBs, but without dissociation of the cluster. This leads to conformational change and consequently, some (but not all) vibrational frequencies change and may be shifted out of resonance, abruptly terminating the absorption process. For modes that are not affected by the conformational change, the IRMPD efficiency remains the same [63]. Particularly lower frequency modes, *e.g.* librational modes, are affected by this process, because they are sensitive to changes in the HB network and also require more absorption cycles before dissociation.

An example of this mechanism is shown in Figure 2.4 for $HSO_4^-(H_2SO_4)_3$. The upper panel shows the IRMPD spectrum, the middle panel the H_2-predissociation spectrum and the lower panel the simulated linear absorption spectrum of the global minimum isomer. Dashed lines indicate IRMPD *transparent* modes. *Transparent* modes are observed with lower than expected or no intensity in the bare cluster, but can be fully recovered by lowering the dissociation limit using the messenger-technique.

(b) The second mechanism involves shallow minima on the potential energy surface. Absorption of a single IR photon is sufficient to overcome the conformational barriers, leading to large amplitude motion and a substantial decrease of the transition dipole moment. As an example the spectra of $NO_3^-(HNO_3)_3$ are shown in Chapter 5.

(c) Finally, a mechanism involving mode-specific fragmentation has been suggested by Pankewitz *et al.* [113] based on the interpretation of the IRMPD spectra of $NH_4^+(H_2O)$ in the OH-stretching region. This spectrum has been remeasured and is shown in Figure 2.5. It displays the symmetric (ν_1) and antisymmetric (ν_3) stretching modes of the two OH oscillators of water, both giving rise to partially-resolved rotational structure, as illustrated for ν_3. The IRMPD spectrum exhibits an unexpected ratio of the $\nu_3(H_2O)$ to $\nu_1(H_2O)$ intensity, which is substantially smaller than observed in single photon absorption spectra and simulated linear absorption spectra. The authors speculate that the fragmentation yield $I(\nu_3)/I(\nu_1)$ varies for different vibrational modes as a consequence of differences in coupling efficiency between the individual oscillators, leading to diverging IVR rates [113].

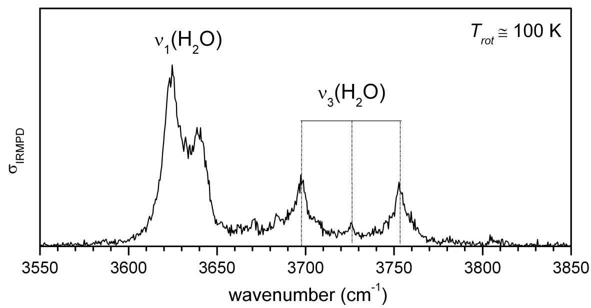

Figure 2.5: IRMPD spectrum of $NH_4^+(H_2O)$ in the O-H stretching region, measured at $T_{rot} \approx 100\,K$. ν_1 corresponds to the symmetric, ν_3 to the antisymmetric O-H stretching mode of H_2O. The observed ratio of both modes is significantly lower (0.4) than by theory predicted (2.7) [113].

As discussed above, the IVR rate must proceed faster than the absorption rate in order to observe photodissociation. Consequently, vibrational modes with the most rapid IVR will be favored over those with slower IVR rates [114].

Infrared Vibrational Predissociation

As discussed in the previous section, the absorption of multiple photons may lead to effects that significantly complicate the assignment of the corresponding IRMPD spectra compared to linear (single photon) IRPD spectra. Furthermore, some clusters are so strongly bound, *e.g.* metal clusters, that even the high photon fluence provided by a free electron laser is not sufficient to induce dissociation.

A useful method to avoid IRMPD is to decrease the dissociation limit using the messenger-technique. This is achieved by attaching a weakly-bound ligand, the so-called messenger, to the cluster [117, 118]

$$AB \cdot M \xrightarrow{\mathrm{h}\nu_{IR}} (AB)^* \cdot M \rightarrow AB + M \tag{2.10}$$

After the absorption of a single photon, the increase in internal energy is already sufficient to overcome the dissociation limit and subsequent IVR into the dissociation coordinate leads to the detachment of the messenger. Typically, the lower internal energies in ion-messenger complexes result in slower IVR rates, which is reflected in significantly reduced lifetime broadening and narrower line widths. This technique is also referred to as Infrared Vibrational Predissociation (IRVPD) [119].

Typically, atoms with small polarizabilities, such as the rare gases Helium (He), Neon (Ne) or Argon (Ar), but also other gases, *e.g.* Hydrogen (H_2), are used as a messenger. These are bound by charge-induced dipole interactions to the cluster. The binding energy can be estimated from their polarizabilities (rare gases [120]) or proton affinities (molecules [121]). Ideally, the ligand acts solely as a messenger, without perturbing the geometric and electronic structure of the absorber, and thus the spectrum of the ion-messenger complex reflects the IR spectrum of the bare ion [105]. Using He as a messenger approaches this ideal picture quite well for singly-charged ions. However, this assumption is not necessarily valid for heavier and more polarizable ligands such as Ar [122]. It has been shown in multiple experiments, mainly involving metal and metal oxide clusters, that certain messengers have a significant impact on the structure or the isomer distribution [110, 122–124]. Also for hydrogen-bonded complexes the influence of the messenger has been systematically studied as a function of the nature of the messenger [95, 125]. The charge delocalization in hydrated proton clusters is very sensitive to changes in the hydration shell environment [95, 125, 126]. One example is shown in Figure 2.6 [125]. Here, the IRMPD spectrum of the protonated water hexamer is compared to

IRPD spectra with various messengers. Spectral signatures of two isomers are observed in the IRMPD spectrum, referred to as "Zundel-type" (red) and "Eigen-type" (blue) structures. Addition of an Ar atom, commonly used as a messenger species, preferentially stabilizes the Zundel-type isomer. Also Kr favors this isomer, whereas N_2 distorts both structures, evidenced by the splitting of some bands (marked with an asterisk). In contrast, tagging with Ne and H_2 is less perturbing and yields isomer distributions similar to the bare, untagged cluster cations.

Since complexes with He and Ne usually are more difficult to form, H_2 is exclusively used throughout this thesis. Another advantage of H_2, compared to heavier messengers, like Ne and Ar, is that collisional excitation of the trapped species is minimized. H_2 also exhibits one internal degree of freedom that facilitates the acceptation of vibrational energy of the trapped ions in a cold environment [127].

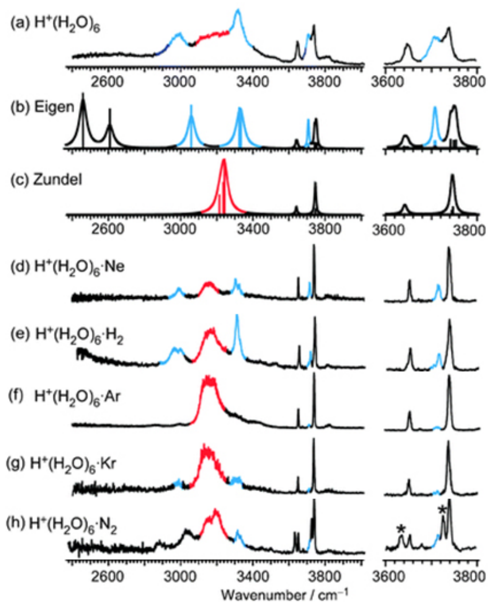

Figure 2.6: Comparison of bare and messenger-tagged IR spectra of $H^+(H_2O)_6$: (a) IRMPD (b) calculated IR spectra of the Eigen- and (c) Zundel-type isomers (d-h) IRPD spectra of $H^+(H_2O)_6 \cdot M$ with different messengers M. The spectra shown in (d) and (e) show the least influence upon tagging. Figure adapted from Ref. [125].

Chapter 3

Experimental Setup and Characterization

The following chapter gives a detailed description of the instrumental setup that has been designed, constructed and implemented as part of my PhD thesis research. The instrument, schematically shown in Figure ref-fig:setup3D, combines a linear nanospray ion source (Section 3.3) with multiple RF devices in order to guide, mass-select and thermalize ions (Section 3.4). A key feature of this instrument is a custom-built linear reflectron double-focusing time-of-flight mass spectrometer (dTOF-MS), which allows for the IR-MS-IR-MS (IR^2MS^2) capability required for IR/IR population labeling spectroscopy (Section 3.6). Section 3.8 briefly outlines the differences and improvements of the new setup compared to the existing 12 K tandem mass spectrometer. The 12 K setup was employed for the experiments presented in Chapters 4-6, and was also equipped with a dTOF-MS as part of this PhD work. The last section of this chapter (Section 3.9) deals with the three different light sources that are used to perform IRPD experiments.

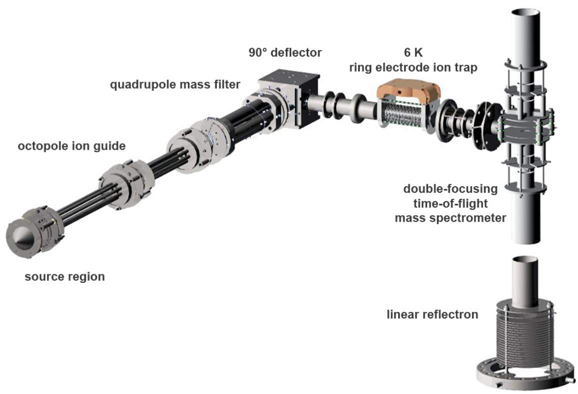

Figure 3.1: Schematic 3D-view of the triple mass spectrometer.

3.1 Triple Mass Spectrometer

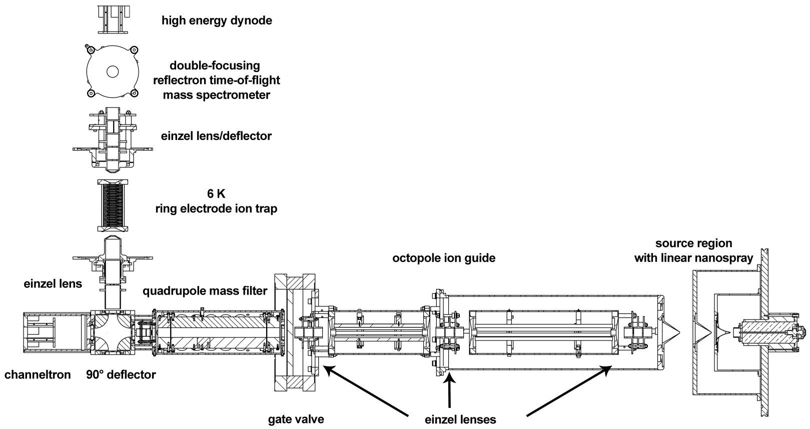

Figure 3.2: Schematic top view of the triple mass spectrometer.

Figures 3.1 and 3.2 show an overview of the ion optics in the new 6 K instrument. Gas phase clusters are generated in a heatable linear nanospray source (Section 3.3) and transferred into vacuum over two differentially pumped pressure stages, separated by skimmers. The ions are then sampled by a third 4 mm skimmer and focused with an einzel lens into a two-stage radio-frequency (RF) octopole ion guide, which collimates and compresses the ion beam in phase space through collisions with a buffer gas (Section 3.4.1). The ion guide is followed by a commercial quadrupole mass filter, with a mass range of 4 to 4000 amu. Mass-selected ions are subsequently deflected by 90° in an electrostatic ion deflector and focused into a RF ring-electrode ion-trap (RET). Here, the ions are thermalized close to the ambient temperature (6 – 300 K) through many collisions with a buffer gas, accumulated, and messenger-tagged, if required (Section 3.4.2). After a variable accumulation time, typically 99 or 199 ms, an ion packet is extracted and focused into a perpendicularly-mounted linear reflectron double-focusing time-of-flight mass spectrometer (Section 3.6). In the center of the dTOF plates, ions are irradiated by one or more laser pulses, typically, from an IR-FEL or an OPO/OPA tabletop laser system (Section 3.9). When the wavelength of the IR laser pulse is in resonance with an IR active transition of the ion, photofragments can be generated and all ions are extracted and accelerated into the field-free TOF region using two properly timed high voltage (HV) pulses applied to the extraction and acceleration plates. Ions are detected by recording TOF mass spectra as a function of the irradiation wavelength using a dual microchannel plate (MCP) detector.

3.2 Vacuum Design

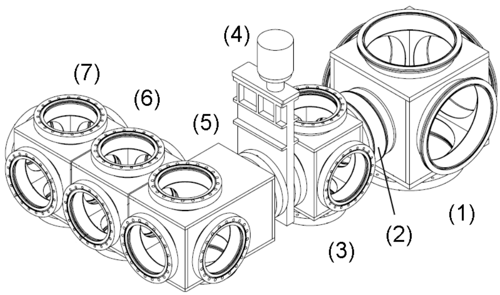

Figure 3.3: Scheme of the vacuum housing. The apparatus consists of five stainless steel cubes which are divided into a high- and a low pressure region by a gate valve. (1) source chamber, (2) stainless steel edge-welded bellow, (3) guide chamber, (4) gate valve, (5) quadrupole chamber, (6) trap chamber, (7) reflectron-dTOF chamber.

Vacuum chamber. The ion optics are housed in five differentially-pumped cubic stainless steel vacuum chambers. The first chamber, the source chamber (1, Figure 3.3), is constructed such that a variety of different ion cluster sources can be installed, *e.g.* a Z-spray, nanospray, electron impact or laser ablation source. It is mounted on a rail system and connected to the neighboring chamber with a ±250 mm long stainless steel edge-welded bellow (2, Figure 3.3), which allows variation of the distance between the source region and the entrance skimmer of the ion guides. This distance has to be overcome by the ions without any guiding devices and has thus a critical influence on the signal intensity. Precise movement, even under vacuum, of the source chamber relative to the ion guide entrance is realized with a lifting gear. The next chamber (3, Figure 3.3) houses the RF ion guide. It is connected to a gate valve (4, Figure 3.3, VAT) which divides the apparatus into two independently ventable regions. The gate valve allows for venting the source region, for cleaning or exchanging the source, while maintaining high vacuum in the rest of the mass spectrometer. The following chambers contain the quadrupole mass filter (5, Figure 3.3), the temperature controllable ion trap (6, Figure 3.3) and the reflectron-dTOF mass spectrometer (7, Figure 3.3). The three adjacent cubes (5-7, Figure 3.3) are connected through special flanges, that are attached to each other with in-vacuum threads and screws surrounded by a CF-160 copper sealing ring. The sealing surface is implemented on the exterior wall of the cube and thus this design permits compact and short connections between the individual chambers. The dimensions of the entire setup (1227 x 798 x 1970 mm) are chosen such that transport without disassembling the vacuum chamber is possible. The apparatus is mounted on an aluminum profile (*item Industrietechnik GmbH*), that is either fixed on height adjustable feet or on swivel castors, which allow for easy movement, for example to external facilities.

Table 3.1: Calculated vacuum parameters: λ is the mean free path; $\tilde{v}$ is the mean velocity; d defines the diameter between orifices of adjacent vacuum chambers; Q is the volumetric throughput; p_1 and p_2 denotes the pressure in the previous and current stage, respectively; and S_{calc} gives the calculated flow rate.

name	λ(cm)	$\tilde{v}$ ($\frac{m}{s}$)	d (mm)	Q^* ($\frac{mbar \cdot l}{s}$)	p_1 (mbar)	p_2 (mbar)	S_{calc} ($\frac{l}{s}$)
Nano 1	0.4	475 (N_2)	0.5	33	1000	15	2
Nano 2	525	475 (N_2)	1	$2 \cdot 10^{-2}$	15	$5 \cdot 10^{-1}$	0.1
Source	$6 \cdot 10^4$	1256 (He)	0.75	$1 \cdot 10^{-1}$	$5 \cdot 10^{-1}$	$1 \cdot 10^{-4}$	700
Guide	$1 \cdot 10^5$	1256 (He)	4	$2 \cdot 10^{-2}$	$1 \cdot 10^{-4}$	$5 \cdot 10^{-5}$	500
Quad	$1 \cdot 10^6$	1256 (He)	15	$2 \cdot 10^{-3}$	$5 \cdot 10^{-5}$	$5 \cdot 10^{-6}$	500
RET	$6 \cdot 10^5$	230 (He)	8	$4 \cdot 10^{-3}$	$5 \cdot 10^{-6}$	$1 \cdot 10^{-5}$	450
TOF	$2 \cdot 10^7$	1256 (He)	8	$1 \cdot 10^{-4}$	$1 \cdot 10^{-5}$	$3 \cdot 10^{-7}$	510

* *For Guide and RET:* $Q = 2 \cdot 10^{-4} + 2 \cdot 10^{-2}$, $Q = 1 \cdot 10^{-5} + 4 \cdot 10^{-3}$, *see text for details.*

Vacuum Generation and Operating Pressures. In order to estimate the vacuum conditions for the seven differentially-pumped stages, two in the nanospray source region and five inside the main chambers, the dimensions, *i.e.* flow rates S, for the required turbomolecular pumps (TMP) were calculated and are listed in Table 3.1.

The highest allowable pressure, p_2, for each stage is given by the requirements of the experiment and the particular ion optic, *e.g.* the quadrupole mass filter must be operated at pressures below 10^{-5} mbar. Within a differentially pumped system p_2 always depends on the pressure in the foregoing stage p_1. With given p_1 and p_2, S is determined by the ratio of the volumetric throughput Q and p_2:

$$S = \frac{Q}{p_2}. \tag{3.1}$$

Q depends on the pressure differences between two adjacent vacuum stages and the conductance C:

$$Q = (p_1 - p_2) \cdot C. \tag{3.2}$$

Depending on the mean free path, λ, of the molecules, the pressure regions in the apparatus can be divided into a high pressure and a low pressure regime, which have different values of C. In the first region, λ is much smaller than the dimensions of the gas container and the behavior of the molecules is governed by intermolecular interactions. The gas flow can be described as viscous and within the nanospray, also as laminar. In the high vacuum region, λ is much larger than the dimensions of the gas container and random motion of the molecules is dominant. Here, the gas flow is characterized as molecular flow [128].

In the case of viscous, laminar flow (nanospray), where the pressure stages are separated by a tube, $C_{vis,tube}$ is proportional to the mean pressure $\overline{p}$ (in mbar). For air at 293 K C is given by

$$C_{vis,tube} = 135 \frac{d^4}{l} \cdot \overline{p}, \tag{3.3}$$

where d is the diameter and l the length (both in cm) of the connecting tube. The second pressure stage is separated by a skimmer and the expression can be simplified to

$$C_{vis,orifice} = 20A, \tag{3.4}$$

where A is the area of the skimmer orifice (in cm^2) between the pressure stages [129]. In the molecular flow regime (Source to TOF region) C is given by [128]

$$C_{mol} = \frac{\tilde{v}A}{4}. \tag{3.5}$$

Combining the different expressions for conductance with throughput yields the flow rate, given by

$$S_{vis,tube} = 180 \cdot \frac{d^4}{l} \cdot \overline{p} \left(\frac{p_1 - p_2}{p_2} \right), \tag{3.6}$$

$$S_{vis,orifice} = 20A \cdot \left(\frac{p_1 - p_2}{p_2}\right), \tag{3.7}$$

$$S_{mol} = \frac{\tilde{v}A_{1,2}}{4} \cdot \left(\frac{p_1 - p_2}{p_2}\right), \tag{3.8}$$

where $\tilde{v}$ is the mean thermal molecular velocity. $\tilde{v}$ can be deduced from the Maxwell-Boltzmann velocity distribution law $\sqrt{8kT/\pi m}$, where k is the Boltzmann constant, $T = 298$ or $10\,\mathrm{K}$ (for the RET region) and m the mass of a helium atom ($m_{He} = 4\,\mathrm{amu}$).

In the case of buffer gas filled devices, *e.g.* the ion guide and the trap, the incoming gas flow, Q_{gas}, applied through a 1 mm polytetrafluoroethylene (PTFE) tube with $p = 0.1\,\mathrm{mbar}$, is added to the equation, yielding $(Q{+}Q_{gas})/p_2$ (see Table 3.1).

Considering that S is slightly reduced by protective meshes, the pump dimensions are chosen larger than calculated. The source chamber is equipped with a 1900 l/s TMP (*Pfeiffer*, HiPace 2300) which is backed by a 10 l/s dual-stage rotary vane pump (*Pfeiffer*, DUO 35). This rotary pump is also connected to the second pressure stage of the nanospray source. The first stage is pumped by a 2.7 l/s single stage rotary vane pump (*Pfeiffer*, UNO 10), resulting in typical pressures of 8, $5{\cdot}10^{-1}$ and 10^{-5} mbar, respectively. The pressure in the source chamber depends on the installed source. For the Z-spray source it is typically on the order of 10^{-3} mbar, due to a higher gas ballast. Each of the subsequent vacuum chambers (guide, quadrupole, RET and dTOF-MS) is pumped by TMPs with a flow rate of 685 l/s (*Pfeiffer*, HiPace 700) and backed by a pumping station (*Pfeiffer*, HiCube Eco 80). The pumping station is a combination of a small TMP (*Pfeiffer*, HiPace 80) and a dry diaphragm backing pump (*Pfeiffer*, MVP 015-2), resulting in a flow rate of 67 l/s. In the latter chambers typical background pressures of 10^{-7} – 10^{-9} mbar are achieved when all leak valves are closed. Typical operating pressures depend on the nature of the experiment and vary between 10^{-3} and 10^{-5} mbar for the source region, 10^{-5} and 10^{-4} mbar for the guide region, 10^{-7} and 10^{-6} mbar for the quadrupole and TOF regions, and 10^{-6} and 10^{-5} mbar in the RET chamber. Higher pressures are typically required for experiments involving messenger-tagging ($\geq 1{\cdot}10^{-5}$ mbar).

Compact full range gauges (*Pfeiffer*, PKR 251) with working ranges from $5{\cdot}10^{-9}$ to 1000 mbar are installed on each chamber for vacuum measurement. Pressure measurement inside the two stages of the nanospray source is achieved by two active Pirani transmitters (TPR 280). All pressure gauges are monitored by two pressure controllers (*Pfeiffer*, TPG 256 A) and the system is fully interlocked over a custom-built interlock device (*FHI ELAB*, # 4903) to provide protection in the event of a vacuum leak.

All rotary pumps are stored within a sound-absorbing rack on heavy-duty rollers (*IT-BUDGET*, Silence Rack) in order to reduce the noise level in the lab and also to allow for easy transportation.

3.3 Electrospray Ionization Sources

Electrospray Ionization (ESI) has emerged as a powerful tool for transferring ions from solution into the gas phase [130],[131]. Though it was primarily intended for bringing biomolecules solvent-free and without fragmentation into the gas phase, this soft ionization technique also allows for the production of weakly bound species, such as large protonated water clusters [132]. The exact formation mechanism is still widely discussed, but the established parts will be briefly outlined in this section. Subsequently, the commercial Z-spray source, which has been used for most of the experiments in this PhD work, will be described and compared to the linear nanospray source, which was developed as part of this thesis.

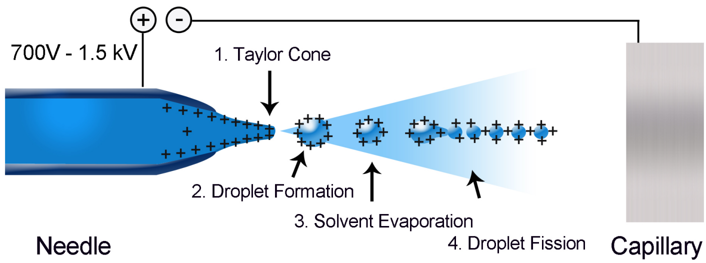

Figure 3.4: Electrospray ionization process: the sample solution is pulled out of the needle tip by capillary forces, and forms a Taylor cone upon the application of a high voltage. Droplet formation is initiated when a threshold voltage is exceeded. Solvent evaporation leads to shrinkage of the droplets and consequently an increase of the charge density at the droplet surface. Coulomb explosion occurs when the Raleigh limit is reached. After several such fission cycles isolated gas phase ions are generated.

General Aspects. The ESI process consists roughly of four steps, depicted in Figure 3.4. The probe solution is pulled out of a conductive needle by capillary forces, effectively forming a meniscus at the opening of the needle. Application of a high voltage leads to the formation of an electric field E with a maximum field strength near the tip where it penetrates the surface of the liquid. Here, the solvent is polarized and the meniscus deformed, until it develops into the shape of a Taylor cone, which is defined by a semi-vertical angle of 49.3° and a rounded tip. When a certain threshold voltage, E_0, is exceeded the rounded tip inverts and droplet formation is initiated. E_0 is given by [133]

$$E_0 = \sqrt{\frac{2\gamma cos 49.3^\circ}{\epsilon_0 r_n}}, \tag{3.9}$$

where ϵ_0 corresponds to the permittivity of vacuum. The onset of droplet formation is therefore directly influenced by two variables: the needle radius r_n and the surface tension γ of the probe solution. Typically, aqueous solutions are used in combination with suitable solvents, such as methanol or acetonitrile, in order to lower the surface tension and thus avoid instabilities and discharges, caused by a high electric field.

The emitted jet is drawn out into small charged droplets with charges localized at the surface. The droplets decrease in size due to solvent evaporation, until the surface charge becomes too large. As a consequence of Coulomb repulsion of the charges, the droplet explodes into several smaller droplets once the Rayleigh limit is reached. This process is referred to as Coulomb fission and repeats until nano-sized gas phase clusters are produced [133],[134].

Z-Spray. Figure 3.5 shows a schematic drawing of the commercial Z-spray source, originally installed on a Waters *Quattro Ultima* mass spectrometer. The solution, containing a dissolved sample of the probe ions (1, Figure 3.5), is pushed through a stainless steel capillary (2, Figure 3.5) with a syringe pump employed at typical flow rates of $10 - 20\,\mu$L/min. A high voltage of 2 to 3 kV is applied to the capillary to initiate the ESI process. A constant flow of nebulizer and heatable desolvation gas (both typically N_2) supports the process of evaporation (3, Figure 3.5). While most neutral (solvent) molecules hit the counter electrode (4, Figure 3.5), charged ions are deflected by 90° towards the first skimmer (5, Figure 3.5) and into the first pressure (inlet) stage. This stage is pumped by a rotary pump and the pressure can be adjusted in order to suppress or support the evaporation process. A detailed discussion of the evaporation process in this stage is given in Ref. [116]. Subsequently, the ions are again deflected by 90° through the second skimmer (6, Figure 3.5) into a cylindrical lens

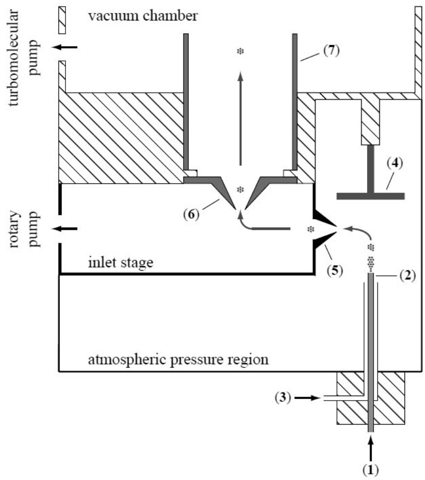

Figure 3.5: Scheme of the commercial Z-spray ion source taken from Ref. [116]. (1) Sample solution, (2) stainless steel capillary, (3) nebulizer gas (N_2), (4) grounded counter electrode, (5) skimmer 1, (6) skimmer 2, (7) cylindrical focus lens.

(7, Figure 3.5) which serves to focus the ions into the ion guide. The degree of fragmentation and the charge state can be controlled by adjusting the inlet pressure as well as the skimmer voltages. While a high inlet pressure (~80 mbar) yields higher hydrated clusters, a high voltage difference between the two skimmers (~100 V) usually leads to increased fragmentation.

Nanospray. In contrast to the Z-spray source which was originally developed to effectively desolvate biomolecular ions, this nanospray source is designed to transfer highly hydrated ions from a low-concentrated (see Table 3.2) solution into the gas phase. A technical drawing of the source is shown in Figure 3.6. Charged droplets are generated from an ion-containing solution within a platinum/palladium-coated borosilicate needle, held at ~800 V. The needle is mounted on a *xyz*-stage to allow precise alignment relative to the center of an 11.5 cm or 12.5 cm long stainless steel capillary (1/16", d_i = 500 - 750 μm) which transfers the ions from atmospheric pressure to vacuum (~15 mbar).

In order to suppress discharges and signal instabilities the needle is kept at a minimum distance d_c with respect to the capillary. d_c strongly depends

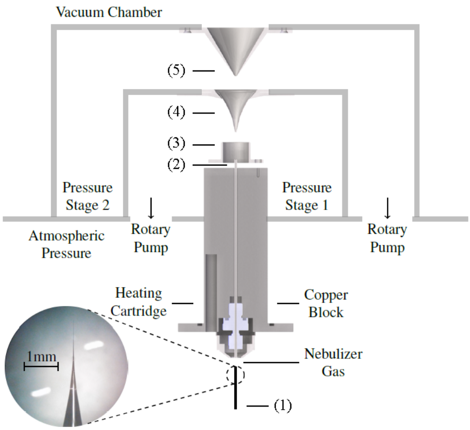

Figure 3.6: Schematic view of the nanospray source including a picture of the glass needle taken through a microscope [135]. (1) Metal-coated borosilicate needle, (2) stainless steel capillary, (3) cylindrical lens, (4) skimmer 1, (5) skimmer 2. Details are given in the text.

on the applied voltage V_n [136] and can be deduced from the relationship:

$$d_c = \frac{r_n}{4} \cdot exp(\frac{2V_c}{E_n r_n}), \tag{3.10}$$

where r_n is the inner radius of the needle. Assuming $E_n \approx E_0$ (determined with Equation 3.9) a minimum distance of 0.8 mm should be kept for 800 V.

The capillary is mounted in a temperature-controllable copper block, which can be heated using a 50 Ω heater cartridge. The copper block is fixed on a KF 250 flange and surrounded by a polyether ether ketone (PEEK) jacket, providing thermal and electrical isolation from the flange. The capillary is typically biased at 10 V and followed by a focusing lens and two skimmers (d = 1 mm, *Beam Dynamics, Inc.*, Model 2 and d = 0.75 mm, home-built). Both skimmers are mounted on the electrically isolated housing of the pressure stages. Voltages can be applied to the capillary, lens and both skimmers. These are crucial for obtaining different cluster sizes through fragmentation and for varying the kinetic energy (E_{kin}) of the cluster beam.

Comparison. The main differences of the nanospray compared to the Z-spray ion source are listed in Table 3.2. The significantly smaller capillary

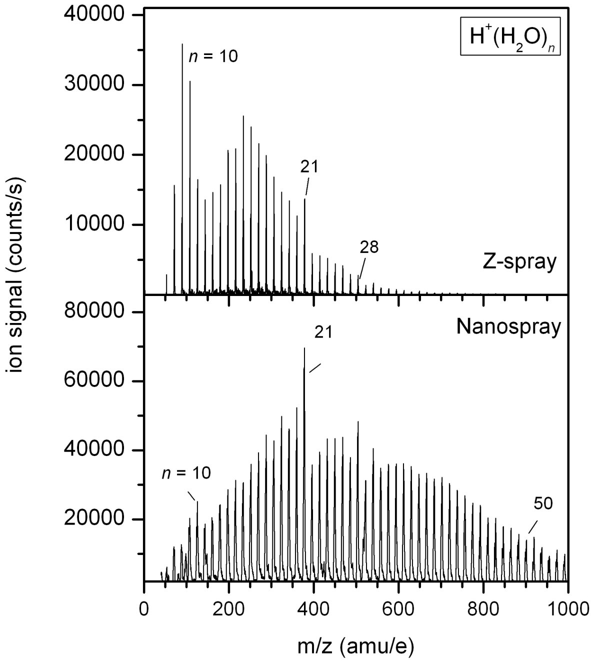

Figure 3.7: Comparison of typical mass spectra of protonated water clusters $H^+(H_2O)_n$, with n up to ~50, optimized for large masses (~400 amu), taken with different sources: the top panel shows a spectrum obtained with the Z-spray, the spectrum in the lower panel is measured with the nanospray ion source.

diameter results in a lower flow rate, and consequently less consumption of the probe substance. Furthermore, the required concentration of the probe solution is typically reduced by one order of magnitude, owing to the high sensitivity of the nanospray ion source.

Figure 3.7 shows two representative mass spectra obtained from a 10 mmol/L HCl/ACN solution, taken with the Z-spray (upper panel), and from a 0.1 mmol/L HCl/ACN measured with the nanospray source (lower panel). Both spectra are optimized for large clusters and are dominated by a $H^+(H_2O)_n$ progression. The differences between both spectra are readily identifiable. Whereas the water progression created with the Z-spray source ends shortly after the intense peak at $m = 379$ amu ($n = 21$), the distribution in the lower panel still shows high intensities for peaks around $m = 1000$ amu. The nanospray source can therefore be used over a wide range, without further optimization, whereas the Z-spray source has to be re-optimized in order to obtain larger clusters. Additionally, signals throughout the entire mass spectrum are generally more intense.

Table 3.2: Comparison of Z-spray- and nanospray-source parameters used for producing $H^+(H_2O)_n$ cluster.

	Nanospray	Z-spray
Flow Rate	20 nL/min	12 μL/min
Concentration (HNO_3)	0.1 mmol/L	10 mmol/L
Capillary diameter d_i	~10 μm	~100 μm
Voltage	800 V	3000 V

The nanospray source facilitates not only the production of much larger hydrated clusters, but also the use of less concentrated solutions. A fact that is particularly helpful when expensive or not readily available substances are analyzed. Table 3.2 lists typical operating parameters for the nano- and Z-spray-sources.

3.4 Radio Frequency Multipoles

The triple mass spectrometer makes use of several RF multipole devices in order to guide, mass select and trap ions. The following section will briefly outline the underlying physical principles, followed by a detailed description of geometrical and electronical parameters of the octopole ion guide, the quadrupole mass filter and the ring electrode trap (RET). The last section evaluates the performance of the trap in terms of maximum ion capacity and lowest achievable ion temperature.

Basic principles. Charged particles with charge q and mass m can be confined in a fast oscillating, inhomogeneous electric field, $V_{RF}\cos(\Omega t)$, that is applied to linear multipole devices with $2n$ number of poles [137]. The poles are arranged tangent to an inscribed circle with radius r_0 and provided with a time-dependent electric potential, Φ_0, that alternates in polarity for adjacent electrodes for a given time. The potential can be described by the sum of a DC and an AC component:

$$\Phi_0 = U + V_{RF} \cos(\Omega t), \qquad (3.11)$$

where U is the amplitude of a DC voltage, and V_{RF} is the amplitude of the AC component with a frequency of $\Omega = 2\pi f$.

The motion of the particle within a multipole device is described by a rapidly oscillating motion around a stable trajectory. If a field oscillates with a sufficiently high frequency Ω, fast and slow components of this trajectory can be separated. Ion trajectories are then governed by the effective potential V^*:

$$V^* = \frac{n^2}{4} \frac{q^2}{m\Omega^2} \frac{V_0^2}{r_0^2} \left(\frac{r}{r_0}\right)^{2n-2}, \qquad (3.12)$$

where r is the distance of the particle from the center of the multipole device. A detailed description of the derivation is given in Ref. [137].

Figure 3.8 displays the radial dependence of the relative effective potentials of the three RF devices used in the current instrument and these are compared to those of a 22-pole trap. The slope of the potential increases rapidly for large n and increasing radius (not shown). In contrast to the harmonic effective potential of the quadrupole, the RET shows a potential with a large field-free region in the middle and steep repulsive walls. This characteristic field-free region is important to avoid heating caused by interaction with the RF field. Only the 22-pole device shows an even steeper potential, but has the drawback that precise control of the ion motion along the z-axis cannot be readily achieved.

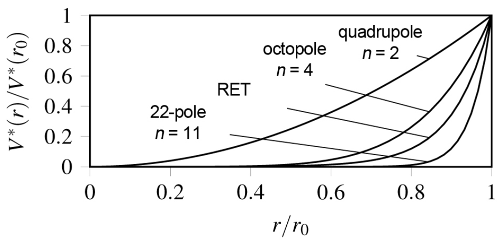

Figure 3.8: Relative effective potentials of linear rod and ring electrode devices as a function of the distance from the center line.

The properties of RF devices are characterized by the adiabaticity parameter η:

$$\eta = 2n(n-1)\frac{qV_{RF}}{m\Omega^2 r_0^2}\left(\frac{r}{r_0}\right)^{n-2}. \tag{3.13}$$

η is used as a criterion for the stability of the ion trajectory, and is thus referred to as the stability parameter. Safe operating conditions within the *adiabatic approximation* are achieved, if [137]

$$\frac{r}{r_0} < 0.8, \tag{3.14}$$

and

$$\eta\left(\frac{r}{r_0} = 0.8\right) < 0.3, \tag{3.15}$$

where r/r_0 is the turning radius of the particle. Within the *adiabatic approximation* conservation of energy ensures that transmission/trapping does not depend on the initial conditions, but only on the maximum transverse energy E_m [138]. E_m defines the maximum energy that ions can have without receiving energy from the electric field, *e.g.* by too closely approaching the electrodes. For the design of an RF device, and thus the choice of appropriate geometries and optimal operating conditions, the *adiabatic approximation* has to be valid. The maximum allowed transverse energy E_m for a given amplitude V_0 is given by [137]

$$E_m = \frac{1}{8}\cdot qV_{RF}\eta\cdot\frac{n}{n-1}\cdot\left(\frac{r}{r_0}\right). \tag{3.16}$$

The minimum guiding amplitude, V_{RF}, for ions with the masses m_1 and m_2 in an octopole ion guide ($n = 4$) can be derived with regard to equations 3.13 and 3.16:

$$V_{RF} = 6\cdot\frac{E_m}{q}\cdot\frac{1}{r_m^4\eta_m}\cdot\left(\frac{m_1}{m_2}\right)^{-\frac{2}{3}}. \tag{3.17}$$

3.4.1 Octopole Ion Guides

Design and Operation. Figure 3.9 shows a photograph of one of the octopole ion guides used in this experiment. The device consists of two sets of eight conducting poles in a sequential arrangement, with rod-lengths of 15.6 cm and 23.8 cm, respectively. A schematic view of the longer guide is shown in Figure 3.10 along with a cross section of the eight electrodes. The rods are arranged on a circle with an inner diameter of 18 mm and have a

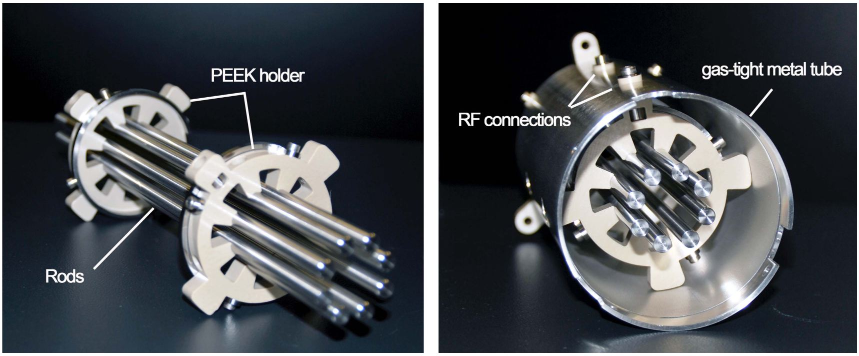

Figure 3.9: Photograph of the shorter octopole ion guide with (right) and without (left) metal housing.

diameter of 6 mm. The polished rod electrodes are mounted and precisely centered using two cylindrical PEEK holders and electrically connected through a stainless steel contact ring. Both guides are mounted in gas-tight metal tubes each of which can be independently filled with a buffer gas through a PTFE tube ($d_i = 1\,\mathrm{mm}$). The buffer gas serves to collimate the ion beam. Both ion guides are capped with an entrance and an exit lens. Three stacks of einzel lenses allow additional focusing before, between and after the ion guides.

The octopoles are operated with variable frequencies of 1-2 MHz and peak-to-peak voltages, V_{RF}, of up to 2 kV. The RF is provided by a home-built RF generator (*FHI ELAB*, # 4325) and can oscillate around an offset (DC) voltage (U_{bias}) of ±175 V which is superimposed on the RF in a RF/DC box (*FHI ELAB*, # 4762).

Example. According to Equations 3.13 and 3.15, the boundary condition ($\eta < 0.3$) is fulfilled if $V_{RF} = 100\,\mathrm{V}$, $m = 500\,\mathrm{amu}$ and $f = 1.7\,\mathrm{MHz}$. Under these conditions ions can have a maximum transverse energy of 4 eV according to Equation 3.16. E_m depends directly on the applied voltage and increases up to 20 eV, if $V_{RF} = 500\,\mathrm{V}$. Taking the safe operating conditions, $\eta = 0.3$ and $r_m = r/r_0 = 0.8$, into account, and assuming that E_m is 2 eV, the minimum guiding voltage for masses in a range from 50 to 1500 amu, is 940 V. This equation shows how V_{RF} is effected by E_m, and that the guided mass range can easily be broadened if E_m is decreased. A decrease of E_m can, for example, be achieved through collisions of the guided ions with a buffer gas.

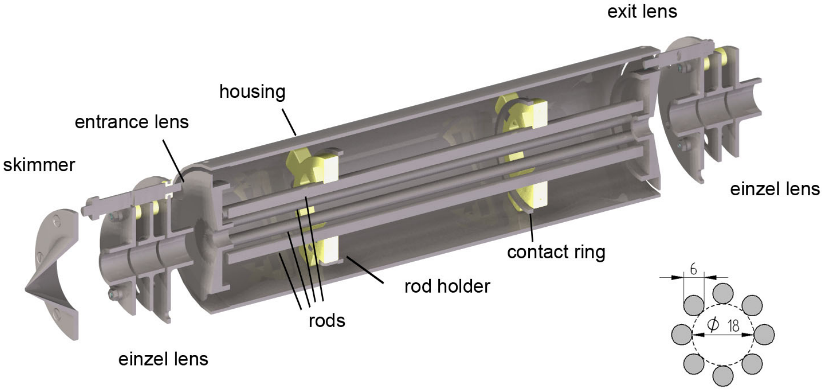

Figure 3.10: Cross section through a schematic drawing of the longer octopole ion guide with skimmer and two stacks of einzel lenses. The small inset shows a sectional view of the rod electrodes with the inscribed diameter.

3.4.2 Quadrupole Mass Filter

Design and Operation A commercial, custom-built quadrupole mass filter/ion deflector assembly from *Extrel, CMS* is used for mass selection. The rods of the quadrupole have a diameter of 19 mm and are arranged tangent to an inscribed circle of 71 mm. The transmission is enhanced by the addition of pre- and post-filters at the end of the rods. The electric fields of these filters oscillate at the same RF as the main filter, but they can be supplied with a separate variable pole bias, therefore generating a more homogeneous field at the edges. The mass filter is operated at a frequency of 440 kHz, provided by a commercial power supply (*Extrel, CMS*). The low frequency in combination with the larger rod diameter results in a mass range of 4 – 4000 amu with a resolution (M/ΔM) of 1500 and a relative transmission of 50 %. Depending on the voltages applied to the ion deflector, mass-selected ions can be either focused with an einzel lens into a channel electron multiplier or deflected by 90° towards the ion trap.

Ring Electrode Trap

The ring electrode trap shown in Figure 3.11 is based on the design of Gerlich [139]. It serves for accumulation, thermalization and messenger-tagging of ions in order to produce pulsed ion packets with high number densities and low internal temperatures. This section describes the design and electronic configuration of the RET and evaluates the performance of the ion trap in terms of capacity, store time and ion temperature as a function of different parameters.

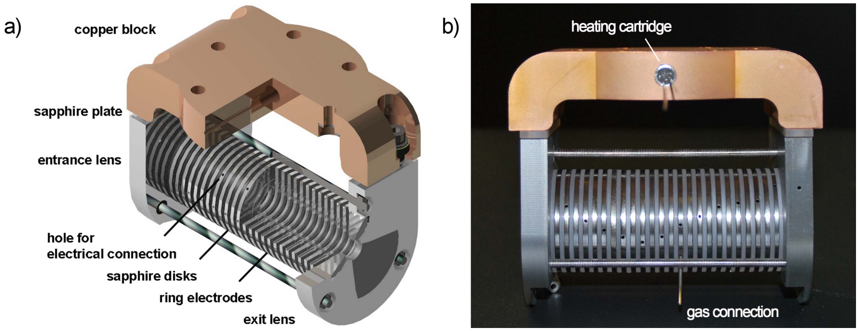

Figure 3.11: a) Schematic half-sectional view and b) photograph of the ring electrode trap.

Design. Figure 3.11 a) shows a schematic 3D-view and b) a photograph of the ion trap. The trap consists of 24 concentric ring electrodes made of molybdenum. Molybdenum was chosen because of its suitable thermal properties, such as the low coefficient of thermal expansion and high level of thermal conductivity, and its small patch potentials. The ring electrodes are 1.5 mm thick, and have outer and inner diameters of $d_o = 32\,\mathrm{mm}$, and $d_i = 11\,\mathrm{mm}$, respectively. For electrical connection, holes of $d = 1\,\mathrm{mm}$ are drilled into the side of the electrodes, in which gold-coated pins are inserted. Electrical isolation is achieved by a set of 1 mm thick sapphire disks in-between the ring electrodes, making the assembly a gas-tight cylinder. The trap can be filled with buffer gas using a PTFE tube ($d_i = 1\,\mathrm{mm}$) which is attached to one of the central electrodes. The electrode/sapphire stack is capped and pressed together by two lenses at both ends.

The lens stack is attached to an oxygen-free copper block and insulated electrically with sapphire plates. The copper block is mounted on the cold head of a two-stage closed-cycle 1 W/4 K helium cryostat (*Sumitomo Heavy*

Industries, RDK-408E2). The temperature is measured using two calibrated Cernox sensors (*Lake Shore, USA*), which are mounted with clamps, one at the bottom of the entrance lens and the other one at the diagonal end of the copper block. The temperature can be continuously tuned from 5.8 to 320 K by the use of a heating cartridge (*Janis*, HTR-50) which is pressed into a hole in the copper block. The coldhead is inserted into the vacuum chamber over an adjustment flange, which allows for external alignment of the trap relative to the ion beam axis. To provide the trap with electrical and gas connections, the adjustment flange is additionally equipped with two 12 pin-, one 10 pin-, one 5 pin-, and two swagelock-feedthroughs.

In order to achieve low temperatures it is critical to shield room temperature and black body radiation effectively from the coldhead and the ion trap. For this purpose the first cooling stage of the coldhead is covered with a radiation shield made of oxygen-free copper which is electro-coated with a 3 μm gold film. The shield surrounds parts of the first cooling stage, the entire second cooling stage and large parts of the RET.

In order to minimize thermal conductivity from the room temperature-feedthroughs to the RET, wires with a small diameter are used for most electrical connections. The ring electrodes are connected by 0.14 mm Kapton insulated manganine wires, entrance and exit lenses with 0.1 mm Kapton insulated copper wire and the resistance heater cartridge with 0.25 mm heavy duty lead wire (PTFE insulated, silver-plated copper wires). The temperature sensors are connected in a four-lead-configuration with phosphor-bronze quad-twist wires in order to minimize the pickup of electromagnetic noise.

To avoid thermal bypasses all cables and tubes, except those providing RF, are precooled through multiple-turn coiling around the first and second cooling stages of the coldhead. The cables are fixed with vacuum-compatible dielectric tape. To ensure good thermal contact in-between all adjacent surfaces, *e.g.* sensors, sapphire plates, cold head and radiation shield, a thin film of cryogenic vacuum grease (*Apiezon*, N Grease) is applied in order to fill any micropores.

Electronic Configuration and Operation. Radial confinement of ions is achieved by the application of an RF voltage with opposite phases to adjacent ring electrodes. The frequency can be continuously varied between 1 and 2 MHz with amplitudes of up to 600 V (peak-to-peak), and is provided by a home-built RF generator (*FHI ELAB*, # 4871). For confining the ions along the trap axis up to 12 individually adjustable DC voltages are superimposed on the RF, within a home-built RF/DC box (*FHI ELAB*, #

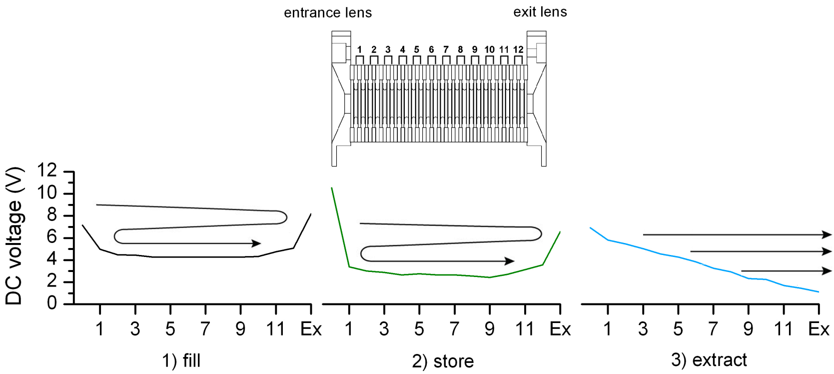

Figure 3.12: Scheme of the three possible electronic configurations (fill, store and extract) that can be applied to the RET. The applied voltage is plotted as a function of electrode number (Ex = exit lens).

4282), and applied to each pair of ring electrodes. The resulting adjustable voltages allow for precise control of the position of the ion packet within the trap. DC voltages are provided by the home-built RET Board (*FHI ELAB*, # 4281). This device also allows for fast switching (∼1 μs) between three different trapping states, displayed in Figure 3.12:

1) Fill: The trap is continuously filled with ions by applying a sufficiently high potential to entrance and exit lens, such that the ions can just pass the potential at the entrance lens. Traversing the trap, they lose kinetic energy through collisions with the buffer gas, are reflected at the exit lens, and, upon reaching the entrance lens again, cannot overcome the applied potential, and are thus again reflected.

2) Store: In the store mode the potential well is similar to the Fill-state with the only distinction that the entrance lens is set to a higher potential, therefore preventing ions from entering or exiting the trap.

3) Extract: After a specified time period all ions are extracted from the trap by switching to a steep, declining voltage ramp in the direction of the exit lens.

All voltage differences are kept as low as possible in order to prevent heating effects such as collisional induced dissociation (CID). In order to facilitate the optimization of the 3x12 RET voltages, a genetic algorithm was developed, which automatically adjusts all voltages for an optimal ion signal [135].

Ion Trap Capacity. The maximum number of ions N that can be stored in the RET is mainly restricted by the geometric volume of the trap and the space charge limit. Assuming a spherical ion cloud with the approximate volume V_{RET} of the trap and the effective potential V_{eff} (~3 eV), the number of storable ions N can be determined:

$$N = \frac{4\pi\epsilon_0 R V_{eff}}{e^2}, \tag{3.18}$$

with

$$R = \left(\frac{3D^2L}{4}\right)^{\frac{1}{3}}, \tag{3.19}$$

where L is the length of the trap (73 mm), D the diameter of the ion cloud (D = 8.8 mm, 80 % of the inner electrode diameter d_i), ϵ_0 the vacuum permittivity, and e the elementary charge. The maximum number of ions is then $3.3 \cdot 10^7$, which corresponds to an electric charge of 5.2 pC.

Experimentally, the number of ions in the RET and their loss rate can be determined by measuring the current of the trapped ions after ion extraction. The current is detected at one of the TOF plates, using an oscilloscope and a picoamperemeter (*Keithley*).

First, the ion capacity is determined by filling the ion trap with Ar^+ for fixed time periods (100 – 2000 ms). Figure 3.13 a) displays the ion

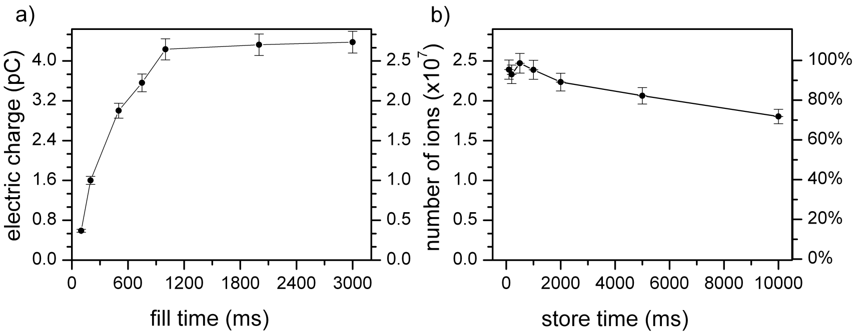

Figure 3.13: Dependence of detected ion current/number of ions on a) fill time and b) store time.

number as a function of fill time. The steep slope for short fill times levels off after 1000 ms and approaches a constant value of ~ 4.3 pC ($\equiv 2.7 \cdot 10^7$) for $t > 1000$ ms. At this point the space charge limit of the ion trap is reached. This result is in good agreement with the theoretically determined maximum number of ions.

The loss rate is determined by keeping the fill time constant at 100 ms and detecting the electric charge for different store times t_{store}. Figure 3.13 b) shows the ion number as a function of t_{store}. For t_{store} up to 500 ms the loss is insignificantly small. For $t_{store} = 2000$ ms, 4 % of the ions are lost and for 10000 ms 27 %. The observed loss is predominantly due to reactive collisions with traces of the background gas [140].

Internal Ion Temperature. The nominal temperature of the ion trap, T_{RET}, is measured with two calibrated Cernox sensors at the copper block and at the entrance lens. T_{RET} can reach minimum values of 5.8 and 7.6 K, respectively, and the temperature of the ring electrodes, lying in-between the sensors, is therefore assumed to be ~ 6.7 K.

Thermalization of ions is achieved through inelastic and elastic collisions with a neutral buffer gas, typically helium. The temperature of the buffer gas is typically defined by the surrounding trap walls. If the number of neutral gas atoms is high enough (on the order of 10^7 to 10^{16} cm^{-3}), *i.e.* the number of collisions between ions and neutrals is sufficient, the trapped ions are assumed to reach a thermal equilibrium with the neutral species [141].

Several effects, however, can increase the internal temperature of the clusters. In order to characterize the rotational temperature dependence on the trapping setting, T_{rot} has been determined for $NH_4{}^+ \cdot H_2O$ under different conditions.

T_{rot} is deduced by measuring the partially-rotationally resolved transitions of the symmetric (ν_1) and antisymmetric (ν_3) NH stretching vibrations of the $NH_4{}^+$ moiety in $NH_4{}^+ \cdot H_2O$. IRMPD spectra of $NH_4{}^+ \cdot H_2O$ in the NH-stretching region are displayed in Figure 3.14 (black line) at trap temperatures T_{RET} of 6.7 and 100 K. The ν_1 absorption band exhibits two maxima at $T_{RET} = 6.7$ K. An additional intermediate peak and inverse relative intensities of the two outer maxima is observed at $T_{RET} = 100$ K. These bands correspond to the rotationally unresolved P, Q and R branches. ν_3, on the other hand, exhibits a partially resolved rotational structure with a characteristic spacing of ~ 10.9 cm^{-1}, which corresponds to a Q branch progression in quantum number K, as depicted in Figure 3.14.

The calculated structure (see Ref. [113] for details) indicates a symmetric

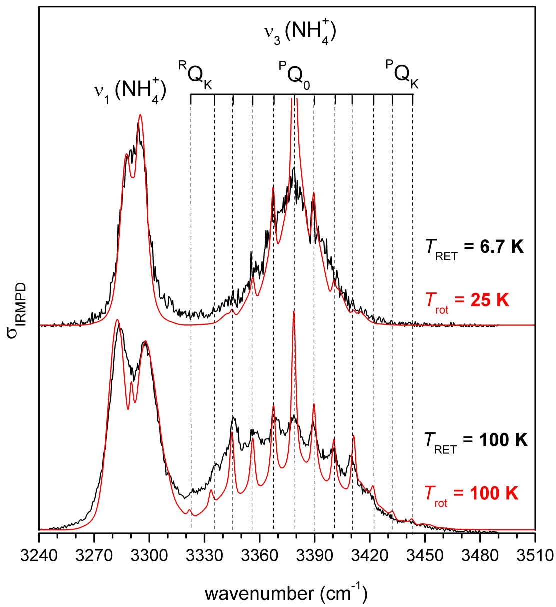

Figure 3.14: Comparison of experimental IRMPD spectra of ${NH_4}^+ \cdot H_2O$ (black line) measured at different trap temperatures to simulated rovibrational profiles (red line). The simulated spectra correspond to rotational temperatures of 25 and 100 K, respectively.

rotor with C_{3v} symmetry and thus the rotational constants are $A > B{=}C$ [113]. A corresponds to the internal rotation of ${NH_4}^+$ about the cluster bond and B to the overall rotation of the cluster. The experimentally determined values for A ($5.9293\,\text{cm}^{-1}$), B ($0.35482\,\text{cm}^{-1}$) and A' ($5.8764\,\text{cm}^{-1}$) for bare ${NH_4}^+$ [142],[143] are used to simulate the rotational spectra, where the prime denotes the vibrationally excited state. The rotational spacing is given by $2(A - B)$ [113]. It is reasonable to use the rotational constants of bare NH_4^+, since B3LYP calculations have shown that the bare ${NH_4}^+$ rotation about the C_3-axis in ${NH_4}^+ \cdot H_2O$ is barrierless, and consequently the structure of the band depends on the rotational constants for the ${NH_4}^+$ rotor [144].

Rotational band contours are simulated within the rigid rotator approximation using the program PGOPHER 8.0 [145] and are also shown in Figure 3.14 (red lines). The simulated spectra are in reasonable agreement with the experimental spectra, except for the ${}^{P}Q_0$-branch of the antisymmetric NH stretch (ν_3), which is either overestimated by the simulation, or less intense in the experimental spectrum due to saturation effects. The simulated spectra correspond to rotational temperatures of 25 and 100 K, respectively.

In order to characterize the temperature dependence of the ion trap on various parameters, IRMPD spectra are measured under different conditions and the resulting spectra are compared to simulated spectra as exemplary shown in Figure 3.14. The results are plotted in Figure 3.15 a) - e).

Figure 3.15 a) displays the simulated temperature T_{rot} as a function of the measured trap temperature T_{RET}. For $T_{RET} > 40$ K all values change linearly and the rotational temperature of the ions equals the measured temperature of the ion trap. The lower temperature region shows a significant deviation between the nominal trap temperature and the rotational temperature (+ 33.3 K). Several reasons are conceivable for this observation.

1) Heating due to black-body radiation.

2) RF heating.

3) Insufficient thermalization, caused by too short residence time.

4) Collisional heating upon extraction: as buffer gas is filled *continuously* into the trap, rotational excitation may arise due to collisions with the neutrals upon ion acceleration during the extraction process.

In order to minimize these heating effects on T_{rot}, individual parameters, that potentially contribute to the heating of the ions, are analyzed in the following section.

1) Trapping of larger clusters often requires a higher RF amplitude which has a measurable heating effect on the ion trap. Upon raising V_{RF} above 150 V (at 1.69 MHz) T_{RET} increases by $\sim$ 2 K, and consequently the temperature of the buffer gas increases by the same amount. The influence of three different amplitudes on T_{rot} is therefore measured as a function of the RF amplitude and the results are plotted in Figure 3.15 b). Raising the RF amplitude from 50 V to 125 V, shows no effect, a further increase changes T_{rot} by 5 K, which corresponds roughly to the increase of T_{RET}.

2) Figure 3.15 c) illustrates how the ion temperature is influenced by the store time. Between 0 ms and 50 ms an additional thermalization effect of 15 K is obtained. This suggests that ions arriving in the ion trap are not completely thermalized until 10-50 ms after initiation of the trapping cycle.

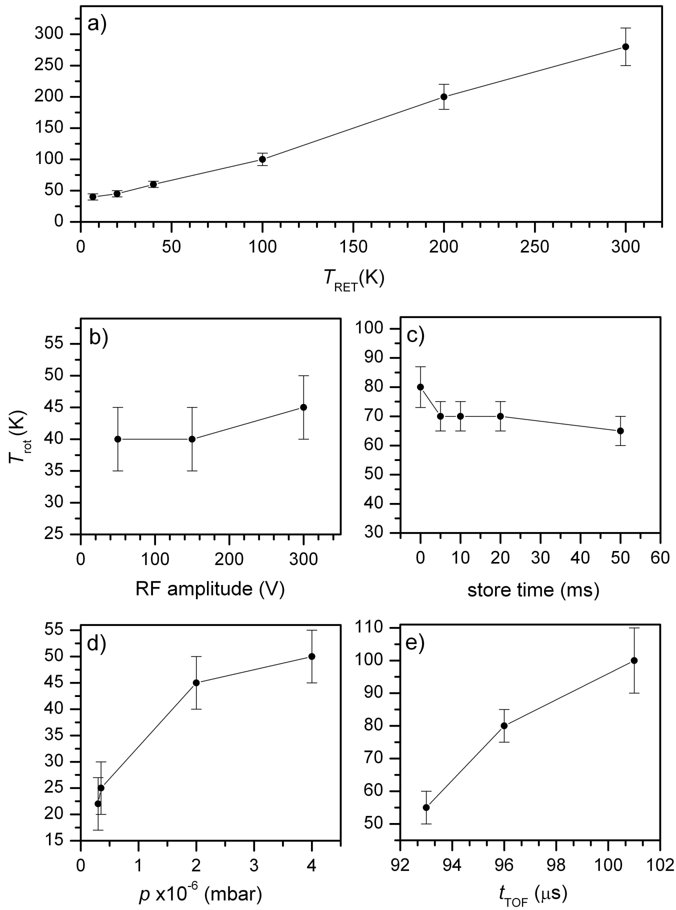

Figure 3.15: Dependence of ion rotational temperature T_{rot} on various parameters. If not given otherwise, the standard conditions are: $f = 1.69\,\text{MHz}$, $T_{RF} = 125\,\text{V}$, $p = 3.5{\cdot}10^{-6}\,\text{mbar}$, $T = 6.7\,\text{K}$, $t_{store} = 0\,\text{ms}$. The simulated rotational temperature T_{rot} is plotted as a function of a) ion trap temperature T_{RET}, b) RF amplitude, c) store time d) buffer gas pressure, and e) TOF delay (see Figure 3.16). Each data point results from a comparison of a simulated spectrum to the experimental IRMPD spectrum, as shown in Figure 3.14.

3) Assuming that the collision frequency in a pressure range between 10^{-7} - 10^{-5} mbar is sufficient to achieve thermalization, the variation of the buffer gas pressure p can be used to determine the heating effect caused by rotational excitation by collisions with neutrals in the process of extraction within this pressure range. Figure 3.15 d) shows T_{rot} as a function of p. The lowest temperature (22 K) is reached with $p = 3{\cdot}10^{-7}$ mbar and increases up to 50 K with rising pressure. Thus collisional excitation upon extraction is the major heating source.

Another possibility to verify this finding is to select those ions which experienced less collisional excitation, *i.e.* that are located close to the exit lens of the ion trap when the extraction process is initiated. These ions arrive typically a few μs earlier in-between the TOF plates and can therefore be probed by tuning the TOF delay (application of high voltage pulses to the plates). Figure 3.15 e) shows the dependence of T_{rot} on different delay times. The ions that are probed at 93 μs are significantly colder (55 K) compared to those that are probed at 100 μs (100 K).

To summarize, the influence of longer store times and the variation of the RF amplitude on T_{rot} is on the order of 5-15 K. T_{rot} can be significantly improved by reducing collisions between neutrals and ions, and therefore minimizing collisional heating. This is achieved by reducing the buffer gas pressure and by probing only a selected part of the ion packet. More effectively, the buffer gas should be removed before the extraction process is initiated. This can, for example, be achieved by inserting the gas in a short, defined gas pulse at the beginning of the trapping cycle [146].

3.5 Detection Scheme and Data Extraction

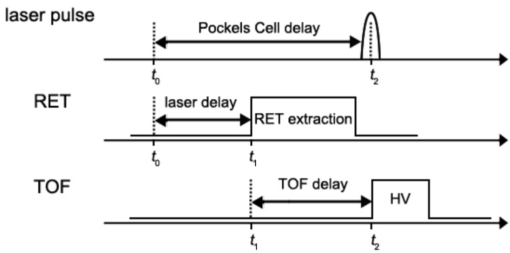

Figure 3.16: Trigger scheme of a one-color IRPD experiment. Details are given in the text.

The ion signal can be detected at three different points inside the instrument; first, with a channeltron detector (*Extrel*) mounted collinear with the quadrupole mass filter. Second, with a high energy dynode detector (*SGE*, DM 283) behind the dTOF-MS, and third with a 40 mm dual stage microchannel plate (MCP) detector (*Jordan TOF Products, Inc.*) at the longer end of the dTOF tube. Ion signal collected with the channeltron and HED detectors is preamplified (*Advanced Instruments Research Corporation*, MTS-100) and read out with a National Instruments counter/timer card. A signal of $6{\cdot}10^6$ counts/s at the electron multipliers corresponds to $\sim 1\,\text{pA}$.

Typically, all ion optics are first optimized with the ion signal detected using the electron multipliers and mass spectra are obtained by scanning the quadrupole mass filter. Subsequently, the mass filter is set to the mass of interest, and mass-selected ions are trapped and analyzed with the Wiley-McLaren type time-of-flight mass spectrometer [147].

TOF mass spectra are detected by separating ions according to their mass-to-charge ratio and recording their intensity as a function of flight time using an MCP detector. Mass separation is achieved by accelerating the ion packet in a homogenous electric field $\mathbf{E}$, to different velocities v, depending on ion mass m and charge z:

$$E_{kin} = z \cdot \mathbf{E} = \frac{1}{2}mv^2 \Leftrightarrow v = \sqrt{2\mathbf{E}\frac{m}{z}}. \tag{3.20}$$

The transient signals from the MCP are first amplified by a preamplifier (*Ortec*, 9305 Fast Preamp) and then sent to a 300 MHz, 12-bit digitizer (*Acquiris* DP310) installed in the PC for real-time data collection.

Figure 3.16 displays the trigger scheme used for single-color photodissociation experiments. The measurement cycle is initiated by the laser system, which provides a trigger at t_0, either 500 μs (FELIX) or 254 μs prior to IR pulse emission. The extraction of the ion packet from the trap at t_1 is delayed in order to tune the arrival time of the ions in-between the TOF plates. t_1 is referred to as the laser delay. After a second delay at t_2 (TOF delay) two high voltage pulses are sent to the TOF plates. In order to achieve temporal overlap of the IR pulse with the ions, the sum of t_1 and t_2 has to equal either 500 or 254 μs. CID (Collisional Induced Dissociation) fragments can be separated from photodissociated fragments, by applying the HV pulse shortly before the IR pulse. In this case the CID fragments are accelerated some tenths of μs earlier than the photodissociation fragments and arrive prior to these fragments (with the same mass) at the detector

[58].

According to Equation 3.20, ions are separated and detected as a function of their flight time. For each mass a time window is defined which allows for determination of the ion yield, I_P, by integration of the signal.

If the frequency of a tunable IR pulse is in resonance with a vibrational transition, depletion of $I_P(\nu)$ is observed, and photofragments $I_F(\nu)$ are generated. Both signals are normalized to the total ion yield in order to cancel out fluctuations in the parent ion signal, caused by variations in the ion source.

An IR action spectrum is derived by plotting the photodissociation cross section σ as a function of the laser frequency (ν). σ_{IRMPD} is obtained by normalizing the frequency-dependent relative abundances of parent $I_P(\nu)$ and fragment ions $I_F(\nu)$ to the frequency-dependent laser pulse energy $P(\nu)$ (assuming a constant interaction area throughout the range of scanned wavelengths)

$$\sigma_{IRMPD} = -ln\left[\frac{I_P(\nu)}{I_F(\nu) + I_P(\nu)}\right]/P(\nu). \tag{3.21}$$

Assuming a single-photon process, *e.g.* if the messenger-technique is employed, all intensities are normalized to the photon fluence F: $F(\nu) = P(\nu)/\mathrm{h}\nu$, such that $\sigma \propto \sigma_{IRMPD}\nu$, as in Equation 2.7) [104].

3.6 Double-Focusing Reflectron Time-of-Flight Mass Spectrometer

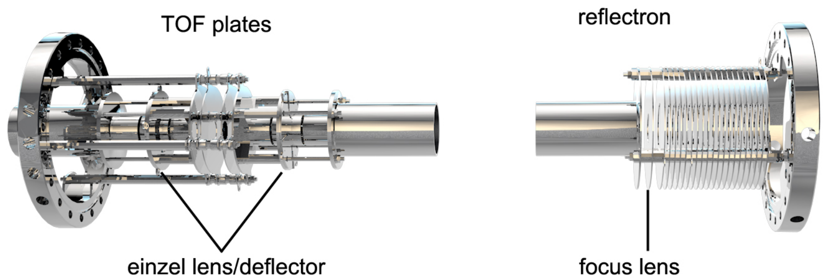

Figure 3.17: Schemtic 3D-view of the flange-mounted dTOF.

Figure 3.17 shows a schematic 3D-view of the linear double-focusing reflectron time-of-flight mass spectrometer. Two similar versions have been built, only differing in minor technical details. The original version is mounted on the 12 K set up, the second version on the 6 K set up, described in this thesis.

In addition to a higher mass resolution that can be achieved by using the reflectron, the dTOF setup also allows for pulsed ion acceleration at two stages of the experiment. This feature can be used for 1) CID background-free measurements and 2) two-color isomer-selective experiments. This section outlines the design, performance, electronic configuration and trigger scheme required to conduct such experiments.

Design. The dTOF-MS consists of a 180° reflectron TOF mass spectrometer which allows for pulsed re-acceleration of ions upon re-entering the extraction/acceleration zone, consisting of four symmetrically arranged plates. The two central TOF plates are separated by 20 mm from each other and 10 mm from the outer, grounded plates. All electrodes have central holes ($d = 10$ mm), covered with nickel-meshes (*Plano*, MN-4) in order to allow for a homogeneous electric field and high ion transmission. The meshes are attached to the plates using a graphite solution. Ceramic spacers are used for electrical isolation in-between the plates and the mounting rods. The spacers are surrounded by stainless steel jackets in order to prevent charging effects. The TOF plates are followed by a set of einzel lens/deflectors at each side. All electrodes are polished in order to avoid discharges.

The linear reflectron is mounted collinearly and opposite to the linear TOF part of the dTOF arrangement. It consists of 20 electrodes which are separated and electrically isolated by 5 mm PEEK spacers. The individual electrodes are connected through 10 MΩ resistors, which are soldered onto the edge of the electrodes in the first version of the dTOF-MS. In the second version the resistors are fixed onto the plates with connector blocks. In order to focus the ions, an additional lens is installed 20 mm before the reflectron stack (see Figure 3.17).

Double-Resonance Experiments. Figure 3.18 illustrates the individual steps of a double-resonance experiment:

1) Mass-selected, messenger-tagged ions are extracted from the RET and focused in the center of the TOF plates. Here, the parent ions (black) interact with a first pulse from a wavelength tunable laser $h\nu_1$ (either table-top laser or FEL), creating photofragments (green), whenever the applied radiation is in resonance with an absorption of one of the isomers.

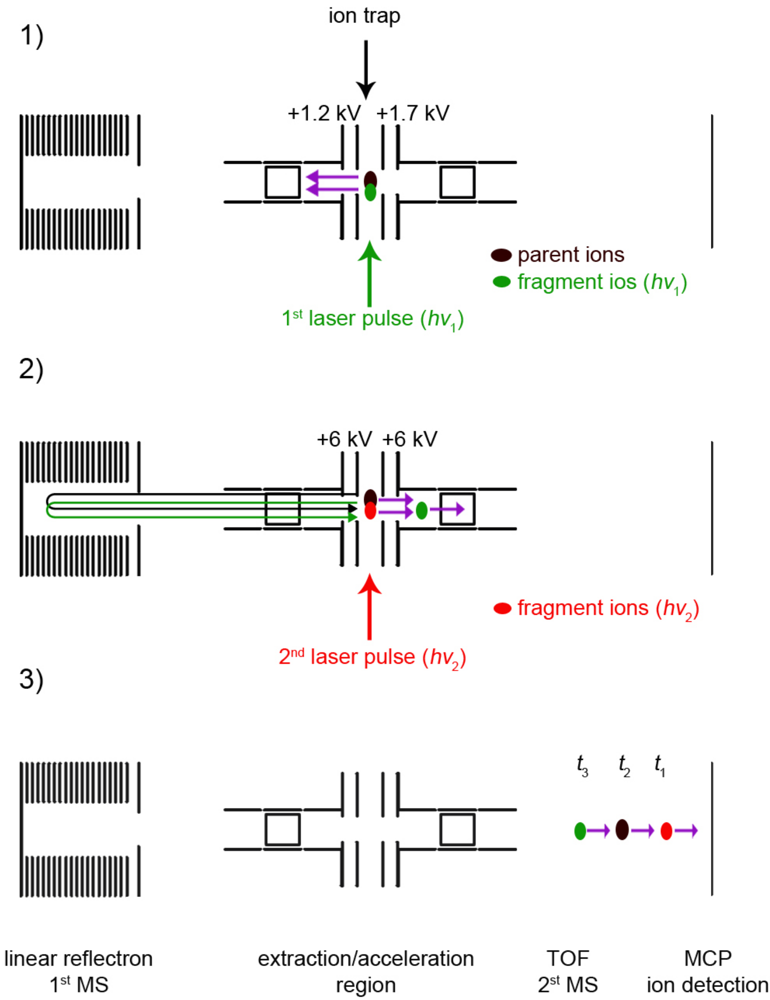

Figure 3.18: Scheme of isomer-specific measurements, which are performed using the population-labeling double resonance method proposed by Johnson [24]. This method requires a triple mass spectrometer in combination with the radiation from two tunable IR sources. One stage of mass-selection is required for initially mass-selecting parent ions, and two for performing IR^2MS^2 experiments. For details see text.

2) Both, photofragments and parent ions are extracted and accelerated towards the reflectron, and separate in time and space, according to their mass-to-charge ratios. After reflection, all ions are refocused into the extraction/acceleration region and a second laser pulse $h\nu_2$ (table-top laser) is timed such that parent ions are irradiated again. Subsequently, a second set of high voltage pulses is applied, extracting the remaining parent ions as well as isomer-specific photofragments (red) in the opposite direction (with respect to the first extraction).

3) Three TOF signals are detected at the MCP detector, corresponding to the fragments from $h\nu_2$ (t_1), undissociated parent ions (t_2) and the fragment ions from $h\nu_1$ (t_3).

Isomer-specific IRPD spectra are measured by scanning $h\nu_1$ and fixing $h\nu_2$ at an isomer-specific wavelength. In this way, the signal measured at t_1 monitors the depletion in one isomer, while the signals at t_2 and t_3 monitor the formation and depletion, respectively, of all isomers. The isomer-specific IRPD spectrum manifests itself in form of dips in the signal measured at t_1 (ion dip spectroscopy).

Typical TOF mass spectra with (bottom) and without (top) laser irradiation in the second acceleration stage are shown in Figure 3.19. Here, the population labeling method is applied to $H^+(H_2O)_6{\cdot}H_2$. In Figure 3.19 a) all ions are accelerated, mass separated and refocused at the point of their initial extraction. A second set of high voltage pulses reaccelerates only $H^+(H_2O)_6{\cdot}(H_2)_{1,2}$. At this point in time the $H^+(H_2O)_6$ ions have already passed the extraction region and are neither reaccelerated nor refocused, thus appearing as a very broad signal in the TOF mass spectra. Due to re-acceleration the $H^+(H_2O)_6{\cdot}(H_2)_{1,2}$ ions now appear before (!) the lighter $H^+(H_2O)_6$ ions, produced by the 1^{st} laser pulse, at the MCP. Careful choice of the timing of the 2^{nd} laser pulse allows selective irradiation only of the $H^+(H_2O)_6{\cdot}H_2$ ions, leading to formation of $H^+(H_2O)_6$ (and $H^+(H_2O)_5$) and re-acceleration of all ions. These are then detected background-free at the MCP detector (Figure 3.19 b). Note, $H^+(H_2O)_6{\cdot}(H_2)_2$ ions are not irradiated by the 2^{nd} laser pulse.

Figure 3.20 displays the resulting IR^2MS^2 spectra compared to AIMD simulations. The black trace (Figure 3.20 c) corresponds to the single-color IRPD spectrum of $H^+(H_2O)_6{\cdot}H_2$, showing spectral signatures of both isomers. Traces a) and e) show the simulated spectra of two isomers, revealing their characteristic absorptions. Isomer-selective spectra (Figure 3.20 b) and d) are obtained by scanning the first laser, while keeping the wave-

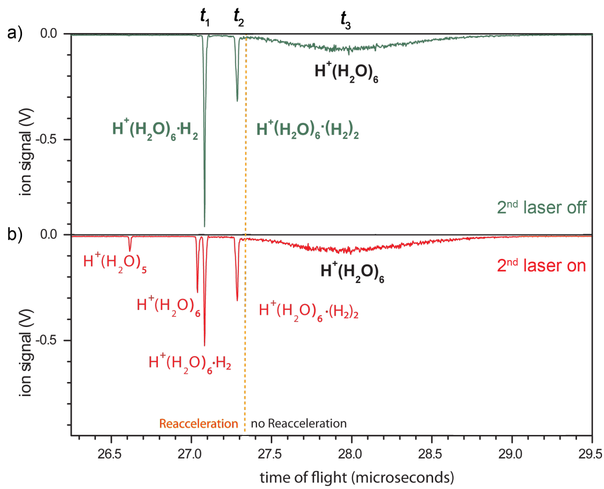

Figure 3.19: TOF mass spectra of $H^+(H_2O)_6{\cdot}H_2$, obtained with the first laser fixed on a vibrational resonance of one of the isomers. The top panel shows the TOF mass spectrum with the second laser off, whereas in the bottom panel the second laser is fixed on a specific absorption of one of the isomers.

length of the second laser constant at one of the characteristic absorptions (indicated by colored arrows).

Trigger Scheme and Electronic Configuration. As described in Section 3.5 the timing of a one-color experiment is typically provided by the trigger outputs of a 80 MHz counter/timer card (*National Instruments* (*NI*), PXI-6602) which is externally triggered by the IR laser system. For managing the complex and precise timing, required for a double resonance experiment, an external 8-channel delay generator with a 250 ps time resolution (*Quantum Composers*, 9528) and a 4-channel delay generator (*SRS*, DG535) are required. HV pulses are sent to two Pulser Boxes (*FHI ELAB*, # 4562, 4580), each containing two HV push-pull switches (*Behlke Electronic GmbH*, HTS-81-03-GSM) that are connected in series in order to allow for fast switching between HV1, HV2 and ground (Figure 3.21). For each Pulser Box Switch A can be switched between two high voltages. The output voltage is then sent to the second switch (Switch B), that supplies one of the TOF plates with either HV1, HV2 or ground.

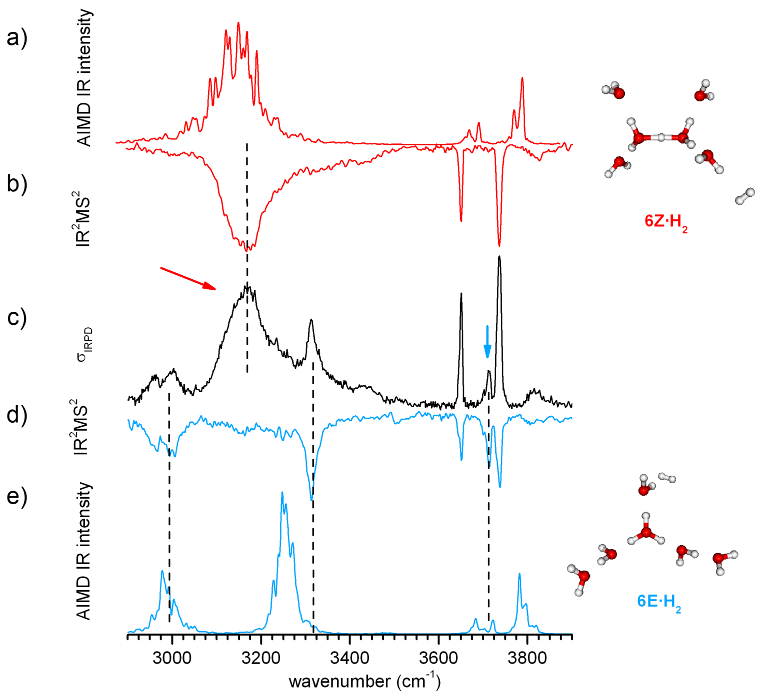

Figure 3.20: a) and e) Simulated anharmonic IR spectra of the two isomers of $H^+(H_2O)_6{\cdot}H_2$, c) one color spectra, b) and d) isomer-specific two-color spectra. For details see text and Section 4.

Figure 3.22 illustrates the trigger scheme applied for the double resonance experiments. A pretrigger is produced by the 1^{st} laser at t_0 and triggers the 8-channel delay generator at a repetition rate of 10 Hz. IR pulse emission occurs at t_2, depending on the laser system, either at 500 μs (FEL) or 254 μs (double OPO/*Powerlite*). The extraction of the ion packet from the trap occurs at t_1 and is chosen such that the ion packet overlaps with the 1^{st} laser pulse only when the packet is inbetween the TOF extraction plates (see Section 3.5). At t_2 the first set of high voltage pulses (HV1) is applied to the TOF plates and ions are extracted towards the reflectron. At t_3 Switch A is triggered and switches to HV2 (Figure 3.21). Subsequently, at t_4, Switch B is also set to HV2. t_4 is chosen such as to optimize the overlap of the parent ion packet with the 2^{nd} laser pulse (in the re-acceleration

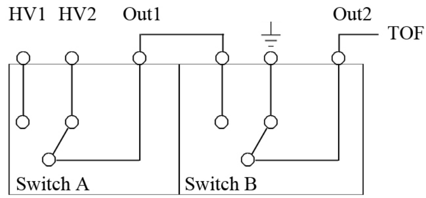

Figure 3.21: Schematic of the high voltage connections within one Pulser Box, containing two *Behlke* switches. Switch B is connected to one of the TOF plates and switches between ground and two different high voltages, provided by Switch A.

region). The time is referred to as the TOF II-delay and is typically in the range of a few nanoseconds. In order to avoid the application of HV2 prior to grounding of the TOF plates, TOF II is referenced to t_3 (see Table 3.3 for details).

The 2^{nd} laser delay is referred to the application of the first set of HV voltages and is therefore determined by the difference of the times the ions need to traverse the reflectron and the Pockels Cell delay of the laser. For example, the pockels cell delay of the single OPO (*Innolas*) is 225 μs. The flight time of the ions equals the sum of the delay between the end of pulse HV1 and t_3 (*e.g.* 12 μs) and TOF II (12.64 μs). The 2^{nd} laser delay is then determined by -225 μs + 12 μs + 12.64 μs = -200.36 μs.

Typical values for a double-resonance experiment using the double OPO (*Powerlite*) as first and the single OPO (*Innolas*) as second laser pulse, are listed in Table 3.3.

3.7 Electronics

Most of the DC voltages used for this setup are provided by custom-made electronic power supplies which provide high stability and low noise DC voltages for all electrostatic ion optics, including the capillary, skimmer, entrance-, exit-, and einzel lenses, pole biases, quadrupole bender and deflectors.

All electronics are computer-controlled using the LabVIEW program "SAPPHIRE"* (Spectra Acquisition Program for Photodissociation InfraRed Experiments) in combination with a *NI* PXI-1033 controller system. The PXI controller is equipped with five *NI* modules, providing digital

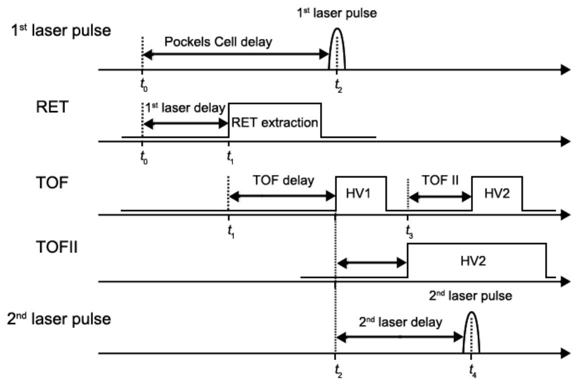

Figure 3.22: Trigger scheme of a double-resonance experiment. Details and values are given in the text and in Table 3.3.

and analog inputs, outputs, counters and timers. “SAPPHIRE” allows for saving and reloading of all settings and has been improved recently with a genetic algorithm, which was designed for adjusting the ion optics, in particular the 3x12 ion trap voltages, in order to optimize the transmitted ion signal [135].

Analog output voltages are provided by a set of three *NI* modules (PXI-6723), each delivering 32 programmable 13-bit control voltages between ±10 V. A monitoring card (PXI-6225) supplies up to 80 analog inputs at 16-bits, 250 kS/s, which are used for all power supplies in order to monitor their current state or control for faults. This module additionally provides 4 analog 16-bit, 833 kS/s outputs, that are necessary for fine control of the mass filter. A 80 MHz counter/timer card (PXI-6602) provides eight additional 32-bit counter/timer outputs.

The outputs are connected to an interface device (*FHI ELAB*, #4761), grouped and then either sent through an amplifying stage or directly to the particular part of equipment (TTL pulse). Two amplifying stages are employed: 1) Analog Output Board (*FHI ELAB*, #4651) and 2) Ring Electrode Trap Board (*FHI ELAB*, #4281). The Analog Output Board contains 32 precision voltage devices (electronic amplifiers with amplification of 17.5) that can generate ±175 V. The Ring Electrode Trap Board works similarly, but contains 36 precision voltage devices, which can

* programmed by K.R. Asmis

Table 3.3: Trigger settings for double-resonance experiments. The first delay generator (*Quantum Composer*) is triggered by the first laser, while the second delay generator (*SRS*) is triggered by the first delay generator.

Channel	Description	t_0	Source	Type	Width (μs)	Delay (μs)
		Quantum Composer				
A	Laser Delay	RET Board	Laser	TTL	150	139.5
B	TOF Delay		A	TTL	50	87.2
C*	TOF Extraction 1	Switch B	B	10 V	10	0
D	TOF II	Switch A	C	10 V	500	12
E*	TOF Extraction 2	C	D	10 V	50	12.64
F	Acquiris	Acquiris	B	TTL	50	0
G	Program	Interface Board	Laser	TTL	150	0
H	OPO	Stanford Box	B	TTL	150	-200.36
		Stanford Box				
A	Flashlamp	FL Trigger	t_0/Laser	TTL	100	
B	Q-Switch	PC Trigger	t_0/Laser	TTL	100	225
C	Pulse Monitor	Interface Board/NI	t_0/Laser	TTL	150	

* the output of Channel E is routed to Channel C, such that a double pulse is provided at Channel C.

be switched between with a precise timing of $0.7 - 2.5\,\mu$s.

High voltages are provided by four HV-Boxes (*FHI ELAB*, # 4650, 4889.1-2, 4890), equipped with 17 bipolar HV power supplies (*Schultz Electronic*, *Applied Kilovolts Ltd.*). To accomplish fast discharging of the TOF plates, the four corresponding HV power supplies are additionally provided with pull-down resistances.

3.8 Tandem Mass Spectrometer

Figure 3.23 shows the 12 K setup, built in 2006 [148], a detailed description of the apparatus is given in Ref. [116]. The new setup is based on the same principles but has some crucial enhancements that improve the overall performance. The most important changes will be briefly outlined in this

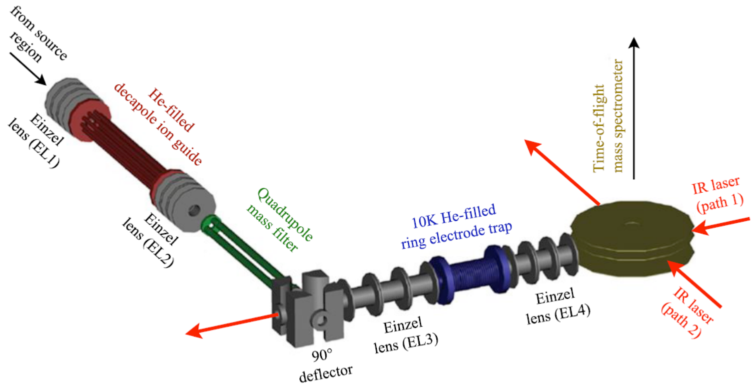

Figure 3.23: Schematic of the guided ion beam tandem mass spectrometer. The beam of ions from the cluster source is skimmed and collimated in a decapole ion guide. Mass-selected ions exit the quadrupole mass filter, are deflected by 90°, and focused into a RF RET (10-300 K). Here, ions are accumulated and thermalized through collisions with a buffer gas. Spectroscopic experiments are performed by extracting all ions into the focus of a perpendicularly mounted TOF-MS. The setup has been equipped with a dTOF-MS unit as described in Section 3.6 (not shown). Figure taken from Ref. [58].

section.

A new nanospray ion source increases the signal intensity and facilitates the generation of large hydrated clusters, concomitant with significantly reduced consumption of the sample solution (Section 3.3). The implementation of a translatable source chamber increases the ion signal and simplifies the use of different sources (Section 3.2). The new mass filter extends the mass range up to 4000 amu and allows for larger systems, such as proteins, large metal clusters and water nano droplets, with a high ion transmission (Section 3.4.2). The new design of the RET provides a larger volume and twice as many zones. This allows for greater flexibility and finally results in increased signal intensity. A more powerful closed-cycle cryostat in combination with an improved cryogenic design allows for more effective thermalization which translates into lower ion trap temperatures, and, more importantly, to lower internal ion temperatures (Section 3.4.2). Both instruments have been equipped with a new dTOF-MS (Section 3.6), which allows for isomer-selective experiments, as well as for higher mass resolution and the possibility of background-free measurements for a wide range of systems.

3.9 Infrared Light Sources

As described in Chapter 2, the low number density of mass-selected ions in the gas phase typically prohibits direct absorption measurements. Action spectroscopy, however, requires intense and tunable radiation sources. The Free Electron Laser for Infrared eXperiments FELIX fulfills these criteria, providing a broad spectral range ($40 - 2500\,\mathrm{cm}^{-1}$) with an output energy up to $< 150\,\mathrm{mJ/macropulse}$. The spectral range can even be increased up to $3500\,\mathrm{cm}^{-1}$, when operated on the third harmonic (with significantly reduced photon fluence) [149]. Recent developments in the field of table-top laser systems, however, make a large spectral region ($770 - 7400\,\mathrm{cm}^{-1}$) accessible [150, 151].

This section will briefly describe the operating principles and key features of the three different IR light sources used for the experiments presented in this thesis.

3.9.1 FELIX

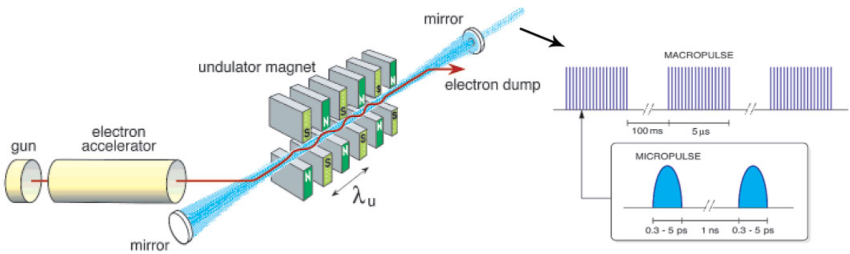

Figure 3.24: Schematic layout of a free electron laser. Free electrons are generated with a gun, accelerated to relativistic energies, injected into an undulator, and then dumped. Within the undulator the electrons are forced into a wiggling motion, leading to emission of light at every turning point. A typical pulse structure of the emitted light is schematically shown on the right. The figures are taken and adapted from Ref. [149].

The lasing medium in free electron lasers (FELs) are unbound electrons, which is in contrast to other types of lasers, where electrons are typically bound inside an atom or molecule. Here, the absorption of the gain medium limits the wavelength range, whereas free electrons can, in principle, produce light of any wavelength.

The scheme of a typical IR FEL is displayed in Figure 3.24. Free electrons are generated by an electron gun und subsequently accelerated to relativistic energies. The electron beam is then injected into an undulator, which consists of two sets of alternating permanent magnets with period λ_u, creating an alternating magnetic field perpendicular to the propagation direction of the electron beam. Due to the Lorentz forces the electrons are forced into a “wiggling” motion. Light is tangentially emitted at each turning point with a wavelength that corresponds to the traveled effective path length per undulator period. Due to a transverse motion, caused by the magnetic field, the path length is extended by a factor of $(1 + K^2)$, where K is a dimensionless parameter, that is directly proportional to the magnetic field strength. The wavelength of the emitted light is also influenced by two relativistic effects: first, the relativistic Lorentz factor γ and second, a strong Doppler effect, which shifts the emitted wavelength by a factor of γ^2. Thus the wavelength of the emitted radiation λ is given by:

$$\lambda = \frac{\lambda_u}{2\gamma^2}(1 + K^2). \tag{3.22}$$

Spontaneous emission (λ) is usually very weak and incoherent, therefore the undulator is placed within an optical cavity. The cavity consists of two highly reflective dielectric mirrors placed at each end of the undulator, which reflect the emitted radiation between both mirrors. The length of the resonator is adapted such that the stored electromagnetic wave can interact with newly injected electron bunches. The ponderomotive force gives rise to a modulation of the electron density along the longitudinal axis of the undulator on the scale of the emitted wavelength and leads to the micropulse structure depicted in Figure 3.24. Highly coherent photons are emitted through a central hole in the outcoupling mirror with typically 10^6 - 10^8 times higher intensity than the previous spontaneous emission.

Figure 3.25 shows a schematic view of two IR beamlines of the FELIX facility and their specifications are given in Table 3.4. An injector, a prebuncher and a buncher produce a $\sim 5\,\mu$s long electron macropulse with a beam energy of 3.8 MeV at a maximum repetition rate of 20 Hz. Two

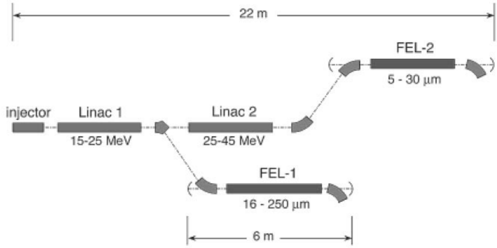

Figure 3.25: Schematic view of two IR FEL beamlines in the FELIX facility. Figure taken from Ref. [149].

RF linear accelerators (Linacs) can be employed to further accelerate the electron beam to either 15-25 MeV (Linac 1) or to 25-45 MeV (Linac 2). Behind each Linac, the electron beam can be deflected into one of the undulators, each placed within an optical resonator. FEL-1 and FEL-2 each consist of a resonator/undulator pair, providing a spectral range of 25-250 or 5-40 μm, respectively. Both undulators have identical parameters and consist of two rows of permanent magnets forming 38 field periods of 65 mm length. The wavelength can be tuned by changing the K-value, *i.e.* by varying the distance between the rows of the magnets (undulator gap). The resulting macropulse consists of several micropulses of 0.3 - 5 ps length, separated by 1 ns. The spectral bandwidth depends on the micropulse length and can be tuned from 300 fs to several picoseconds. Narrower pulses typically result in lower pulse energies. For the experiments presented in this thesis, the micropulse length was tuned such that a bandwidth of ~0.2-0.3 % root mean square of the central wavelength was obtained [152].

3.9.2 OPO/OPA Infrared Laser Systems

Two optical parametric oscillator/optical parametric amplifier (OPO/OPA) table-top laser systems developed by *LaserVision* [150] are used to produce tunable IR radiation over a spectral range from 770 to 4200 cm^{-1}. The systems differ in the number of OPO crystals and the pump laser. The high-power system (referred to as double OPO) contains two nonlinear KTP ($KTiPO_4$) crystals and is pumped by a pulsed, seeded Nd:YAG laser (*Continuum*, Powerlite DLS 8000) that produces 7 ns long pulses with pulse energies up to 1.05 J at a repetition rate of 10 Hz. The other system (referred to as single OPO) contains one KTP crystal and is pumped by

Table 3.4: Characteristics of FELIX compared to the OPO/OPA IR laser systems.

	FELIX	double OPO*	single OPO
spectral range	40 - 2500 cm^{-1}	770 - 4200 cm^{-1}	2000 - 4200 cm^{-1}
repetition rate	5/10 Hz	10 Hz	10 Hz
pulse energy	< 150 mJ	< 34 mJ	< 12 mJ
pulse duration	~ 5 μs	7 ns	7 ns
spectral bandwidth	0.2 - 1 % FWHM	~ 1.8 cm^{-1}	~ 3.6 cm^{-1}

* seeded

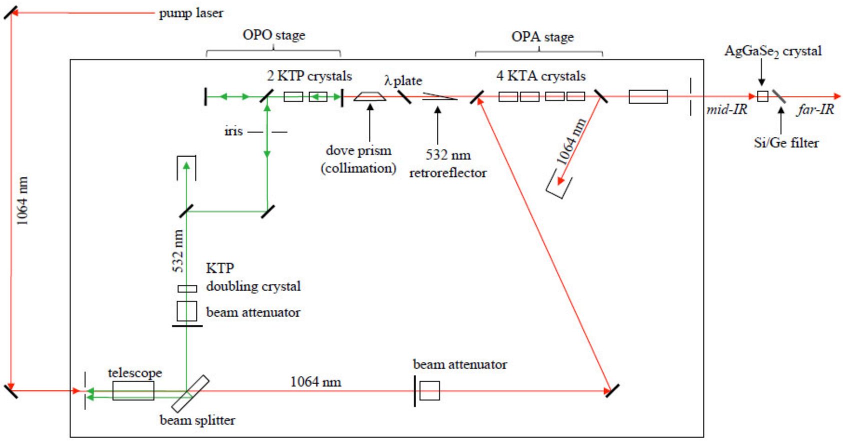

Figure 3.26: Schematic overview of the OPO/OPA IR laser system. Red and green arrows indicate the different beam paths. The 1064 nm fundamental of a Nd:YAG laser is used to pump the OPO and OPA stages. After several non-linear optical processes the fundamental is converted into tunable IR radiation in the mid and near-IR. Extension of the spectral range to far-IR is achieved by difference frequency mixing in an additional $AgGaSe_2$ crystal [116].

a pulsed, unseeded Nd:YAG laser (*Innolas*, Spitlight 600), providing 7 ns long pulses with pulse energies up to 800 mJ at 10 Hz. Specifications for both systems are given in Table 3.4.

The operating principle is the same for both systems and schematically shown in Figure 3.26 for the double OPO. The 1064 nm fundamental of the pump laser is collimated to match the size of the crystals by means of a telescope and is then split into two components by a beam splitter. The intensity of both components can be controlled by two attenuators. One part of the fundamental is frequency doubled by second harmonic generation (SHG) in a KTP crystal, subsequently serving as a pump for the OPO stage. The OPO stage consists of two KTP crystals placed within an optical cavity. Here, the frequency conversion is accomplished by non-linear optical processes. A pump photon (λ_{pump}) entering the resonator produces one signal (λ_{signal}) and one idler (λ_{idler}) photon in the near and intermediate IR. By conservation of energy, the sum of signal and idler energy has to be equal to the energy of the pump:

$$\frac{1}{\lambda_{pump}} = \frac{1}{\lambda_{signal}} + \frac{1}{\lambda_{idler}} \tag{3.23}$$

For an efficient conversion process, the phase matching condition $\mathbf{k}_{pump} = \mathbf{k}_{signal} + \mathbf{k}_{idler}$ has to be fulfilled. In order to achieve phase matching, the angular position of both crystals can be precisely controlled with stepper motors.

λ_{idler} is then used to seed λ_{signal} of the OPA stage. The OPA stage consists of four KTA ($KTiOAsO_4$) crystals and is pumped by the delayed 1064 nm beam. The idler wave together with the 1064 nm fundamental pump light produces radiation in the mid-IR region. Tunability of the wavelength is achieved by varying the crystal positions with precise stepper motors, ultimately producing radiation in a spectral range from 1350 to 2120 nm and from 2136 to 5020 nm.

Both, λ_{idler} and λ_{signal} from the OPA stage are used to pump a $AgGaSe_2$ crystal. Difference frequency mixing within the crystal generates radiation in the far-IR, covering a range from 5 to 13 μm.

The laser wavelength is calibrated using either a photoaccoustic cell filled with a suitable gas (*e.g.* methane or ethylene) or a *Princeton Instruments spectrometer* (VM-504).

Chapter 4

Isomer-Specific Spectroscopy on Protonated Water Clusters

The properties of hydrogen ions in aqueous solution, $H^+(aq)$, are governed by the ability of water to incorporate ions in a dynamical hydrogen-bond network, characterized by a structural variability which complicated the development of a consistent molecular level description of $H^+(aq)$. Isolated protonated water clusters, $H^+(H_2O)_n$, serve as finite model systems for $H^+(aq)$, which are amenable to highly sensitive and selective gas phase spectroscopic techniques.

The first part of this chapter aims to give an overview of how the vibrational spectra of messenger-tagged $H^+(H_2O)_n{\cdot}H_2$ clusters evolve for $n = 5$-10 (Section 4.3.1). The vibrational absorption features are assigned and discussed in context of results from previous studies.

In order to shed new light on a long-standing discussion regarding the contribution of different isomers to these spectra, isomer-selective double-resonance population labeling (IR^2MS^2) spectroscopy is employed. First, $H^+(H_2O)_6 \cdot H_2$ is discussed in the spectral range from 260 to 3900 cm^{-1} (Section 4.3.2). The IR signatures of the Zundel-type and Eigen-type isomer of $H^+(H_2O)_6$ are isolated and assigned down into the terahertz spectral region. AIMD simulations qualitatively recover the IR^2MS^2 spectra of the two isomers and allow attributing the increased width of IR bands associated with hydrogen-bonded moieties to anharmonicities rather than excited state lifetime broadening.

In Section 4.3.3 the contribution of multiple isomers to the IRPD spectra of clusters with $n = 5$,7-10 is disentangled by probing the spectral region of the free and bonded O-H stretching vibrations (from 2880 to 3850 cm^{-1}) isomer-specifically. For the protonated water heptamer evidence for at least four isomers is found. Surprisingly, the IR^2MS^2 spectra of all other cluster sizes show no indication for the contribution of more than one absorbing species. The chapter ends with a discussion of the advantages and limits of IR^2MS^2-spectroscopy.

4.1 Introduction

Understanding how protons are hydrated in solution remains an important and challenging research area [29, 70, 80, 83, 85–91]. The anomalously high proton mobility of water is typically explained by a periodic isomerization between the symmetrically solvated hydronium ion ${H_9O_4}^+(aq)$, originally proposed by Eigen [76], and the equally shared proton in the Zundel ion, ${H_5O_2}^+(aq)$ [77], even though the detailed mechanism is considerably more complex. A prominent example is the infrared (IR) spectrum of the hydrogen ion in water, which consists of a combination of a few discrete absorption bands on top of a continuous broad absorption across the entire IR spectrum. Neither the concepts of the Eigen- or the Zundel-form, nor models involving the rapid interconversion between these two structural motifs [153] seem to satisfactorily explain this characteristic IR fingerprint of $H^+(aq)$. In an attempt to resolve this issue, Stoyanov *et al.* have recently put forth the notion of a stable $H^+(H_2O)_6(aq)$ species, a Zundel-type ion in the sense that the proton is equally shared between two water molecules, but with more charge delocalization and consequently an unusually long central $O\cdots O$ distance of 2.57 Å [154]. Recent molecular dynamics simulations, on the other hand, suggest a distorted, non-symmetric Eigen-type cation rests at the heart of a dynamic electronic charge defect, spanning multiple water molecules [80].

While it remains difficult to pinpoint characteristic binding motifs of the rapidly interconverting species in aqueous solution experimentally, these can be isolated, stabilized and characterized in the form of gas-phase clusters, serving as benchmark systems for a computational treatment of proton hydration in solution. Just as neutral water clusters [155, 156] represent finite model systems for water in its different forms, protonated water clusters serve as prototypes for $H^+(aq)$. The potential energy (PE) landscape of these isolated clusters can be accurately probed with sensitive and selective gas phase spectroscopic techniques [87, 157], delivering, for example, data for the development of accurate interaction potentials. The most detailed structural information on how hydrogen ions are hydrated in finite systems is gained from IRPD experiments on $H^+(H_2O)_n$ clusters [83, 84, 86, 87, 89, 94, 95, 125, 158–160]. In order to identify the signal

Chapter based on:
Isomer-Selective Detection of Hydrogen-Bond Vibrations in the Protonated Water Hexamer
N. Heine, M. R. Fagiani, M. Rossi, T. Wende, G. Berden, V. Blum, and K. R. Asmis, *J. Am. Chem. Soc.* **2013**, 135, 8266 – 8273. DOI: 10.1021/ja401359t

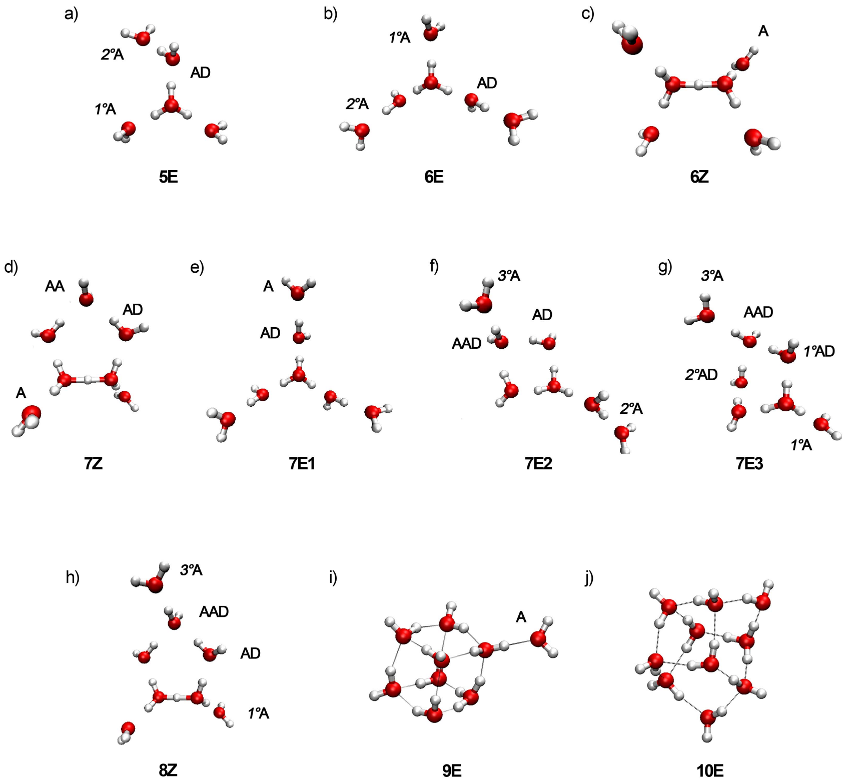

Figure 4.1: Minimum energy structures of $H^+(H_2O)_{5-10}$.* **E** refers to an Eigen-type and **Z** to a Zundel-type structure. The water molecules are classified according to their function as hydrogen-bond acceptor (A) and/or donor (D). 1°, 2°, 3° refer to the first, second and third hydration shell, respectively.

* Calculations for n=5,9,10 were performed by J.A. Fournier in the group of M.A. Johnson at Yale University.

carrier, the clusters are size-selected and photoabsorption is measured indirectly by monitoring the photodissociation yield.

The location of the excess charge has been shown to respond markedly sensitive to a change in the hydration environment, and it is size-dependent for protonated water clusters with n up to 10. The clusters can adopt either a Zundel- or a Eigen-type binding motif and for each type multiple isomers may coexist, which differ in the precise arrangement of the water molecules in the hydration shell. Despite significant experimental and theoretical efforts, the precise assignment of isomers for a particular cluster size remains controversial.

For the last decade there has been a consensus that up to $n \leq 5$ either Zundel-type ($n = 2$) or Eigen-type (n = 3-5) structures are present [29, 83, 84, 87, 94–98]. Recently, however, Kulig *et al.* anticipated the appearance of two different isomers in the n = 4,5 clusters, based on AIMD simulations. The authors suggest that the IR spectrum of $n = 4$ contains contributions from both Zundel- and Eigen-type isomers, whilst an Eigen/Zundel hybrid, along with a four-membered ring Eigen-type isomer is present for $n = 5$ [92, 93]. Previous experimental evidence, however, only supports the presence of the Eigen-type isomer in both cases (Figure 4.1 a).

The assignment for $n \geq 6$ clusters to specific structural motifs is more challenging. For the protonated water hexamer both isomers, the Zundel- and the Eigen-type, (Figure 4.1 b, c) are present [84, 98, 125]. With increasing number of water molecules in a protonated water cluster, one would intuitively expect that the number of energetically low-lying isomers increases. Indeed, the contribution of at least three isomers to the IR spectrum of $n = 7$ has been suggested [84, 95] (Figure 4.1 d, e, g), but, surprisingly, for even larger clusters no experimental evidence for multiple isomers has been found yet [84, 95].

Whereas the smaller protonated water clusters ($n < 9$) exhibit a sheet-like structure, larger clusters start to form three-dimensional (3D) network cage morphologies [85, 159]. In the intermediate size range, including the protonated water nonamer and decamer, the ordering of the isomers is anticipated to be temperature dependent. Theoretical studies predict that at lower temperatures closed 3D structures (Figure 4.1 i) are stabilized, while at higher temperatures open structures, partially net-like or with dangling H_2O molecules are entropically favored (Figure 4.1 h). The smallest experimentally observed protonated water cluster exhibiting a *closed* 3D structure is $n = 10$ [86, 87, 159].

In order to answer the controversial question regarding the isomeric distribution as a function of cluster size, double-resonance population labeling (IR^2MS^2) spectroscopy [24–27] is applied for the first time to protonated water clusters to resolve the spectral signatures of the individual isomers contributing to the corresponding IRPD spectra. IR^2MS^2 spectroscopy is an only recently developed method, which allows one to measure IR spectra of coexisting isomers isomer-specifically. It is a particularly attractive variant of ion dip spectroscopy [19, 22, 161–163], since it does not require the presence of an UV-VIS chromophore in the cluster. Instead, this detection scheme makes use of two tunable IR lasers in combination with two stages of mass separation (MS), hence the abbreviation IR^2MS^2.

The first system investigated with the Berlin tandem mass spectrometer was $H^+(H_2O)_6$. To the present date, $H^+(H_2O)_6$ is the smallest protonated water cluster that has unambiguously been confirmed to exhibit Zundel- and Eigen-type binding motifs [84, 125], and it therefore represents a prototypical system for studying structure-dependent charge delocalization on a single PE surface. However, large parts of the PE surface of $H^+(H_2O)_6$ have remained experimentally unexplored, including most of the fingerprint vibrations of the Eigen-type isomers and, more importantly, the hydrogen-bond (HB) vibrations of both species in the terahertz region. In Section 4.3.2 IR^2MS^2 is used to shed new light on the PE surface in the vicinity of the minima corresponding to the Eigen-type (**E**) and Zundel-type (**Z**) isomers (see Figure 4.1 b,c) over nearly the entire IR spectral range. A precise characterization of the PE surface supporting the "librational" and "translational" IR bands is a prerequisite for understanding HB network rearrangement dynamics ultimately leading to proton transfer and serves as a sensitive test for quantum chemical calculations [155, 156]. Since anharmonic effects are known to play a critical role in protonated water clusters, see for example Refs. [30, 32, 33, 35, 164, 165] and Refs. therein, *ab initio* molecular dynamics simulations (AIMD) are employed for interpreting the IRPD spectra.

In the subsequent section IR^2MS^2 spectroscopy in the O-H stretching region is used to disentangle the contributions of specific isomers of the remaining protonated water clusters with n = 5,7-10. Spectral signatures are assigned by comparison to the results from previous experimental and theoretical studies (Section 4.3.3).

The reliable assignment of IR bands to specific isomers typically requires that gas phase IR photodissociation spectra are measured of (internally) cold clusters and in the linear absorption regime, such that observed band positions and intensities can be directly compared with predicted ones from quantum chemical calculations. Smaller protonated water clusters ($n \leq 7$) have dissociation energies of at least 45 kJ/mol (3740 cm^{-1}) [166, 167]. Hence, single-photon photodissociation experiments on cold clusters across large parts of the IR spectrum cannot be performed on the bare clusters (see also Section 2.2 for details). Thus, the messenger technique [117] has been used for measuring vibrational spectra which showed that the charge delocalization in hydrated proton clusters is very sensitive to changes in the hydration shell environment and that addition of messenger species can have a marked effect on the isomer distribution [87, 94, 95, 125, 126] (Section 2.2). Attachment of H_2 or D_2 to the protonated water clusters leave the isomer distribution essentially unchanged compared to the bare cluster [95]. Thus, they are used as messenger species in the following experiments.

4.2 Experimental and Computational Section

4.2.1 Experimental Setup

The IRPD experiments are carried out using the ion-trap tandem mass-spectro-meter described in Section 3.8, enhanced by a custom-built 180° reflectron stage (see Figure 4.2 and Section 3.6). The IR^2MS^2 experiments on $H^+(H_2O)_6$ make use of the tunable IR radiation from FELIX [152] (260 – 2000 cm^{-1}) in combination with the on-site Laservision OPO/OPA IR laser [150] (2050 – 3900 cm^{-1}), both operated at 10 Hz (Section 3.9). Additional experiments above 2050 cm^{-1} and all measurements on n = 5,7-10 were performed in Berlin using two Laservision OPO/OPA IR lasers. The bandwidth of the FELIX pulses is ~0.2% RMS of the central wavelength and that of the OPO/OPA laser pulses 2-3 cm^{-1}. IR pulse energies are kept <10 mJ to avoid saturation. The photodissociation cross section σ is determined from the relative abundances of parent and photofragment ions, I_0 and $I(\nu)$, and the frequency-dependent laser fluence $F(\nu)$ using

$$\sigma = -\frac{ln[I(\nu)/I_0]}{F(\nu)}. \tag{4.1}$$

At very low laser fluence this normalization procedure introduces additional noise to the spectra (see, for example, the 2050-2300 cm^{-1} region in Figure 4.5).

Protonated water clusters are produced by electrospray of a 10 mM HNO_3 solution in a 1:4 water/acetonitrile mixture. Mass-selected parent ions are

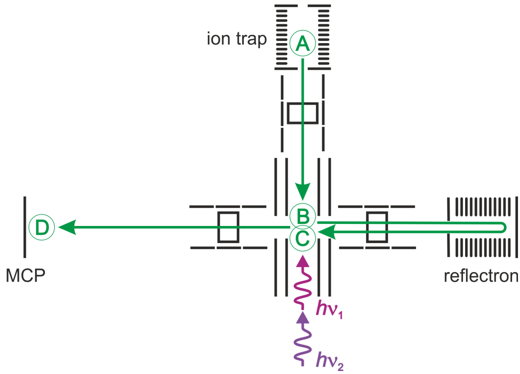

Figure 4.2: IR^2MS^2 experimental setup and scheme. Ions are extracted from the ion trap (**A**) and focused into the extraction zone of a reflectron TOF mass spectrometer. After irradiation by the first IR laser pulse ($h\nu_1$), ions are accelerated into the 180° reflectron stage (**B**) and refocused. The second IR laser pulse ($h\nu_2$) is timed such as to optimize temporal overlap with the parent ion packet. (**C**) Subsequently, ions are re-accelerated into the linear TOF section and a TOF mass spectrum is measured at the MCP detector (**D**). See Section 3.6 for a more detailed description.

accumulated, thermalized, and messenger-tagged in a cryogenically-cooled RF ring-electrode ion-trap. The trap is continuously filled with H_2 buffer-gas at 15 K and $H^+(H_2O)_n{\cdot}H_2$ complexes are stabilized through three-body collisions [58, 168].

IR^2MS^2 Scheme

Every 100 ms all ions are extracted from the trap (**A** in Figure 4.2) and focused both temporally and spatially into the center of the extraction region of an orthogonally-mounted linear reflectron time-of-flight tandem mass spectrometer (dTOF-MS). Here, the parent ions, $H^+(H_2O)_n{\cdot}H_2$, are irradiated with the first IR laser pulse, producing a first set of photofragment ions (**B**). Subsequently, all ions are accelerated into the 180° reflectron stage by application of a first set of high voltage pulses. They separate out in time and space according to their mass/charge ratio and are refocused at the original interaction zone. The second (probe) laser pulse is timed such that temporal overlap with the parent ion packet is optimized, producing a second set of photofragment ions (**C**). All ions in between the acceleration plates are re-accelerated towards the MCP detector, into the linear TOF stage of the mass spectrometer by a second set of high voltage pulses. For each laser shot a TOF mass spectrum is measured (**D**), which contains (at least) three separate ion signals, corresponding to the parent ions, fragment ions from the first IR laser pulse and the fragment ions from the second IR laser pulse. IR^2MS^2 spectra are recorded by tuning the wavelength of the probe laser ($h\nu_2$) to an isomer-specific transition and monitoring all ion intensities as the laser wavelength of the first laser ($h\nu_1$) is scanned (50-100 measurements per wavelength step) [24].

4.2.2 Computational Details

The density-functional theory (DFT) calculations were performed with the all-electron, localized basis FHI-aims program package [169]. The PBE [170] semi-local exchange-correlation functional corrected with a $C_6[n]/R^6$ term (as proposed in Ref. [171]) was used in order to account for van-der-Waals dispersion-interactions (PBE+vdW). *Tight* settings for basis sets and numerical grids were used, as described in Ref. [169]. These settings yield essentially converged energetics, free of basis set superposition errors [169],[172]. Harmonic vibrations were calculated through finite differences. Anharmonic IR spectra were calculated through the Fourier transform of the dipole autocorrelation function, obtained from microcanonical AIMD (Born-Oppenheimer) runs, using a time step of 0.5 fs. For the **6Z**$\cdot H_2$ and **6E**$\cdot H_2$ isomers it is averaged over 4 and 5 trajectories of 10 ps each, respectively, starting from different thermalized geometries. These initial geometries were taken from a 10 ps long thermalization run at 50 K. It is checked that the isomers remain close to their overall initial geometry throughout the simulations.*

4.3 Results and Discussion

4.3.1 Single-Color IRPD Spectra of $H^+(H_2O)_{5-10}$

In order to assess the influence of the ion temperature and the messenger species, the single-color IRPD spectra of messenger-tagged $H^+(H_2O)_{5-10}$ in the O-H stretching region are first compared to previous experimental

*Calculations were performed by M. Rossi in the group headed by V. Blum at the Theory Department of the Fritz-Haber-Institute.

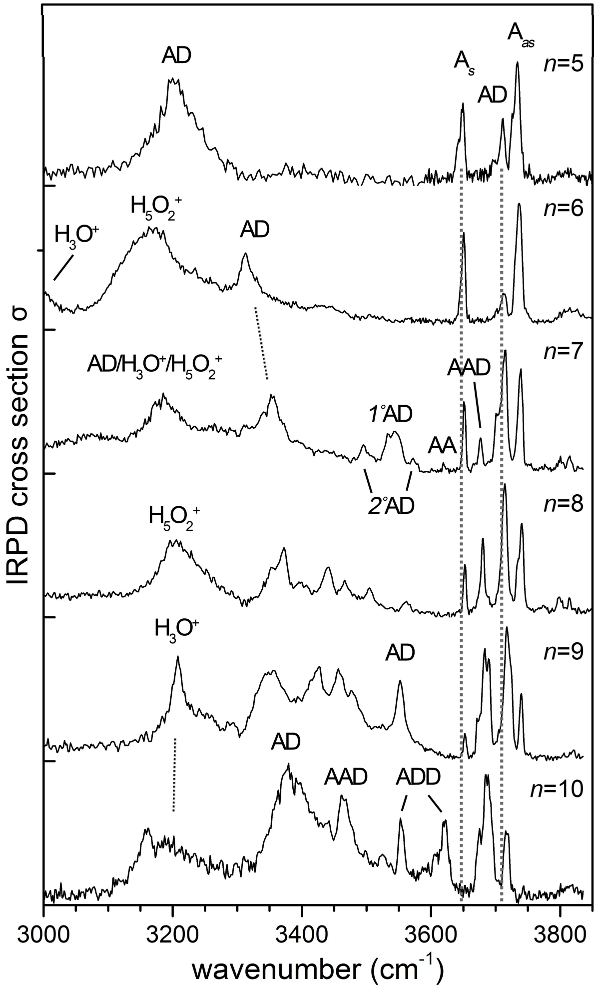

Figure 4.3: IRPD spectra of $H^+(H_2O)_n{\cdot}H_2/D_2$, with n = 5-10, in the O-H stretching region (3000 – 3900 cm^{-1}). Band assignments are based on the function of the respective water molecule with regard to hydrogen-bonding. A = hydrogen-bond acceptor, D = hydrogen-bond donor, s = symmetric, as = antisymmetric, *1°* = 1^{st} hydration shell, *2°* = 2^{nd} hydration shell.

[84, 86, 87, 159] and theoretical [173–175] studies, which allows assigning the most characteristic bands and their change in evolution of size for H_2/D_2-tagged clusters. Figure 4.3 gives an overview of IRPD spectra of $H^+(H_2O)_n{\cdot}H_2/D_2$, with n = 5-10 from 3000 to 3850 cm^{-1}. The sharp features above 3700 cm^{-1} are assigned to free O-H stretching vibrations, and the region below 3700 cm^{-1} is attributed to modes associated with hydrogen-bonded (HB) O-H oscillators [86]. The bands are labeled according to their assignment to either modes of the ionic core (H_3O^+ or $H_5O_2{}^+$) or of HBed H_2O molecules, which are classified according to their function as hydrogen-bond donor (D) and/or acceptor (A).

The highest frequency region (>3630 cm^{-1}) provides a clear diagnostic of structures with dangling water molecules, *i.e.* singly-accepting H_2O molecules (A), and rings of water molecules [86]. For $n = 5$ and 6 this region is dominated by the symmetric (s) and antisymmetric (as) free O-H stretches of dangling H_2O molecules (A-H_2O). Bands associated with A-H_2O persist up to $n = 9$ and are not observed in the spectrum of $n = 10$ (Figure 4.3). This is in agreement with the previously measured Ar-tagged spectra [87] and signals the onset of *closed* 3D structures for $n > 9$. This onset is shifted to larger clusters ($n > 10$) for bare protonated water clusters [86], which has been attributed [174] to the population of more isomers as a result of their higher internal energy compared to the messenger-tagged species.

The less intense band at ~3715 cm^{-1} in the $n = 5$ spectrum originates from a single acceptor-single donor (AD) H_2O and is observed throughout the spectra up to $n = 10$. Starting with $n = 7$ a new feature evolves at 3676 cm^{-1} (AAD), attributed to a triply-coordinated H_2O located in the second solvation shell. This band becomes the most intense feature in the free O-H stretching region for $n = 10$ and has been shown to be characteristic for structures containing rings [84].

In the region of the HBed O-H stretches (3300 – 3700 cm^{-1}), the complexity of the IRPD spectra increases with n. While the spectrum of $n = 5$ is still noticeably flat, except for a weak and broad absorption at ~3400 cm^{-1}, the addition of two more water molecules, $n = 7$, already gives rise to five new features. These are attributed to the symmetric and antisymmetric stretches of an AD-H_2O in the first (~3544, 3532 and 3352 cm^{-1}) or second (3573 and 3495 cm^{-1}) solvation shell [87]. The number of binding sites for n = 8-10 increases significantly and an unambiguous assignment is currently not possible [174].

The broad absorption in-between 3100 – 3300 cm^{-1} is related to O-H stretches in contact with the excess positive charge, *i.e.* the four HBed O-H stretches of the H_2O moieties in ${H_5O_2}^+$ as well as some of the O-H stretches of HBed H_3O^+ [84, 87].

In order to isolate and identify the contributing isomers to the IRPD spectra displayed in Figure 4.3, IR^2MS^2 spectra of $H^+(H_2O)_n{\cdot}H_2/D_2$ with n = 5-10 are measured. For n = 6 we demonstrate that this technique can be applied nearly across the complete IR region and spectra.

4.3.2 Isomer-Selective Detection of Hydrogen-Bond Vibrations in $H^+(H_2O)_6$

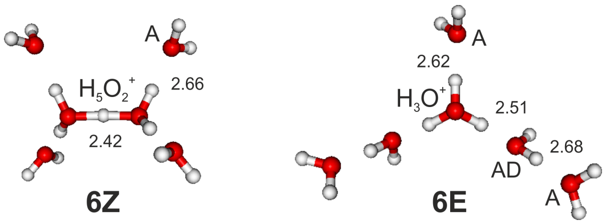

Figure 4.4: DFT PBE+vdW local minimum energy structures of the Zundel-type (**6Z**) and Eigen-type (**6E**) isomers of $H^+(H_2O)_6$. Water molecules are classified according their function as HB acceptor (A) and donor (D). O· · ·O distances are given in Å.

The IRPD spectrum of $H^+(H_2O)_6{\cdot}H_2$ in the scanning range of the IR-FEL (260 – 2000 cm^{-1}) and the IR-OPO/OPA laser (2050 – 3900 cm^{-1}) are shown in Figures 4.5 (trace B). $H^+(H_2O)_6{\cdot}H_2$ absorbs throughout the IR spectrum, exhibiting more than twenty absorption bands, of which the most intense ones are labeled a_1 to a_{19} (see Table 4.1 for band positions and assignments). Several bands are significantly broadened, *e.g.* a_6, a_{9-10}, a_{14} and a_{15}, throughout the entire spectral range. This broadening has recently been attributed to shorter excited state life times as a result of fast intramolecular vibrational energy redistribution (IVR) due to hydrogen-bonding [94].

Two complimentary IR spectra are obtained using the isomer-selective IR^2MS^2 technique (Figure 4.5, traces C and D in Figure 4.5) indicating two structurally very different absorbing species. Moreover, these two spectra suffice to account for all the IR bands observed in the IR spectrum of the isomeric mixture (Figure 4.5, trace B). Trace C is obtained by probing band

a'_6 (3167 cm^{-1}), corresponding to the O-H stretching modes of the two hydrogen-bonded water moieties of the $H_5O_2{}^+$-core in isomer **6Z**. Figure 4.5, trace D is obtained by probing band a''_3 (3714 cm^{-1}), the free O-H stretching modes of the two AD water molecules of **6E** (see Figure 4.4). Each of these vibrational modes is specific to one of the isomers and therefore a high isomer selectivity of larger then 80% is observed in the IR^2MS^2 spectra. Figure 4.6 shows that IR^2MS^2 spectra with similar contrast to those shown in Figure 4.5 are obtained when probing the isomer-specific bands a'_{14} (1050 cm^{-1}) and a''_9 (1951 cm^{-1}), supporting that there are only two isomers present. For comparison and later discussion, the IR spectrum of the $H^+(aq)$ ion in ionized strong aqueous acids from Ref. [154] is also shown at the top of Figure 4.5, trace A.

AIMD Simulations. In order to aid in the assignment of the IR spectra, *ab initio* molecular dynamics (AIMD) calculations were performed. These explicitly include anharmonic effects and were carried out for $H^+(H_2O)_6{\cdot}H_2$ as well as $H^+(H_2O)_6$. The following discussion mainly makes use of the results including the messenger molecule, because this species is probed in the experiments. Note, the comparison of the results with and without messenger suggests that the overall changes to the IR spectrum are rather small (see Table A.1, Appendix A).

The simulated anharmonic IR spectra at an average temperature $\langle T \rangle =$ 50 K of the **6Z**$\cdot H_2$ and **6E**$\cdot H_2$ isomers, derived from the AIMD calculations, using the PBE [170] semi-local functional corrected for van der Waals (vdW) dispersion interactions [171], are also shown in Figure 4.5 (see traces E and F, respectively). For the most intense absorption features a satisfactory and unambiguous qualitative agreement is observed between the **6Z**$\cdot H_2$ (trace E) and the **6E**$\cdot H_2$ (trace F) calculated anharmonic spectra and the corresponding experimental IR^2MS^2 spectra (traces C and D). The AIMD simulations qualitatively reproduce the experimental band widths and shapes, suggesting that anharmonicity rather than excited state lifetime broadening (as a result of very fast internal vibrational energy redistribution) [94] is the main cause of the observed broadening. The simulated peak positions are typically shifted to higher energies with respect to the experimentally observed positions. The larger shifts between experiment and theory, especially (i) when the motion of the hydrated proton is involved and (ii) in the free O-H stretch region, are commonly attributed to limitations of existing DFT functionals, as well as the neglect of nuclear quantum effects, but there is no question as to the unambiguous qualitative correspondence between experimental and theoretical spectra.

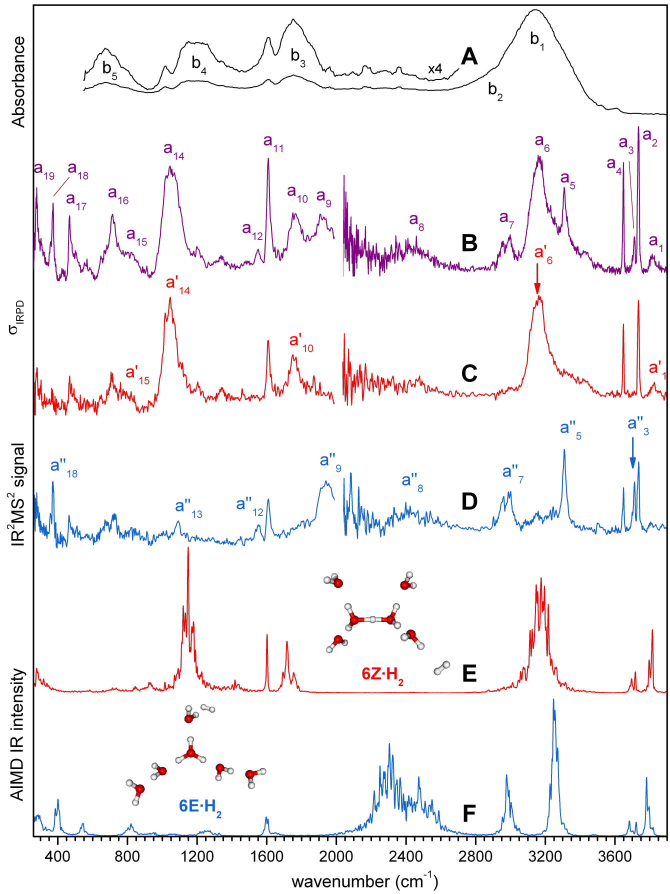

Figure 4.5: Solution phase IR absorption spectrum of the $H^+(aq)$ ion in ionized strong aqueous acids from Ref. [154] (A, black), gas phase IRPD spectrum of $H^+(H_2O)_6{\cdot}H_2$ (B, purple), IR^2MS^2 spectra of $H^+(H_2O)_6{\cdot}H_2$, obtained by probing either the transition indicated by the red (C, 3159 cm^{-1}) or the blue (D, 3715 cm^{-1}) arrow, and anharmonic IR spectra of **6Z**$\cdot H_2$ (E, red) and **6E**$\cdot H_2$ (F, blue) obtained from PBE+vdW AIMD simulations at 50 K, from 260 to 3900 cm^{-1}. Spectra B to D each consist of two traces, corresponding to separate measurements in the scanning range of the IR-FEL (260 – 2000 cm^{-1}) and the IR-OPO/OPA laser (2050 – 3900 cm^{-1}). Experimental bands are labeled from a_1 to a_{19} (gas phase)and b_1 to b_5 (solution) (see Table 4.1 for band positions and assignments).

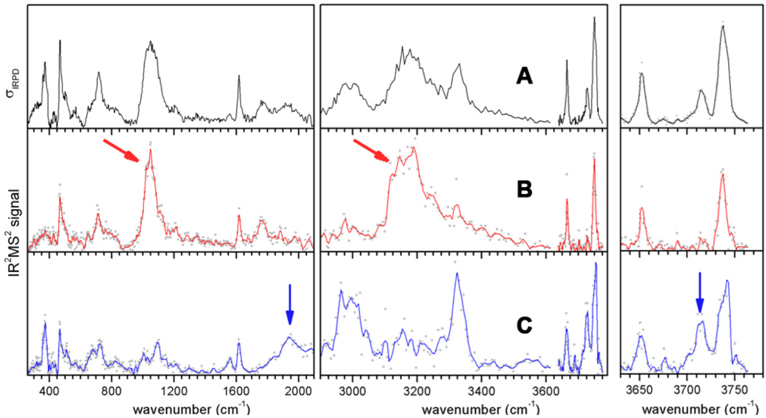

Figure 4.6: IRPD spectrum of $H^+(H_2O)_6{\cdot}H_2$ (black), IR^2MS^2 spectra of $H^+(H_2O)_6{\cdot}H_2$, obtained by probing either the transition indicated by the blue (1951 and 3738 cm^{-1}) or the red (1050 and 3167 cm^{-1}) arrow. While scanning the OPO ($h\nu_1$), FELIX is used to probe the low-frequency transitions at 1050 and 1951 cm^{-1} ($h\nu_2$), and vice versa.

In fact, it has been shown by Vendrell *et al.* [176] for ${H_5O_2}^+$ that such effects can be eliminated completely by probing the full-dimensional, with respect to the vibrational degrees of freedom, PE surface quantum mechanically, but such a treatment is not feasible here due to computational cost. Note that the simulated spectra (traces E and F) of both isomers, **6Z**$\cdot H_2$ and **6E**$\cdot H_2$, exhibit a splitting of the free O-H stretching bands ($> 3600\,cm^{-1}$), which is not observed in the experimental spectra. Simulations of the bare clusters **6Z** and **6E** do not yield this splitting and show sharp peaks in good agreement with experiment (see Figure A.1 in Appendix A). This indicates that the clusters probed in the experiment have sufficient internal energy to overcome the small barriers separating the basins corresponding to the nearly isoenergetic H_2-binding sites, leading to a delocalization of H_2 and consequently an averaging-out of this effect, while the propagation time in the simulations of 40 and 50 ps, essentially limited by computational constraints, was not long enough for the H_2 molecule to explore all possible binding positions.

Zundel-type Isomer. The IR^2MS^2 spectrum of **6Z**$\cdot H_2$ (trace C in Figure 4.5) reveals four characteristically broad absorption bands at 3167 (a'_6), 1759 (a'_{10}), 1050 (a'_{14}), and 805 cm^{-1} (a'_{15}). Their increased width suggests that they all originate from vibrational modes involving the same moiety, namely, the symmetrically hydrated $H_5O_2^+$ core. Hence, these bands are attributed to hydrogen-bonded O-H stretching (a'_6) and H-O-H bending (a'_{10}) modes of the shared-proton, as well as a doublet associated with the shared proton stretching mode (a'_{14}, a'_{15}). These are observed at $\sim$ 3650, 1763, 1047 and 928 cm^{-1} in bare $H_5O_2{}^+$ and their assignment is widely accepted now [165],[96],[97],[176]. The increased charge delocalization in $H_5O_2{}^+(H_2O)_4$, compared to $H_5O_2{}^+$, results in a pronounced shift to lower energies of bands a'_6 and a'_{15}, while bands a'_{10} and a'_{14} remain nearly unaffected. Assuming that the effective shared proton frequency corresponds to the centroid of the observed doublet (a'_{14}, a'_{15}) [115], this frequency is also red-shifted, in agreement with an increase of the proton affinity of the waters sharing the proton in $H_5O_2{}^+(H_2O)_4$, compared to $H_5O_2{}^+$, as a result of cooperativity.

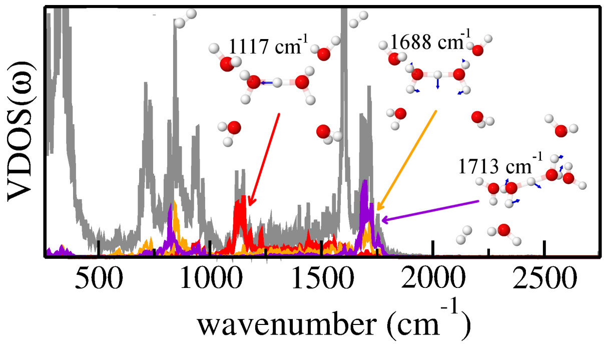

Figure 4.7: Vibrational density of states (VDOS) obtained from the Fourier transform of the velocity autocorrelation function of a 26 ps long microcanonical AIMD run of **6Z**·H_2 with <T> = 50 K. In grey, the total VDOS. In red, the projection of the VDOS on the harmonic normal mode that corresponds to the shared proton stretch motion (harmonic frequency at 1117 cm^{-1} with PBE+vdW). In orange and violet, the projections on harmonic normal modes corresponding to the shared proton bending motion coupled to HOH bending motions (harmonic frequencies at 1688 and 1713 cm^{-1}, respectively).

The characteristic IR fingerprint of the symmetrically hydrated Zundel ion, *i.e.*, bands a'_6, a'_{10}, a'_{14} and a'_{15} in Figure 4.5, is qualitatively reproduced by the anharmonic calculations (see Figure 4.5, trace E). Moreover, the intensity ratio of bands a'_{14} and a'_{10}, associated with the shared proton stretching and bending modes, is in excellent agreement with the predictions from theory. In contrast, recent molecular dynamics simulations [91] find the main IR intensity of the proton transfer mode in $H_5O_2^+(H_2O)_4$ at 1750 cm^{-1}, with only little intensity around 1100 cm^{-1}. To test this prediction, the total vibrational density of states (VDOS), defined as the Fourier transform of the velocity autocorrelation function, is calculated from an AIMD run of the **6Z**·H_2 isomer, as well as its projection onto the well defined harmonic normal modes. The results, shown in Figure 4.7, confirm that the intense peak at 1135 cm^{-1} found in the PBE+vdW anharmonic IR spectra, corresponding to a'_{14} in the experiment, is essentially due only to the shared proton stretch motion (red trace in Figure 4.7). The peaks around 1700 cm^{-1}, corresponding to a'_{10} in the experiment, instead, owe most of their intensity to bending motions of the shared proton (motion perpendicular to the O···H$^+$···O-axis) coupled to the internal H-O-H bending motions (violet and orange traces in Figure 4.7).

However, it is necessary to comment separately on the a'_{15} feature and its calculated counterpart structure in the **6Z**·H_2 isomer. In the bare Zundel ion ($H_5{O_2}^+$), a structure in the same wavenumber region arises purely due to anharmonic mode couplings, with no harmonic counterpart [32, 33, 165]. In contrast, there are corresponding *harmonic* modes in this region for the microhydrated Zundel ion studied here (**6Z/6Z**·H_2 isomer; see Figure A.2, and Figure A.4, Appendix A). In the AIMD spectrum (Figure 4.5, trace E), there is indeed some statistically relevant intensity in this range. Its structure emerges clearly when enhanced by a factor of five (Figure A.2, Appendix A). Interestingly, especially its highest-lying component (just below 1000 cm^{-1} in the calculations) is not simply due to a single harmonic mode, but contains significant contributions from other modes as well (VDOS decomposition in Figure A.3, Appendix A). The a'_{15} structure is thus analogous to what is known as the lower doublet peak of the bare Zundel ion, but not identical, since a corresponding harmonic contribution exists as well. Note, the coupling of the shared proton stretching and bending modes increases with temperature and has been predicted to be significant at room temperature [177]. The remaining three narrower bands above 1500 cm^{-1} observed in trace C (Figure 4.5) are then assigned to vibrational modes involving the terminal water molecules (see Table 4.1). These are the free O-H stretching (a'_2, a'_4) and the H_2O bending (a'_{11}) modes.

Table 4.1: Position (in cm^{-1}) and assignment of the vibrational bands observed in the IRPD spectra of bare and messenger-tagged $H^+(H_2O)_6$.

	IR^{2}MS^2 (3159 cm^{-1})	**IR^{2}MS^2 (3715 cm^{-1})**	**Previous Exp.**	**Isomer**	**Assignment^d**
3815 (a_1)	3827 (a'_1)		3817^a	6Z	*combination band*
3737 (a_2)	3737 (a'_2)	3738 (a''_2)	3741^a, 3740^b, 3739^c	6Z,6E	*free O-H stretch (antisym, A-H_2O)*
3713 (a_3)		3714 (a''_3)	3713^a, 3716^c	6E	*free O-H stretch (AD-H_2O)*
3651 (a_4)	3651 (a'_4)	3651 (a''_4)	3651^a, 3650^b, 3652^c	6Z,6E	*free O-H stretch (sym, A-H_2O)*
3312 (a_5)		3312 (a''_5)	3320^a, 3304/3325^c	6E	*O-H stretch (AD-H_2O)*
3163 (a_6)	3167 (a'_6)		3178^a, 3160^b, 3160^c	6Z	*O-H stretch ($H_5O_2{}^+$)*
3003 (a_7)		3007 (a''_7)	2988^a, 2991^c	6E	*O-H stretch (H_3O^+)*
	~2480 (a'_8)			6Z	
~2425 (a_8)		~2425 (a''_8)		6E	*O-H stretch (H_3O^+)*
1917 (a_9)		1951 (a''_9)		6E	*O-H stretch (H_3O^+)*
1760 (a_{10})	1759 (a'_{10})			6Z	*shared proton bend ($H_5O_2{}^+$)*
1618 (a_{11})	1618 (a'_{11})	1618 (a''_{11})		6Z,6E	*H_2O bend (A-H_2O)*
1558 (a_{12})		1561 (a''_{12})		6E	*H_2O bend*
		1097 (a''_{13})		6E	*H_3O^+ umbrella*
1049 (a_{14})	1050 (a'_{14})		1055^b	6Z	*shared proton stretch ($H_5O_2{}^+$)*
~805 (a_{15})	~805 (a'_{15})			6Z	*shared proton bend ($H_5O_2{}^+$)/H_2O libration*
		831 (a''_{15})		6E	*H_3O^+ libration*
717 (a_{16})	708 (a'_{16})	729 (a''_{16})		6Z,6E	*H_2O libration*
469 (a_{17})	469 (a'_{17})	465 (a''_{17})		6Z,6E	*H_2O libration*
373 (a_{18})		358/373 (a''_{18})		6E	*H-bond stretch (AD-$H_2O\cdots H_3O^+$)*
279 (a_{19})	279 (a'_{19})	279 (a''_{19})		6Z,6E	*H-bond stretch/A-H_2O wag*

^{a} Bare $H^+(H_2O)_6$ data from Ref. [84]. ^{b} Ar-predissociation data from Ref. [87]. ^{c} Ne-predissociation data from Ref. [95]. ^{d} A = HB acceptor, D = HB donor, sym = symmetric, antisym = antisymmetric.

Eigen-type Isomer. At least eight characteristic bands are observed in the IR^2MS^2 spectrum associated with structure **6E**$\cdot H_2$ (Figure 4.5, trace D). Only three of these have been reported previously (see Table 4.1) [84]. These are the free (a_3'') and hydrogen-bonded (a_5'') O-H stretching modes of the two AD water molecules (see Figure 4.4) above 3200 cm^{-1}, as well as the highest energy O-H stretching mode of the H_3O^+ core (a_7'') at ~3000 cm^{-1}. The remaining two O-H stretching modes of H_3O^+ are expected to be significantly red-shifted [87] and can therefore be attributed to the two characteristically broad bands observed at 2425 cm^{-1} (a_8'') and 1951 cm^{-1} (a_9''). The anharmonic IR spectrum of **6E**$\cdot H_2$ (Figure 4.5, trace F) qualitatively reproduces nearly all of these features, in particular the varying widths of bands a_2'' - a_8'', confirming the present assignment. The only significant discrepancy between experiment and anharmonic calculations is found for band a_9'', which is predicted ~400 cm^{-1} higher in energy. This assignment is in line with previous results for $H^+(H_2O)_3\cdot Ar$ and $H^+(H_2O)_5\cdot Ar$. Both of these systems exhibit an asymmetrically hydrated H_3O^+ core, which is characterized by an O-H stretching band red-shifted below 2000 cm^{-1} (1880 cm^{-1}) [87],[160]. This region (around 2000 cm^{-1}) is experimentally more difficult to access, because the pulse energies of either laser source used in the present experiments decrease in this spectral region, leading to lower signal-to-noise ratios. The other two bands above 1000 cm^{-1} are attributed to an H_2O bending mode (a_{12}'') and the H_3O^+ umbrella mode (a_{13}'').

HB Stretch and Librational Modes. An expanded view of the IR spectra from Figure 4.5 in the region between 260 and 1000 cm^{-1} is shown in Figure 4.8. The IR^2MS^2 spectrum of **6E**$\cdot H_2$ (trace E) reveals a rather complex absorption pattern with at least five groups of absorption bands (a_{15}''-a_{19}'') of varying width. The IR band intensities are again qualitatively reproduced by the simulated anharmonic spectrum of **6E**$\cdot H_2$ (trace D), but the band positions are systematically predicted too high in energy. At the highest energy a H_3O^+ libration (a_{15}'', 831 cm^{-1}) is observed. This is followed by two groups of AD-H_2O librational bands (a_{16}'' and a_{17}'') in the 775 – 450 cm^{-1} region, of which the absorption at higher (lower) energies corresponds to a frustrated rotation of the AD water molecules parallel (perpendicular) to the plane spanned by the three H atoms of the hydronium ion.

HB stretching modes are observed, for the first time, below 400 cm^{-1}. The sharp doublet at 358/373 cm^{-1} (a_{18}''), predicted at 385/405 cm^{-1}, is assigned to frustrated translations of the hydrated hydronium ion. The

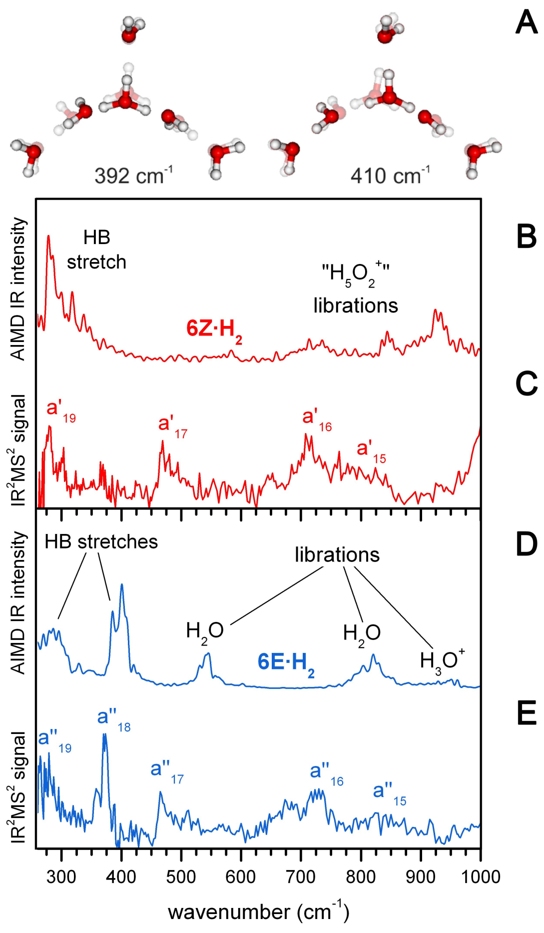

Figure 4.8: Schematic of the two characteristic hydrogen-bond (HB) stretching normal modes and PBE+vdW harmonic frequencies of **6E** assigned to the two components of band a''_{18} (trace A). For clarity, the corresponding motion without H_2 attached is shown. Expanded view of the calculated (AIMD, traces B and D) and experimental (traces C and E) IR spectra from Figure 4.5 in the HB stretching and librational region.

corresponding IR-active harmonic normal modes are schematically shown in part A of Figure 4.8. These "translational" bands correspond to the symmetric and antisymmetric combination of the two HB stretches involving H_3O^+ and the two AD water molecules. The third HB stretch involving H_3O^+ and the terminal water molecule is predicted below 300 cm^{-1}. Indeed, evidence is found for an intense band centered at 279 cm^{-1} (a''_{19}), which is assigned to this HB stretching mode, but it may also contain contributions from terminal water wagging modes, which are expected in the same spectral range, but with lower IR intensity. The observation of isomer-specific bands as low as 358 cm^{-1} is important, as it demonstrates that the IR^{2}MS^2 technique remains isomer-selective down to a photon energy that is comparable to the dissociation limit of the complex. For **6Z**·H_2 the agreement between the experimental and the anharmonic spectra below 1000 cm^{-1} is less satisfactory. While band a'_{19} is reproduced and attributed, similar to a''_{19} of **6E**·H_2, to HB-stretch and terminal water-wagging modes, the intensities of bands a'_{15} to a'_{17} are underestimated. Bands a'_{16} and a'_{17} are similar in shape and position to bands a''_{16} and a''_{17} (Figure 4.8, trace E). Therefore, a tentative assignment of these bands to H_2O librations involving the H_2O moieties of $H_5O_2{}^+$ is reasonable.

Comparison to Liquid Phase Spectra. Finally, the comparison of the IR fingerprints of the Zundel-type and Eigen-type isomers of the protonated water hexamer in the gas phase (Figure 4.5, traces C and D) to the IR spectrum of $H^+(aq)$ in solution allows gaining a more detailed understanding of the condensed phase spectrum. To this end the IR spectrum from Ref. [154], obtained by a subtraction procedure from the IR spectrum of an aqueous solution of 0.75 M HNO_3, is also shown in Figure 4.5 (trace A). It reveals four broad bands at 3146 (b_1), 1747 (b_3), 1198 (b_4), and 672 cm^{-1} (b_5), as well as a shoulder at 2855 cm^{-1} (b_2). These five characteristic features are attributed to the peripheral O-H stretching modes (b_1), the O-H stretching (b_2), bending (b_3) and torsional (b_5) modes of the H_2O moieties in $H_5O_2{}^+$, as well as the antisymmetric stretching mode involving the shared proton (b_4) of a Zundel-type isomer with exceptionally long O$\cdots$O separation [154]. Taking into consideration that the free O-H stretches (bands a_2 and a_4 in Figure 4.5) are absent in the solution phase data and that bands may be significantly thermally broadened at room temperature compared to the bands observed in the spectra of the clusters at cryogenic temperatures, trace A agrees surprisingly well with trace B, and in particular with trace C, confirming (i) the applicability of these protonated water clusters as model systems for testing computational models that ultimately try to describe $H^+(aq)$ in solution, and (ii) the notion of a meta-stable hydrated Zundel ion in solution. However, the question remains, whether spectrum A excludes contributions from Eigen-type isomers? Trace A in Figure 4.5 shows, that Eigen-type isomers may still be present. Moreover, the most intense signature bands of **6E** (a_5'', a_7'' and a_9'') can account for the extended flanks of band b_1, including shoulder b_2, as well as the high energy shoulder of b_3. This finding is thus consistent with the original picture of interconverting limiting structures in solution, where slight changes in the hydration network lead to shuttling of the proton between Eigen- and Zundel-type configurations, rather than the dominance of a single, stable absorbing species.

Conclusions: $\mathbf{H^+(H_2O)_6}$. The present experimental approach combined with AIMD simulations allows to spectroscopically isolate and assign the IR fingerprints of the Zundel and Eigen isomers of the protonated water hexamer down into the terahertz region of the electromagnetic spectrum. Experimental information, in particular, on the "translation" bands involving HB stretching motion, represents a first critical step towards understanding the proton transfer mechanism in this prototypical system, in particular, the vehicular component related to the translational diffusion of the hydrated proton solvation structure [80]. The present results are also important for planning experiments that eventually will yield information on the barrier heights involved in this process [178]. Anharmonicities of the potential energy surface play a significant role, even at low temperatures, for these protonated water clusters and are the cause of the different widths of the observed IRPD bands. For a superior agreement between experiment and simulation inclusion of nuclear quantum effects in the theoretical evaluation of IR spectra is proposed, which should also help to recover the experimental broadening at lower temperatures, *i.e.*, closer to the experimental temperature.

4.3.3 Disentangling Contributions of Multiple Isomers for $H^+(H_2O)_{5,7-10}$

This section presents isomer-selective spectra of n = 5,7-10, measured in the O-H stretching region (2880 – 3850 cm^{-1}). Here, the spectral signatures are assigned to individual isomers by comparison to previous experimental and theoretical data.

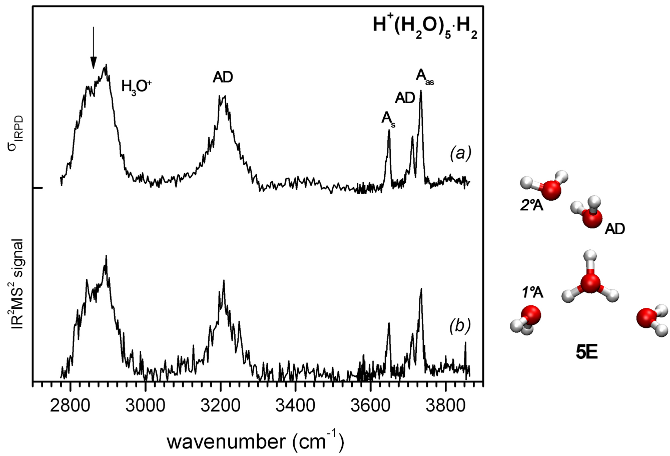

Figure 4.9: IRPD (a) and IR^{2}MS^2 spectra (b) of $H^+(H_2O)_5{\cdot}H_2$, measured from 2774 to 3860 cm^{-1}. The IR^{2}MS^2 spectrum is obtained by probing at 2886 cm^{-1}, indicated by the vertical arrow in trace (a). The structure of the assigned isomer **5E** is plotted on the right side.

$H^+(H_2O)_5{\cdot}H_2$

Figure 4.9 shows the (a) IRPD and (b) IR^{2}MS^2 spectra, probed at 2886 cm^{-1}, of the H_2-tagged protonated water pentamer. Both spectra are identical within the experimental uncertainty, indicating the presence of a single Eigen-type isomer. The spectra show five distinct absorption features. The HB region is characterized by the broad symmetric and anti-symmetric O-H stretches of the H_3O^+-core at ~2900 cm^{-1} and the O-H stretch of AD-H_2O at ~3200 cm^{-1} [84, 95]. The three sharp bands above 3600 cm^{-1} are attributed to the coupled (A_s and A_{as} of 1° and 2° A-H_2O) and uncoupled (AD-H_2O) free O-H stretching modes. In agreement with the majority of previous experimental and computational studies, this spectrum can be assigned to the single Eigen-type structure displayed in Figure 4.9 [84, 86, 87, 95].

In contrast to these findings, recent AIMD simulations by Kulig *et al.*, find a better agreement for a mixture of an Eigen-type ring isomer and an Eigen/Zundel-type hybrid isomer. In these simulations, both of the isomers are predicted to contribute at high frequencies, but only the hybrid isomer accounts for all prominent low-frequency bands [92]. In order to get a more conclusive picture of possible coexisting isomers in this cluster, further isomer-selective studies down to the fingerprint region of the IR spectral range are required.

$H^+(H_2O)_7{\cdot}H_2$

Figure 4.10 compares the single-color IRPD spectrum (a) to two-color IR^2MS^2 spectra (b-e) of $H^+(H_2O)_7{\cdot}H_2$. The IR^2MS^2 spectra are measured at probe energies of (b) 3542 cm^{-1}, (c) 3351 cm^{-1}, (d) 3676 cm^{-1}, and (e) 3492 cm^{-1}, indicated by vertical arrows. The experimental band positions and their assignments are compared to values from previous experimental work in Table 4.2.

First, trace (b) in Figure 4.10, measured at a probe energy of 3542 cm^{-1} is considered. This probe energy is characteristic for the only Zundel-type isomer present. In more detail, it probes the HBed O-H stretch of the 1°AD-H_2O of the global minimum structure **7Z** (see Figure 4.10) [84, 95]. The IR^2MS^2 spectrum shows two characteristic features, a very broad absorption at 3171 cm^{-1}, attributed to the HBed O-H stretches of the $H_5O_2^+$ core [87], and a somewhat narrower, intense band at 3545 cm^{-1}, close to the probe energy. This particular feature is associated with a Zundel-type "Ring" isomer [84, 95] and corresponds to the symmetric and antisymmetric combinations of the HBed O-H stretches of the two AD water molecules in the first solvation shell (see Figure 4.10). In addition, two features, which are observed in the single-color spectrum (a) at 3495 and 3676 cm^{-1}, and which are characteristic for Eigen-type structures, are missing from this two-color spectrum, confirming the assignment to a Zundel-type structure. Finally, the weak absorption band at 3619 cm^{-1} (AA in Figure 4.10) can be assigned to the symmetric O-H stretch of the AA water molecule, characteristic for ring formation, and exclusively present in **7Z** [84, 95].

Next, the characteristic HBed O-H stretch of 1°AD-H_2O of **7E1** at

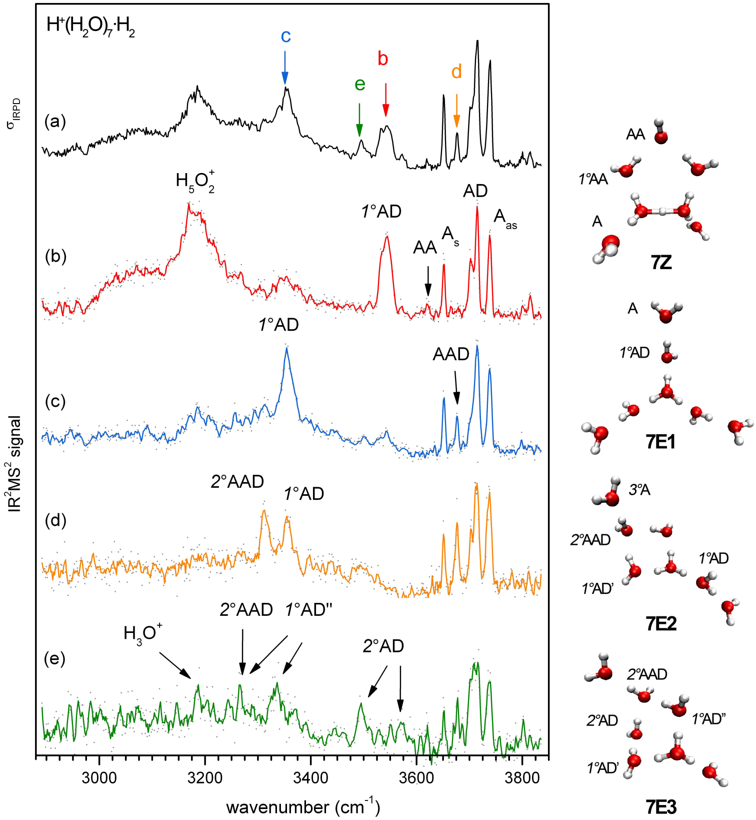

Figure 4.10: IRPD (a) and IR^{2}MS^2 spectra (b)-(e) of $H^+(H_2O)_7{\cdot}H_2$. Isomer-selective spectra are obtained by probing the energies: (b) 3542 cm^{-1}, (c) 3351 cm^{-1}, (d) 3676 cm^{-1}, (e) 3492 cm^{-1}, from 2880 to 3850 cm^{-1}. Probe energies are indicated by vertical arrows in trace (a). Data points are shown as dots and a weighted three-point-running average (solid black line) is added to guide the eye. A = Hydrogen-bond acceptor, D = Hydrogen-bond donor, s = symmetric, as = antisymmetric, 1° = 1st hydration shell, 2° = 2nd hydration shell. Minimum energy structures of the assigned isomers are plotted on the right side.

3351 cm^{-1} is probed (Figure 4.10, trace (c) [28, 84, 95]. **7E1** is a chain structure with an Eigen ion core, similar to the Eigen structure in the protonated water hexamer, but with three instead of two second hydration shell water molecules. The IR^2MS^2 spectrum (c) looks distinctly different from (b): the most intense absorption is found at 3351 cm^{-1}, *i.e.* close to the probe energy (1°AD-H_2O of **7E1**), and an absorption peak is observed at 3676 cm^{-1}, the region of the free O-H stretches of AAD water molecules, which are also characteristic for ring formation. While the features of **7Z** are not completely absent from spectrum (c), they are greatly reduced in intensity. A complete discrimination against other isomers is difficult in the present case, due to the width of the absorption bands, which leads to the overlapping of bands from different isomers. Spectrum (c) is in reasonable agreement with the previously simulated spectrum of **7E1** [84] and with the experimental spectrum of bare $H^+(H_2O)_7$, which is mainly attributed to the same species [95]. However, in the free O-H stretching region only three absorption features are predicted by theory, but the experimental spectrum shows four sharp bands instead. Hence, the band attributed to an AAD-H_2O, at 3676 cm^{-1}, indicative of ring formation, must be due to the contribution from a cyclic Eigen-type isomer, which also absorbs substantially at the probe energy of 3351 cm^{-1} (see below). Note, the **7Z** isomer also contributes to this IR^2MS^2 spectrum, as it absorbs weakly at 3354 cm^{-1} (see trace b). The isomers **7Z** and **7E1** account for most of the intenser spectral features in the single-color spectrum (a) and thus are the most abundant isomers of $H^+(H_2O)_7{\cdot}H_2$ under the present experimental conditions. Therefore it is also likely that their contributions are picked up in the remaining two IR^2MS^2 spectra (d) and (e).

The bottom two IR^2MS^2 spectra were probed at energies corresponding to the remaining two bands. Figure 4.10, trace (d) displays the IR^2MS^2 spectrum measured at 3676 cm^{-1}. Spectrum (d) is characteristically different from spectra (b) and (c). It reveals a relative enhancement of the probed band together with a new band at 3312 cm^{-1} and significant absorption in the 3380 – 3575 cm^{-1} range. The first two features are characteristic for a triply-coordinated AAD-H_2O, where the first band corresponds to the free and the second to the HBed O-H stretching mode. For $n = 7$ this motif appears exclusively for Eigen-type ring isomers [84, 95]. Moreover, spectrum (d) is in reasonable agreement with the simulated spectrum of structure **7E2** (Figure 4.10) and Ref. [84]). This isomer consists of a four-membered ring involving an H_3O^+ ion and singly-coordinated H_2O molecule starting a second and third solvation shell.

However, the contribution of other cyclic Eigen-isomers cannot be excluded, for example **7E3**, which contains an AAD-H_2O as part of a 5-membered ring and also has a predicted absorption band close to the probed frequency [84].

The final IR^2MS^2 spectrum is therefore measured at 3492 cm^{-1} (Figure 4.10, trace e) and indeed suggests the presence of a fourth isomer, as again a characteristically different IR^2MS^2 spectrum is obtained. Even though the signal/noise ratio of this spectrum is worse compared to the other spectra, it is sufficient to suggest the occurrence of a third ring isomer. The most characteristic feature is the increased relative intensity of the band at 3493 cm^{-1}. In addition, this spectrum exhibits a substantial broad absorption in the HB O-H stretching region between 2880 and 3170 cm^{-1}, as well as three bands at 3339, 3264 and 3189 cm^{-1}. Here, the best candidate is the 5-membered ring Eigen-isomer **7E3**, whose simulated spectrum [84] satisfactorily reproduces the above mentioned bands and assigns them to HBed O-H stretches of 2°AD-H_2O (3493 cm^{-1}), 1°AD-H_2O + 2°AAD-H_2O (3339 and 3264 cm^{-1}) and H_3O^+ (3189 cm^{-1}).

$H^+(H_2O)_8{\cdot}H_2$

After observing two isomers for the protonated water hexamer, and at least four isomers for the protonated water heptamer, one would intuitively expect even more isomers for $n = 8$ and larger water clusters. However, the IRPD studies of Jiang *et al.* [84] and Mizuse *et al.* [95] already suggest that a single isomer, a Zundel-type isomer derived from the **7Z** structure with the additional water binding to the H_2O (AA) site (Figure 4.11), can account satisfactorily for the observed experimental peaks in the O-H stretching region.

The IR^2MS^2 spectra of $n = 8$ confirm this assumption. Figure 4.11 shows four IR^2MS^2 spectra, measured at probe energies of 3713, 3679, 3489 and 3204 cm^{-1}, respectively. The experimental spectrum of $H^+(H_2O)_8{\cdot}H_2$ is characterized by four distinct absorption bands in the free O-H stretching region, attributed to the free O-H stretches of A_s, A_{as}, AD and AAD-H_2O molecules. The HB region exhibits several features on top of a broad background that originate from AD and AAD-H_2O molecules [175]. The broad absorption band below 3500 cm^{-1} is assigned to the $H_5O_2^+$-moiety. All isomer-selective spectra (traces b-e) are identical within the experimental uncertainty and show satisfactory agreement with the simulated linear absorption spectrum of the global minimum energy structure **8Z** in Refs.

Table 4.2: Position (in cm^{-1}) and assignment of the vibrational bands observed in the IRPD spectra of bare and messenger-tagged $H^+(H_2O)_7$.

H_2-prediss.	**IR^2MS^2 (7E2)**	**IR^2MS^2 (7Z)**	**IR^2MS^2 (7E3)**	**IR^2MS^2 (7E1)**	**Previous Exp.**	**Isomer**	**Assignment[c]**
3815		3815				7Z	*combination band*
3800		3800	3802	3799	3791[a]	7Z, 7E1, 7E3	*combination band*
3739	3737	3739	3735	3737	3742[a],3741[b]	7Z, 7E1, 7E2, 7E3	*free O-H stretch (as, A-H_2O)*
3716	3716	3714	3717	3713	3717[a],3716[b]	7Z, 7E1, 7E3, 7E2	*free O-H stretch (2° AD-H_2O)*
3701	3703	3701	3702		3710[a]	7Z, 7E1, 7E3	*free O-H stretch (1° AD-H_2O)*
3676	3676		3679	3676	3679[a],3679[b]	7E1, 7E3	*free O-H stretch (2° AAD-H_2O)*
3651	3651	3651	3651	3651	3652[a],3654[b]	7Z, 7E1, 7E2, 7E3	*free O-H stretch (s, A-H_2O)*
3619		3619	3619			7Z	*free O-H stretch (s, AA-H_2O)*
3573			3573		3581[a]	7E3	*bonded O-H stretch (2° AD-H_2O)*
3544		3545	3542		3555[a], 3555[b]	7Z	*bonded O-H stretch (as,1° AD-H_2O)*
3532		3532			3544[a]	7Z	*bonded O-H stretch (s,1° AD-H_2O)*
3495			3486	3493	3500 3502[a]	7E3	*bonded O-H stretch (s,2° AD-H_2O)*
3352	3352	3354	3352		3360[a],3351/3570[b]	7E1	*bonded O-H stretch (1° AD-H_2O) or $H_5O_2^+$*
3341			3339			7E3	*antisym. bonded O-H stretch (1° AD″-H_2O) + bonded O-H stretch (2° AAD-H_2O)*
3310	3312				3310/3325[b]	7E2	*bonded O-H stretch (2° AAD-H_2O)*
		3268	3264			7E3	*sym. bonded O-H stretch (1° AD″-H_2O) + bonded O-H stretch (2° AAD-H_2O)*
3185		3171	3189	3185	3198[a],3194[b]	7Z, 7E3	*bonded O-H stretch (1° AD′-H_2O) or H_3O^+ or $H_5O_2^+$*
∼3070		3073				7Z	
2957			∼2960			7E3	*sym. bonded O-H stretch (H_3O^+)*

[a] Bare $H^+(H_2O)_7$ data from Ref. [84].
[b] Ne-predissociation data from Ref. [95].
[c] A = HB acceptor, D = HB donor, s = symmetric, as = antisymmetric.

[84, 95, 175]. Even though some of the probed features are not well resolved, one would at least expect a change in intensity upon the presence of another isomer, as it is observed in the case of **7Z** or **7E1**. But even trace (d), probed at 3679 cm^{-1}, an energy where solely the global minimum isomer is predicted to absorb, does not exhibit any change in intensity or band shape.

$H^+(H_2O)_9{\cdot}H_2$ and $H^+(H_2O)_{10}{\cdot}D_2$

Figure 4.12 shows IRPD spectra (a) and IR^2MS^2 spectra (b)-(e) of A) $H^+(H_2O)_9{\cdot}H_2$ and B) $H^+(H_2O)_{10}{\cdot}D_2$. For both isomers Karthikeyan *et al.* predicted a strong thermodynamical dependence of the global minimum structure. They find that a netlike structure is preferred above 200 K, while at 150 K a 3D structure with a dangling H_2O molecule is more likely. Below 150 K the global minimum of both clusters are expected to exhibit a closed 3D structure [173, 174].

The IRPD spectrum of $n = 9$ shows a similar absorption pattern as the spectrum of $n = 8$, with additional structure in the HB O-H stretching regime. Four discrete bands are observed in the free O-H stretching region and several broader features with significant background absorption are found in the HB O-H stretching region. The IR^2MS^2 spectra of the protonated water nonamer (Figure 4.12A, traces b-e), probed at 3546, 3199, 3355 and 3449 cm^{-1}, are all very similar within the experimental uncertainty, indicating the presence of only one isomer. On the other hand the study of Karthikeyan *et al.* anticipates at least eight isomers lying within 8 kJ/mol of the global ground state, all exhibiting similar absorption features throughout the entire O-H stretching region [174]. Hence, there are two possibilities: (i) the presence of exclusively a single isomeric species, or (ii) many isomers with very similar IRPD spectra.

The spectrum of $n = 10$ shows a slightly less complicated absorption pattern than $n = 9$, with broad absorption at 3161 cm^{-1}, and four bands on a broad background at 3377, 3463, 3554 and 3621 cm^{-1}. As mentioned earlier, only two bands are present in the free O-H stretching region, attributed to AD and AAD-H_2O molecules. IR^2MS^2 spectra, displayed in Figure 4.12B), are measured at probe energies of 3362, 3160 and 2741 cm^{-1}. The different traces show no significant differences, supporting the assumption that a closed 3D structure is present. A more detailed assignment to a specific isomer is currently not possible. However, the presented results again favor the presence of only a single isomer.

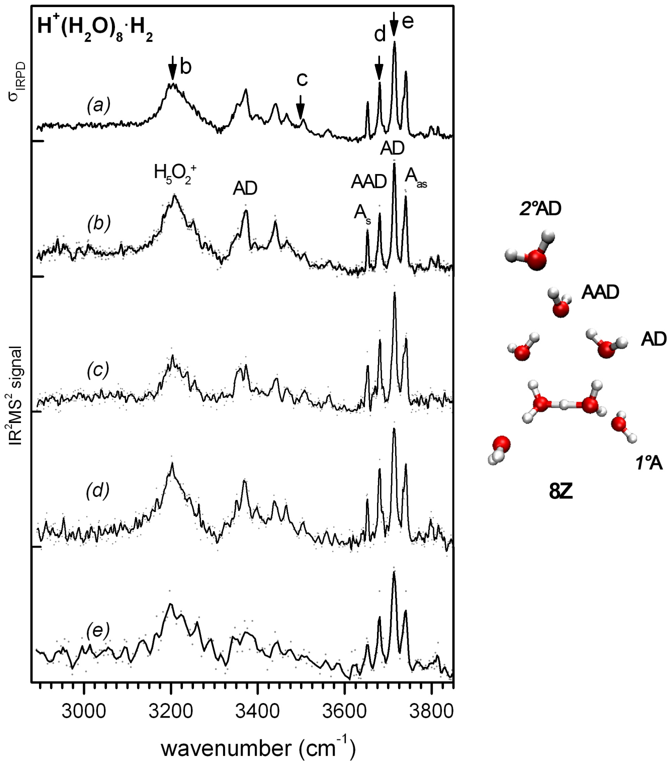

Figure 4.11: IRPD (a) and IR^{2}MS^2 spectra (b)-(e) of $H^+(H_2O)_8{\cdot}H_2$. IR^{2}MS^2 spectra are obtained by probing the energies: (b) 3713 cm^{-1}, (c) 3489 cm^{-1}, (d) 3679 cm^{-1} and (e) 3204 cm^{-1}. Probe energies are indicated by vertical arrows in trace (a). Data points are shown as dots and a weighted three-point-running average (solid black line) is added to guide the eye. Minimum energy structure of the assigned isomer is plotted on the right side.

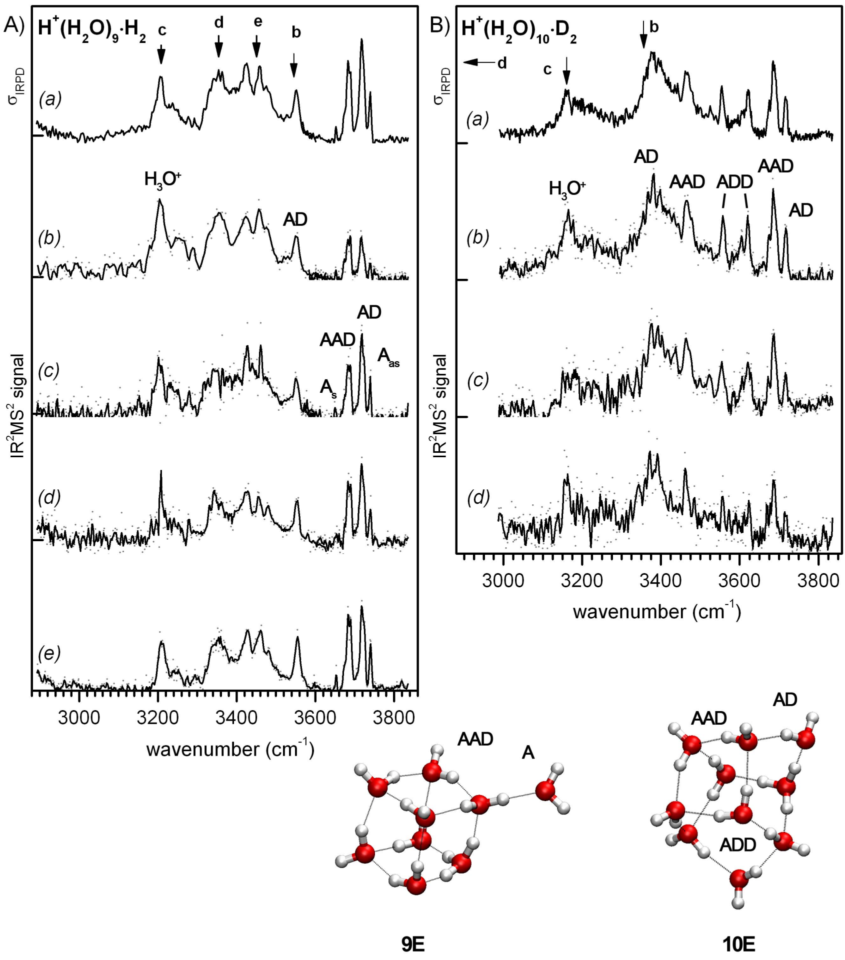

Figure 4.12: IRPD spectra (a) and IR^2MS^2 spectra (b)-(e) of A) $H^+(H_2O)_9{\cdot}H_2$ and B) $H^+(H_2O)_{10}{\cdot}D_2$. IR^2MS^2 spectra for A) are obtained by probing at the following energies: (b) 3546 cm^{-1}, (c) 3199 cm^{-1}, (d) 3355 cm^{-1}, (e) 3449 cm^{-1}, from 2880 to 3850 cm^{-1}. IR^2MS^2 spectra for B) are obtained by probing the energies: (b) 3362 cm^{-1}, (c) 3160 cm^{-1} and (d) 2741 cm^{-1}. Probe energies are indicated by vertical arrows in trace (a). Data points are shown as dots and a weighted three-point-running average (solid black line) is added to guide the eye.

Conclusions: $H^+(H_2O)_{5,7-10}$

This section resolves several matters regarding the structure of small protonated water clusters. 1) The contribution of four isomers to the spectrum of the protonated water heptamer is established. The spectral signatures are assigned to a Zundel-type and three Eigen-type isomers, featuring a chain, as well as 5- and 4-membered-ring structures. 2) A single isomeric species, attributed to an Eigen-type isomer, contributes to the spectrum of the protonated water pentamer. In contrast to predictions from AIMD simulation, a single isomer can account for all spectral features of $n = 5$ above $2800\,cm^{-1}$. Further measurements in the Terahertz region (see Chapter 7) confirm this assignment. 3) The contribution from individual isomers is clearly shown up to $n = 7$. For the larger clusters the experiment suggests the presence of predominantly a single isomer. In these cases extending the spectral range, as shown for $n = 6$, would be helpful to confirm this assignment. 4) The presence of only closed 3D structures in the spectrum of the protonated water decamer is shown. This finding is in contrast to previous experiments on untagged protonated water clusters and suggests a lower vibrational temperature in the present study.

4.4 Advantages and Limits of IR^2MS^2 Spectroscopy

The main advantage of IR^2MS^2 spectroscopy, compared to conventional IR/UV double-resonance spectroscopy, is that this technique does not require the presence of an UV-VIS chromophore and hence extends the applicability of ion dip spectroscopy significantly. In addition, the knowledge of the position of electronically excited states of the UV-VIS chromophore and their relaxation dynamics is not necessary. Instead, it is now possible to probe every messenger-tagged complex and possibly also clusters with binding energies that allow probing in a single-photon dissociation process.

The main requirement for the applicability of IR^2MS^2 spectroscopy is that each isomer must exhibit one characteristic IR band, which is at least partially separated from IR active bands of other isomers. When this requirement is fulfilled, isomer-specific IR^2MS^2 spectra of messenger-tagged ions can be measured down to the terahertz region, close to and even below the binding energy of the complex. Hence, the method is mainly limited by the availability of the appropriate laser sources.

In HBed complexes the existence of several isomers with similar absorption patterns is very likely. It is demonstrated in Section 4.3.3 that IR^2MS^2

spectroscopy can also be successfully applied in the case of more than two isomers contributing to the spectrum. A separation of the spectral signatures is achievable, even with overlapping characteristic absorption bands.

However, the same section also reveals the limits of IR^2MS^2 spectroscopy. In the case of the protonated water nonamer the existence of several isomers is feasible, but no evidence can be found in the IR^2MS^2 spectra. Comparison to theoretical work shows the existence of a large number of energetically low-lying isomers with many overlapping absorption bands that can probably not be separated due to a strong coupling and/or overlapping of these bands. Also the interconversion of different isomers already at low temperatures is a conceivable explanation, which may lead to indistinguishable spectra.

Another remaining restriction is associated with the efficiency and time scale of the photodissociation process itself. Each photoabsorption event necessarily needs to lead to dissociation with near unit efficiency on a faster time scale than the ion flight time within the extraction/acceleration region of the time-of-flight mass spectrometer; otherwise either internally hot, undissociated parent ions will be probed or the population can be pumped into one single isomeric species.

The IR^2MS^2 technique also requires a higher experimental effort, since the pump and probe steps both lead to the formation of isomers with the same mass-to-charge (m/z) ratio. In order to pump and probe previously mass-selected ions, two additional mass-selection stages are therefore required. Consequently, the time of data acquisition increases due to a higher averaging rate. This rate must naturally increase owing to signal loss in the process of triple mass selection, and the fluctuation of two laser pulses contributing to signal fluctuations.

Despite the extra experimental efforts, IR^2MS^2 spectroscopy has proven to be a versatile and powerful tool to disentangle spectral signatures of multiple isomeric species in the infrared spectral range.

Chapter 5

Microsolvation of Nitrate-Nitric Acid Clusters

This chapter describes the solvent-mediated structural evolution with size of $NO_3^-(HNO_3)_m(H_2O)_n$-clusters with $m = 1$-3 and up to $n = 8$. The cluster structure is studied with IRMPD and IRVPD spectroscopy in the fingerprint region ($550 - 1880\,cm^{-1}$). Here, NO-stretching modes, as well as bending and other lower frequency modes can be directly probed, and assigned by comparison to electronic structure calculations.

The IRMPD spectrum of the $m = 1$, $n = 0$ cluster is distinctly different from the spectra of the larger clusters. This is the result of strong hydrogen bonding, which effectively leads to an equally shared proton in-between two nitrate moieties ($O_2NO^- \cdots H^+ \cdots {}^-ONO_2$). The spectrum exhibits a strong absorption at $877\,cm^{-1}$ (shared proton stretch) and lacks the NO_2-antisymmetric stretch/NOH-bending mode absorption close to $1650\,cm^{-1}$, that is characteristic for an intact HNO_3 unit in the cluster. Addition of at least one more nitric acid molecule or two more water molecules weakens the hydrogen bond network and breaks the symmetry of this arrangement. Consequently, the proton is localized near one of the nitrate cores, effectively forming HNO_3 hydrogen-bonded to NO_3^-.

The comparison to quantum chemical calculations shows that not all IR active modes are observed in the IRMPD spectra of the bare nitrate-nitric acid clusters. Addition of a water or a hydrogen molecule lowers the dissociation threshold of the complexes and relaxes (H_2O) or lifts (H_2) this IRMPD transparency.

Chapter based on:
Infrared Photodissociation Spectroscopy of Microhydrated Nitrate-Nitric Acid Clusters $NO_3^-(HNO_3)_m(H_2O)_n$
N. Heine, T. Y. Yacovitch, F. Schubert, C. Brieger, D. M. Neumark, and K. R. Asmis, *J. Phys. Chem. A* **2014**, 118, 7613 – 7622.
DOI: 10.1021/jp412222q

5.1 Introduction

Nitrate-containing ions play an important role in chemical and physical processes in the atmosphere, such as electrical conductivity and the formation of new particles through ion nucleation [36, 38]. Nitrate (NO_3^-) and nitrate clusters with nitric acid (HNO_3) and water are among the most abundant anions in the atmosphere. They were first measured in the stratosphere in 1978 [47] and, five years later, in the troposphere by Arnold with a balloon-borne mass spectrometer [179]. While $NO_3^-(HNO_3)_2$ accounts for over 90% of all negative ions at heights around 27-30 km [48], $NO_3^-(HNO_3)(H_2O)$ dominates in tropospheric regions (<15 km), due to the high abundance of water vapor [180]. A major source of these clusters is oxidation of NO_x to HNO_3 and subsequent deprotonation via galactic cosmic rays, radioactivity and electrical discharges [38]. The resulting NO_3^- reacts promptly with trace gases via ion-molecule reactions forming $NO_3^-(HNO_3)_m(H_2O)_n$ clusters. Understanding the structure, stability, reactivity, and growth rates of nitrate-containing clusters is crucial for improving atmospheric ion chemistry models [181].

Here, vibrational spectroscopy of gas phase cluster anions is used in combination with electronic structure calculations to investigate the geometric structure and stability of $NO_3^-(HNO_3)_m(H_2O)_n$ clusters with m = 1-3 and up to n = 8, in order to complement mass spectrometric as well as kinetics experiments and to test structural predictions from earlier computational studies [182, 183]. Previous experimental [184–187] and theoretical [188, 189] studies have mainly focused on the $m = 1$, $n = 0$ cluster, also referred to as hydrogen dinitrate ($O_2NO^- \cdots H^+ \cdots {}^-ONO_2$), due to the presence of an equally shared proton as a consequence of strong hydrogen bonding [190]. A variety of salts has been investigated with X-ray and neutron diffraction [191, 192], as well as infrared (IR) [193] and resonance Raman spectroscopy [194], showing that the nominally planar and centrosymmetric D_{2h} structure can be distorted depending on the counterions. Rate constants, reaction enthalpies and bond energies have been determined experimentally for $NO_3^-(HNO_3)_m(H_2O)_n$ using mass spectrometry, in order to investigate the process of dissociation/formation [195–198]. These experiments show similar clustering behavior as was recently reported for sulfate/sulfuric acid/water clusters [63]: the formation of $A^-(HA)_{1-3}$ with A = HSO_4^- or NO_3^-, is preferred over $A^-(H_2O)$ because the acid molecule binds more strongly to the conjugate base anion than the water molecule. For example, in the reaction $NO_3^- \cdot H_2O$

+ $HNO_3 \rightarrow NO_3^- \cdot HNO_3 + H_2O$ ($k = 5.5 \cdot 10^{-10}\,cm^3/s$), water is rapidly replaced by nitric acid [195]. The experimentally determined sequential enthalpies of complexation for 1-3 molecules of HNO_3 to NO_3^- are -113, -67 and -54 kJ/mol, respectively; these relatively high values indicate strong association complexes of nitric acid with nitrate [199, 200]. The most extensive *ab initio* calculations on $NO_3^-(HNO_3)_m$ with m = 1-3 have been performed by Galvez *et al.* [183] They found planar global minimum-energy structures for all three clusters and non-planar relative minima only slightly higher in energy. For $m > 1$, they predict a distortion of the symmetric $O_2NO^- \cdots H^+ \cdots {}^-ONO_2$ arrangement, leading to asymmetric $O_2NO^- \cdots$·H-$ONO_2(HNO_3)_{m-1}$ structures, as the hydrogen bond network grows in the cluster.

In a previous IRMPD study on microhydrated $NO_3^-(H_2O)_{1-6}$ clusters [57], our group demonstrated that (a) the degeneracy of the antisymmetric NO_3^- stretching vibration ν_3 can be exploited as a sensitive indicator for the symmetry of the microhydration shell/hydrogen bond (HB) network and (b) that NO_3^- favors surface hydration in contrast to the internal solvation of the sulfate dianions [201, 202]. Recent studies on mixed bisulfate/nitrate/neutral acid clusters explored the influence of acid solvation on the conjugated base anion and showed not only that the charge localization can vary unexpectedly upon cluster composition, but also revealed the sensitivity of the NO_2-antisymmetric stretch/NOH-bending mode to the presence of an intact HNO_3 molecule [61]. Studies on bisulfate/sulfuric acid clusters demonstrated that certain normal modes, mainly those that are localized on the HB network, show a large degree of IRMPD transparency [63]. Upon messenger-tagging with H_2, the linear IR intensity of these modes can be recovered, since photodissociation can then occur already upon the absorption of a single photon (see Section 2.2 for details).

The present investigation of the structure and energetics of nitrate/nitric acid/water clusters is aimed at ultimately shedding new light on the early steps in the formation of nitric acid aerosols. In this chapter IRMPD spectra of mass-selected clusters are presented from 550 to 1880 cm^{-1}, the spectral region covering the vibrational modes of the nitrate ion and characteristic modes of the solvent molecules. When possible, messenger-tagging with H_2 is employed to probe the linear absorption spectra. The vibrational spectra are assigned to a particular structure or family of structures based on a comparison to simulated IR spectra from electronic structure calculations. The analysis shows that the first water molecule does not disturb the shared proton motif of the $m = 1$ cluster, but that additional solvent molecules disrupt the symmetric arrangement.

5.2 Experimental and Theoretical Methods

The IRMPD experiments are carried out using the ion-trap tandem-mass-spectrometer, described in Section 3.8. Microsolvated nitrate/nitric acid clusters, $NO_3^-(HNO_3)_m(H_2O)_n$, are produced by electrospray in a modified commercial Z-spray source from a 10 mM solution of HNO_3 in a 1:1 water/acetonitrile solvent mixture. The beam of ions is skimmed and collimated in a decapole ion guide, and subsequently mass-selected in a commercial quadrupole mass filter. After mass selection, the cluster anions are deflected by 90° using an electrostatic quadrupole deflector and focused into a cryogenically-cooled ion trap, held at 10 K. Here, the anions are collected for 99 ms and thermalized through collisions with a buffer gas (He/H_2). In a 5 or 10 Hz cycle, ions are extracted and focused into the center of the extraction region of a time-of-flight mass spectrometer, where they interact with a single FELIX macropulse. If the wavelength of the IR radiation is in resonance with a vibrational transition, fragmentation of the (parent) cluster anions occurs. All anions are extracted by a set of high voltage pulses and are detected as a function of their flight-time using an MCP detector. Photodissociation spectra in the linear absorption regime are obtained by condensing molecular hydrogen onto the observed cluster in the ion trap. The photodissociation cross section σ_{IRMPD} is determined from the relative abundances of the parent and photofragment ions, $I_P(\nu)$ and $I_F(\nu)$, and the frequency dependent energy fluence (assuming a constant interaction area throughout the range of scanned wavelengths) $P(\nu)$ using Equation 3.21. Regarding the tagged species, a single-photon process is assumed. Intensities are therefore normalized to the photon fluence [104], as described in Section 3.5.

In order to support the analysis of the experimental spectra DFT calculations were performed* using the TURBOMOLE program package [203–205]. The B3LYP hybrid functional [206–208] (gridsize m5) was employed in combination with Dunning aug-cc-pVTZ basis sets [209]. Structure optimizations used tight convergence criteria, Cartesian gradients smaller than $1 \cdot 10^{-4}$ Hartree/Bohr, and energy changes smaller than $1 \cdot 10^{-6}$ Hartree (see Appendix B for total energies). The SCF convergence criterion was

*Calculations have been performed by K.R. Asmis.

$1{\cdot}10^{-7}$ Hartree for the energy and $1{\cdot}10^{-7}$ a.u. for the root mean square of the density. Harmonic vibrational frequencies were obtained from second analytic derivatives [210]. It is known that B3LYP vibrational frequencies are systematically too large (see, e.g., Ref. [211, 212]). Agreement with observed frequencies can be improved by scaling, which accounts for neglected anharmonicities as well as systematic errors of the calculated harmonic force constants. A scaling parameter of 0.968 was used, which falls into the known ranges for the B3LYP functional [211, 212].

5.3 Results

5.3.1 Trends in the experimental IRMPD spectra

Overviews of the IRMPD spectra of $NO_3^-(HNO_3)_m(H_2O)_n(H_2)_z$ clusters in the fingerprint region (530 – 1880 cm^{-1}) are shown in Figures 5.1 and 5.2. The stoichiometry of the clusters is abbreviated by (m,n,z). The spectra of the m = 1-3 clusters without water (n = 0) are compared to the thin film IR-spectrum of pure HNO_3 [213], measured at 45 K, in Figure 5.1. Figure 5.2 compares the spectra of the m = 1 and m = 2 clusters with up to eight water molecules to a thin film IR spectrum of a diluted HNO_3:H_2O binary amorphous mixture [213], measured at 45 K. The spectra are arranged from top to bottom according to increasing number of neutral acid and/or water molecules. The hydrogen-tagged equivalents, when available, are shown above the IRMPD spectrum of the corresponding bare cluster anion. Spectral features are labeled with **A**, **B** and **P** according to their assignment to modes of nitric acid molecules (**A**), those of the conjugate base nitrate anion (**B**) and to shared proton (**P**) modes. The detailed assignments, described in the analysis section, together with experimental and calculated band positions, are listed in Table 5.1. The band assignments are derived from the local modes (see Table 5.2) of the bare nitrate (${}^B\nu_1$ - ${}^B\nu_4$), nitric acid (${}^A\nu_1$ - ${}^A\nu_9$) and of the shared proton (${}^P\nu_{x,y,z}$).

The following description of the experimental IRMPD spectra first focuses on identifying general trends. The spectral features are tentatively assigned based on a comparison to previous IRMPD results on related systems [63] as well as IR and Raman measurements of solid complexes [185], matrix-isolated species [218], condensed phase samples [213, 216] and nitric acid vapor [214]. This preliminary assignment is then evaluated in more detail in Section 5.3.2, where the experimental data is compared to simulated IR

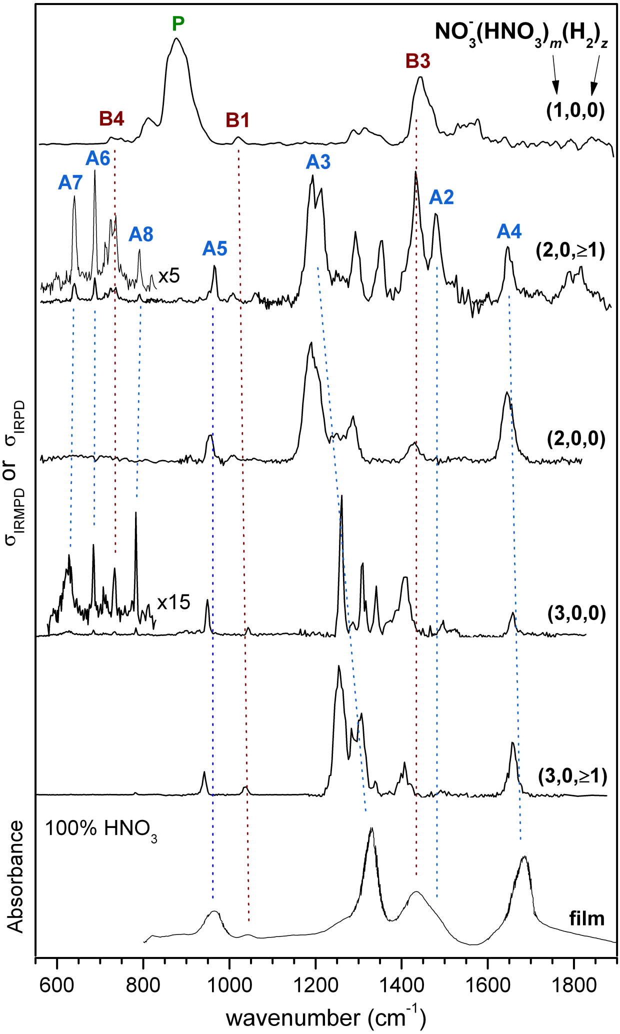

Figure 5.1: Experimental IRMPD spectra of $NO_3^-(HNO_3)_m(H_2O)_n(H_2)_z$ clusters with m = 1-3 and n = 0 abbreviated as (m,n,z). Peaks are labeled according to their assignment to modes of the neutral acid molecule (**A**), of the conjugate base anion (**B**) or to shared proton stretching mode (**P**). See also Table 5.1 for peak positions and assignments.

Table 5.1: Experimental and calculated IR band positions (in cm^{-1}) of $NO_3^-(HNO_3)_m$ clusters with m = 1-3. The experimental band positions are determined from the IRMPD spectra shown Figure 5.1. The calculated positions are determined from the simulated B3LYP/aug-cc-pVTZ IR-spectra of the lowest energy isomers shown in Figures 5.3 - 5.7. Vibrational modes (ν) are numbered and labeled with **A**, **B** and **P** according to their assignment to the normal modes of the nitric acid molecule (**A**), of the conjugate base nitrate anion (**B**) or of the shared proton (**P**) (see Table 5.2).

Band	$m = 1$			$m = 2$		$m = 3$	
	Exp.	1w0a[a]	1w0b[a]	Exp.	2w0a[a]	Exp.	3w0a[a]
A4				1647	1629 ${}^A\nu_4$,${}^A\nu_2$	1658	1635 ${}^A\nu_4$, ${}^A\nu_2$
A2				1478	1439 ${}^A\nu_4$, ${}^A\nu_2$	1409	1397 ${}^A\nu_2$, ${}^A\nu_4$
B3"	1554		1490 ${}^B\nu_3$, ${}^P\nu_x$				
B3	1437	1422 ${}^B\nu_3$, ${}^P\nu_y$	1401 ${}^B\nu_3$, ${}^P\nu_y$	1432	1393 ${}^B\nu_3$	1341	1359 ${}^B\nu_3$
B3'	1330		1319 ${}^B\nu_3$, ${}^P\nu_z$	1355	1322 ${}^A\nu_3$, ${}^B\nu_3$	1310	1347 ${}^B\nu_3$
A3'				1292	1288 ${}^A\nu_3$		
A3				1193	1224 ${}^A\nu_3$, ${}^B\nu_3$	1261	1269 ${}^A\nu_3$
A9'	~1162	1186 ${}^P\nu_z$		1059			
A9				1008	1025 ${}^A\nu_9$		
B1	1015	1053 ${}^B\nu_1$, ${}^P\nu_x$	1045 ${}^B\nu_1$, ${}^P\nu_x$			1043	1053 ${}^B\nu_1$
A5				964	946 ${}^A\nu_5$	949	932 ${}^A\nu_5$
P	877	919 ${}^B\nu_4$,${}^P\nu_x$	868 ${}^B\nu_4$,${}^P\nu_x$				
A8				791	780 ${}^A\nu_8$	783	775 ${}^A\nu_8$
B4	725	711 ${}^B\nu_4$,${}^P\nu_x$	709 ${}^B\nu_4$, ${}^P\nu_y$	723,736	704 ${}^B\nu_4$	734	717 ${}^B\nu_4$
A6				687	674 ${}^A\nu_6$	684	669 ${}^A\nu_6$
A7				640	631 ${}^A\nu_7$	627	623 ${}^A\nu_7$

[a] See Figures 5.3 - 5.7 for the corresponding structures of the listed isomers and Table 5.3 for the relative energies.

Table 5.2: Labeling, description and experimental values (in cm^{-1}) of the normal modes of the nitric acid molecule (HNO_3) and the nitrate anion (NO_3^-).

Nitric Acid Molecule (A)			Nitrate Anion (B)		
Mode	Description	Exp.	Mode	Description	Exp.
${}^{A}\nu_1$	O-H stretch	3550[a]	${}^{B}\nu_1$	NO sym. stretch	1049[c]
${}^{A}\nu_2$	NO_2 antisym. stretch	1710[b]	${}^{B}\nu_2$	Out-of-plane deformation	825[c]
${}^{A}\nu_3$	NO_2 sym. stretch	1331[a]	${}^{B}\nu_3$	NO antisym. stretch	1349[d]
${}^{A}\nu_4$	H-O-N bend	1325[a]	${}^{B}\nu_4$	in-plane rocking	719[c]
${}^{A}\nu_5$	(H)O-N stretch	879[a]			
${}^{A}\nu_6$	NO_2 scissor	647[a]			
${}^{A}\nu_7$	(H)O-N-O bend	579[a]			
${}^{A}\nu_8$	NO_2 wag	762[a]			
${}^{A}\nu_9$	HONO torsion	456[a]			

[a] Gas phase, Ref. [214], [b] Gas phase, Ref. [215], [c] Solution, Ref. [216], [d] Gas phase, Ref. [217].

spectra.

Bare Cluster Anions

The IRMPD spectra presented in Figure 5.1 show a rich structure of IR active peaks of varying widths and positions. Several general trends are observed. First, the H_2-tagged spectra show the most bands and these are typically narrower than their counterparts in the IRMPD spectra. The absence of IR bands in the spectra of the untagged anions is reminiscent of observations made in the IRMPD study on bisulfate/sulfuric acid/water clusters (see Section 2.2 and Ref. [63] for details), where it was discussed in terms of "IRMPD transparent" modes, although the origin of this IRMPD transparency is slightly different here (see Section 5.4). Second, the IRMPD spectrum of (1,0,0) is characteristically different from the spectra of the larger clusters, suggesting a significantly different binding motif in this cluster. IR and Raman studies of solid $m = 1$, $n = 0$ complexes [185, 218] find evidence for exceptionally strong hydrogen bonds and a dramatically red-shifted hydrogen bonded O-H stretching mode ($\sim$600 cm^{-1}), indicative of a hydrogen dinitrate species containing a shared proton. The IR spectrum of (1,0,0) indeed exhibits an intense band at 877 cm^{-1} (**P**), not observed in the spectra of the larger clusters, and band **P** is therefore attributed to the shared-proton stretching mode in $O_2NO^- \cdots H^+ \cdots {}^-ONO_2$.

Most of the other observed spectral features in Figure 5.1 can be assigned to characteristic absorptions of nitrate ions and nitric acid molecules by comparison to previous experiments. The four normal modes of nitrate (see Table 5.2) have been observed at 1404/1348 (${}^B\nu_3$), 1049 (${}^B\nu_1$), 825 (${}^B\nu_2$) and 719 cm^{-1} (${}^B\nu_4$) in liquid alkali nitrate solution [216]. Here, the ${}^B\nu_3$ mode, the nominally doubly degenerate and intense antisymmetric stretch of the NO_3^- moiety, splits into two components due to asymmetric solvation. Previous experiments on $NO_3^-\cdot Ar$ in the gas phase [217] showed that this splitting is not seen in the absence of perturbing solvent molecules. The infrared photodissociation spectrum of $NO_3^-\cdot Ar$ is therefore characterized by a single, intense band, observed at 1349 cm^{-1} [217]. In the present spectra, signal attributed to three of these modes (${}^B\nu_3$, ${}^B\nu_1$ and ${}^B\nu_4$) is observed and correlates to the bands labeled **B1** (1437 cm^{-1}), **B3** (1015 cm^{-1}), and **B4** (725 cm^{-1}), respectively. As will be shown later, the ${}^B\nu_3$ modes of both nitrate moieties actually couple strongly, leading to the observed splitting into the three groups of peaks in-between 1250 and 1600 cm^{-1}.

Four modes of neutral nitric acid molecules can be assigned by comparison with the data from IR measurements on thin films of pure HNO_3 (see lowest spectrum labeled “film” in Figure 5.1) [213]. The NO_2 antisymmetric stretch (${}^A\nu_4$), N-O-H bend (${}^A\nu_2$), NO_2 symmetric stretch (${}^A\nu_3$), and the N-O(H) stretch (${}^A\nu_5$) are located at 1686, ∼1480, 1328 and 965 cm^{-1} in the condensed phase spectrum and the corresponding bands in the presented gas phase spectra are labeled with **A4**, **A2**, **A3** and **A5**. The nitric acid core bends ${}^A\nu_{6-8}$ (550 – 791 cm^{-1}) are known from IR absorption spectra of nitric acid vapor (579 – 762 cm^{-1}) [214], as well as in a N_2 matrix (597 – 767 cm^{-1}) [218] and correlate with bands **A6** to **A8**.

Hydrated Cluster Anions

In addition to the bare clusters, also IRMPD spectra of partially hydrated nitrate/nitric acid clusters for $m = 1$ and $m = 2$ were measured. These are shown in Figure 5.2, where they are also compared to the thin film IR spectrum of a HNO_3:H_2O binary amorphous mixture [213] containing predominantly dissociated acid molecules. For $m = 1$, addition of a single water molecule to hydrogen dinitrate leads to partial lifting of some of the IRMPD transparent modes (see 5.3.2), but otherwise perturbs the band positions in the IR spectrum rather weakly. Solvation by at least two water molecules or another nitric acid molecule, on the other hand,

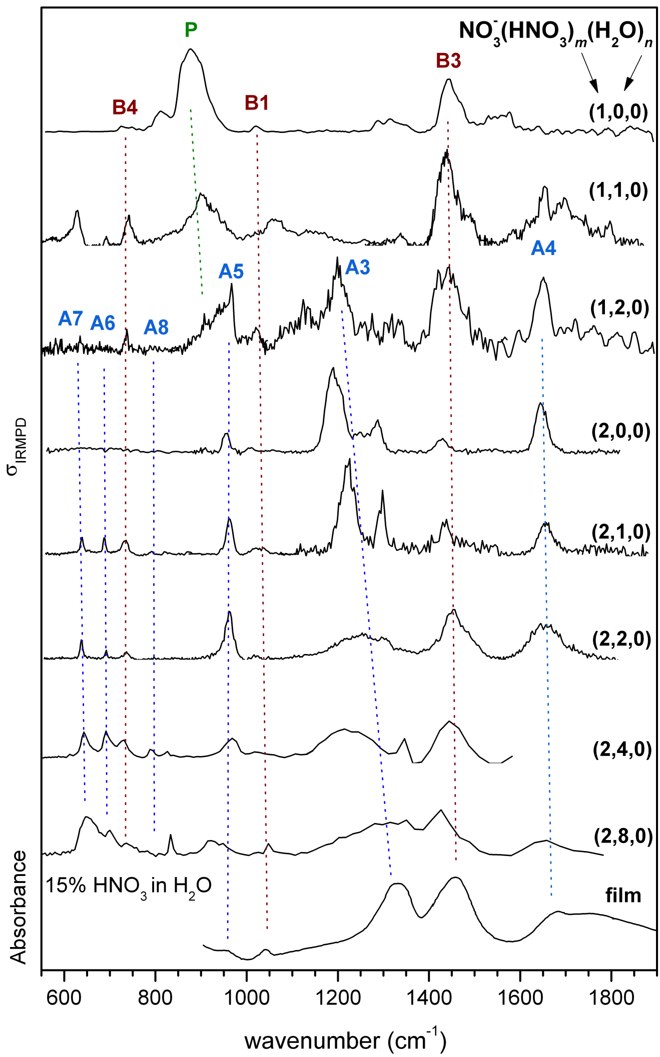

Figure 5.2: Experimental IRMPD spectra of $NO_3^-(HNO_3)_m(H_2O)_n(H_2)$ clusters with $m = 2$, n = 1-8 (top panels) compared to absorption spectra [213] of amorphous 15% HNO_3 in H_2O. Peaks are labeled according to their assignment to modes of the neutral acid molecule (**A**), of the conjugate base anion (**B**) or to shared proton stretching mode (**P**).

leads to more significant changes in the IRMPD spectrum, namely the appearance of the intense bands **A3** and **A5** and the disappearance of the shared-proton mode **P**. For $m = 2$, the addition of a single water molecule is sufficient to recover the IRMPD transparent modes **B4** and **A6-A8** in the core bend region ($\leq 850\,cm^{-1}$). The most striking change in the gas phase spectra upon hydration with up to eight water molecules is the blue shift of band **A3** from $1190\,cm^{-1}$ in the (2,0,0) spectrum to above $1300\,cm^{-1}$ in the (2,8,0) spectrum, indicating a strengthening of the nitric acid N=O bonds upon hydration. Moreover, band **B3**, associated with the antisymmetric stretch of the nitrate anion, increases in relative intensity upon microhydration, while the bands attributed to intact nitric acid decrease. Comparison of the thin film IR spectrum to the gas phase IRMPD spectrum of (2,8,0) in Figure 5.2 shows that most absorption features have nearly converged towards the condensed phase limit with regard to position and width. Hence, the formation of a local hydrogen bond network is mainly responsible for the increase in width of the absorption features and already quite reasonably reproduced by the addition of a few water molecules ($n \geq 4$) to $NO_3^-(HNO_3)_2$.

5.3.2 Analysis

The experimental IRMPD spectra of the nitrate/nitric acid/water clusters are compared to simulated IR spectra derived from harmonic frequencies and intensities in Figure 5.3 to Figure 5.7, respectively. Band positions and scaled harmonic frequencies as well as an approximate normal mode description are listed in Table 5.1. Table 5.3 gives an overview of relative energies and symmetries of the discussed isomers. The H_2-tagged spectra are shown at the top of each figure, containing tagged results, followed by the IRMPD spectrum of the bare cluster and then the spectra of the microhydrated clusters with increasing number of water molecules. For each cluster, two simulated spectra are shown. Calculated geometries are shown alongside the figures, labeled according to cluster size, number of water molecules, and energetic ordering (*e.g.* a, b, ...) For instance, **1w0a** refers to the lowest energy structure of the $m = 1$, $n = 0$-cluster. A complete list of all calculated structures, their relative energies, and simulated IR spectra is given in Appendix B.

The delocalized nature of the calculated normal modes complicates their description. Therefore the bands are assigned based on a comparison to the normal modes of the individual moieties. These combinations of

Table 5.3: Symmetry and relative energies (in kJ/mol) without (ΔE) and with zero-point-energy corrections (ΔE_{ZPE}) of the lowest energy B3LYP/aug-cc-pVTZ minimum-energy structures for $NO_3^-(HNO_3)_m(H_2O)_n$ clusters (see Appendix B for a complete list of all isomers considered).

Cluster	Symbol	Symmetry	ΔE	ΔE_{ZPE}
$NO_3^-(HNO_3)$	1w0a	C_s	0.0	0.0
	1w0b	C_1	0.2	0.1
$NO_3^-(HNO_3)(H_2O)$	1w1a	C_s	0.0	0.0
	1w1b	C_1	3.6	0.2
	1w1c	C_1	0.2	0.4
	1w1d	C_1	0.3	0.5
	1w1e	C_s	2.2	0.6
	1w1f	C_1	3.8	1.4
	1w1g	C_1	3.7	2.0
$NO_3^-(HNO_3)(H_2O)_2$	1w2a	C_1	0.0	0.0
	1w2b	C_s	1.4	0.1
	1w2c	C_s	2.4	0.2
	1w2d	C_1	3.0	1.0
	1w2e	C_s	4.3	1.5
	1w2g	C_s	4.3	1.5
	1w2h	C_1	4.3	1.6
	1w2i	C_1	5.3	2.2
$NO_3^-(HNO_3)_2$	2w0a	C_1	6.8	8.4
	2w0b	C_2	0.0	0.0
	2w0c	C_{2v}	0.4	0.0
	2w0d	C_1	0.2	0.2
	2w0e	C_s	0.6	0.6
	2w0a	C_s	1.3	1.1
$NO_3^-(HNO_3)_3$	3w0a	C_1	0.2	0.0
	3w0b	C_1	0.0	0.0
	3w0c	$C_1(C_3)$	1.0	0.8
	3w0d	C_{3h}	2.1	1.4

“localized” normal modes were identified qualitatively by eye. In several cases significant mixing occurs between these modes, in particular for the

${}^{A}\nu_2/{}^{A}\nu_4$ and ${}^{A}\nu_3/{}^{B}\nu_3$ pairs, introducing some ambiguity in the assignment.

The following sections comprise a detailed technical analysis of the single clusters, a summary of the most important points is given in Section 5.4.

$NO_3^-(HNO_3)$

The two lowest energy structures **1w0a** and **1w0b** both exhibit a shared-proton motif, $O_2NO^- \cdots H^+ \cdots {}^-ONO_2$ (see Figure 5.3). The B3LYP/aug-cc-pVTZ global minimum energy structure **1w0a** is planar and has C_s symmetry. A first-order transition state of D_{2h} symmetry, connecting the two possible C_s isomers along the proton-transfer coordinate, is found only +0.2 kJ/mol higher in energy (see Table 5.3). Thus, while the minimum-energy structure is asymmetric with respect to the position of the proton in-between the two nitrate moieties, inclusion of zero-point energy (zpe) is sufficient to overcome the barrier to proton transfer and this cluster effectively contains an equally shared proton. This is also reflected in the relatively short O-O distance (r_{OO}) of the $O \cdots H^+ \cdots O$ moiety (2.45 Å), indicating the presence of short strong hydrogen bonds (SSHB) [219]. In addition, a non-planar isomer **1w0b** (C_1-symmetry) is found only +0.2 kJ/mol higher in energy, with the corresponding first-order transition state (C_2-symmetry) at +0.3 kJ/mol relative to the C_s structure. Consequently, the potential energy hypersurface in the vicinity of the central proton is very flat with regard to proton transfer as well as non-planarity and one thus expects a symmetrically delocalized proton combined with large amplitude motion of nitrate moieties already in the vibrational ground state. Strong anharmonic effects in the vibrational signature of strong hydrogen bonds are well documented [115, 190], and therefore the assignments based on harmonic calculations are only tentative in nature. Anharmonic calculations on this system are currently in preparation, and first results, showing good agreement with the presented analysis, in particular with the widths of the bands. The AIMD simulations are displayed in Figure B.1, Appendix B.

The presence of both isomeric forms is needed to explain the experimental IRMPD spectra, which is a reasonable assumption, given the low predicted barriers to isomerization. The simulated IR spectra of **1w0a** and **1w0b** (see Figure 5.3) are rather similar, differing mainly in the 1300 – 1500 cm^{-1} region. Both spectra exhibit extended mode-coupling of the shared proton stretching (${}^{P}\nu_x$) and bending (${}^{P}\nu_y$ and ${}^{P}\nu_z$) local modes with the nitrate local modes (${}^{B}\nu_{1-4}$) on each nitrate moiety and only the leading terms are indicated above each band in Figure 5.3. The intense band **P** (877 cm^{-1})

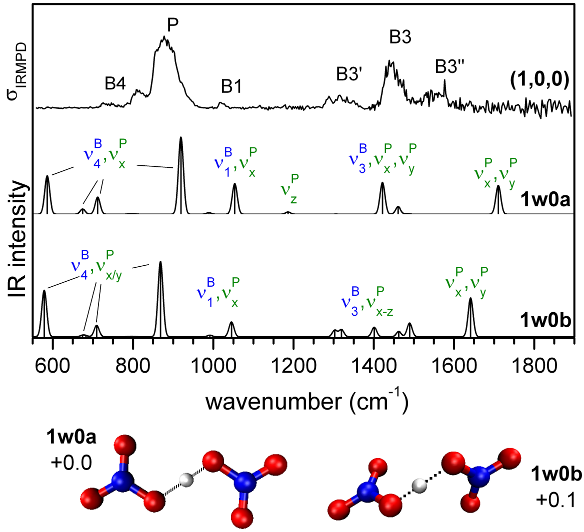

Figure 5.3: Experimental IRMPD and simulated linear absorption spectra of $NO_3^-(HNO_3)$. Simulated spectra, derived from B3LYP/aug-cc-pVTZ scaled (0.968) harmonic frequencies and intensities are convoluted using a Gaussian line shape function with a fwhm of 15 cm^{-1}. The geometry, relative energy (in kJ/mol) and IR spectra of the two lowest isomers are shown. Experimental peaks and simulated vibrational modes (ν) are labeled according to their assignment to modes of the neutral acid molecule (**A**) or of the conjugate base anion (**B**) (see Table 5.2).

is assigned to the shared proton stretching mode $^P\nu_x$, but since this mode strongly couples to the NO symmetric stretching ($^B\nu_1$) and NO_3 in-plane rocking ($^B\nu_4$) modes, it also contributes to the weaker bands **B1** ($^B\nu_1$, $^P\nu_x$) and **B4** ($^B\nu_4$, $^P\nu_x$). $^P\nu_x$ is predicted to considerably red-shift from the planar (919 cm^{-1}) to the non-planar (868 cm^{-1}) isomer. Thus, isomerization between the two structures probably contributes significantly to the extended width of the shared proton band **P** (as well as all other bands). Combinations of the nitrate antisymmetric stretching modes ($^B\nu_3$), which couple to the $^P\nu_{x,y}$ modes, are predicted around 1450 cm^{-1} and account for the **B3** bands. The planar isomer **1w0a** exclusively contributes to band **B3**, while **1w0b** also accounts for the satellite bands at lower (**B3'**) and higher energies (**B3"**). Notably missing from the experimental spectrum are the predicted bands above 1600 cm^{-1} and below 600 cm^{-1}, which we attribute to the inefficiency of the IRMPD process [63, 220]. Note that these bands are recovered upon addition of a water molecule (see below), which lowers the dissociation limit of the cluster and thus reduces the number of absorbed photons required to induce dissociation.

$NO_3^-(HNO_3)(H_2O)$

Two nearly iso-energetic, characteristically different binding motifs are predicted for the $m = 1$, $n = 1$ cluster. The global minimum energy structure (**1w1a**) is planar (C_s) with the water molecule bound to a single nitrate moiety in a double donor (DD) fashion (see Figure 5.4). A non-planar (C_1) isomer (**1w1b**) containing a bridging DD water molecule is calculated +3.6 kJ/mol higher in energy, but the zpe-correction reduces the energy difference down to only +0.2 kJ/mol (see Table 5.3). The latter isomer is characterized by a shorter r_{OO} distance between the nitrate moieties (2.46 Å vs. 2.52 Å, see Figure 5.8), indicating stronger central hydrogen bonds and leading to a more symmetric proton binding with O-H bond lengths of 1.12 Å and 1.34 Å, compared to 1.06 Å/1.46 Å in **1w1a**. At least five more isomers with similar water binding motifs are found within +2 kJ/mol (including zpe) of **1w1a** (see Table 5.3 and Figure B.2).

The simulated IR spectra of **1w1a** and **1w1b** (see Figure 5.4) are markedly different, reflecting the different water binding motif as well as the different hydrogen bond lengths involving the central proton. The IR spectrum of **1w1a** is characterized by a single intense band at 1226 cm^{-1} ($^{A}\nu_3$, $^{B}\nu_3$), while the **1w1b** spectrum exhibits four similar intense bands at 1739 ($^{P}\nu_x$, $^{P}\nu_y$), 1419 ($^{B}\nu_3$, $^{P}\nu_y$), 1023 ($^{B}\nu_1$, $^{P}\nu_x$) and 946 cm^{-1} ($^{P}\nu_x$, $^{B}\nu_4$). Note that the normal modes of **1w1a** are better understood in terms of an asymmetric $NO_3^- \cdots (HNO_3)$ complex, while those of **1w1b**, which exhibits stronger central hydrogen bonds, reflect the shared proton motif. Satisfactory agreement with the experimental spectrum is only found for the **1w1b** spectrum, which predicts all observed bands (see Figure 5.4). Hence, the first water molecule adds to hydrogen dinitrate in a bridging fashion *without* significantly perturbing the SSHB.

Again, this result is in good agreement with first results of AIMD simulations (Figure B.4, Appendix B). Additionally, first measurements of the O-H stretching region, as well as results from IR^{2}MS^2 measurements (Figure B.4, Appendix B) support the presented analysis.

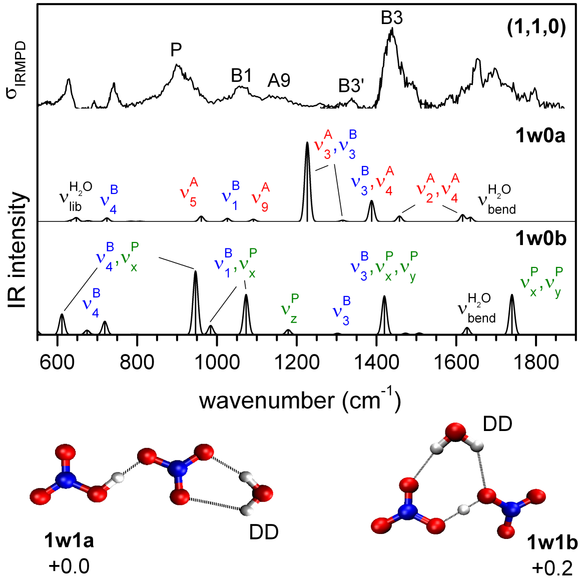

Figure 5.4: Experimental IRMPD and simulated linear absorption spectra of $NO_3^-(HNO_3)(H_2O)_1$ (see Figure 5.3 for a detailed description).

$NO_3^-(HNO_3)(H_2O)_2$

For $m = 1$, $n = 2$ a large number of energetically low-lying, planar and non-planar isomers are found, seven within +2 kJ/mol (including zpe) of the global ground state, which only differ in how the water molecules bind to a hydrogen dinitrate core (see Table 5.3 and Figure B.5). The two lowest energy isomers contain an acceptor/donor/donor (ADD) bridging water molecule (see Figure 5.3), with the planar isomer **1w2b** minimally higher in energy (+0.1 kJ/mol) than the non-planar **1w2a**. The next two isomers, **1w2c** (+0.2 kJ/mol, planar) and **1w2d** (+1.0 kJ/mol, non-planar), contain DD waters that bind to the same nitrate moiety. These are followed by two isomers, **1w2e** (+1.5 kJ/mol, planar) and **1w2f** (+1.5 kJ/mol, non-planar), which contain two DD water molecules, one of them in a bridging position. Isomers containing two bridging waters are found higher in energy (≥2.8 kJ/mol). Similar to the $m = 1$, $n = 1$ clusters, the central hydrogen bonds are strengthened by bridging water molecules, reflected in

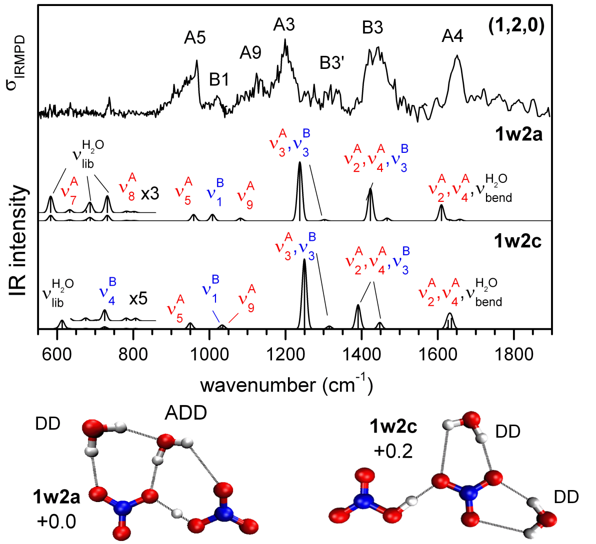

Figure 5.5: Experimental IRMPD and simulated linear absorption spectra of $NO_3^-(HNO_3)(H_2O)_2$ (see Figure 5.3 for a detailed description).

the dependence of r_{OO} on the presence of zero (**1w2c**: 2.56 Å), one (**1w2a**: 2.53 Å) and two (**1w2i**: 2.48 Å) bridging water molecules.

The simulated IR spectra of the six lowest energy isomers are all quite similar with three characteristic IR active modes of decreasing intensity at $\sim$1250 cm^{-1} ($^A\nu_3$, $^B\nu_3$), $\sim$1400 cm^{-1} ($^B\nu_3$, $^A\nu_2$, $^A\nu_4$) and $\sim$1600 cm^{-1} ($^A\nu_2$, $^A\nu_4$, $^{H_2O}\nu_{bend}$). Compared to the experimental spectrum of (1,2,0), the predicted IR spectra of **1w2a** to **1w2d** fit equally well (see Figures 5.5 and B.5), making an assignment to a particular water binding motif difficult. It is probable that multiple, interconverting isomers (with slightly different IR spectra) are present, accounting for the broad IR bands observed in the experimental spectra. The appearance of band **A5** and the intense band **A3** (see Figure 5.5), which are not observed in the experimental spectra of the smaller clusters, however, signals that solvation by two water molecules is sufficient to asymmetrically perturb the central SSHB.

$NO_3^-(HNO_3)_2$

The most stable binding motif for the $m = 2$ clusters consists of a central nitrate-moiety solvated by two nitric acid molecules. The global minimum-energy structure is the non-planar C_2-structure **2w0a** (see Figure 5.6). The planar C_{2v} structure **2w0b** is calculated +0.4 kJ/mol higher in energy, but inclusion of zpe reduces the energy difference to +0.01 kJ/mol. Three additional isomers with a similar binding motif (**2w0c-e**, see Figure B.6) lie within +1.1 kJ/mol (including zpe) of **2w0a** (Table 5.3).

All five structures **2w0a-e** yield similar IR spectra with the most notable differences in the 1300 to 1500 cm^{-1} region, where strongly-coupled NO_2 symmetric (${}^A\nu_3$) and antisymmetric (${}^A\nu_2$) stretching, nitrate antisymmetric stretching (${}^B\nu_3$) as well as NOH bending (${}^A\nu_4$) modes are predicted. The simulated IR spectrum of **2w0b** fits particularly well (see Figure 5.6), because it reproduces the relative positions and intensities of bands **A2-A9**, **B3** and **B4**. Only the relative intensity of the most intense peak at 1224 cm^{-1} (${}^A\nu_3$, ${}^B\nu_3$), which corresponds to band **A3**, is apparently overestimated, but this is the case for all isomers, indicating a breakdown of the double harmonic approximation for the intensities in this case. The spectrum of this isomer cannot account for the feature at ~1800 cm^{-1} as well as band **A9'** (see Figure 5.6). Band **A9'** can be nicely reproduced by considering the presence of a second isomer **2w0a**, whose H-O-NO torsion mode (${}^A\nu_9$) is blue-shifted by +55 cm^{-1} compared to **2w0b**. The feature at ~1800 cm^{-1}, on the other hand, is not predicted in any of the simulated spectra. The OH stretching mode (${}^A\nu_1$) is predicted at 2445 cm^{-1} and is therefore too high to account for this feature, so it is more likely due to combination bands.

$NO_3^-(HNO_3)_3$

The lowest energy structures for the $m = 3$ clusters all contain a centrally-solvated nitrate ion with three nitric acid molecules binding to the three terminal O-atoms. In the global minimum energy structure **3w0a** (see Figure 5.7), one of the nitric acid ligands lies nearly in the same plane as the nitrate ion, while the other two lie almost perpendicular to this plane. The corresponding N-O···H-O dihedral angles are 168°, 86°, and -87°. Consequently, the N-atoms of the three nitric acid units are arranged in (in, ~180°), above (up, >0°) and below (down, <0°) the nitrate plane and this arrangement is referred to as the in/up/down configuration. **3w0b**, also shown in Figure 5.7, exhibits an up/up/down configuration (94°/84°/-

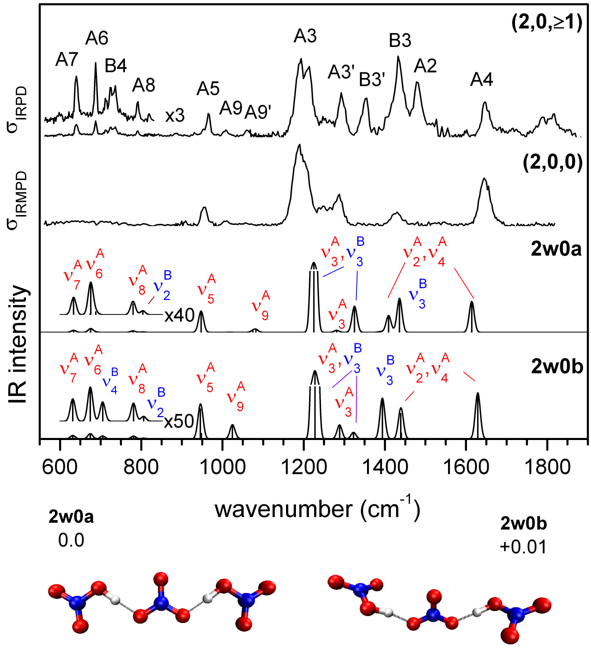

Figure 5.6: Experimental IRMPD and simulated linear absorption spectra of $NO_3^-(HNO_3)_2$ (see Figure 5.3 for a detailed description).

84°) and is calculated only +0.2 kJ/mol above **3w0a**. Inclusion of zpe makes these two conformers nearly isoenergetic (see Table 5.3). The symmetric (C_3) up/up/up (97°/97°/97°) conformer **3w0c** lies +1.0 kJ/mol (+0.8 kJ/mol) above **3w0a**. The planar in/in/in (180°/180°/180°) configuration of C_{3h} symmetry lies +2.1 kJ/mol above **3w0a** and is not a minimum on the potential energy surface, but rather a first-order transition state, indicating that the barriers to interconversion are small.

The simulated IR spectra of the three lowest isomers (see Figures 5.7 and B.7) all qualitatively reproduce the experimental IRMPD spectra. Bands **A2** to **A5** are assigned to modes predominantly involving the ${}^{A}\nu_{2-5}$ vibrations of the nitric acid ligands. Bands **B3** and **B3'**, separated by ~30 cm^{-1}, are tentatively attributed to the two components of the nitrate N=O antisymmetric stretch (${}^{B}\nu_3$), signaling an asymmetric solvation environment. This splitting is seen particularly well in the H_2-tagged spectrum (3,0,≥1)

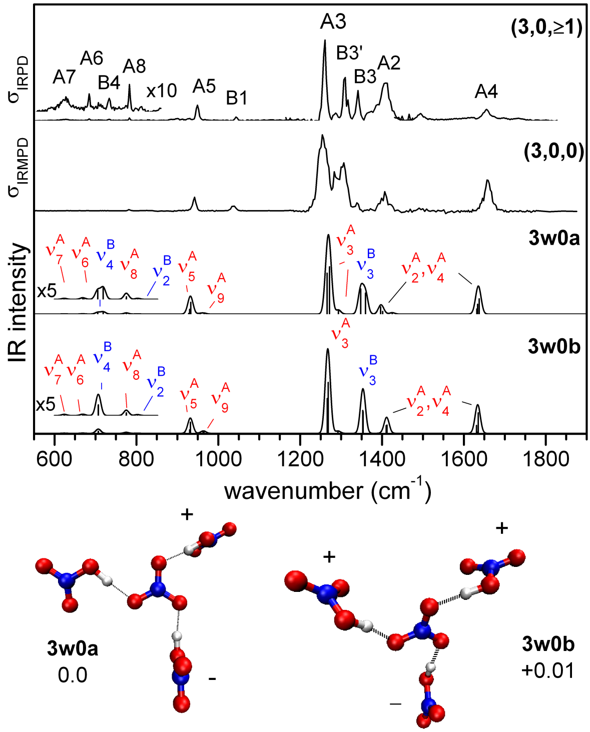

Figure 5.7: Experimental IRMPD and simulated linear absorption spectra of $NO_3^-(HNO_3)_3$ (see Figure 5.3 for a detailed description). HNO_3 groups above the NO_3^--plane are denoted with +, those below are denoted with - (see text for details).

in Figure 5.7, suggesting that messenger-tagging traps this conformer in a shallow local minimum. The IRMPD spectrum of the bare anion probes a somewhat hotter ion distribution, in which this effect is averaged out by rapid isomerization and thus mainly a single band (**B3'**) is observed in this region. Band **B1** is attributed to the nitrate symmetric stretch ($^B\nu_1$), which is nominally IR-inactive in the bare nitrate ion, but obtains its IR intensity due to non-centrosymmetric solvation. Bands **A5-A8** are assigned to the N-O(H) stretching mode ($^A\nu_5$) as well as the nitric acid core bending modes $^A\nu_8$, $^A\nu_6$, and $^A\nu_7$, respectively, while band **B4** is the in-plane rocking mode of the nitrate core.

5.4 Discussion

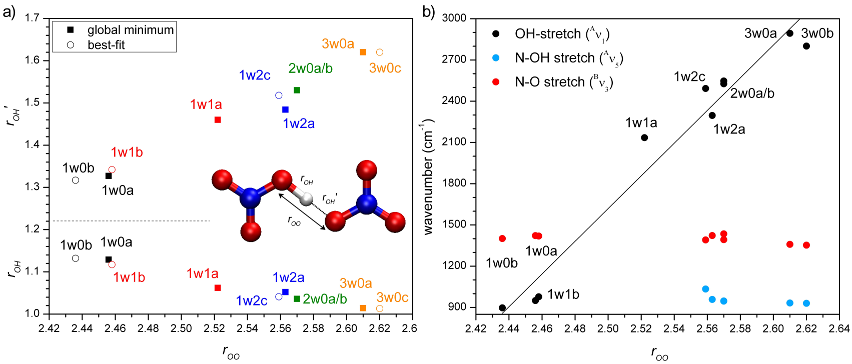

Figure 5.8: a) Calculated OH bond lengths r_{OH} and $r_{OH}^{'}$, as a function of r_{OO}. All distances are given in Å. b) Calculated O-H, N-OH and N-O stretching frequencies as a function of r_{OO} (in Å).

Shared Proton Regime

The consideration of anharmonic effects in full dimensionality is essential for a quantitative description of the IR signature of prototypical systems containing SSHBs, as was recently shown for example for $H_5O_2{}^+$ and $H_3O_2{}^-$ [176, 221]. Hence, the apparent qualitative agreement of the predicted harmonic IR spectra of $H^+(NO_3-)_2$ and $H^+(NO_3-)_2(H_2O)$ with the experimental IRMPD spectra is interesting but possibly fortuitous. Therefore it would be helpful to use another criterion to confirm the assignment of the shared proton stretching band (ν_x^p). For proton-bound heterodimers it has been shown by Johnson and coworkers, that ν_x^p can be estimated from the difference in proton affinity (ΔPA) of the two groups [115].

In the case of proton-bound homodimers (ΔPA = 0) one may use the dependence of ν_x^p on the distance r_{AB} of the (heavy) atoms sharing the proton, *i.e.* r_{OH} in the present case, as a criterion for the assignment of ν_x^p in the equally-shared proton regime. Comparison of available gas phase values reveals that ν_x^p of $H^+(NH_3)_2$, $H^+(OH^-)_2$, $H^+(NO_3^-)$, and $H^+(H_2O)_2$ are 374 cm^{-1} [222], 697 cm^{-1} [223], 877 cm^{-1} (present work) and 1047 cm^{-1} [97], respectively, while the predicted values for r_{OO} (for the equally-shared proton configuration) are 2.75 Å [222], 2.51 Å [223], 2.44 Å (present work, C_{2h} geometry), and 2.40 Å [224], respectively. Hence, the vibrational frequency of the shared proton stretching mode increases monotonically with decreasing r_{OO} in the equally-shared proton regime. Simply put, stronger confinement of the motion of the shared proton along the internuclear (heavy atom) axis leads to an increase of the spacing of the vibrational levels and hence an increase of the fundamental vibrational transitions, supporting this assignment. This relationship should hold as long as the barrier for proton transfer is non-existent or small compared to the zero-point energy.

Influence of Solvation

The central proton in hydrogen dinitrate sensitively responds to solvation by water or nitric acid molecules. Figure 5.8a) shows calculated O-H bond lengths, r_{OH} and r'_{OH}, as a function of r_{OO} for the relevant cluster geometries described in Section 5.3.2. The interatomic separation r_{OO} can be used as a measure for the HB strength. These are typically categorized according to bond distance in long (r_{OO} >2.8 Å), intermediate (2.8 Å> r_{OO} >2.5 Å) and short (r_{OO} <2.5 Å), corresponding to hydrogen bond strengths from weak to strong, respectively.

The non-planar conformer of hydrogen dinitrate (**1w0b**) exhibits the shortest O-O distance (2.44 Å), followed by its planar counterpart (**1w0a**: 2.46 Å). Addition of a single water molecule does not necessarily destabilize this arrangement if it binds in a bridging fashion (**1w1b**). However, if the water adds to a single nitrate moiety (**1w1a**) or two water molecules are added (**1w2a**, **1w2c**), then r_{OO} increases (>2.52 Å) and the SSHB motif is replaced by a short covalent O-H and a longer HB. An even more pronounced effect (2.57 Å) is observed upon addition of a second nitric acid molecule (**2w0a**, **2w0b**). Finally, the third nitric acid molecule completes the first solvation shell around the nitrate ion and exhibits the weakest ($r_{OO} \geq$ 2.62 Å) HBs. Hand in hand with the softening of the SSHB, the N-O(H) bond lengths increase from 1.33 Å to 1.37 Å in the nitric acid units and decreases to 1.25 Å in the nitrate core.

The predicted softening of the SSHB in hydrogen dinitrate upon solvation has several effects on its experimental IR signature. In the spectrum of the bare hydrogen dinitrate anion, the characteristic shared proton mode is observed at 877 cm^{-1}. Addition of one water molecule leads to a blue shift of 21 cm^{-1} in the IRMPD spectrum. Addition of more than one water molecule or nitric acid molecules moves it to higher energies and out of the investigated spectral range. Concomitant with the weakening of the SSHB the characteristic IR active bands of nitric acid appear in the IR spectrum. This effect is qualitatively captured by the harmonic calculations. As described above, the clusters with short O-O distance ($r_{OO} < 2.46$ Å) are characterized by a strongly red-shifted shared proton stretching mode ($<1000\,\text{cm}^{-1}$). As r_{OO} increases upon solvation with additional water or nitric acid molecules, the O-H stretching mode of the nitric acid moiety ($^{A}\nu_1$) increases nearly linearly (see Figure 5.8b). In contrast, the changes in the N-O distances in either the nitrate or the nitric acid moieties upon solvation, also shown in Figure 5.8b), are only weakly reflected in the predicted harmonic frequencies of the corresponding N-O stretching modes ($^{A}\nu_5$ and $^{B}\nu_3$), which differ by less than $100\,\text{cm}^{-1}$.

IRMPD Transparency

Upon messenger-tagging with H_2, bands emerge in the N=O stretching and core bend regions for the $m > 1$ clusters, which are not observed in the IRMPD spectra of the corresponding bare species. Moreover, the spectra of the H_2-tagged clusters are in much better agreement with the simulated linear absorption spectra predicted by the harmonic calculations. There are two reasons for this behavior. First, fewer photons are needed to photodissociate the H_2-anion complex and hence the IRMPD intensities are closer to the linear absorption cross sections. Second, the H_2-anion complexes are colder, since the overall internal energy must lie close to or below the anion-H_2 bond dissociation energy ($\sim 600\,\text{cm}^{-1}$) [225] for the tagged complex to survive. The observation of IRMPD transparent bands, which has been discussed in Section 2.2, is different to those observed in the bisulfate/sulfuric acid system, where it was connected to a disruption of the HB network. Here, the origin of the observed IRMPD transparency is different, as no hydrogen bonds are or can be broken without immediate dissociation. Rather, in the present case, the large amplitude motion due to conformational fluctuations of the clusters leads already at low internal energies to a less efficient absorption process. Presumably, this is a consequence of a "smearing out" of the transition strengths for the first few absorption steps and results in the absence of peaks in the IRMPD spectra of the hotter bare clusters compared to the single-photon (or few-photon) IRPD-spectra of the colder H_2-tagged clusters.

5.5 Summary and Conclusions

The present study reports the first IRMPD spectra of nitrate/nitric acid/water clusters in the fingerprint region. It shows that IRMPD spectroscopy is a sensitive method for probing the solvation environment of charged clusters and emphasizes the exceptional solvation behavior of the $m = 1$ cluster. While addition of a single water molecule does not destabilize the shared proton motif, additional solvation is sufficient to induce an asymmetry in the central strong hydrogen bonds, leading to a solvated nitrate/nitric acid motif for the larger clusters. The change in solvation motif is reflected in the concomitant disappearance of the shared proton mode and the appearance of characteristic HNO_3 modes.

Similar to previously reported results for microsolvated conjugated base anions [60, 63, 220], this work provides additional examples for systems with IRMPD transparent modes. Tagging with H_2 molecules or addition of water lowers the dissociation limit of the cluster such that this transparency is lifted or relaxed, leading to additional bands in the core bend and N=O stretching region. The tagged spectra are in much better agreement with the calculated frequencies and intensities.

The IRMPD spectra of the higher hydrated $m = 2$ clusters show a strong resemblance to the thin film results, suggesting that upon addition of the first eight water molecules the IR spectra and hence the structures have nearly converged. However, further spectroscopic experiments on microsolvated conjugate base anions are necessary to determine the degree of acid dissociation in $NO_3^-/HNO_3/H_2O$ clusters as a function of the cluster composition and temperature.

Chapter 6

Anharmonicity in the IR spectra of Hydrogen-bonded Clusters

As shown in the previous chapters, the interpretation of the IR spectra of small HBed systems is not always straightforward, owing to the presence of different isomers or anharmonic effects. For instance, clusters with significant charge transfer show broadening of the corresponding transitions. But also strong coupling of multiple modes as well as overtone transitions can extensively complicate an unambiguous assignment of the IRPD spectra. This chapter deals with the anharmonic effects in the IRMPD spectra of the singly-hydrated conjugated base anions $H_2PO_4^-{\cdot}H_2O$, $NO_3^-{\cdot}H_2O$, $NO_3^-{\cdot}D_2O$ and $NO_3^-{\cdot}HDO$. These systems were chosen, because their spectra exhibit a rich structure in the O-H stretching region, which cannot be explained within a simple harmonic picture, and more sophisticated approaches are applied to reproduce the experimentally observed absorption patterns. Owing to the nature of the observed anharmonic effects, the chapter is divided into two sections. In Section 6.1 the vibrational spectra of $H_2PO_4^-{\cdot}H_2O$, measured in the O-H stretching ($2700 - 3900\,cm^{-1}$) and fingerprint ($600 - 1800\,cm^{-1}$) region, are discussed. The comparison to AIMD simulations reveals that the water molecule undergoes large amplitude motion, even at low internal temperatures. The anharmonic effects of the low-barrier isomerization reaction on the infrared intensities can be qualitatively captured by the dipole time correlation function.

In Section 6.2 the IRMPD spectrum of the nitrate-water complex is studied in the OH/D stretching region. All spectra show a series of multiple discrete peaks in a spectral region, characteristic of a double hydrogen bond donor binding motif. Vibrational configuration interaction calculations confirm that much of the structure observed in the IRMPD spectra derives from progressions in the water rock resulting from strong cubic coupling between the O-H (O-D) stretch and water rock degrees of freedom. Additionally, the spectra of both $NO_3^-{\cdot}H_2O$ and $NO_3^-{\cdot}D_2O$ display a strong peak that does not derive from the water rock progression but results instead from a Fermi resonance between the O-H (O-D) stretch and H-O-H (D-O-D) bend overtone.

6.1 Large Amplitude Motion in Monohydrated Dihydrogen Phosphate

6.1.1 Introduction

Phosphate anions play a key role in biological and agricultural systems [226–228]. They are found in various esters, *e.g.* in adenosine phosphates, and in aqueous solution in the form of conjugate base anions $H_{3-x}PO_4^{x-}$ with x = 1-3 (inorganic phosphates). At physiological pH, $H_2PO_4^-$ and HPO_4^{2-} are abundant and important in acid-base equilibria involved in metabolic pathways. Loss of water from dihydrogen phosphate ($H_2PO_4^-$) leads to metaphosphate (PO_3^-), which is proposed to be a key intermediate in the aqueous hydrolysis of phosphate monoesters [226]. However, its identification in solution remains elusive. How phosphate ions are hydrated (and dehydrated) at the molecular level is thus crucial for a mechanistic understanding of hydrolysis reactions, but difficult to extract from condensed phase measurements.

Early studies on the PO_3^- + H_2O reaction in the gas phase [229] found that metaphosphate is unreactive, even though $H_2PO_4^-$ is thermodynamically more stable, owing to a high activation barrier. High pressure mass spectroscopic investigations by Keesee and Castleman [230], supported by electronic structure calculations [231, 232], suggested that formation of dihydrogen phosphate does occur in the third hydration step and that $PO_3^-(H_2O)_3$ is in equilibrium with $H_2PO_4^-(H_2O)_2$ with a four-center transition-state structure [232]. Later, Kebarle and coworkers determined hydration energies of $H_2PO_4^-$ with up to two water molecules using electrospray-ionization mass spectrometry [233], but found no evidence for the formation of $PO_3^-(H_2O)_3$ from dehydrated dihydrogen phosphate. Fourier-transform infrared (FTIR) spectra of the $H_2PO_4^-$ anions in aqueous solution have been recorded at 300 K [234] and interpreted by comparison to

Chapter based on:
"*Large Amplitude Motion in Cold Monohydrated Dihydrogen Phosphate Anion $H_2PO_4^-(H_2O)$: Infrared Photodissociation Spectroscopy combined with Ab Initio Molecular Dynamics Simulations*" L. Jiang, S.-T. Sun, N. Heine, J.-W. Liu, T. I. Yacovitch, T. Wende, Z.-F. Liu, D. M. Neumark, and K. R. Asmis, *Phys. Chem. Chem. Phys.* **2014**, 16, 1314 – 1318. DOI:10.1039/C3CP54250E

first-principles molecular dynamics simulations [235]. Electronic structure calculations predict that the global ground state of $H_2PO_4^- \cdot H_2O$ contains water in a double donor (DD) configuration bound to the two unprotonated phosphoryl O-atoms [232, 236–238]. An alternative arrangement with the water in an acceptor-donor (AD) motif is found to be higher in energy [236]. However, no experimental gas-phase data regarding the cluster structures are available.

In the following section IRMPD spectra of bare and monohydrated $H_2PO_4^-$ clusters are presented. First, the spectra are compared to simulated harmonic IR spectra, showing that the spectrum of $H_2PO_4^- \cdot H_2O$ reveals pronounced anharmonic effects that can only be understood on the basis of the results derived from AIMD simulations.

6.1.2 Experimental Details

IRMPD experiments are carried out using the ion trap - tandem mass spectrometer, described in Section 3.8. Briefly, gas-phase ions are continuously produced in a commercial Z-spray source from a $1 \cdot 10^{-3}$ M aqueous solution of phosphate acid in a 1:1 water/acetonitrile solvent. A beam of negative ions passes through a 4 mm diameter skimmer and is then collimated in a radio frequency decapole ion guide. Parent ions are mass-selected in a quadrupole mass filter, deflected by 90° in an electrostatic quadrupole deflector and focused into a gas-filled RF ring-electrode ion-trap. Here, the anions are collected for 99 ms and thermalized through collisions with a He buffer gas. In a 10 Hz cycle, ions are extracted and focused into the center of the extraction region of a time-of-flight mass spectrometer, where they interact with the radiation of a tunable and pulsed IR laser. If the wavelength of the IR radiation is in resonance with a vibrational transition, fragmentation of the (parent) anions occurs. All anions are extracted by a set of high voltage pulses and are detected as a function of their TOF using an MCP detector. A mass spectrum is obtained for each laser shot. IR spectra are recorded by averaging over 50-70 TOF mass spectra per wavelength and scanning the laser wavelength.

Pulsed IR radiation is either provided by FELIX (600 – 1800 cm^{-1}) or an OPO/OPA IR laser system. The fluence as well as the optical path length of the OPO/OPA IR laser pulse is increased using a Herriott-type multipass cell, displayed in Figure 6.1 [59]. FELIX is operated at 10 Hz with a bandwidth of $\sim$ 0.2% RMS of the central wavelength and typical pulse energies of up to 30 mJ. The Laservision OPO/OPA IR laser produces

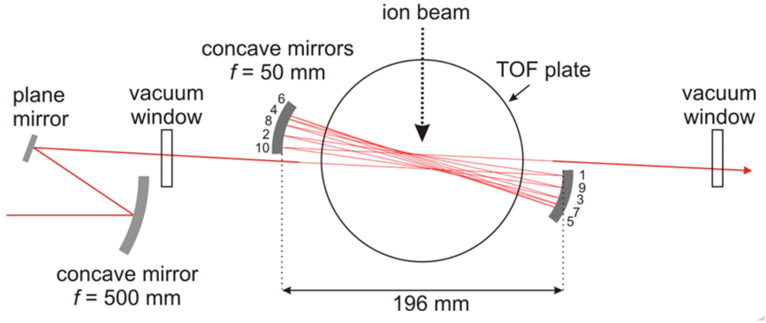

Figure 6.1: Schematic view of the multipass cell-setup as used in the presented experiments. Figure adapted from Ref. [59].

7 ns/2 mJ pulses at 10 Hz with a spectral bandwidth of ∼2 cm^{-1} and the laser wavelength is calibrated using a photoaccoustic cell filled with methane. The photodissociation cross section $\sigma(\nu)$ is determined from the relative abundances of the parent and photofragment ions, $I_P(\nu)$ and $I_F(\nu)$, and the frequency-dependent laser energy $P(\nu)$, as described in Section 3.5.

6.1.3 Results and Discussion

$H_2PO_4^-$

To determine that dihydrogenphosphate is actually formed and not metaphosphate, the IRMPD spectrum of $H_2PO_4^-$ is recorded in the fingerprint region by monitoring the H_2O loss channel (Figure 6.2). Comparison of the experimental band positions, labeled H-K in Figure 6.2, to those in the simulated MP2/aug-cc-pVDZ harmonic vibrational spectra of $H_2PO_4^-$ and $PO_3^-(H_2O)$ yields satisfactory agreement only with the spectrum of dihydrogen phosphate, allowing assignment of the four IR-active features to the antisymmetric (H, 1299 cm^{-1}) and symmetric (I, 1094 cm^{-1}) P=O stretching, POH bending (J, 1049 cm^{-1}) and antisymmetric P=OH stretching (K, 770 cm^{-1}) modes. Poorer agreement between 600 – 1400 cm^{-1} as well as the lack of any signal in the water bending region (∼1700 cm^{-1}) rules out any contribution from the monohydrated metaphosphate anion, which is also predicted to lie +37.4 kJ/mol higher in energy. Discrepancies regarding the IRMPD vs. the linear harmonic intensities are attributed to the IRMPD mechanism (see Section 2.2). The predicted dissociation energy of $H_2PO_4^-$ is 50 kJ/mol, leading to the formation of PO_3^- + H_2O. However, there is an even higher barrier in the dissociation channel of 122.1 kJ/mol (MP2/aug-cc-pVDZ level including zero point energy and BSSE corrections), which amounts to the absorption of at least 11 photons at 1000 cm^{-1}, assuming ions with negligible internal energy.

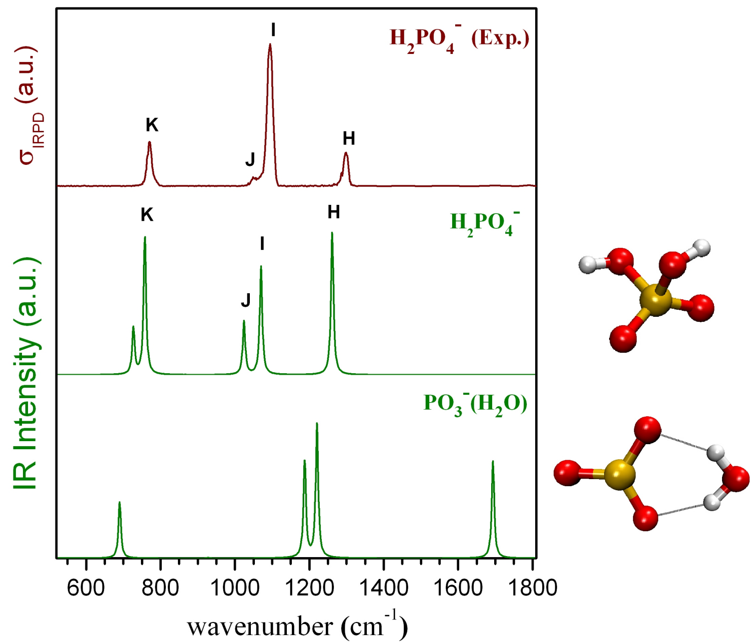

Figure 6.2: Comparison of the experimental (red) IRMPD spectrum of $H_2PO_4^-$ (top) and simulated (green) MP2/aug-cc-pVDZ harmonic vibrational spectra of the minimum-energy structures of $H_2PO_4^-$ (center) and $PO_3^- \cdot H_2O$ (bottom). The MP2 spectra are scaled with a factor of 0.99 (see Appendix C for scale factors and the method for convoluting the stick spectra of harmonic frequencies).

$H_2PO_4^- \cdot H_2O$

The experimental IRMPD spectrum of $H_2PO_4^- \cdot H_2O$, recorded from 550 – 1800 and 2600 – 3950 cm^{-1} in the H_2O loss channel, is shown in Fig-

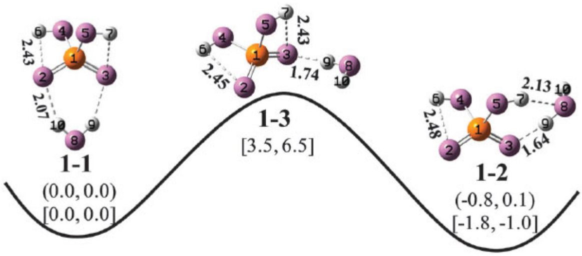

Figure 6.3: Minimum energy (**1-1** and **1-2**) and first-order transition state (**1-3**) structures for the $H_2PO_4^- \cdot H_2O$ complex. B3LYP/aug-cc-pVDZ and MP2/ aug-cc-pVDZ relative energies (in kJ/mol) are listed with (inside round brackets) and without (inside square brackets) ZPE corrections. The MP2 hydrogen bond lengths are given in Å.

ure 6.4. Corresponding band positions and assignments are listed in Table 6.1. Six features, labeled A-F, are observed in the O-H stretching region (>2700 cm^{-1}). Only band A lies above 3600 cm^{-1}, which is in the region of the free O-H stretching modes [12]. Consequently, bands B-F (<3600 cm^{-1}) are attributed to progressively more strongly hydrogen bonded O-H stretching modes. The hydrogen bond strength is reflected in the extent of the red-shift (compared to the energy of the free O-H stretch), as well as in the width of the absorption band. In contrast, all bands below 1800 cm^{-1} (G-L) appear relatively narrow. The band around 1700 cm^{-1} (G) is assigned to the water bending mode [239]. The bands below 1500 cm^{-1}, similar to those observed for bare $H_2PO_4^-$ (Figure 6.2), are due to P-O and P=O stretches, as well as bending and other lower-frequency modes [234].

The two most stable predicted structures for $H_2PO_4^- \cdot H_2O$ are the complexes containing either a DD- or an AD-water molecule, labeled **1-1** and **1-2**, respectively, shown in Figure 6.3. In **1-1**, the H_2O molecule donates two HBs to the PO_2^- moiety, yielding a more symmetric structure (C_{2v}), in which the negative charge in $H_2PO_4^-$ is stabilized on the PO_2^- moiety. The HB distances of 2.07 Å are only slightly longer than the distance of 2.00 Å in the water dimer [240], implying that the interactions are of comparable strength. In the asymmetric structure **1-2**, the H_2O molecule donates a

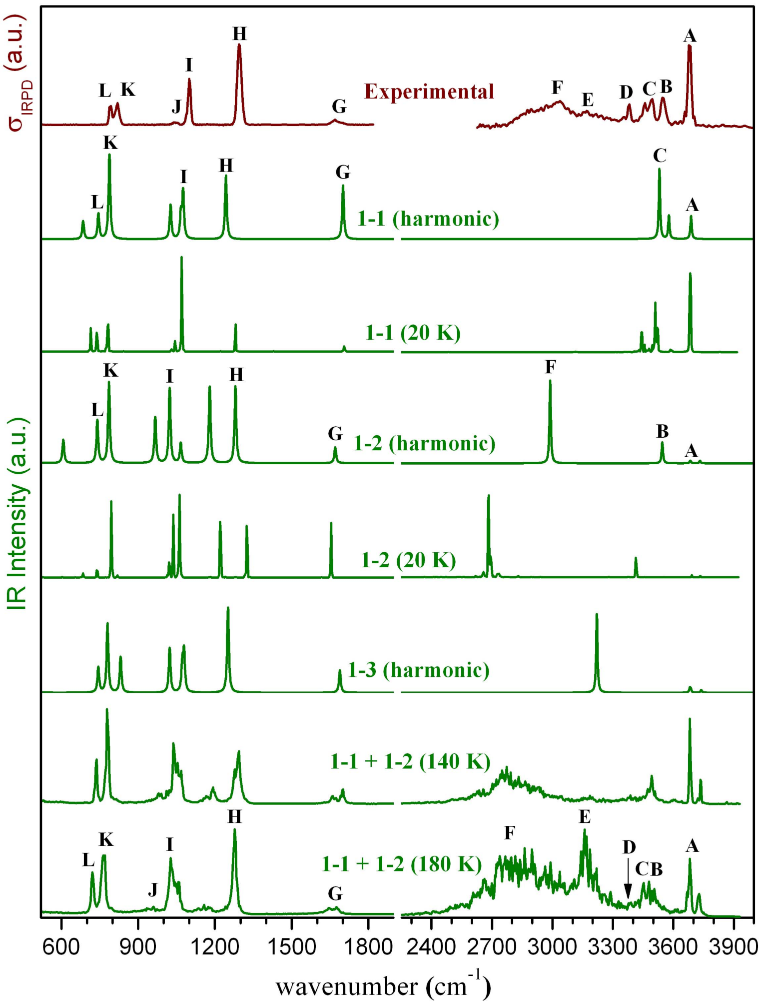

Figure 6.4: Comparison of the experimental IRMPD spectrum of $H_2PO_4^-\cdot H_2O$ (top) and simulated MP2/aug-cc-pVDZ harmonic and DTCF spectra from 200 ps trajectories of isomers **1-1** and **1-2**, and transition state **1-3** (see text).

Table 6.1: Assignment and band position (in cm^{-1}) of the vibrational bands observed in the IR spectra of $H_2PO_4^-(H_2O)_{0,1}$ shown in Figures 6.2 and 6.4.

Label	**$H_2PO_4^-$**		**$H_2PO_4^-(H_2O)$**			**Assignment**
	Exp.	MP2	Exp.	MP2	DTCF	
A			3684	3688(**1-1**) 3684(**1-2**)	3684	free PO-H stretch
B			3546	3545(**1-2**)	3504	HBed PO-H stretch
C			3410-3520	3578(**1-1**) 3531(**1-2**)	3479 3453	O-H stretch of H_2O
D			3382		3380	
E			3100-3300		3080-3280	HB O-H stretch of H_2O in transient **1-3**
F			2700-3100	2989(**1-2**)	2600-3100	broadened O-H stretch of strong HBs
G			1671	1701(**1-1**) 1671(**1-2**)	1674 1644	water bend
H	1299	1290	1294	1243(**1-1**) 1280(**1-2**)	1277	antisymmetric P=O stretch
I	1094	1070	1099	1079(**1-1**) 1023(**1-2**)	1027	symmetric P=O stretch
J	1049	1024	1020-1070	966(**1-2**)	~961	P-OH bend
K	770	758	820	787(**1-1**) 786(**1-2**)	760	antisymmetric P-OH stretch
L		727	793	744(**1-1**) 740(**1-2**)	720	symmetric P-OH stretch

strong HB (1.64 Å) to one P=O group, and accepts a weaker one (2.13 Å) from one of the hydroxyl groups. The other P=O and P-OH groups do not interact substantially with the water molecule and form a weak internal hydrogen bond (2.48 Å).

The energetic ordering of these two isomers depends on the model used. B3LYP predicts **1-2** as the global minimum energy structure and **1-1** +0.8 kJ/mol higher in energy, including zero point energies (ZPE). In contrast, MP2 places **1-2** +0.1 kJ/mol above **1-1**. These two minimum energy structures are separated by a small barrier (B3LYP: +3.5 kJ/mol; MP2: +6.5 kJ/mol) at the first-order transition state (TS) **1-3** (Figure 6.3), indicating a fairly flat potential energy surface. In structure **1-3**, the H_2O molecule forms only a single HB with one of the phosphoryl groups. The MP2/aug-cc-pVDZ binding energies between $H_2PO_4^-$ and water in **1-1** and **1-2** are 52.8 and 50.0 kJ/mol including zero point energy and BSSE corrections, respectively, which are close to the experimental value of 58.6 kJ/mol determined mass spectrometrically.

Simulated MP2 harmonic spectra of **1-1** and **1-2** are shown below the experimental IRMPD spectrum in Figure 6.4. Upon first glance, a satisfactory agreement between experiment and harmonic theory may be observed for isomer **1-1**, especially below 2000 cm^{-1}. The harmonic spectrum of **1-1** accounts for all the experimentally observed peaks (G-L), while the spectrum of **1-2** predicts additional intense bands at 1170 cm^{-1} (symmetric O=P=O stretch) and 966 cm^{-1} (water wag) that are not observed in the experiment. Above 2000 cm^{-1}, the spectrum of **1-1** also accounts for peak A (free PO-H stretch) and the doublet C (HBed water symmetric and antisymmetric stretches) at ~3450 cm^{-1}. However, the harmonic spectrum of **1-1** leaves bands B and D-F unassigned. On the other hand, the harmonic spectrum of **1-2** yields reasonable assignments for bands A (free HO-H stretch), B (HBed PO-H stretch) and F (HBed H-OH stretch) in the O-H stretching region, leaving C-E unassigned. In particular, the strongest hydrogen bond in **1-2** (1.64 Å) nicely accounts for the characteristically red-shifted band F (2700 – 3100 cm^{-1}), even though its width cannot be rationalized at the harmonic level. In summary, neither harmonic IR spectra of the two isomers nor a linear combination of the two can satisfactorily explain the experimental IRMPD spectrum shown in Figure 6.4.

Ab Initio Molecular Dynamics Simulations*

To disentangle the discrepancies between the harmonic and experimental IRMPD spectra, AIMD simulations were performed. Briefly, vibrational profiles at finite temperature are obtained by the Fourier transform of the dipole time correlation function (DTCF), which accounts for anharmonic as well as dynamic effects. Two sets of long AIMD simulations were performed at 140 K and 180 K for a more extensive sampling of the phase space. At each temperature, two trajectories were propagated, one starting from **1-1** and the other from **1-2**, lasting 200 ps. Each trajectory was then cut into 10 ps intervals that were Fourier-transformed, and all 40 frequency profiles were then added up to produce the DTCF spectrum at a specific temperature. The DTCF spectra from both trajectories differ only slightly from each other as shown in Figure 6.3, indicating that **1-1** and **1-2** interconvert readily at these temperatures. DTCF spectra were also determined from AIMD simulations at 20 K (10 ps trajectory) starting from the two isomers. All simulations are shown in Figure 6.4.

The AIMD simulations at 20 K are helpful to test the quality of the potential energy surface, but do not correspond to a physically achievable temperature since zero-point energies are not considered. The general appearance of the 20 K DTCF spectra is indeed similar to the previously discussed harmonic spectra, with the HBed O-H stretching modes showing the largest shifts relative to the harmonic modes due to the use of different methods (PBE vs. MP2). Interestingly, the relative band intensities of experimental features A-C and G-L, with the exception of band H, are reproduced better by the **1-1** simulation already at 20 K compared to the harmonic spectrum (Figure 6.4). The spectrum of **1-2** at 20 K, on the other hand, still mainly reflects the harmonic intensities, but does capture the pronounced red-shift of band F. To determine ZPE and finite temperature effects, the simulation temperature is raised to 140 K and 180 K, shown in the bottom panels of Figure 6.4.

There is considerably better agreement between the experimental spectra and the DTCF spectra at higher simulation temperatures (140 or 180 K) throughout the spectral range with respect to band positions and relative intensities. At these simulation temperatures, isomers **1-1** and **1-2** can interconvert. The complexity of the features in the O-H stretching region as well as the number and relative intensities of the bands in the fingerprint

*Calculations have been performed by the group of Prof. Z.-F Liu at the Chinese University of Hong Kong.

region are qualitatively reproduced. The increased broadening of the HBed O-H stretching bands B-F with increasing strength of the HBs, is also captured.

In more detail, peak A remains sharp at 140 and 180 K, indicative of an O-H stretching mode of a free PO-H group. Peak B is due to the O5-H7 stretch in **1-2** (Figure 6.3). The O8-H9 and O8-H10 stretches in **1-1** are responsible for the double peaks C. These three peaks are similar in width (around 50 cm^{-1}) and the lengths of the respective HBs involved are all predicted close to ∼2.1 Å, indicating comparable HB strengths. Band F is the broadest predicted and observed feature and involves the strongest hydrogen bond (O3· · ·H9 in **1-2**). Consequently, the integrated intensity of the sharp peak F in the harmonic spectrum (and also in the 20 K spectrum) of **1-2** is distributed over a much larger energy range. Similar broadening has been observed for other cluster ions [114, 241–246]. The reduced relative intensity and broadening of the water bending mode (band G) relative to the harmonic spectra, is also nicely reproduced by the DTCF spectra.

Between 1000 and 1300 cm^{-1}, eight IR active P=O stretching and the P-O-H bending modes, three for **1-1** and five for **1-2**, are predicted by the harmonic analysis, while in the experimental spectrum only three bands, two intense bands (H and I in Figure 6.4) and one weaker band (J), are observed. This region is, again, better reproduced by the DTCF spectra.

In the region below 900 cm^{-1}, there are several bands related to wagging and rocking modes (harmonic analysis). The mode involving H atoms is broadened and smeared out at a simulation temperature above 140 K. Only the antisymmetric (K) and symmetric (L) stretching modes of P-OH bonds, are left, which is in good agreement with the experimental observation of peaks K and L.

The above analysis leaves bands D and E unassigned, as these cannot be attributed to normal modes of either structure **1-1** or **1-2**. Is there a third species responsible for these absorptions? The DTCF spectrum at 180 K indeed reproduces a broad feature centered at 3161 cm^{-1}, near the experimental peak E. This feature is also observed in the 140 K spectrum but with much less intensity. Interconversion between **1-1** and **1-2** involves considerable displacement of the water molecule across a nearly flat potential energy surface with a barrier of less than 7 kJ/mol. At 140 K, the cluster is mainly confined in the potential well of **1-1** or **1-2** and does not visit the transition region (**1-3**) much. Increasing the simulation temperature to 180 K leads to a different situation. The cluster spends considerably more time in the vicinity of **1-3**. This transition state region is loosely bound and thus favored by entropy. The clusters undergo large amplitude motion, and as a consequence vibrational frequencies associated with structure **1-3** contribute to the spectrum.

This assignment is further supported by MP2 harmonic analysis on **1-3**, which predicts this mode at 3220 cm^{-1} (Figure 6.4). Summarizing, these results indicate that peak E is due to the HBed O-H stretching mode of water in the transient structure **1-3**. Similar signatures of broken HB networks at elevated ion temperatures have been observed in Ar-tagged $Br^-(H_2O)_{2,3}$ complexes [12]. Note that the roaming water molecule observed in the present study is qualitatively different from the water migration reported for cold anion monohydrates in the excited OH stretching manifold [247]. Here, water migration occurs on the vibrational ground state potential and over larger distances, involving HB disruption and formation.

6.1.4 Conclusions: $H_2PO_4^- \cdot H_2O$

The IRMPD spectra of $H_2PO_4^- \cdot H_2O$ show evidence for isomerization even at cryogenic temperatures. Because the clusters undergo large amplitude motion over a small barrier, key aspects of the spectra cannot be interpreted within the framework of the harmonic approximation. AIMD simulations provide insight into these effects and qualitatively reproduce the experimental IRMPD spectra. The remaining differences can be attributed to approximations in the simulations, including the limited sampling time, the use of pseudopotentials and the neglect of nuclear quantum effects. Experimentally, the measured IRMPD intensities expectedly deviate from the linear absorption cross sections. The isomerization at low temperatures observed here may be indicative of a highly functional water network around dihydrogen phosphate and therefore it will prove important to also study the larger hydrated clusters, work that is currently in progress (see Figures C.1 and C.2 in Appendix C). Such studies can then also resolve the questions regarding the interconversion of $H_2PO_4^-(H_2O)_n$ to $PO_3^-(H_2O)_{n+1}$ that is predicted for $n > 1$.

6.2 Cubic Coupling between High- and Low-Frequency Modes in Nitrate-Water Clusters

6.2.1 Introduction

Nitrate ions in aqueous media play an important role in a wide range of environmental and biological processes. For example, the nitrate anion is the major chromophore in the Antarctic snow [248], one of the most abundant tropospheric ions and also a major constituent of sea salt and mineral dust aerosols [179, 249]. Therefore, a fundamental understanding of how nitrate ions are hydrated in the bulk [250] as well as at the air-aqueous interface [251] is of importance with respect to understanding atmospheric aerosol chemistry. Spectroscopic studies of anion-water clusters in the gas phase [15, 252–255], in general, and on nitrate-water clusters [57], in particular, play an important role in elucidating the nature of ion-water interactions at a molecular level, in the absence of counter ions, and of an extended solvation network.

Studies of other water-anion complexes [12, 247, 256, 257] have shown that there is a significant red-shift of the water O-H stretch vibration in the complexes compared to the gas-phase water monomer. In addition, in the case of $HCO_2^-\cdot H_2O$, $CH_3NO_2^-\cdot H_2O$ and $CH_3CO_2^-\cdot H_2O$, the vibrational spectra in the O-H stretching region display progressions of up to five members with observed spacings of about $80\,\mathrm{cm}^{-1}$. These progressions result from a large cubic force constant coupling of the O-H stretch and water rock degrees of freedom.

Robertson *et al.* [12] have found that for complexes adopting a single ionic hydrogen-bond motif (SIHB), the red-shift of the O-H stretch is well-correlated to the proton affinity of the anion. In contrast for the double ionic hydrogen bond motif (DIHB), the red-shift is about $200\,\mathrm{cm}^{-1}$ smaller than for SIHB complexes with similar proton affinities. Furthermore, $NO_2^-\cdot H_2O$ exhibits a SIHB structure, although $HCO_2^-\cdot H_2O$, $CH_3NO_2^-\cdot H_2O$ and $CH_3CO_2^-\cdot H_2O$ adopt DIHB structures. Therefore, it is not clear *a priori* which bonding motif would be adopted by the $NO_3^-\cdot H_2O$ complex. Anion photoelectron spectroscopy [255] as well as IRMPD experiments [57]

Chapter based on:
Vibrational Spectroscopy of the Water-Nitrate Complex in the O-H Stretching Region
N. Heine, E. Kratz, R. Bergmann, D. Schofield, K.R. Asmis, K.D. Jordan, and A.B. McCoy, *J. Phys. Chem. A* **2014**, 118, 8188 – 8197. DOI: 10.1021/jp500964j

in the fingerprint region (600 – 1800 cm^{-1}) are not conclusive, even though both favor the DIHB motif based on predictions from electronic structure calculations. However, the exact nature of the DIHB global minimum energy structure, either a symmetric C_{2v} isomer with two equivalent hydrogen bonds [258–260] or a slightly asymmetric variant of C_s symmetry, [57, 255, 261–263] remains unclear. Prior theoretical studies indicate that the global minimum of $NO_3^- \cdot H_2O$ is asymmetric but only 0.2-0.3 kJ/mol more stable than the C_{2v} transition state structure.

In the present study temperature-dependent vibrational spectra of the gas phase isotopologues $NO_3^- \cdot H_2O$, $NO_3^- \cdot D_2O$, and $NO_3^- \cdot HDO$ are reported in the O-H (and O-D) stretching region, obtained by employing temperature-dependent infrared multiphoton dissociation (IRMPD) spectroscopy. In order to aid in assigning the experimentally observed IRMPD spectra of $NO_3^- \cdot H_2O$, $NO_3^- \cdot D_2O$, and $NO_3^- \cdot HDO$, calculations of the vibrational spectra of these species were carried out, using model Hamiltonian approaches that allow for O-H (O-D) stretch-rock cubic coupling as well as for Fermi resonances with the water bend overtone. The calculations confirm that the situation is more complex for the nitrate-water system compared to the previously discussed complexes. The expectation is confirmed that the progressions in all three isotopologues is due to the water stretch-rock coupling. The additional features in the H_2O and D_2O cases, are identified as a Fermi resonance between the O-H (O-D) stretch modes and the water bend overtones.

6.2.2 Experimental and Computational Details

IRMPD experiments are carried out as described in Section 6.1.2 in the O-H stretching region. Nitrate-water complexes are produced from a 1 mM solution of HNO_3 (Fluka) in a 1:3 mixture of 15 MΩ·cm deionized water and acetonitrile. For the isotopologues, 1.5 mM solutions of 1.5 mmol/L DNO_3 in 1:3 deuterium oxide (both 99 atom % D, *Sigma Aldrich*) and acetonitrile are used. The deuterated solutions are prepared and stored under N_2-atmosphere. A typical cluster distribution of $NO_3^- \cdot (H_2O)$ and its isotopologues is shown in Figure 6.5.

The geometry optimizations and the calculations of the quadratic and cubic force constants were performed at the CCSD(T)/aug-cc-pVDZ [264–267] level of theory with the *CFOUR* package [268]. To examine the sensitivity of the geometry and harmonic frequencies to the basis set, additional calculations were carried out at the CCSD(T)/aug-cc-pVTZ,

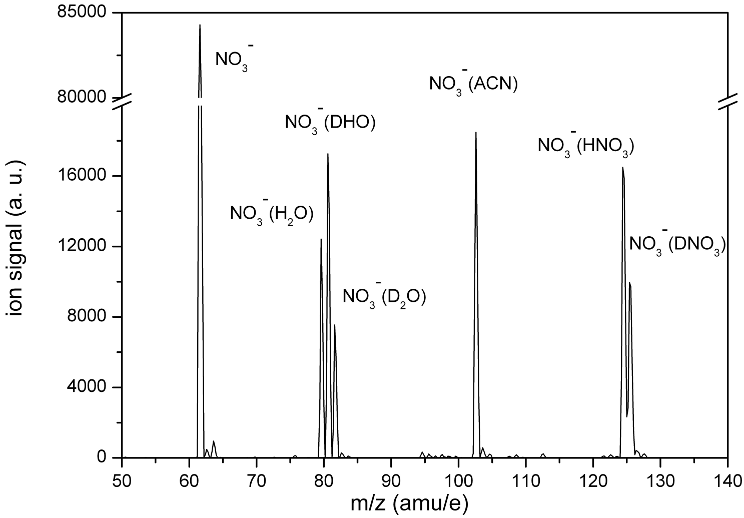

Figure 6.5: Quadrupole mass spectrum of ions formed by electrospraying a 1 mM solution of deuterated nitric acid in D_2O/acetonitrile. The spectrum has been optimized for $NO_3^-\cdot(D_2O)$. $NO_3^-\cdot H_2O$ and $NO_3^-\cdot$DHO complexes are formed by substitution reactions with trace amounts of H_2O in-between the capillary and the skimmer.

CCSD(T)-F12b [269]/VDZ-F12 [270], and CCSD(T)-F12b/VTZ-F12 levels of theory. The F12 calculations were carried out with the *Molpro* package [271] since *CFOUR* lacks the explicitly correlated F12 method. Transitions in the simulated spectra have Gaussian widths with a half-width of 15 cm^{-1}, close to that of the peaks in the experimental spectrum of the $NO_3^-\cdot H_2O$ complex obtained at $T = 15\,K$.*

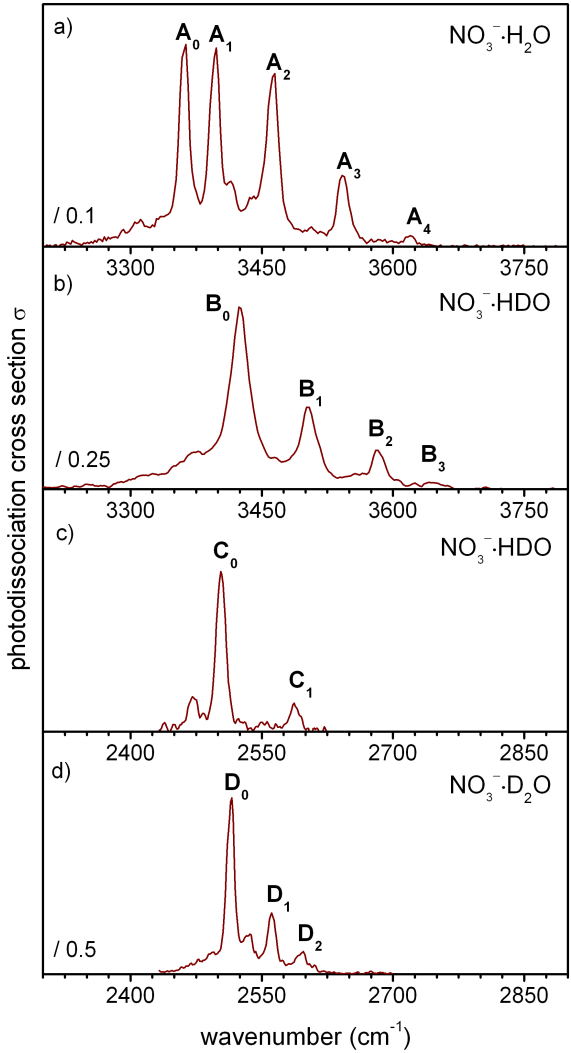

Figure 6.6: Experimental IRMPD spectra of the hydrogen-related isotopologues of the nitrate-water complex in the O-H and the O-D stretching region measured at an ion trap temperature of 15 K: a) $NO_3^-{\cdot}H_2O$, b-c) $NO_3^-{\cdot}HDO$, d) $NO_3^-{\cdot}D_2O$. See Table 6.2 for peak positions.

6.2.3 Results and Discussion

Experimental Spectra

15 K Spectra. Figure 6.6 shows an overview of the experimental IRMPD spectra of $NO_3^- \cdot H_2O$ and its hydrogen related isotopologues $NO_3^- \cdot D_2O$ and $NO_3^- \cdot HDO$, covering the O-H (3200 – 3800 cm^{-1}) and O-D (2300 – 2900 cm^{-1}) stretching regions. Band positions are listed in Table 6.2. The spectra are measured at an ion trap temperature of 15 K, and the only observed photofragment is NO_3^-. The energy of at least two photons is required to overcome the predicted dissociation limit (see below) and hence the IRMPD intensities plotted in Figure 6.6 may deviate from a linear absorption behavior.

The experimental IRMPD spectrum of cold $NO_3^- \cdot H_2O$ (see Figure 6.6a) shows a surprisingly rich structure in the hydrogen-bonded O-H stretching region (<3600 cm^{-1}) [254] and little or no signal in the regions of the symmetric (ν_s, 3657 cm^{-1}) and antisymmetric (ν_a, 3756 cm^{-1}) stretching vibrational frequencies of the free water molecule, [272] suggesting the exclusive presence of a double ionic hydrogen bond (DIHB) complex. For such a complex, harmonic calculations predict two bands in the O-H stretching region, originating from the symmetric and antisymmetric HB O-H stretching modes (Table 6.3). In contrast, at least five characteristic peaks are observed at 3363, 3398, 3464, 3542 and 3620 cm^{-1} in the experimental spectrum. These are labeled A_0 to A_4, respectively. A closer look reveals a weak background throughout the 3200 – 3650 cm^{-1} range and several smaller features. The observation of a series of peaks in-between 3363 and 3620 cm^{-1} suggest that the two O-H oscillators are coupled to one (or more) lower frequency modes. Indeed, the spectrum shows similarities with those reported earlier by Myshakin *et al.* [247] for Ar-tagged $CH_3NO_2^- \cdot H_2O$ and $CH_3CO_2^- \cdot H_2O$ and by Gerardi *et al.* [256], where this structure was assigned to a progression in the water rocking mode built on top of an O-H stretching fundamental. In the present case, the spectrum appears more complex, as peaks A_0 to A_4 are not equidistantly spaced, but separated by 35 cm^{-1} (A_1-A_0), 66 cm^{-1} (A_2-A_1), 77 cm^{-1} (A_3-A_2), and 78 cm^{-1} (A_4-A_3).

Further insight into the assignment of the IRMPD spectra can be gained by isotopic substitution. The IRMPD spectrum of cold $NO_3^- \cdot HDO$ in the

*Calculations have been performed by E. Kratz and D. Schofield in the groups headed by K.D. Jordan at the University of Pittsburgh and A.B. McCoy at The Ohio State University.

Table 6.2: Positions (in cm^{-1}) of the main bands observed in the IRMPD spectra of $NO_3^- \cdot H_2O$, $NO_3^- \cdot HDO$ and $NO_3^- \cdot D_2O$ shown in Figure 6.6.

$NO_3^- \cdot H_2O$	$NO_3^- \cdot HDO$	$NO_3^- \cdot D_2O$
3363 (A_0)	2503 (C_0)	2516 (D_0)
3398 (A_1)	2587 (C_1)	2561 (D_1)
3464 (A_2)	3423 (B_0)	2598 (D_2)
3542 (A_3)	3501 (B_1)	
3620 (A_4)	3583 (B_2)	
	3646 (B_3)	

O-H stretching region (see Figure 6.6b) shows a similar, but simpler and slightly blue-shifted progression (B_0 to B_3) with an origin at 3423 cm^{-1} (B_0). Peaks B_0 to B_3 (see Table 6.2) are more evenly spaced: 78 cm^{-1} (B_1-B_0), 82 cm^{-1} (B_2-B_1) and 63 cm^{-1} (B_3-B_2). A shorter progression of similar spacing (84 cm^{-1}) is also observed in the O-D stretching region (see Figure 6.6c) consisting of only two peaks at 2503 (C_0) and 2587 cm^{-1} (C_1). These observations are consistent with an assignment to progressions in the water rock mode (80 cm^{-1}), whose frequency is not expected to show a pronounced isotope-dependence, built on top of either the O-D or O-H stretching fundamental. They also suggest that the progression for $NO_3^- \cdot H_2O$ has an extra feature near the origin due to Fermi-type coupling to the water bend overtone $2\nu_b$ [273]. The origin of the more than twice as broad peaks in the O-H stretching region in the $NO_3^- \cdot HDO$ spectrum compared to the peaks observed in all the other spectra reported in Figure 6.6 remains unclear.

Finally, the IRMPD spectrum of cold $NO_3^- \cdot D_2O$ (see Figure 6.6d) looks similar to the $NO_3^- \cdot HDO$ spectrum in the O-D stretching region (see Figure 6.6c), but exhibits an additional band at 2561 cm^{-1} (D_1). Assuming similar rocking vibrational frequencies for the H_2O, HDO and D_2O complexes, peaks D_0 and D_2, separated by 82 cm^{-1}, correlate to bands C_0 ad C_1. They thus correspond to the origin and first member of the stretch-rock progressions, of which the one observed in the $NO_3^- \cdot D_2O$ spectrum lies 13 cm^{-1} higher in energy. This leaves peak D_1 unassigned, which is tentatively attributed to overtone excitation of the D_2O bending vibration.

Temperature Dependent Spectra. IRMPD spectra of hotter $NO_3^- \cdot D_2O$ and $NO_3^- \cdot H_2O$ complexes, measured at ion trap temperatures up to room temperature, are compared to the 15 K spectra, discussed above, in Figure 6.7. The ions probed in the 50 K IRMPD spectra appear only slightly hotter than those in the 15 K spectra. This finding supports the assumption, described in Section 3.4.2, that the present experimental procedure of filling and extracting the ions, using a continuous buffer gas flow, allows for efficient thermalization of the ions slightly below 50 K, but not completely down to the lowest possible ion trap temperature of 15 K. At 100 K, the observed features in the IRMPD spectra significantly broaden and hot bands (to the red of the origins) gain in intensity. At the highest temperatures measured, 200 K for $NO_3^-{\cdot}D_2O$ and 300 K for $NO_3^-{\cdot}H_2O$, the discrete features cannot be distinguished anymore and a continuous absorption is observed from 2300 to 2700 cm^{-1} ($NO_3^-{\cdot}D_2O$) and 3150 – 3700 cm^{-1} ($NO_3^-{\cdot}H_2O$). At these ion trap temperatures a new feature is observed in the free O-D and free O-H stretching regions (indicated by an arrow), respectively, signaling the breaking of one of the two hydrogen bonds and formation of SIHB complexes.

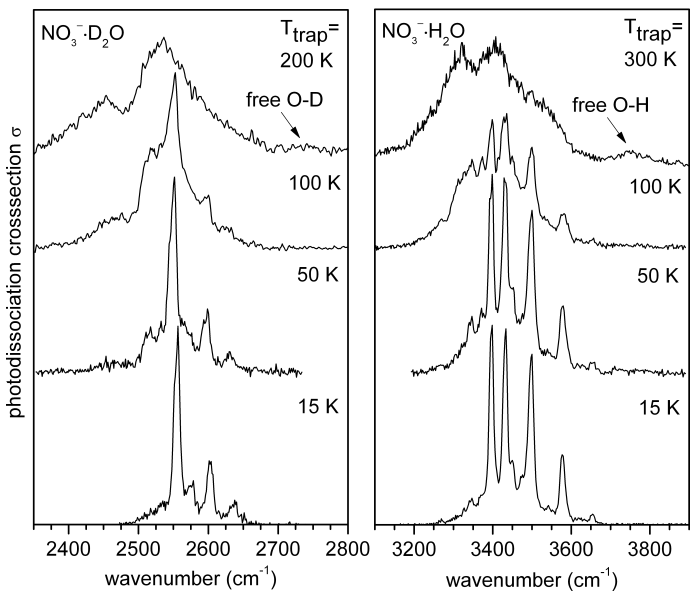

Figure 6.7: Experimental IRMPD spectra of $NO_3^-{\cdot}D_2O$ (left) and $NO_3^-{\cdot}H_2O$ (right) measured at ion trap temperatures of 15, 50, 100, 200 and 300 K. The 15 K spectra are the same as shown in Figure 6.6.

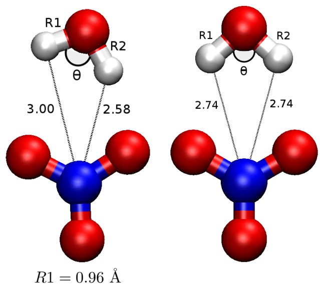

Analysis

Table 6.3: Selected harmonic frequencies and cubic force constants (cm^{-1}) of $NO_3^-{\cdot}H_2O$ and all H/D isotopic substituted complexes.

Harmonic frequencies				
Mode	$NO_3^- \cdot H_2O$	$NO_3^- \cdot D_2O$	$NO_3^- \cdot HDO$	$NO_3^- \cdot DHO$
ω_s	3799.85	2763.94	2760.46	3797.68
ω_l	3571.29	2591.82	3571.60	2597.64
ω_b	1713.01	1246.16	1541.49	1476.68
ω_r	84.09	76.34	77.91	82.33
Cubic force constants				
Type	$NO_3^- \cdot H_2O$	$NO_3^- \cdot D_2O$	$NO_3^- \cdot HDO$	$NO_3^- \cdot DHO$
ω_{ssr}	-105.65	-78.54	-76.57	-106.10
ω_{llr}	242.42	169.11	234.97	174.47
ω_{sbb}	-99.33	-55.48	15.01	-268.60
ω_{lbb}	151.72	104.49	314.03	-12.39

Figure **??** shows the two most stable CCSD(T)/aug-cc-pVDZ minimum-energy structures predicted for the $NO_3^-{\cdot}H_2O$ complex, containing either a double donor or a single donor water molecule. In the global minimum-energy structure the water molecule donates two HBs to the NO_3^--moiety, a shorter (2.58 Å) and a longer one (3.00 Å), resulting in a structure of C_s symmetry with asymmetric hydrogen-bonds. On the other hand, symmetric HBs are found for $HCO_2^-{\cdot}H_2O$, $CH_3NO_2^-{\cdot}H_2O$ and $CH_3CO_2^-{\cdot}H_2O$ complexes [247, 256]. However, the C_{2v} transition state for conversion in-

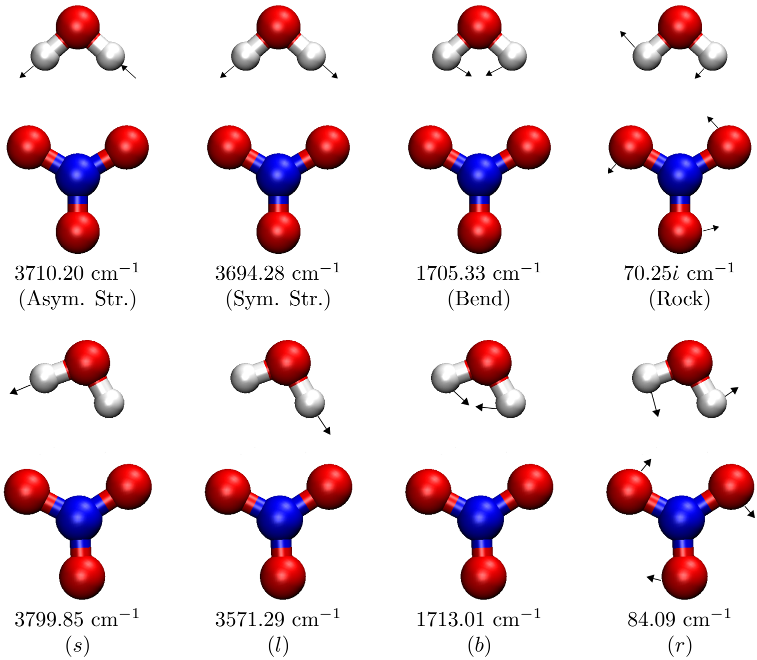

Figure 6.8: CCSD(T)/aug-cc-pVDZ harmonic frequencies of the four key vibrational modes of $NO_3^- \cdot H_2O$. Results for the C_{2v} potential energy minimum are shown at the top of the figure and those for the C_s transition state structure are shown at the bottom. For the C_{2v} structure the depicted normal modes are the antisymmetric stretch, symmetric stretch, water bend (b), and intermolecular rock (r), with the rock mode having an imaginary frequency. For the C_s minimum, the two water stretch vibrations are labeled as the long stretch (l) and short stretch (s), where long and short refer to the O-H bond lengths. The bend and rock modes are labeled as (b) and (r), respectively.

between the two equivalent C_s structures of $NO_3^- \cdot H_2O$ is calculated to be only +0.1 kJ/mol above these minima, in agreement with previous results [57]. A common aspect of the geometries of the $NO_3^- \cdot H_2O$, $HCO_2^- \cdot H_2O$, $CH_3NO_2^- \cdot H_2O$ and $CH_3CO_2^- \cdot H_2O$ complexes is the small water H-O-H angle, θ, which is 97.8° for the $NO_3^- \cdot H_2O$ complex. The second lowest minimum lies +11.5 kJ/mol higher in energy, and is considerably further distorted away from the C_{2v}-symmetry. As a result of a larger H-O-H angle, one of the HBs is disrupted and the complex effectively adopts a SIHB motif. The DIHB complex has a predicted binding energy of 67 kJ/mol. Thus, the absorption of multiple photons is required for dissociation.

Figure 6.8 shows the four key vibrational modes that are important for understanding the structure in the O-H stretch region of the $NO_3^- \cdot H_2O$ spectrum. These are the symmetric (s) and antisymmetric (a) O-H stretches, the water bend (b), and the water rock (r). The vibrations and their frequencies are shown for the C_{2v} (top) and C_s structures (bottom). The two O-H stretch modes are localized in the C_s structure, and the l and s labels refer to the long and short O-H bonds, respectively. The calculated harmonic frequencies of these modes and the relevant cubic force constants for all isotopic substituted complexes are listed in Table 6.3.

Effective Hamiltonian. First, a simplified model is used to explain the experimental spectra. Briefly, the employed model is based on the adiabatic "stretch-rock" model, proposed by Myshakin *et al.* [247]. In their study of the $CH_3NO_2^- \cdot H_2O$ and $CH_3CO_2^- \cdot H_2O$ complexes, Myshakin *et al.* introduced a model Hamiltonian employing harmonic O-H stretch and water rock degrees of freedom together with a cubic coupling of these normal coordinates. The cubic coupling accounts for the symmetric and antisymmetric O-H stretch normal coordinates together with the water rock normal coordinate, hence "stretch-rock" model. The model was quite successful at reproducing the observed vibrational spectra in the O-H stretch region of $CH_3NO_2^- \cdot H_2O$ and $CH_3CO_2^- \cdot H_2O$. Here, it is further extended to account for both O-H (O-D) stretch local modes. Furthermore, the extended model accounts for the highly anharmonic rock potential, that was calculated for $NO_3^- \cdot H_2O$ (see Appendix C for details).

Figures 6.9, 6.10 and 6.11 compare the experimental IRMPD spectra (trace a) to the effective Hamiltonian calculations (trace b). Qualitatively, this method can reproduce the trends in the experimental spectra except for the origin of the O-H (O-D) stretch-rock progression, which is significantly blue-shifted in the calculations in all cases, and the extra features that are due to Fermi resonances, which are not accounted for by the model.

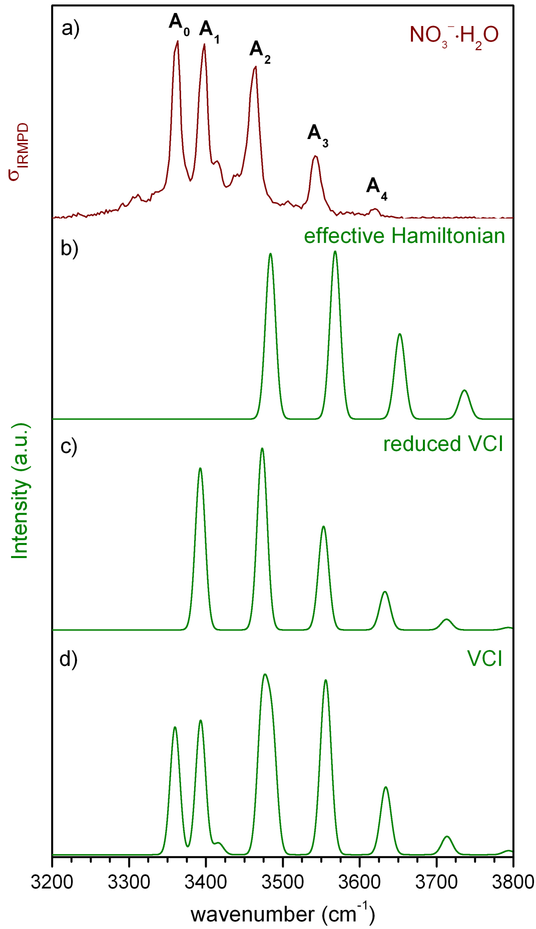

Figure 6.9: Comparison of experimental and calculated vibrational spectra of $NO_3^-\cdot H_2O$ at 15 K in the OH stretching region. a) Experimental spectrum; b) spectrum generated using the effective Hamiltonian given by Equation C.11 and with intensities calculated using Equation C.4, both given in Appendix C; c) spectrum calculated with VCI employing the ω_{llr} force constant (Equation C.14, Appendix C); d) spectrum calculated with VCI employing ω_{llr} and ω_{lbb} force constants (Equation C.14, Appendix C). The calculations for c) and d) employed scaled frequencies as described in the text.

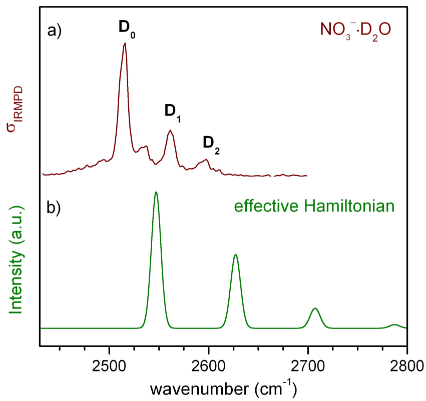

Figure 6.10: Comparison of experimental IRMPD spectra of NO_3^-·HDO to simulated spectra, generated using the effective Hamiltonian given by Equation C.11 and with intensities calculated using Equation C.4, both given in Appendix C.

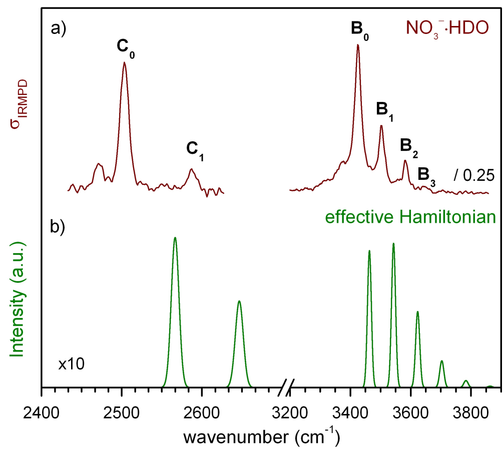

Figure 6.11: Comparison of experimental IRMPD spectra of NO_3^-·HDO to simulated spectra, generated using the effective Hamiltonian given by Equation C.11 and with intensities calculated using Equation C.4, both given in Appendix C.

Specifically, the model predicts red-shifts in the origin of the O-H stretch-rock progression about two times larger than those found for O-D, which is in qualitative agreement with experimentally observed isotopic shifts.

While the separation of the peaks in the stretch-rock progression is relatively good captured for $NO_3^- \cdot H_2O$ (Figure 6.9b) and $NO_3^- \cdot HDO$ (Figure 6.11), in the IRMPD spectrum of $NO_3^- \cdot D_2O$ (Figure 6.10), the spacing is overestimated by a factor of two. It is likely, however, that the bend overtone couples to the O-D stretch and that peak D_1 is due to a Fermi resonance, which appears between the $n_r = 0$ (D_0) and $n_r = 1$ (D_2) O-D stretch-rock transitions (n_r gives the number of quanta in the water rock).

The agreement between the IRMPD spectra and those of the model Hamiltonian calculations is satisfactory; however, the model seems to incorrectly predict the relative shifts of the isotopologues. For instance the O-H stretch vibration of $NO_3^- \cdot H_2O$ is blue-shifted above the $NO_3^- \cdot HDO$ O-H stretch. This is likely due to the influence of the stretch-bend coupling, which is strongest for the H_2O and D_2O isotopologues. Although the model Hamiltonian predicts that the stretch-rock progression is shorter for $NO_3^- \cdot D_2O$ than for $NO_3^- \cdot H_2O$ in agreement with the experiment, the lengths of both progressions are overestimated. In part, this reflects the inadequacy of this model to calculate the relative intensities.

Vibrational CI. Although the effective Hamiltonian approach gives already a qualitatively satisfactory description of the experimental spectra, a more sophisticated treatment is required to include the participation of Fermi resonances with the water bend overtone. To accomplish this, vibrational configuration interaction calculations (VCI) were performed within the local mode approximation using an extended Hamiltonian, that accounts for the H-O-H bend, and couples the O-H stretch modes to the rock and the bend modes (Equation C.14 in Appendix C).

Since the strength of the Fermi resonance between the O-H stretch and H-O-H bend overtone strongly depends on the values of the fundamental frequencies, scaled frequencies were employed to correct for anharmonic interactions not included in the model. The frequencies used for $NO_3^- \cdot H_2O$ are 3485 and 1700 cm^{-1} for the O-H stretch and H-O-H bend modes, respectively. These frequencies were chosen to match the origin of the progression and to bring the bend overtone into near degeneracy with the origin of the rock progression accompanying excitation of the O-H stretch fundamental of $NO_3^- \cdot H_2O$. A value of 80 cm^{-1} was chosen for the water rock frequency as that closely corresponds to the observed spacings (in the absence of Fermi resonances). The cubic force constants employed are listed in Table 6.3.

The results of the VCI calculations for $NO_3^- \cdot H_2O$ are shown in Figure 6.9 c) and d). Figure 6.9 c) shows the vibrational spectrum obtained neglecting the Fermi resonance with the water bend overtone. This spectrum is similar to that obtained with the effective Hamiltonian (Figure 6.9 b). Figure 6.9 d) shows the spectrum calculated including the Fermi resonance with the bend overtone. The first member of the rock progression in Figure 6.9c) is now replaced by a pronounced doublet. An interesting feature of the calculated spectrum is the appearance of a weak feature near $3415\,cm^{-1}$. Based on an analysis of the CI coefficients, this extra peak results from both O-H stretch local modes interacting with the bend overtone simultaneously. The calculated spectrum is in good agreement with that measured experimentally in terms of the locations of the peaks, but less successful at reproducing the experimentally observed intensity distribution. This most likely reflects the need to consider the highly anharmonic nature of the rock motion associated with the ground state potential energy surface when calculating the intensities.

6.2.4 Conclusions: Nitrate-Water

IRMPD spectroscopy of cryogenically cooled water-nitrate complexes combined with anharmonic vibrational calculations reveals strong anharmonic coupling in the O-H stretch region of the IR spectrum of $NO_3^- \cdot H_2O$ and its isotopologues. This anharmonicity gives rise to a progression in the water rock vibration and to a strong Fermi resonance of the O-H stretch with the water bend overtone in the H_2O and D_2O complexes. The assignment is confirmed by effective Hamiltonian and VCI calculations. As found earlier for $HCO_2^- \cdot H_2O$, $CH_3NO_2^- \cdot H_2O$ and $CH_3CO_2^- \cdot H_2O$, the water stretch-rock coupling causes a red-shift in the origin of the rock progression. Interestingly, in the absence of this red-shift, the energy gap between the water bend overtone and the O-H stretch fundamental would be too great for there to be significant mixing between the O-H stretch and bend overtone.

$NO_3^- \cdot H_2O$ belongs to the class of anion-water complexes with a double ionic hydrogen bond motif, which is consistent with the structures found for the $HCO_2^- \cdot H_2O$, $CH_3NO_2^- \cdot H_2O$ and $CH_3CO_2^- \cdot H_2O$ complexes. But in contrast to these clusters, the adiabatic ground state rock potential is highly anharmonic in the case of $NO_3^- \cdot H_2O$. Increasing the internal energy of $NO_3^- \cdot H_2O$, close to room-temperature, leads to the rupture of one hydrogen-bond, and the DIHB is replaced by a SIHB.

Chapter 7

Summary and Future Perspectives

IRPD spectroscopy of mass-selected and thermalized clusters in the gas phase is a generally applicable tool for determining their geometric structure. In the work presented here four goals were to be achieved. Firstly, the development and implementation of new experimental techniques in order to study systems under conditions that were not accessible before. Secondly, the application of these techniques to protonated water clusters, in particular, unraveling the individual contribution of multiple isomers to the IR spectra. Thirdly, gaining new structural information of clusters that are involved in the early steps of aerosol formation using the example of microsolvated nitrate/nitric acid/water clusters, adding solvent molecules in a stepwise fashion. Lastly, anharmonic effects in the IR spectra of small deprotonated acid clusters were identified using state-of-the-art theoretical approaches. The following section gives a brief summary, followed by future research directions.

7.1 Summary

The successful development and implementation of a new experimental setup, which allows for the generation of a wide range of cluster ions is shown in Chapter 3. In particular, the apparatus represents a novel approach to investigate highly hydrated ions under well-defined conditions. Established gas-phase techniques such as electrospray ionization and quadrupole mass filtering are combined with a buffer-gas cooled cryogenic ion trap and a double-focusing reflectron-time-of-flight mass spectrometer. The ion trap is optimized for a high ion capacity, which effectively reaches the theoretical space charge limit (Section 3.4.2). The lowest achievable ion temperature is subsequently characterized using the partially rotationally resolved spectrum of ${NH_4}^+ \cdot H_2O$ under varying conditions. The dTOF-MS allows for IR/IR double-resonance spectroscopy, a recently developed method that makes use of two IR lasers in order to spectroscopically separate signatures from multiple isomers.

This technique is applied first to measure isomer-specific IR^2MS^2 spectra of the Eigen-type and Zundel-type conformers of the protonated water hexamer across nearly the entire IR spectral range (260 – 3900 cm^{-1}) in Chapter 4. Comparison to *ab initio* molecular dynamics simulations provides insight into the mechanism responsible for the characteristically broad IR absorptions attributed to hydrogen-bonded O-H stretching modes. Furthermore, the hydrogen-bond stretching vibrations in protonated water clusters in the terahertz region (<400 cm^{-1}) are observed for the first time. This study was then extended to protonated water clusters $H^+(H_2O)_n$, with n = 5,7-10, addressing the question of how the number of isomers evolves with the size of the hydration shell. For the protonated water heptamer, $H^+(H_2O)_7$, four isomers are assigned and their contributions to the IR spectrum could be isolated. In contrast, for the even larger clusters the presence of mainly one isomer is confirmed (Chapter 4). Protonated water clusters serve as model system for studying the mechanism of proton transfer in the macroscopic system. These measurements are not only crucial for benchmarking ab initio calculations, but also allow for new insights into the IR spectroscopy of $H^+(aq)$ and will ultimately contribute to a better understanding of proton transport and hydrogen bond dynamics in aqueous solution, as they provide fundamental insights into the structure of the water network and the accommodation of the excess charge within this network.

Chapters 5 and 6 describe the early steps of acid solvation as a function of cluster size. In Chapter 5 the structure of the atmospherically-relevant nitrate/nitric acid/water clusters are studied. In particular, the solvation behavior upon addition of multiple acid or water molecules. These experiments follow how the hydrogen-bonded solvent network around the anion evolves, one solvent molecule at a time. The study shows that the spectrum of the smallest cluster, hydrogen dinitrate, is distinctly different from the spectra of the larger clusters. This is the result of strong hydrogen-bonding, which effectively leads to an equally shared proton ($O_2NO^- \cdots H^+ \cdots ONO_2^-$), an arrangement that is surprisingly not disrupted by addition of a single water molecule. Only additional solvation with either more water or acid molecules weakens the hydrogen bond network and leads to the formation of the asymmetric $O_2NO^- \cdots$·H-$ONO_2(HNO_3)_{m-1}$ motif. Consequently, the proton is localized near one of the nitrate cores, effectively forming HNO_3 hydrogen-bonded to NO_3^-. This chapter also demonstrates that the IR spectra of the small hydrated clusters show a strong resemblance to the thin film results already upon addition of the first eight water molecules. Hence, the structure of the gas phase clusters has nearly converged to this of the condensed phase. Furthermore, this chapter provides excellent examples for the phenomena of "IRMPD transparent" modes in the IRMPD spectrum.

Chapter 6 also deals with the first solvation step of deprotonated acids, but primarily focuses on unraveling different challenges that are connected to the IRPD studies of hydrogen-bonded clusters in the gas phase. It is demonstrated that next to the presence of different isomers, also anharmonic effects can complicate an unambiguous assignment of spectral features. The studied systems exhibit rather complex vibrational spectra, requiring sophisticated anharmonic calculations for their assignment. The spectrum of $H_2PO_4^- \cdot H_2O$ is characterized by significantly broadened bands in the HB O-H stretching region. The comparison to AIMD simulations reveals that the water molecule undergoes large amplitude motion, even at low internal temperatures. The anharmonic effects of the low-barrier isomerization reaction on the infrared intensities can be qualitatively captured by the dipole time correlation function. In contrast, the spectrum of the singly-hydrated nitrate anion, exhibits additional sharp spectral features. These can be explained by comparison to vibrational configuration interaction (VCI) calculations. Origin of the complex pattern in the spectrum is a strong anharmonic coupling between the O-H stretching fundamental and low-frequency modes. Additionally, the spectra of $NO_3^- \cdot H_2O$ and $NO_3^- \cdot D_2O$ display a strong peak that does not derive from the water rock progression but results instead from a Fermi resonance between the O-H (O-D) stretch and H-O-H (D-O-D) bend overtone.

7.2 Future Perspectives

The new FHI free electron laser opens new opportunities to study atomic and molecular clusters, as well as biomolecules, in the gas phase and at the boundary to liquid phase. Present limits can be pushed towards studying larger, more complex systems and the underlying fundamental physical and chemical processes. The now on-site available wide range from 200 – 4000 cm^{-1} (FEL/OPO) in combination with the new experimental techniques offers a unique opportunity to extend the ongoing research but also to study new perspectives. In particular, the significantly larger photon fluence provided by the FEL enables efficient optical pumping even of weak IR active modes. This is especially interesting in the ranges around 2000 cm^{-1} and $<$1000 cm^{-1}, where the readily-available tabletop IR systems have weak points concerning the fluence.

Technical Design. In order to further extend the performance of the new apparatus, several improvements are planned. A higher signal intensity can be achieved by improving the design of the nanospray. For instance, the capillary inlet of the nanospray ion source represents a major bottleneck for an efficient ion transfer. The maximum ion transmission can thus be enhanced by implementing a hydrodynamic funnel interface as suggested in Ref. [274]. The thermalization of the ion temperature in the RET can be enhanced by two modifications: 1) The design of the ion guide facilitates pre-bunching of continuous ion sources like the nanospray source. The coincidental arrival of one compact ion packet in the ion trap will consequently lead to a more effective thermalization owing to a significantly reduced spread of the residence time in the trap. 2) Insertion of the buffer gas into the ion trap using a short, defined gas pulse at the beginning of the trapping cycle [146], in order to prevent collisional excitation upon extraction.

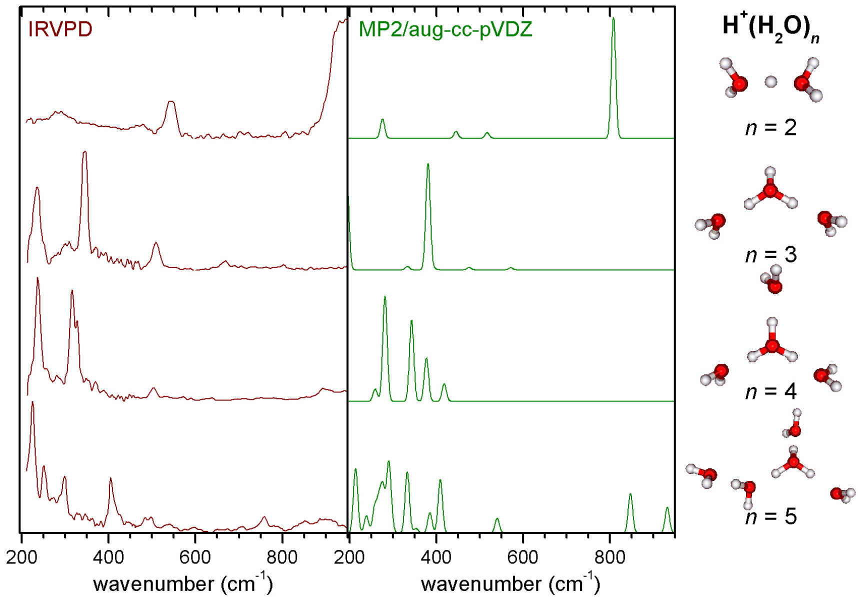

Figure 7.1: IRPD spectra of $H_2(H_2O)_n$, with n = 2-5, compared to MP2/aug-cc-pVDZ calculations.

Where is the proton? Concerning protonated water clusters, further steps towards the condensed phase and to resolve the latest discussions, regarding the location of the proton and the structure of the small clusters, have very recently been achieved. The new triple mass spectrometer was used in combination with the FHI FEL to measure protonated water clusters in the Terahertz region over a size range from $n = 2$ to 28. Figure 7.1 shows IRPD spectra compared to MP2 simulations of selected D_2-tagged clusters in a region from 220 to 1000 cm^{-1}, probing the translational and librational modes of water. All spectra for $n < 5$ are in good agreement with an Eigen-type structure, as indicated by previous measurements in the O-H stretching region and below.

Furthermore, comparison to anharmonic calculations, studies including IR^2MS^2 measurements and deuteration experiments are planned, and will yield deeper insight into the discussed topics.

Towards Aerosols. The new experimental setup allows for studying significantly larger systems. The presented research can thus be extended up to nanosize particles in order to unravel the process of nucleation. Furthermore, these studies can be followed in dependence of atmospherically more relevant temperatures, *i.e.* in a range from 210 to 320 K. Comparison to the corresponding cold spectra can yield detailed information about structure and growth.

Recently, volatile organic compounds (VOC) have been shown to contribute to new particle (aerosol) formation. VOCs are believed to interact with inorganic aerosols (*e.g.* nitrate/nitric acid aerosols) to form secondary organic aerosols (SOA). SOA formation is a great source of uncertainty in climate modeling. The new instrument allows to follow the formation, growth and aging of these particles at a molecular-level, by combining kinetics studies, which can be easily carried out in the ring electrode ion trap, with structural investigation. Particularly attractive is the combination with an UV laser in order to study the photochemistry of these systems.

Additional temperature-dependent and isomer-selective measurements may add valuable pieces of information to the currently primarily mass spectrometric investigations. These can be used, in general, to obtain a better understanding of air quality and climate, and in particular to improve estimations of aerosol climate forcing.

Appendix A

Protonated Water Cluster

Computational Details*

MP2 numbers presented here were calculated using TURBOMOLE V6.2 [275] and QZVPP basis sets. The six internal orbitals were kept frozen, the RI approximation was used, and other settings were kept standard. Density-functional theory (DFT) simulations were calculated using the PBE exchange correlation functional corrected with a $C_6\,[n]/R^6$ term (as proposed in Ref. [171]) in order to account for van der Waals dispersion interactions, which we call PBE+vdW. The calculations were performed with the all-electron, localized basis program package FHI-aims [169]. Tight settings are used for the numeric atom-centered orbital basis sets and integration grids (see Ref. [169] for further details). Anharmonic IR spectra were calculated according to Ref. [276],

$$I \propto \omega^2 \int_0^\infty dt\, \langle \mu(t)\mu(0) \rangle\, e^{i\omega t}, \tag{A.1}$$

where μ is the dipole moment of the molecule, obtained as the first moment of the electronic density. The MP2 and PBE+vdW energetics agree well, as shown in Table A.1.

*Calculations have been performed by Dr. M. Rossi in the group headed by Prof. V. Blum at the Theory Department of the Fritz Haber Institute.

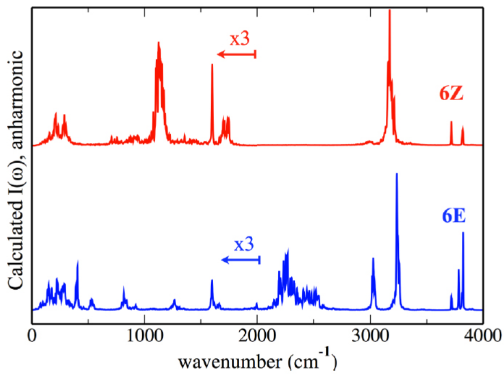

Figure A.1: Calculated anharmonic IR spectra (PBE+vdW, <T> = 50 K) of the bare **6Z** and **6E** geometries of $H^+(H_2O)_6$. Below 2000 cm^{-1} the intensities are multiplied by three for better visualization. Spectra are normalized to one for the intensity of the highest peak.

Table A.1: MP2 and PBE+vdW relative energies ΔE, and zero point energy corrected relative energies ΔE_{ZPE}, of the **6Z**, **6Z**$\cdot H_2$, **6E** and **6E**$\cdot H_2$ geometries of $H^+(H_2O)_6$ and $H^+(H_2O)_6 \cdot H_2$.

Method	System	ΔE (kcal/mol)	ΔE_{ZPE}(kcal/mol)
MP2	**6Z**	0.0	0.0
	6E	-0.3	0.9
PBE+vdW	**6Z**	0.0	0.0
	6E	-0.3	0.5
MP2	**6Z**$\cdot H_2$	0.0	0.0
	6E$\cdot H_2$	-0.4	1.0
PBE+vdW	**6Z**$\cdot H_2$	0.0	0.0
	6E$\cdot H_2$	-0.4	0.4

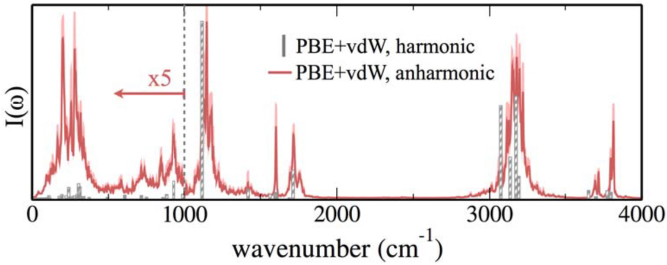

Figure A.2: Calculated harmonic (grey) and anharmonic (red) IR spectra (PBE+vdW, <T>=50 K) of the **6Z**·H_2 isomer. The anharmonic spectrum is obtained from an average over four AIMD runs of 10 ps each. The light shaded area corresponds to the statistical error (standard deviation divided by the square root of the number of measurements) of the average of the intensities. Below 1000 cm^{-1} the anharmonic intensities were multiplied by five for a better visualization.

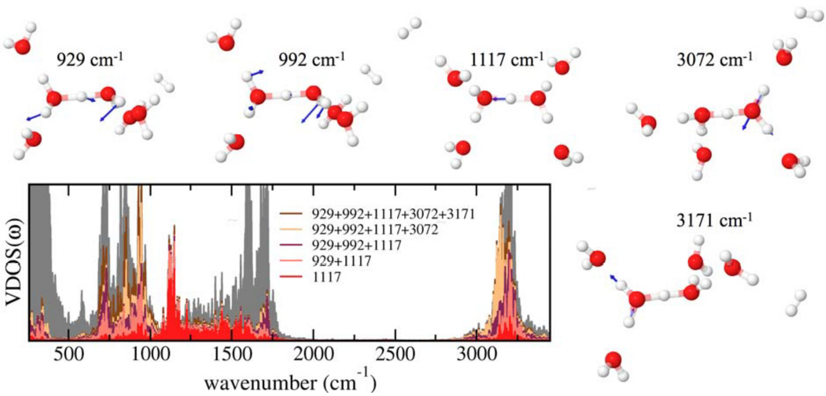

Figure A.3: Full VDOS of the **6Z**·H_2 isomer (grey) calculated from a 20 ps long AIMD PBE+vdW trajectory (<T>=50 K). In red, salmon, purple, yellow, and brown the sum of the PVDOS in specific normal modes of vibration, labeled in the figure. The peak just below 1000 cm^{-1} owes its full intensity to a coupling between several modes. The vibrations corresponding to the normal modes in question are shown around the plot.

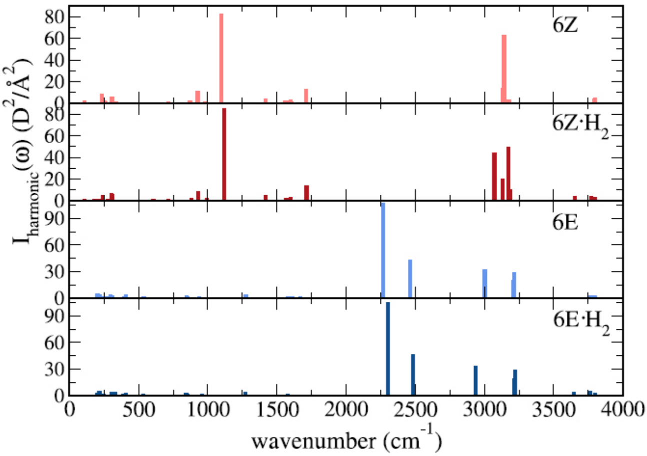

Figure A.4: Visualization of the harmonic frequencies (PBE+vdW, FHI-aims tight settings, not scaled).

Appendix B

Microsolvation of Nitrate-Nitric Acid Clusters

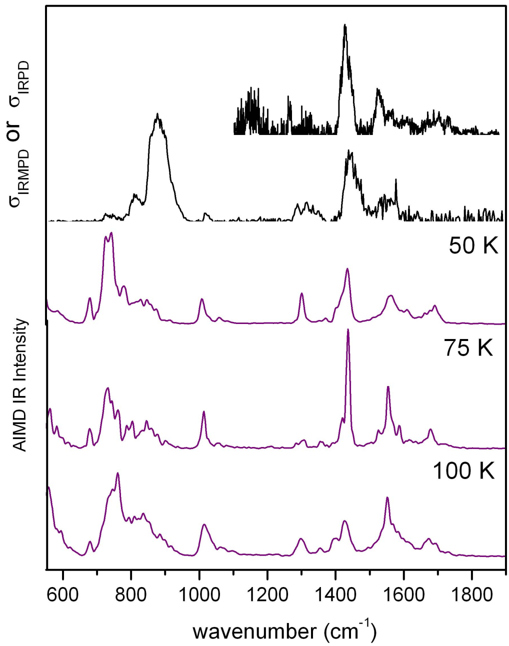

Figure B.1: Comparison between experimental IRPD spectra of $NO_3^-(HNO_3)\cdot H_2$, $NO_3^-(HNO_3)$ and anharmonic IR spectra of for $NO_3^-(HNO_3)$, obtained from 10 PBE+vdW AIMD simulations of 8 ps at 50, 75 and 100 K.*

*Calculations have been performed by Dr. M. Rossi and F. Schubert in the group headed by Prof. V. Blum at the Theory Department of the Fritz Haber Institute.

Table B.1: B3LYP/aug-cc-pVTZ structures (including symmetry) and relative SCF energies without (ΔE) and with vibrational zero point energy (ΔE_{ZPE}) derived from scaled (0.968) harmonic frequencies of low energy minima for $NO_3^-(HNO_3)$.

Symbol	Symmetry	ΔE (kJ/mol)	ΔE_{ZPE}(kJ/mol)
1w0a (02)	C_S	0.0^a	0.0^b
1w0b (03)	C_1	0.2	0.07

^{a} ΔE = -561.293307 a.u., ^{b} ΔE_{ZPE} = -561.255944 a.u.

Table B.2: B3LYP/aug-cc-pVTZ structures (including symmetry) and relative SCF energies without (ΔE) and with vibrational zero point energy (ΔE_{ZPE}) derived from scaled (0.968) harmonic frequencies of low energy minima for $NO_3^-(HNO_3)(H_2O)_1$.

Symbol	Symmetry	ΔE (kJ/mol)	ΔE_{ZPE}(kJ/mol)
1w1a (02)	C_S	0.0^a	0.0^b
1w1b (02)	C_1	3.6	0.17
1w1c (02)	C_1	0.2	0.35
1w1d (02)	C_1	0.3	0.45
(12)	C_S	2.2	0.53
(08)	C_1	2.2	0.57
1w1e (07)	C_S	2.2	0.60
(17)	C_1	2.3	0.66
(05)	C_1	2.3	0.81
1w1f (06)	C_1	3.8	1.4
1w1g (04)	C_1	3.7	2.0

^{a} ΔE = -637.738867 a.u., ^{b} ΔE_{ZPE} = -637.6764602 a.u.

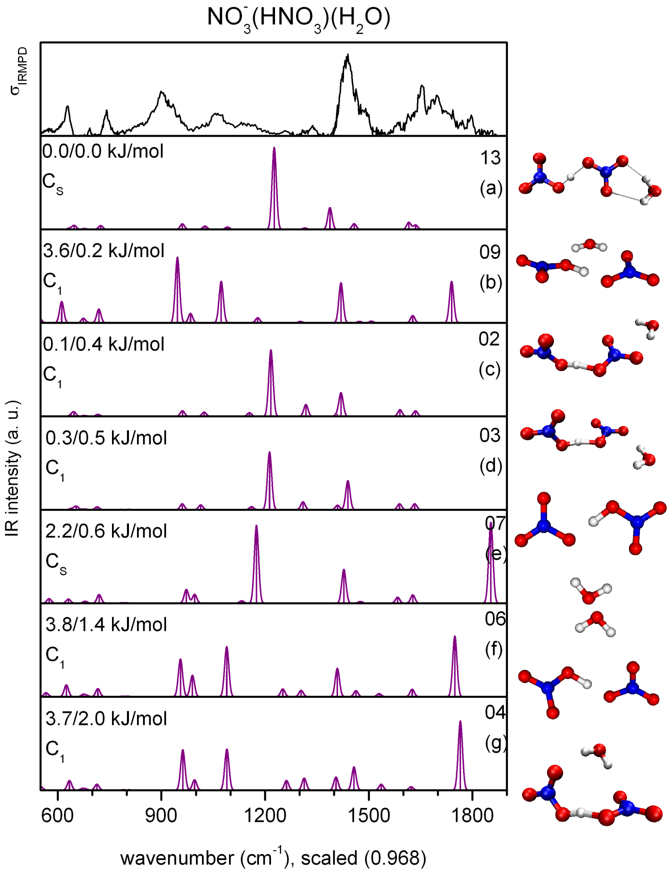

Figure B.2: Comparison between experimental IRPD spectra of and simulated IR intensities of $NO_3^-(HNO_3)(H_2O)_1$, calculated at the B3LYP/aug-cc-pVTZ level of theory.

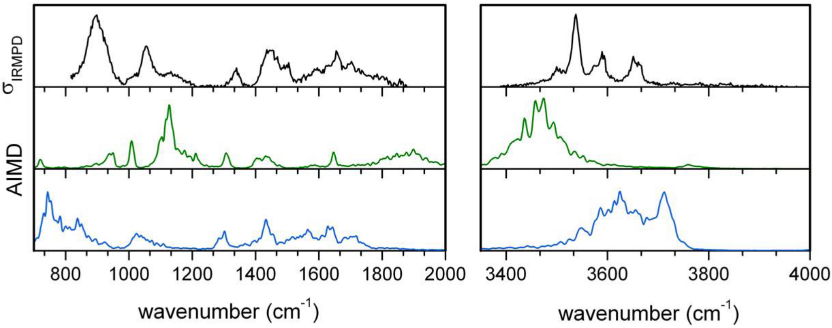

Figure B.3: Comparison between experimental IRPD spectra of $NO_3^-(HNO_3)$ and anharmonic IR spectra, obtained from 10 PBE+vdW AIMD simulations of 8 ps at 75 K, of the planar global minimum (green trace, **1w1a**) and the bridged (blue trace, **1w1b**) structures. The equally spaced progression in the O-H stretching region indicates either the presence of a second isomer or an anharmonic coupling of high- and low- frequency modes, as it is the case for $NO_3^-(H_2O)$, described in Chapter 6.2.

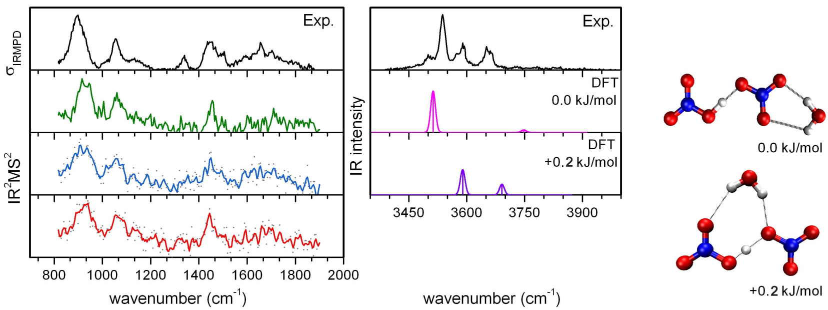

Figure B.4: IRPD spectrum (black trace) and IR^2MS^2 spectra of $NO_3^-(HNO_3)(H_2O)$, probed at 3537 (green), 3589 (blue), and 3653 cm^{-1} (red). All spectra are measured with the 6 K ion-trap triple mass spectrometer and with the FHI free electron laser (800 – 1900 cm^{-1}) or double OPO (3390 – 3985 cm^{-1}). All IR^2MS^2 spectra are identical within the experimental uncertainty.

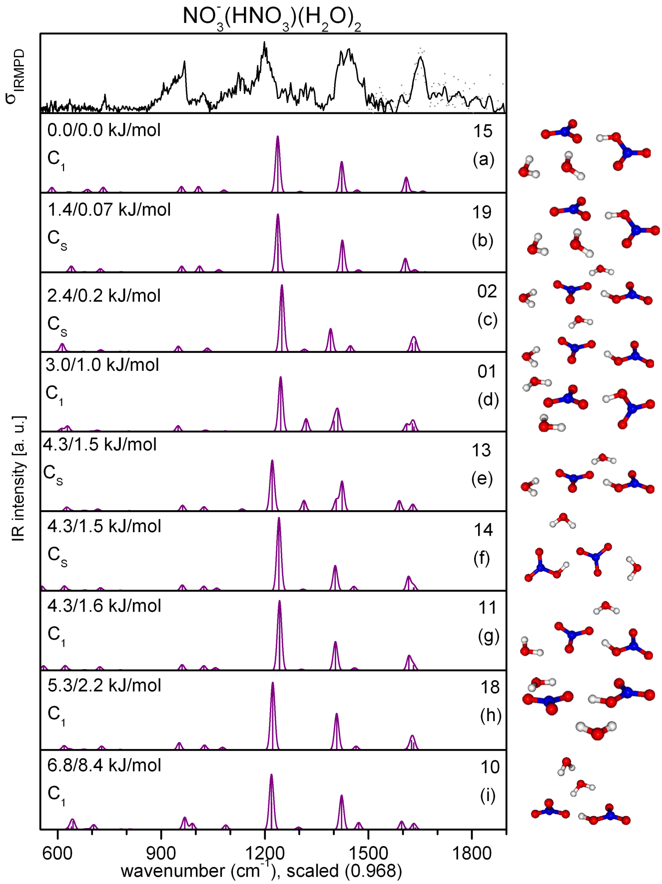

Figure B.5: Comparison between experimental IRPD spectrum and simulated IR intensities of $NO_3^-(HNO_3)(H_2O)_2$, calculated at the B3LYP/aug-cc-pVTZ level of theory.

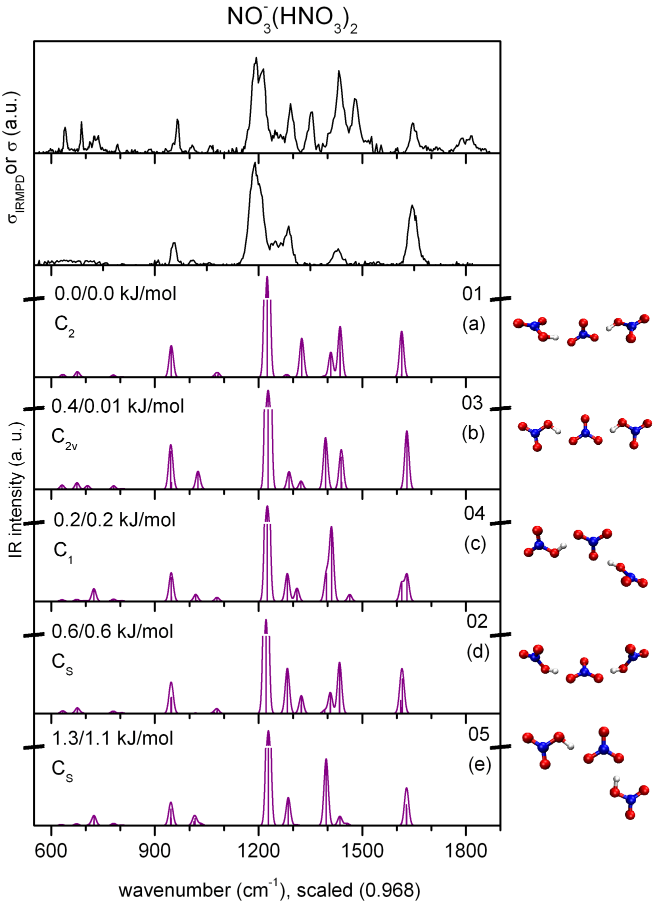

Figure B.6: Comparison between experimental IRPD spectrum and simulated IR intensities of $NO_3^-(HNO_3)_2$, calculated at the B3LYP/aug-cc-pVTZ level of theory.

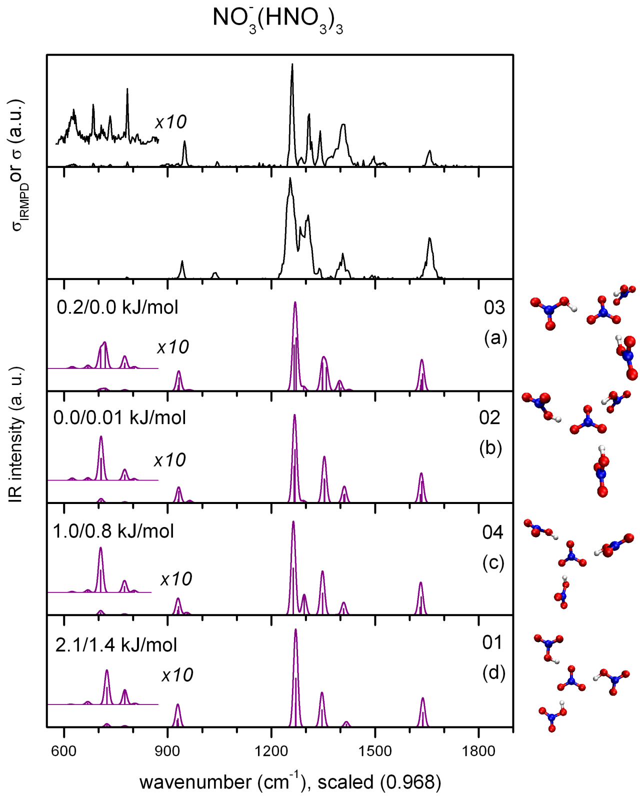

Figure B.7: Comparison between experimental IRPD spectra of and simulated IR intensities of $NO_3^-(HNO_3)_3$, calculated at the B3LYP/aug-cc-pVTZ level of theory.

Appendix C

Anharmonic Effects in Monohydrated Acid Clusters

Large Amplitude Motion in Monohydrated Dihydrogen Phosphate

Computational Details*

Optimized structures and harmonic frequencies are obtained from standard density functional theory (DFT) calculations, using the Gaussian 03 package. The dynamic motion of the clusters is simulated by the *Ab Initio* Molecular Dynamics (AIMD) method, in which the atoms are treated as classical particles and the potential energy and forces on the atoms are calculated within the framework of DFT at each time step.

For 0 K structure, energy optimization is performed at the level of B3LYP/ 6-311++G(d,p) by Gaussian 03 package. Initial structures are generated by running molecular dynamic simulations over tens of thousands time steps at 200 K and taking random configurations along the trajectories. Harmonic frequencies are calculated by using a larger basis set, at the level of MP2=full/aug-cc-pVDZ. A scale factor is used to facilitate the comparison between the experimental and theoretical peak positions. In the high frequency region, the MP2 value for peak A is aligned to the experimental position, yielding a scale factor of 0.9646. In the low frequency region, the MP2 value for peak G is aligned, giving a scale factor of 0.9993. The resulting stick spectra are convoluted using a Gaussian line shape function with a fwhm width of 4 cm^{-1} to account for the laser bandwidth, as well as broadening due to rotational excitation.

The CP2K package is employed for the AIMD simulations [277]. The wave functions are expanded in a double zeta Gaussian basis set, while the electron density is expanded in Gaussians and auxiliary plane waves with an

*Calculations have been performed by the group headed by Prof. Z.-F Liu at the Chinese University of Hong Kong.

energy cutoff at 320 Rydberg for the electron density for the long 200 ps run. The atomic cores are modeled by the Goedecker-Teter-Hutter (GTH) type pseudopotentials. The exchange and correlation energy is calculated by PBE functional, with additional Grimme's dispersion correction at D3 level, which produces harmonic frequencies in better agreement with experiment in our test calculations. A scaling factor of 1.0100 for is used for the low frequency region with respect to experimental peak G, and 0.9830 for the high frequency region with respect to experimental peak A.

A cluster ion is put at the center of a periodic cubic box, and the effects of the periodic charge density images are corrected by the decoupling technique developed by Martyna and Tuckerman [72]. The box length is 16 Å for $(HO)_2PO_2^-(H_2O)$. The convergence criterion for the SCF electronic procedure is set to be 10^{-7} a.u. at each time step. For molecular dynamics at a specific temperature, the temperature is controlled by a Nose-Hoover thermostat [278, 279] with a time step of 0.5 fs. An equilibration period of up to 10 ps (10 ps trajectory) is performed first, with the temperature scaled to an interval of 20 K around the intended value. A data collection run is then followed in the NVE ensemble. Two sets of long AIMD simulations (140 K and 180 K) were performed, for a more extensive sampling of the phase space. At each temperature, two trajectories were simulated, one starting with **1-1** and the other with **1-2**, each lasting 200 ps (200 ps trajectory). Each trajectory was then cut into 10 ps interval for Fourier transform, and all 40 frequency profiles were then added up to produce the DTCF spectrum for a specific temperature.

Hydrated clusters are bound by hydrogen bonds, which are relatively weak and therefore fairly flexible at finite temperature. Dynamic simulations are essential for sampling the solvation structures and for examining the thermal stability of a particular structure. More importantly, the hydrogen bonds could have strong effects on the vibrations, which could be captured by the AIMD simulations. A vibrational spectrum can be directly simulated by the Fourier transformation of the dipole time-correlation function (DTCF).

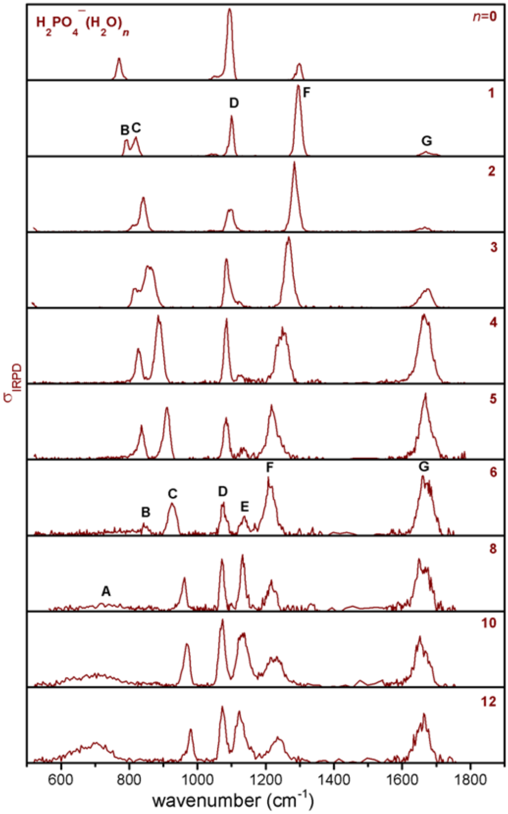

Figure C.1: Experimental IRMPD spectra of $H_2PO_4^-(H_2O)_n$ clusters with n = 1-12 in the fingerprint stretching region. The photodissociation cross section is plotted as a function of of the photon energy (cm^{-1}).

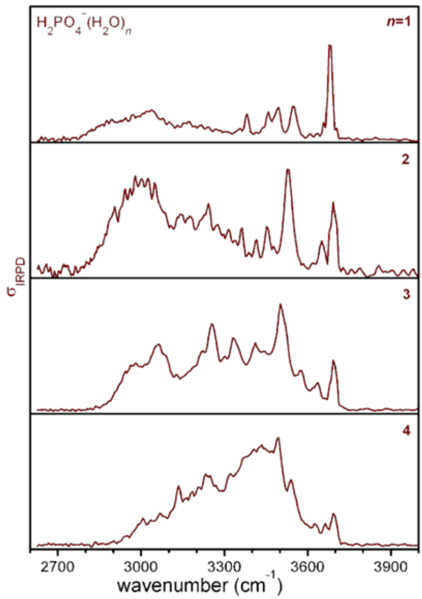

Figure C.2: Experimental IRMPD spectra of $H_2PO_4^-(H_2O)_n$ clusters with n = 1-4 in the O-H stretching region. The photodissociation cross section is plotted as a function of of the photon energy (cm^{-1}).

Cubic Coupling of High- and Low-Frequency Modes in Nitrate-Water

Computational Details*

Geometrical Structure and Adiabatic Potentials

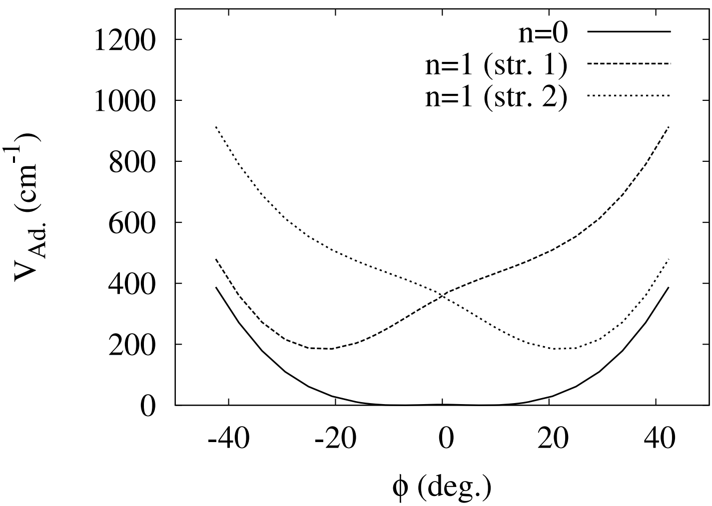

Figure C.3: Adiabatic rock potentials for the $NO_3^- \cdot H_2O$ complex with 0 and 1 quanta in the O-H stretch determined at the CCSD(T)/aug-cc-pVDZ level of theory. The O-H stretch excited state potentials (str. 1 and 2) are depicted in the local mode representation. The excited state potentials have been shifted downwards by 3350 cm^{-1} for convenience.

In considering the distortion of the complex from C_{2v} symmetry it is useful to define the angle ϕ between the vectors bisecting the H-O-H angle of the water molecule and the O-N-O angle of the nitrate ion. The vectors are oriented so that the angle between them is 0° for the C_{2v} structure.

*Calculations have been performed by the groups of A.B. McCoy (The Ohio State University) and K.D. Jordan (Pittsburgh University).

At the minimum energy structure shown in Figure **??** the value of the ϕ angle is 15° compared to 0° in the transition state structure. The value of the ϕ angle at the potential energy minimum is very sensitive to the atomic basis set employed. As the basis set is expanded along the sequence aug-cc-pVDZ, aug-cc-pVTZ VDZ-F12, and VTZ-F12 the minimum energy structure becomes closer to C_{2v} symmetry, and the water rock harmonic frequency decreases. Here VnZ-F12 refers to CCSD(T)-F12b calculations with the VnZ-F12 basis set. With the largest basis sets employed, the value of the ϕ angle is only 4-7° at the potential energy minimum and the rock frequency is calculated to be only 20-35 cm^{-1} within the harmonic approximation. Thus it is possible that, in the limit of a complete basis set, the global minimum could have a C_{2v} structure.

Insight into the vibrational spectra of $NO_3^- \cdot H_2O$ and its isotopologues is provided by calculating the adiabatic rock potentials for the complex with zero and one quanta in the O-H stretch local mode degrees of freedom.

$$V_{Ad.}^{g.s.} = E_{B.O.}(\phi) + E_{ZPE}(\phi) \;, \tag{C.1}$$

and

$$V_{Ad.}^{ex.} = E_{B.O.}(\phi) + E_{ZPE}(\phi) + \omega_{loc}(\phi) \;, \tag{C.2}$$

where $V_{Ad.}^{g.s.}$ and $V_{Ad.}^{ex.}$ refer to the ground and excited state potentials, respectively, $E_{B.O.}(\phi)$ is the Born-Oppenheimer energy obtained from the geometry optimization at a fixed ϕ value, $E_{ZPE}(\phi)$ is the harmonic zero-point energy (ZPE) calculated using the optimized geometry and excluding the rock degree of freedom, and the last term in Eq. C.2, $\omega_{loc}(\phi)$, is the frequency of the O-H stretch local mode. Figure C.3 reports the adiabatic rock potentials with zero or one quanta in the O-H stretch obtained at the CCSD(T)/aug-cc-pVDZ level of theory. In the adiabatic ground state the rock potential is very flat, and, even in the absence of the small barrier at $\phi = 0$, the potential is highly anharmonic. The minima in the excited state potentials are displaced to $\phi = \pm 21°$, and the resulting potentials are more harmonic than the ground state potential. The crossing point of the two excited state potentials occurs about 175 cm^{-1} above their minima. Since the experimentally observed spacing in the progressions in the O-H (O-D) stretch region is about 80 cm^{-1}, the third energy level in the progression lies above the crossing point. In addition, given the shape of the excited state potentials shown in Figure C.3, the spacing between the $n_r = 1$ and $n_r = 2$ levels would be expected to be smaller than that between the $n_r = 0$ and $n_r = 1$ levels. This suggests that the ϕ angle, as defined above, is not fully satisfactory for representing the rock coordinate. It is also likely that the shape of the $n_{loc} = 1$ potentials would differ if the curves were generated using the anharmonic frequencies for E_{ZPE} and ω_{loc}.

Effective Hamiltonian

	Harmonic frequencies			Force constants	
Species	ω_1	ω_2	ω_r	ω_{11r}	ω_{22r}
$NO_3^- \cdot H_2O$	3571.29	3571.29	80.00	242.42	-242.42
$NO_3^- \cdot D_2O$	2591.82	2591.82	80.00	169.11	-169.11
$NO_3^- \cdot$HDO	3571.60	2597.64	80.00	234.97	-174.47

Table C.1: Frequencies and reduced cubic force constants (cm^{-1}) used in the effective Hamiltonian calculations. The force constants for $NO_3^- \cdot$HDO are taken from the long O-H (O-D) stretch modes from the calculations on $NO_3^- \cdot$HDO and $NO_3^- \cdot$DHO (Table **??**).

The $n_{loc} = 0 \longrightarrow 1$ O-H stretch absorption spectrum is given by

$$\Delta E(n_r) = \omega_{loc} - \frac{\omega_{asr}^2}{8\omega_r} + n_r\omega_r \ , \tag{C.3}$$

where ω_{loc} is the frequency of the O-H stretch local mode, the second term on the right-hand side gives the red-shift of the origin, and n_r is the number of quanta in the $n_{loc} = 1$ potential, ω_r and ω_{asr} are, respectively, the rock frequency and the cubic force constant in wavenumbers. *asr* denotes *a*-antisymmetric O-H stretch, *s* symmetric O-H stretch, and *r* water rock.

The transition intensities for this model can be calculated using the overlap of harmonic oscillator wave functions of the ground and excited displaced harmonic potentials. Assuming that the ground state is in its zero-point level, the relative intensities of the levels in the progression are given by [247]:

$$I_{n_r} \propto \frac{exp(-0.5\Delta q_r^2)(\Delta q_r)^{2n_r}}{2^{n_r} n_r!} \ , \tag{C.4}$$

where q denotes the the water rock normal coordinate.

The observed energy levels in the O-H and OD stretch regions of $NO_3^- \cdot H_2O$ and its isotopologues are described by

$$\Delta E(n_r) = \omega_{loc} - \Delta + n_r\omega_r \ , \tag{C.5}$$

where Δ is a frequency shift that depends on the anharmonic coupling, ω_r is the rock frequency associated with the $n_{loc} = 1$ potential.

The model of Myshakin *et al.* is extended and now allows for both O-H (O-D) stretch local modes. The relevant model Hamiltonian is given by

$$H = H_1 + H_2 + H_r + H_c \ , \tag{C.6}$$

$$H_i = \frac{p_i^2}{2} + \frac{\omega_i^2 q_i^2}{2} \ , \quad i = 1, 2, r \ , \tag{C.7}$$

and

$$H_c = \frac{\lambda_1 q_1^2 q_r}{2} + \frac{\lambda_2 q_2^2 q_r}{2} \ , \tag{C.8}$$

where H is the total Hamiltonian, H_1, H_2, and H_r are the Hamiltonians for the O-H (O-D) stretch and rock modes, H_c is the coupling Hamiltonian, and p_i, ω_i, q_i and λ_i are, respectively, the momentum, harmonic frequency, mass-scaled coordinate and cubic coupling constants for mode i. The two local modes are designated "1" and "2", while, as above, the rock mode is labeled by "r".

The effect of the cubic coupling on the frequencies of the O-H (O-D) stretch modes can be approximated as a first-order perturbation to the ground state energy.

$$E_i = \frac{\omega_i}{2} + \frac{\lambda_i}{2} \langle 0 | q_i^2 q_r | 0 \rangle = \frac{\omega'_i}{2} \ , \tag{C.9}$$

where

$$\omega'_i = \omega_i + \frac{\lambda_i q_r}{2\omega_i} \ , \quad i = 1, 2 \ . \tag{C.10}$$

The same result can be obtained by completing the square giving, $\omega'_i = \sqrt{\omega_i^2 + \lambda_i q_r}$, and retaining the first two terms of the Taylor series expansion of the right-hand side.

Assuming that the stretch vibrations behave as harmonic oscillators with the new frequencies ω'_i, the effective Hamiltonian becomes

$$\begin{aligned} H^{eff} &= \frac{p_1^2}{2} + \frac{p_2^2}{2} + \frac{p_r^2}{2} \\ &+ \frac{\omega'^2_1 q_1^2}{2} + \frac{\omega'^2_2 q_2^2}{2} + \frac{\omega_r^2 q_r^2}{2} \ , \end{aligned} \tag{C.11}$$

which can be solved, within the adiabatic approximation, as if the system contains three independent harmonic oscillators.

With the assumption that the O-H stretch ground state is initially in the $n_r = 0$ level, the excitation energies are given by:

$$\Delta E_1(n_r) = \omega_1 - \frac{\omega_{11r}^2}{4\omega_r} - \frac{\omega_{11r}\omega_{22r}}{8\omega_r} + n_r\omega_r \ , \qquad \text{(C.12)}$$

where ω_{11r} and ω_{22r} are the reduced cubic coupling constants in inverse centimeter units,

$$\omega_{iir} = \frac{\lambda_i}{\omega_i\sqrt{\omega_r}} \ . \qquad \text{(C.13)}$$

An analogous expression, $\Delta E_2(n_r)$, is obtained for the second O-H stretch local mode. It should be noted that Eq. C.12 reduces to Eq. C.3 when ω_{11r} and ω_{22r} are of equal magnitude with opposite signs, as occurs at C_{2v} symmetry. Since the CCSD(T)/aug-cc-pVDZ force constants are calculated with a ϕ value near the minimum in the $n_i = 1$ potentials, the local environment experienced by the long O-H stretch can be assumed to provide a good approximation for the stretch local modes. In light of this, for $NO_3^- \cdot H_2O$ we take $\omega_1 = \omega_2 = \omega_l$, $\omega_{11r} = \omega_{llr}$, and $\omega_{22r} = -\omega_{llr}$. We further take $\omega_r = 80$ cm^{-1}. With these assumptions, the model gives potentials that approximately reproduce those in Figure C.3. As with the original C_{2v} model, the transition intensities are estimated by Eq. C.4.

This model Hamiltonian can be readily applied to the $NO_3^- \cdot D_2O$, $NO_3^- \cdot$DHO, and $NO_3^- \cdot$HDO isotopologues. Table C.1 lists the values of the O-H stretch and rock frequencies and the *iir* force constants used in the effective Hamiltonian calculations of the isotopologues. The assumptions for $NO_3^- \cdot D_2O$ are the same as for $NO_3^- \cdot H_2O$. However, since the two water stretching modes are not identical in the HDO (DHO) isotopologue, the effective Hamiltonian was constructed by employing the O-H stretch parameters calculated for both $NO_3^- \cdot$DHO and $NO_3^- \cdot$ HDO. Specifically the harmonic frequencies are defined as $\omega_1 = \omega_l$ (HDO) and $\omega_2 = \omega_l$ (DHO), and the cubic coupling constants for this system are taken to be $\omega_{11r} = \omega_{llr}$ (HDO) and $\omega_{22r} = \omega_{llr}$ (DHO).

Vibrational CI

For the inclusion of the Fermi resonances with the water bend overtone to the spectra, vibrational configuration interaction (VCI) calculations were performed within the local mode approximation using the Hamiltonian:

$$H = H_1 + H_2 + H_b + H_r + H_c \ , \qquad \text{(C.14)}$$

where H_1, H_2, and H_r are as defined above, H_b is the Hamiltonian for the

H-O-H bend, and

$$H_c = \frac{\omega_{llr}}{2}(q_1^2 - q_2^2)q_r + \frac{\omega_{lbb}}{2}(q_1 + q_2)q_b^2 \ , \qquad \text{(C.15)}$$

The basis functions used in the calculations are of the form $|n_1, n_2, n_b, n_r\rangle$, where n_1, n_2, n_b, and n_r refer to the number of quanta in the local O-H stretch, H-O-H bend, and rock degrees of freedom, respectively. Based on a series of exploratory calculations, the VCI calculations are found to be well converged with a basis set using up to five quanta in the water O-H stretch, bend, and rock modes, and up to twenty quanta in the stretch-rock progressions.

Bibliography

[1] Graedel, T. E.; Crutzen, P. J. *Chemie der Atmosphäre: Bedeutung fuer Klima und Umwelt*; Spektrum Akademischer Verlag, 1995.

[2] Rudich, Y.; Donahue, N. M.; Mentel, T. F. *Annu. Rev. Phys. Chem.* **2007**, *58*, 321 – 352.

[3] Kulmala, M. *Science* **2003**, *302*, 1000 – 1001.

[4] Zhang, Q.; Worsnop, D. R.; Canagaratna, M. R.; Jimenez, J. L. *Atmos. Chem. Phys.* **2005**, *5*, 3289 – 3311.

[5] Almeida, J.; et al. *Nature* **2013**, *502*, 359 – 363.

[6] Gruenloh, C. J.; Carney, J. R.; Arrington, C. A.; Zwier, T. S.; Fredericks, S. Y.; Jordan, K. D. *Science* **1997**, *276*, 1678 – 1681.

[7] Ebata, T.; Fujii, A.; Mikami, N. *Int. Rev. Phys. Chem.* **1998**, *17*, 331 – 361.

[8] Beyer, M.; Williams, E. R.; Bondybey, V. E. *J. Am. Chem. Soc.* **1999**, *121*, 1565 – 1573.

[9] Bieske, E. J.; Dopfer, O. *Chem. Rev.* **2000**, *100*, 3963 – 3998.

[10] Duncan, M. A. *Int. J. Mass Spectrom.* **2000**, *200*, 545 – 569.

[11] Robertson, E.; Simons, J. *Phys. Chem. Chem. Phys.* **2001**, *3*, 1 – 18.

[12] Robertson, W. H.; Price, E. A.; Weber, J. M.; Shin, J. W.; Weddle, G. H.; Johnson, M. A. *J. Phys. Chem. A* **2003**, *107*, 6527 – 6532.

[13] Kamariotis, A.; Boyarkin, O. V.; Mercier, S. R.; Beck, R. D.; Bush, M. F.; Williams, E. R.; Rizzo, T. R. *J. Am. Chem. Soc.* **2006**, *128*, 905 – 916.

[14] Lisy, J. M. *J. Chem. Phys.* **2006**, *125*, 132302.

[15] Asmis, K. R.; Neumark, D. M. *Acc. Chem. Res.* **2012**, *45*, 43 – 52.

[16] Wyttenbach, T.; von Helden, G.; Bowers, M. T. *J. Am. Chem. Soc.* **1996**, *118*, 8355 – 8364.

[17] Papadopoulos, G.; Svendsen, A.; Boyarkin, O. V.; Rizzo, T. R. *Faraday Discuss.* **2011**, *150*, 243 – 255.

[18] Pierson, N. A.; Chen, L.; Valentine, S. J.; Russell, D. H.; Clemmer, D. E. *J. Am. Chem. Soc.* **2011**, *133*, 13810–13813.

[19] Dian, B. C.; Longarte, A.; Zwier, T. S. *Science* **2002**, *296*, 2369 – 2373.

[20] Chin, W.; Compagnon, I.; Dognon, J.-P.; Canuel, C.; Piuzzi, F.; Dimicoli, I.; von Helden, G.; Meijer, G.; Mons, M. *J. Am. Chem. Soc.* **2005**, *127*, 1388 – 1389.

[21] Selby, T. M.; Meerts, W. L.; Zwier, T. S. *J. Phys. Chem. A* **2007**, *111*, 3697 – 3709.

[22] Cocinero, E. J.; Carcabal, P.; Vaden, T. D.; Simons, J. P.; Davis, B. G. *Nature* **2011**, *469*, 76 – 79.

[23] Nagornova, N. S.; Rizzo, T. R.; Boyarkin, O. V. *Science* **2012**, *336*, 320 – 323.

[24] Elliott, B. M.; Relph, R. A.; Roscioli, J. R.; Bopp, J. C.; Gardenier, G. H.; Guasco, T. L.; Johnson, M. A. *J. Chem. Phys.* **2008**, *129*, 094303.

[25] Guasco, T. L.; Elliott, B. M.; Johnson, M. A.; Ding, J.; Jordan, K. D. *J. Phys. Chem. Lett.* **2010**, *1*, 2396 – 2401.

[26] Relph, R. A.; Guasco, T. L.; Elliott, B. M.; Kamrath, M. Z.; McCoy, A. B.; Steele, R. P.; Schofield, D. P.; Jordan, K. D.; Viggiano, A. A.; Ferguson, E. E.; Johnson, M. A. *Science* **2010**, *327*, 308 – 312.

[27] Leavitt, C. M.; Wolk, A. B.; Fournier, J. A.; Kamrath, M. Z.; Garand, E.; Van Stipdonk, M. J.; Johnson, M. A. *J. Phys. Chem. Lett.* **2012**, *3*, 1099 – 1105.

[28] Heine, N.; Fagiani, M. R.; Rossi, M.; Wende, T.; Berden, G.; Blum, V.; Asmis, K. R. *J. Am. Chem. Soc.* **2013**, *135*, 8266 – 8273.

[29] Asmis, K. R.; Pivonka, N. L.; Santambrogio, G.; Brümmer, M.; Kaposta, C.; Neumark, D. M.; Wöste, L. *Science* **2003**, *299*, 1375 – 1377.

[30] Iyengar, S. S.; Petersen, M. K.; Day, T. J. F.; Burnham, C. J.; Teige, V. E.; Voth, G. A. *J. Chem. Phys.* **2005**, *123*, 084309.

[31] Gregoire, G.; Gaigeot, M. P.; Marinica, D. C.; Lemaire, J.; Schermann, J. P.; Desfrancois, C. *Phys. Chem. Chem. Phys.* **2007**, *9*, 3082 – 3097.

[32] Vendrell, O.; Gatti, F.; Meyer, H.-D. *Angew. Chem. Int. Ed.* **2007**, *46*, 6918 – 6921.

[33] Kaledin, M.; Kaledin, A. L.; Bowman, J. M.; Ding, J.; Jordan, K. D. *J. Phys. Chem. A* **2009**, *113*, 7671 – 7677.

[34] Cimas, A.; Maitre, P.; Ohanessian, G.; Gaigeot, M.-P. *J. Chem. Theory Comput.* **2009**, *5*, 2388 – 2400.

[35] Baer, M.; Marx, D.; Mathias, G. *Angew. Chem. Int. Ed.* **2010**, *49*, 7346 – 7349.

[36] A. W. Castleman, J.; Tang, I. N. *J. Chem. Phys.* **1972**, *57*, 3629 – 3638.

[37] Yu, F.; Turco, R. P. *Journal of Geophysical Research: Atmospheres* **2001**, *106*, 4797 – 4814.

[38] Arnold, F. *Space Sci. Rev.* **2008**, *137*, 225 – 239.

[39] Andreae, M. O.; Jones, C. D.; Cox, P. M. *Nature* **2005**, *435*, 1187 – 1190.

[40] Wang, S.; Zordan, C. A.; Johnston, M. V. *Anal. Chem.* **2006**, *78*, 1750 – 1754.

[41] Kulmala, M.; et al. *Science* **2007**, *318*, 89 – 92.

[42] Jiang, J.; Zhao, J.; Chen, M.; Eisele, F. L.; Scheckman, J.; Williams, B. J.; Kuang, C.; McMurry, P. H. *Aerosol Sci. Technol.* **2011**, *45*, ii–v.

[43] Sorokin, A.; Arnold, F.; Wiedner, D. *Atmos. Environ.* **2006**, *40*, 2030 – 2045.

[44] Kirkby, J.; et al. *Nature* **2011**, *476*, 429 – 433.

[45] Froyd, K. D.; Lovejoy, E. R. *J. Phys. Chem. A* **2012**, *116*, 5886 – 5899.

[46] Arijs, E.; Nevejeans, D.; Frederick, P.; Ingels, J. *Geophys. Res. Lett.* **1981**, *8*, 121 – 124.

[47] Arnold, F.; Henschen, G. *Nature* **1978**, *275*, 521 – 522.

[48] Viggiano, A.; Arnold, F. *Planet. Space Sci.* **1981**, *29*, 895 – 906.

[49] Ramanathan, V.; Crutzen, P. J.; Kiehl, J. T.; Rosenfeld, D. *Science* **2001**, *294*, 2119 – 2124.

[50] Finlayson-Pitts, B. J. *Chem. Rev.* **2003**, *103*, 4801 – 4822.

[51] Carslaw, K.; Harrison, R.; Kirkby, J. *Science* **2002**, *298*, 1732 – 1737.

[52] *https://indico.cern.ch/event/52576/material/slides/0.*

[53] CLOUD Collaboration (Collaboration, C.); *2011 Progress Report on PS215/CLOUD*; Tech. Rep. CERN-SPSC-2012-015. SPSC-SR-101; CERN; Geneva; 2012.

[54] Goken, E.; Castleman, A. W. *J. Geophys. Res.* **2010**, *115*, D16203 1 – 8.

[55] Karl, M.; Brauers, T.; Dorn, H.-P.; Holland, F.; Komenda, M.; Poppe, D.; Rohrer, F.; Rupp, L.; Schaub, A.; Wahner, A. *Geophys. Res. Lett.* **2004**, *31*, L05117 1–4.

[56] Duplissy, J.; et al. *Atmos. Chem. Phys.* **2010**, *10*, 1635 – 1647.

[57] Goebbert, D. J.; Garand, E.; Wende, T.; Bergmann, R.; Meijer, G.; Asmis, K. R.; Neumark, D. M. *J. Phys. Chem. A* **2009**, *113*, 7584 – 7592.

[58] Goebbert, D. J.; Wende, T.; Bergmann, R.; Meijer, G.; Asmis, K. R. *J. Phys. Chem. A* **2009**, *113*, 5874 – 5880.

[59] Jiang, L.; Wende, T.; Bergmann, R.; Meijer, G.; Asmis, K. R. *J. Am. Chem. Soc.* **2010**, *132*, 7398 – 7404.

[60] Garand, E.; Wende, T.; Goebbert, D. J.; Bergmann, R.; Meijer, G.; Neumark, D. M.; Asmis, K. R. *J. Am. Chem. Soc.* **2010**, *132*, 849 – 856.

[61] Yacovitch, T. I.; Heine, N.; Brieger, C.; Wende, T.; Hock, C.; Neumark, D. M.; Asmis, K. R. *J. Chem. Phys.* **2012**, *136*, 241102.

[62] Heine, N.; Yacovitch, T. I.; Schubert, F.; Brieger, C.; Neumark, D. M.; Asmis, K. R. *J. Phys. Chem. A* **2014**, accepted.

[63] Yacovitch, T.; Heine, N.; Brieger, C.; Wende, T.; Hock, C.; Neumark, D.; Asmis, K. *J. Phys. Chem. A* **2013**, *117*, 7081 – 90.

[64] Tuck, A. F. *Chemistry of Atmospheres*; John Wiley & Sons, Ltd, 1991; Vol. 118, pp 413 – 413.

[65] Hynes, J.; Klinman, J.; Limbach, H.-H.; Schowen, R. *Hydrogen-Transfer Reactions Volume 1*; Wiley-VCH Verlag GmbH & Co. KGaA, 2007.

[66] Franks, F. *Water, a Comprehensive Treatise*; Plenum, New York, 1972 – 1985; Vol. 1 – 7.

[67] Buszek, R. J.; Francisco, J. S.; Anglada, J. M. *Int. Rev. Phys. Chem.* **2011**, *30*, 335 – 369.

[68] Ball, P. *Nature* **2008**, *452*, 291 – 292.

[69] Tokmakoff, A. *Science* **2007**, *317*, 54 – 55.

[70] Cukierman, S. *Biochim. Biophys. Acta, Bioenerg.* **2006**, *1757*, 876 – 885.

[71] Schmitt, U.; Voth, G. A. *J. Chem. Phys.* **1999**, *111*, 9361 – 9381.

[72] Martyna, G.; Tuckerman, M. *J. Chem. Phys.* **1999**, *110*, 2810 – 2821.

[73] von Grotthuss, C. *Ann. Chim.* **1806**, *LVII*, 54.

[74] Agmon, N. *Chem. Phys. Lett.* **1995**, *244*, 456 – 462.

[75] Marx, D. *Chem. Phys. Chem.* **2006**, *7*, 1848 – 1870.

[76] Eigen, M. *Angew. Chem. Int. Ed.* **1964**, *3*, 1 – 19.

[77] Zundel, G. *The Hydrogen Bond: Recent Developments in Theory and Experiments.*; Schuster, P.; Zundel, G.; Sandorfy, C., Eds.; North-Holland: Amsterdam, 1976.

[78] Kim, J.; Schmitt, U. W.; Gruetzmacher, J. A.; Voth, G. A.; Scherer, N. E. *J. Chem. Phys.* **2002**, *116*, 737 – 746.

[79] Xu, J.; Zhang, Y.; Voth, G. A. *J. Phys. Chem. Lett.* **2011**, *2*, 81 – 86.

[80] Knight, C.; Voth, G. A. *Acc. Chem. Res.* **2012**, *45*, 101 – 109.

[81] Searcy, J. Q.; Fenn, J. B. *J. Chem. Phys.* **1974**, *61*, 5282 – 5288.

[82] Yang, X.; Zhang, X.; Jr., A. C. *Int. J. Mass Spectrom. Ion Processes* **1991**, *109*, 339 – 354.

[83] Yeh, L. I.; Okumura, M.; Myers, J. D.; Price, J. M.; Lee, Y. T. *J. Chem. Phys.* **1989**, *91*, 7319 – 7330.

[84] Jiang, J.-C.; Wang, Y.-S.; Chang, H.-C.; Lin, S. H.; Lee, Y. T.; Niedner-Schatteburg, G.; Chang, H.-C. *J. Am. Chem. Soc.* **2000**, *122*, 1398 – 1410.

[85] Miyazaki, M.; Fujii, A.; Ebata, T.; Mikami, N. *Science* **2004**, *304*, 1134 – 1137.

[86] Shin, J.-W.; Hammer, N. I.; Diken, E. G.; Johnson, M. A.; Walters, R. S.; Jaeger, T. D.; Duncan, M. A.; Christie, R. A.; Jordan, K. D. *Science* **2004**, *304*, 1137 – 1140.

[87] Headrick, J. M.; Diken, E. G.; Walters, R. S.; Hammer, N. I.; Christie, R. A.; Cui, J.; Myshakin, E. M.; Duncan, M. A.; Johnson, M. A.; Jordan, K. D. *Science* **2005**, *308*, 1765 – 1769.

[88] Mohammed, O. F.; Pines, D.; Dreyer, J.; Pines, E.; Nibbering, E. T. J. *Science* **2005**, *310*, 83 – 86.

[89] Mizuse, K.; Mikami, N.; Fujii, A. *Angew. Chem. Int. Ed.* **2010**, *49*, 10119 – 10122.

[90] Fournier, J. A.; Johnson, C. J.; Wolke, C. T.; Weddle, G. H.; Wolk, A. B.; Johnson, M. A. *Science* **2012**.

[91] Kulig, W.; Agmon, N. *Nat Chem* **2013**, *5*, 29 – 35.

[92] Kulig, W.; Agmon, N. *Phys. Chem. Chem. Phys.* **2014**, *16*, 4933 – 4941.

[93] Kulig, W.; Agmon, N. *J. Phys. Chem. B* **2014**, *118*, 278 – 286.

[94] Douberly, G. E.; Walters, R. S.; Cui, J.; Jordan, K. D.; Duncan, M. A. *J. Phys. Chem. A* **2010**, *114*, 4570 – 4579.

[95] Mizuse, K.; Fujii, A. *J. Phys. Chem. A* **2012**, *116*, 4868 – 4877.

[96] Yeh, L.; Lee, Y.; Hougen, J. *J. Mol. Spectrosc.* **1994**, *164*, 473 – 488.

[97] Hammer, N. I.; Diken, E. G.; Roscioli, J. R.; Johnson, M. A.; Myshakin, E. M.; Jordan, K. D.; McCoy, A. B.; Huang, X.; Bowman, J. M.; Carter, S. *J. Chem. Phys.* **2005**, *122*, 244301.

[98] Servage, K. A.; Silveira, J. A.; Fort, K. L.; Russell, D. H. *J. Phys. Chem. Lett.* **2014**, *5*, 1825 – 1830.

[99] Demtröder, W. *Atoms, molecules and photons: An introduction to atomic-, molecular-, and quantum-physics.*; Springer, Berlin London, 2006.

[100] Morse, P. M. *Phys. Rev.* **1929**, *34*, 57 – 64.

[101] Czeslik, C.; Seemann, H.; Winter, R. In *Basiswissen Physikalische Chemie*; Vieweg+Teubner, 2010.

[102] Wheeler, M. D.; Newman, S. M.; Orr-Ewing, A. J.; Ashfold, M. N. R. *J. Chem. Soc., Faraday Trans.* **1998**, *94*, 337–351.

[103] Casaes, R.; Provencal, R.; Paul, J.; Saykally, R. J. *J. Chem. Phys.* **2002**, *116*, 6640 – 6647.

[104] Gruene, P.; Lyon, J.; Fielicke, A. In *Handbook of Nanophysics*; CRC Press, 2010.

[105] Asmis, K. R.; Fielicke, A.; von Helden, G.; Meijer, G. In *Atomic Clusters: From Gas Phase to Deposited Atomic Clusters*; Woodruff, D. P., Ed.; Elsevier, 2007; Vol. 12, Chapter 8.

[106] Black, J. G.; Yablonovitch, E.; Bloembergen, N.; Mukamel, S. *Phys. Rev. Lett.* **1977**, *38*, 1131 – 1134.

[107] Grant, E. R.; Schulz, P. A.; Sudbo, A. S.; Shen, Y. R.; Lee, Y. T. *Phys. Rev. Lett.* **1978**, *40*, 115 – 118.

[108] Bagratashvili, V. N.; Letokhov, V. S.; Makarov, A. A.; Ryabov, E. A. *Multiple Photon Infrared Laser Photophysics and Photochemistry*; Harwood Academic Publishers, 1985.

[109] Makarov, A. A.; Petrova, I. Y.; Ryabov, E. A.; Letokhov, V. S. *J. Phys. Chem. A* **1998**, *102*, 1438 – 1449.

[110] Asmis, K. R.; Sauer, J. *Mass Spectrom. Rev.* **2007**, *26*, 542 – 562.

[111] Lehmann, K. K.; Scoles, G.; Pate, B. H. *Annu. Rev. Phys. Chem.* **1994**, *45*, 241 – 274.

[112] Akulin, V.; Alimpiev, S.; Karlov, N.; Prokhorov, A.; Sartakov, B.; Khokhlov, E. *JETP Lett.* **1977**, *25*, 400 – 403.

[113] Pankewitz, T.; Lagutschenkov, A.; Niedner-Schatteburg, G.; Xantheas, S. S.; Lee, Y.-T. *J. Chem. Phys.* **2007**, *126*, 074307.

[114] Beck, J. P.; Lisy, J. M. *J. Chem. Phys.* **2011**, *135*, 044302.

[115] Roscioli, J. R.; McCunn, L. R.; Johnson, M. A. *Science* **2007**, *316*, 249 – 254.

[116] Wende, T.; Doktorarbeit; Freie Universität Berlin; 2012.

[117] Okumura, M.; Yeh, L. I.; Myers, J. D.; Lee, Y. T. *J. Chem. Phys.* **1986**, *85*, 2328 – 2329.

[118] Okumura, M.; Yeh, L. I.; Myers, J. D.; Lee, Y. T. *J. Phys. Chem.* **1990**, *94*, 3416 – 3427.

[119] Johnson, M. A. In *The Encyclopedia of Mass Spectrometry: Theory and Ion Chemistry*; Armentrout, P. B.; Gross, M. L.; Caprioli, R., Eds.; Elsevier: Oxford, UK, 2003.

[120] Orcutt, R. H.; Cole, R. H. *J. Chem. Phys.* **1967**, *46*, 697 – 702.

[121] Hunter, E. P. L.; Lias, S. G. *J. Phys. Chem. Ref. Data* **1998**, *27*, 413 – 656.

[122] Asmis, K. R.; Wende, T.; Brümmer, M.; Gause, O.; Santambrogio, G.; Stanca-Kaposta, E. C.; Döbler, J.; A., N.; Sauer, J. *Phys. Chem. Chem. Phys.* **2012**, *14*, 9377 – 9388.

[123] Knickelbein, M. B. *J. Chem. Phys.* **1994**, *100*, 4729 – 4737.

[124] Gruene, P.; Rayner, D. M.; Redlich, B.; van der Meer, A. F. G.; Lyon, J. T.; Meijer, G.; Fielicke, A. *Science* **2008**, *321*, 674 – 676.

[125] Mizuse, K.; Fujii, A. *Phys. Chem. Chem. Phys.* **2011**, *13*, 7129 – 7135.

[126] Cheng, T. C.; Bandyopadhyay, B.; Mosley, J. D.; Duncan, M. A. *J. Am. Chem. Soc.* **2012**, *134*, 13046 – 13055.

[127] Wang, Y.-S.; Tsai, C.-H.; Lee, Y. T.; Chang, H.-C.; Jiang, J. C.; Asvany, O.; Schlemmer, S.; Gerlich, D. *J. Phys. Chem. A* **2003**, *107*, 4217–4225.

[128] Wutz, M. *Wutz Handbuch Vakuumtechnik : mit 124 Tabellen und 102 Beispielen*; Jousten, K., Ed.; Vieweg + Teubner, 2010.

[129] Moore, J. H.; Coplan, M. A.; Davis, C. C. *Building scientific apparatus : a practical guide to design and construction*; Perseus Books, 2003.

[130] Fenn, J. B.; Mann, M.; Meng, C. K.; Wong, S. F.; Whitehouse, C. M. *Science* **1989**, *246*, 64 – 71.

[131] Fenn, J. B.; Mann, M.; Meng, C. K.; Wong, S. F.; Whitehouse, C. M. *Mass Spectrom. Rev.* **1990**, *9*, 37 – 70.

[132] Wang, X. B.; Yang, X.; Wang, L. S. *Int. Rev. Phys. Chem.* **2002**, *21*, 473–498.

[133] Kebarle, P. *J. Mass Spectrom.* **2000**, *35*, 804 – 817.

[134] Wilm, M. S.; Mann, M. *Int. J. Mass Spectrom. Ion Processes* **1994**, *136*, 167 – 180.

[135] Esser, T.; Masterarbeit; Freie Universität Berlin; 2013.

[136] Cole, R. B. *J. Mass Spectrom.* **2000**, *35*, 763 – 772.

[137] Gerlich, D.; Horning, S. *Chem. Rev.* **1992**, *92*, 1509 – 1539.

[138] Gerlich, D. *J. Anal. At. Spectrom.* **2004**, *19*, 581 – 590.

[139] Luca, A.; Schlemmer, S.; Cermak, I.; Gerlich, D. *Rev. Sci. Instrum.* **2001**, *72*, 2900 – 2908.

[140] Gerlich, D. *Adv. Chem. Phys.* **1992**, *82*, 1 – 176.

[141] Gerlich, D. *The Production and Study of Ultra-Cold Molecular Ions. In: Low Temperatures and Cold Molecules*; Smith, I., Ed.; Imperial College Press: London, 2008.

[142] Crofton, M. W.; Oka, T. *J. Chem. Phys.* **1983**, *79*, 3157 – 3158.

[143] Crofton, M. W.; Oka, T. *J. Chem. Phys.* **1987**, *86*, 5983 – 5988.

[144] McCoy, A. B.; *(personal communication, April 27, 2014).*

[145] PGOPHER*, a Program for Simulating Rotational Structure, C. M. Western, University of Bristol, http://pgopher.chm.bris.ac.uk.*

[146] Svendsen, A.; Lorenz, U. J.; Boyarkin, O. V.; Rizzo, T. R. *Rev. Sci. Instrum.* **2010**, *81*, 073107.

[147] Wiley, W. C.; McLaren, I. H. *Rev. Sci. Instrum.* **1955**, *26*, 1150 – 1157.

[148] Goebbert, D. J.; Meijer, G.; Asmis, K. R. *AIP Conf. Proc.* **2009**, *1104*, 22 – 29.

[149] von Helden, G.; van Heijnsbergen, D.; Meijer, G. *J. Phys. Chem. A* **2003**, *107*, 1671 – 1688.

[150] Bosenberg, W. R.; Guyer, D. R. *J. Opt. Soc. Am. B* **1993**, *10*, 1716 – 1722.

[151] http://www.deanguyer.com/.

[152] Oepts, D.; van der Meer, A. F. G.; van Amersfoort, P. W. *Infrared Phys. Technol.* **1995**, *36*, 297 – 308.

[153] Vuilleumier, R.; Borgis, D. *J. Chem. Phys.* **1999**, *111*, 4251 – 4266.

[154] Stoyanov, E. S.; Stoyanova, I. V.; Reed, C. A. *Chem. Sci.* **2011**, *2*, 462 – 472.

[155] Keutsch, F. N.; Saykally, R. J. *Proc. Natl. Acad. Sci. U. S. A.* **2001**, *98*, 10533 – 10540.

[156] Saykally, R. J.; Wales, D. J. *Science* **2012**, *336*, 814 – 815.

[157] Perez, C.; Muckle, M. T.; Zaleski, D. P.; Seifert, N. A.; Temelso, B.; Shields, G. C.; Kisiel, Z.; Pate, B. H. *Science* **2012**, *336*, 897 – 901.

[158] Schwarz, H. A. *J. Chem. Phys.* **1977**, *67*, 5525 – 5534.

[159] Lin, C.-K.; Wu, C.-C.; Wang, Y.-S.; Lee, Y. T.; Chang, H.-C.; Kuo, J.-L.; Klein, M. L. *Phys. Chem. Chem. Phys.* **2005**, *7*, 938 – 944.

[160] Wu, C.-C.; Lin, C.-K.; Chang, H.-C.; Jiang, J.-C.; Kuo, J.-L.; Klein, M. L. *J. Chem. Phys.* **2005**, *122*, 074315.

[161] Chin, W.; Dognon, J.-P.; Canuel, C.; Piuzzi, F.; Dimicoli, I.; Mons, M.; Compagnon, I.; von Helden, G.; Meijer, G. *J. Chem. Phys.* **2005**, *122*, 054317.

[162] Stearns, J. A.; Boyarkin, O. V.; Rizzo, T. R. *J. Am. Chem. Soc.* **2007**, *129*, 13820 – 13821.

[163] Abo-Riziq, A.; Grace, L.; Crews, B.; Callahan, M. P.; van Mourik, T.; Vries, M. S. d. *J. Phys. Chem. A* **2011**, *115*, 6077 – 6087.

[164] Park, M.; Shin, I.; Singh, N. J.; Kim, K. S. *J. Phys. Chem. A* **2007**, *111*, 10692 – 10702.

[165] Dietrick, S. M.; Iyengar, S. S. *J. Chem. Theory Comput.* **2012**, *8*, 4876 – 4890.

[166] Kebarle, P.; Searles, S. K.; Zolla, A.; Scarborough, J.; Arshadi, M. *J. Am. Chem. Soc.* **1967**, *89*, 6393 – 6399.

[167] Lau, Y. K.; Ikuta, S.; Kebarle, P. *J. Am. Chem. Soc.* **1982**, *104*, 1462 – 1469.

[168] Brümmer, M.; Kaposta, C.; Santambrogio, G.; Asmis, K. R. *J. Chem. Phys.* **2003**, *119*, 12700 – 12703.

[169] Blum, V.; Gehrke, R.; Hanke, F.; Havu, P.; Havu, V.; Ren, X.; Reuter, K.; Scheffler, M. *Comput. Phys. Commun.* **2009**, *180*, 2175 – 2196.

[170] Perdew, J. P.; Burke, K.; Ernzerhof, M. *Phys. Rev. Lett.* **1996**, *77*, 3865 – 3868.

[171] Tkatchenko, A.; Scheffler, M. *Phys. Rev. Lett.* **2009**, *102*, 073005.

[172] Chutia, S.; Rossi, M.; Blum, V. *J. Phys. Chem. B* **2012**, *116*, 14788 – 14804.

[173] Karthikeyan, S.; Kim, K. S. *J. Phys. Chem. A* **2009**, *113*, 9237 – 9242.

[174] Karthikeyan, S.; Kim, K. S. *Mol. Phys.* **2009**, *107*, 1169 – 1176.

[175] Karthikeyan, S.; Park, M.; Shin, I.; Kim, K. S. *J. Phys. Chem. A* **2008**, *112*, 10120 – 10124.

[176] Vendrell, O.; Gatti, F.; Meyer, H.-D. *J. Chem. Phys.* **2007**, *127*, 184303.

[177] Agostini, F.; Vuilleumier, R.; Ciccotti, G. *J. Chem. Phys.* **2011**, *134*, 084302.

[178] Relph, R. A.; Elliott, B. M.; Weddle, G. H.; Johnson, M. A.; Ding, J.; Jordan, K. D. *J. Phys. Chem. A* **2009**, *113*, 975 – 981; PMID: 19152322.

[179] Heitmann, H.; Arnold, F. *Nature* **1983**, *306*, 747 – 751.

[180] Beig, G.; Brasseur, G. *J. Geophys. Res.* **2000**, *105*, 22671 – 22684.

[181] MacTaylor, R.; Castleman, J., A.W. *J. Atmos. Chem.* **2000**, *36*, 23 – 63.

[182] Dunlap, B. I.; Robert J. Doyle, J. *J. Phys. Chem.* **1996**, *100*, 5281 – 5285.

[183] Galvez, O.; Gomez, P. C.; Pacios, L. F. *J. Phys. Chem. A* **2006**, *110*, 3750 – 3758.

[184] Gillard, R. D.; Ugo, R. *J. Chem. Soc.* **1966**, *A*, 549 – 552.

[185] Detoni, S.; Diop, L.; Gunde, R.; Hadzi, D.; Orel, B.; Potier, A.; Potier, J. *Spectrochim. Acta, Part A* **1979**, *35*, 443 – 454.

[186] Emsley, J. *Chem. Soc. Rev.* **1980**, *9*, 91 – 124.

[187] Dobinson, G. C.; Mason, R.; Russell, D. R. *Chem. Commun. (London)* **1967**, 62 – 63.

[188] Gunde, R.; Solmajer, T.; Azman, A.; Hadzi, D. *J. Mol. Struct.* **1975**, *24*, 405 – 408.

[189] B. Barlic, B. O., D. Hadzi *Spectrochim. Acta* **1981**, *37A*, 1047 – 1048.

[190] Asmis, K. R.; Neumark, D. M.; Bowman, J. M. In *Gas Phase Vibrational Spectroscopy of Strong Hydrogen Bonds. In Hydrogen-Transfer Reactions*; Hynes, J. T.; Klinman, J. P.; Limbach, H.-H.; Schowen, R. L., Eds.; Wiley-VCH: Weinheim, Germany, 2007.

[191] B. D. Faithful, S. C. W. *Chem. Commun. (London)* **1967**, 1211 – 1211.

[192] Rozière, J.; Lehmann, M. S.; Potier, J. *Acta Crystallogr., Sect. B: Struct. Sci.* **1979**, *35*, 1099 – 1102.

[193] Ahlijah, G.; Mooney, E. *Spectrochim. Acta* **1969**, *25A*, 619 – 627.

[194] Waterland, M. R.; Kelley, A. M. *J. Chem. Phys.* **2000**, *113*, 6760 – 6773.

[195] Fehsenfeld, F. C.; Howard, C. J.; Schmeltekopf, A. L. *J. Chem. Phys.* **1975**, *63*, 2835 – 2841.

[196] Lovejoy, E. R.; Curtius, J. *J. Phys. Chem. A* **2001**, *105*, 10874 – 10883.

[197] Lovejoy, E. R.; Bianco, R. *J. Phys. Chem. A* **2000**, *104*, 10280 – 10287.

[198] Sekimoto, K.; Takayama, M. *J. Mass Spectrom.* **2010**, *45*, 50 – 60.

[199] Davidson, J. A.; Fehsenfeld, F. C.; Howard, C. J. *Int. J. Chem. Kinet.* **1977**, *9*, 17 – 29.

[200] Wlodek, S.; Luczynski, Z.; Wincel, H. *Int. J. Mass Spectrom. Ion Phys.* **1980**, *35*, 39 – 46.

[201] Zhou, J.; Santambrogio, G.; Brümmer, M.; Moore, D. T.; Wöste, L.; Meijer, G.; Neumark, D. M.; Asmis, K. R. *J. Chem. Phys.* **2006**, *125*, 111102.

[202] OBrien, J. T.; Prell, J. S.; Bush, M. F.; Williams, E. R. *J. Am. Chem. Soc.* **2010**, *132*, 8248 – 8249.

[203] TURBOMOLE*, V6.2 2010, a development of University of Karlsruhe and Forschungszentrum Karlsruhe GmbH, 1989-2007,* TURBOMOLE *GmbH, since 2007; available from http://www.turbomole.com.*

[204] Ahlrichs, R.; Bär, M.; Häser, M.; Horn, H.; Kölmel, C. *Chem. Phys. Lett.* **1989**, *162*, 165 – 169.

[205] Treutler, O.; Ahlrichs, R. *J. Chem. Phys.* **1995**, *102*, 346 – 354.

[206] Becke, A. D. *Phys. Rev. A* **1988**, *38*, 3098 – 3100.

[207] Becke, A. D. *J. Chem. Phys.* **1993**, *98*, 5648 – 5652.

[208] Lee, C.; Yang, W.; Parr, R. G. *Phys. Rev. B* **1988**, *37*, 785 – 789.

[209] Kendall, R. A.; Thom H. Dunning, J.; Harrison, R. J. *J. Chem. Phys.* **1992**, *96*, 6796 – 6806.

[210] Deglmann, P.; Furche, F.; Ahlrichs, R. *Chem. Phys. Lett.* **2002**, *362*, 511 – 518.

[211] Scott, A. P.; Radom, L. *J. Phys. Chem.* **1996**, *100*, 16502 – 16513.

[212] Halls, M. D.; Velkovski, J.; Schlegel, H. B. *Theor. Chem. Acc.* **2001**, *105*, 413 – 421.

[213] Marchand, P.; Marcotte, G.; Ayotte, P. *J. Phys. Chem. A* **2012**, *116*, 12112 – 12122.

[214] McGraw, G. E.; Bernitt, D. L.; Hisatsune, I. C. *J. Chem. Phys.* **1965**, *42*, 237 – 244.

[215] Maki, A.; Wells, J. *J. Mol. Spectrosc.* **1980**, *82*, 427 – 434.

[216] Irish, D. E.; Davis, A. R. *Can. J. Chem.* **1968**, *46*, 943 – 951.

[217] Relph, R. A.; Bopp, J. C.; Johnson, M. A.; Viggiano, A. A. *J. Chem. Phys.* **2008**, *129*, 064305.

[218] Barnes, A. J.; Lasson, E.; Nielsen, C. J. *J. Mol. Struct.* **1994**, *322*, 165 – 174.

[219] Jeffrey, G. A. *An Introduction to Hydrogen Bonding*; Oxford Univ. Pr., 1997.

[220] Yacovitch, T. I.; Wende, T.; Jiang, L.; Heine, N.; Meijer, G.; Neumark, D. M.; Asmis, K. R. *J. Phys. Chem. Lett.* **2011**, *2*, 2135 – 2140.

[221] Pelaez, D.; Sadri, K.; Meyer, H.-D. *Spectrochim. Acta: Part A* **2014**, *119*, 42 – 51.

[222] Yang, Y.; Kühn, O.; Santambrogio, G.; Goebbert, D. J.; Asmis, K. R. *J. Chem. Phys.* **2008**, *129*, 224302 p1–5.

[223] Diken, E. G.; Headrick, J. M.; Roscioli, J. R.; Bopp, J. C.; Johnson, M. A.; McCoy, A. B. *J. Phys. Chem. A* **2005**, *109*, 1487 – 1490.

[224] Ojamäe, L.; Shavitt, I.; Singer, S. J. *Int. J. Quantum Chem. Symp.* **1995**, *29*, 657 – 668.

[225] Kamrath, M. Z.; Relph, R. A.; Guasco, T. L.; Leavitt, C. M.; Johnson, M. A. *Int. J. Mass spectrom.* **2011**, *300*, 91 – 98.

[226] Westheimer, F. H. *Chem. Rev.* **1981**, *81*, 313 – 326.

[227] Nishizuka, Y. *Science* **1986**, *233*, 305 – 312.

[228] Westheimer, F. *Science* **1987**, *235*, 1173 – 1178.

[229] Henchman, M.; Viggiano, A. A.; Paulson, J. F.; Freedman, A.; Wormhoudt, J. *J. Am. Chem. Soc.* **1985**, *107*, 1453 – 1455.

[230] Keesee, R. G.; Castleman, A. W. *J. Am. Chem. Soc.* **1989**, *111*, 9015 – 9018.

[231] Ma, B.; Xie, Y.; Shen, M.; Schaefer, H. F. *J. Am. Chem. Soc.* **1993**, *115*, 1943 – 1951.

[232] Wu, Y. D.; Houk, K. N. *J. Am. Chem. Soc.* **1993**, *115*, 11997 – 12002.

[233] Blades, A. T.; Ho, Y.; Kebarle, P. *J. Am. Chem. Soc.* **1996**, *118*, 196 – 201.

[234] Klähn, M.; Mathias, G.; Kötting, C.; Nonella, M.; Schlitter, J.; Gerwert, K.; Tavan, P. *J. Phys. Chem. A* **2004**, *108*, 6186 – 6194.

[235] Pluharova, E.; Oncak, M.; Seidel, R.; Schroeder, C.; Schroeder, W.; Winter, B.; Bradforth, S. E.; Jungwirth, P.; Slavicek, P. *J. Phys. Chem. B* **2012**, *116*, 13254 – 13264.

[236] Zhang, L.; Xie, D.; Xu, D.; Guo, H. *J. Phys. Chem. A* **2005**, *109*, 11295 – 11303.

[237] Ruben, E. A.; Chapman, M. S.; Evanseck, J. D. *J. Phys. Chem. A* **2007**, *111*, 10804 – 10814.

[238] Brandan, S. A.; Diaz, S. B.; Picot, R. C.; Disalvo, E. A.; Altabef, A. B. *Spectrochim. Acta, Part A* **2007**, *66*, 1152 – 1164.

[239] Hammer, N. I.; Shin, J.-W.; Headrick, J. M.; Diken, E. G.; Roscioli, J. R.; Weddle, G. H.; Johnson, M. A. *Science* **2004**, *306*, 675 – 679.

[240] Xu, X.; Goddard, W. A. *J. Phys. Chem. A* **2004**, *108*, 2305 – 2313.

[241] Walters, R. S.; Pillai, E. D.; Duncan, M. A. *J. Am. Chem. Soc.* **2005**, *127*, 16599 – 16610.

[242] Bush, M. F.; Saykally, R. J.; Williams, E. R. *Journal of the American Chemical Society* **2008**, *130*, 15482 – 15489.

[243] Rodriguez, J. D.; Lisy, J. M. *J. Phys. Chem. A* **2009**, *113*, 6462 – 6467.

[244] Rodriguez, J. D.; Vaden, T. D.; Lisy, J. M. *J. Am. Chem. Soc.* **2009**, *131*, 17277 – 17285.

[245] Rodriguez, J. D.; Lisy, J. M. *J. Am. Chem. Soc.* **2011**, *133*, 11136 – 11146.

[246] OBrien, J. T.; Williams, E. R. *J. Am. Chem. Soc.* **2012**, *134*, 10228 – 10236.

[247] Myshakin, E. M.; Jordan, K. D.; Sibert, E. L.; Johnson, M. A. *J. Chem. Phys.* **2003**, *119*, 10138 – 10145.

[248] Domine, F.; Shepson, P. B. *Science* **2002**, *297*, 1506 – 1510.

[249] Prather, K. A.; Hatch, C. D.; Grassian, V. H. *Annu. Rev. Anal. Chem.* **2008**, *1*, 485 – 514.

[250] Thogersen, J.; Rehault, J.; Odelius, M.; Ogden, T.; Jena, N. K.; Jensen, S. J. K.; Keiding, S. R.; Helbing, J. *J. Phys. Chem. B* **2013**, *117*, 3376 – 3388.

[251] Xu, M.; Tang, C. Y.; Jubb, A. M.; Chen, X.; Allen, H. C. *J. Phys. Chem. C* **2008**, *113*, 2082 – 2087.

[252] Markovich, G.; Pollack, S.; Giniger, R.; Cheshnovsky, O. *J. Chem. Phys.* **1994**, *101*, 9344 – 9353.

[253] Cabarcos, O. M.; Weinheimer, C. J.; Lisy, J. M.; Xantheas, S. S. *J. Chem. Phys.* **1999**, *110*, 5 – 8.

[254] Robertson, W. H.; Johnson, M. A. *Annu. Rev. Phys. Chem.* **2003**, *54*, 173 – 13.

[255] Wang, X.-B.; Yang, X.; Wang, L.-S.; Nicholas, J. B. *J. Chem. Phys.* **2002**, *116*, 561 – 570.

[256] Gerardi, H. K.; DeBlase, A. F.; Su, X.; Jordan, K. D.; McCoy, A. B.; Johnson, M. A. *J. Phys. Chem. Lett.* **2011**, *2*, 2437 – 2441.

[257] Schneider, H.; Boese, A. D.; Weber, J. M. *J. Chem. Phys.* **2005**, *123*, 084307.

[258] Pathak, A. K.; Mukherjee, T.; Maity, D. K. *J. Phys. Chem. A* **2008**, *112*, 3399 – 3408.

[259] Shen, M.; Xie, Y.; Schaefer, H. F.; Deakyne, C. A. *J. Chem. Phys.* **1990**, *93*, 3379 – 3388.

[260] Waterland, M. R.; Stockwell, D.; Kelley, A. M. *J. Chem. Phys.* **2001**, *114*, 6249 – 6258.

[261] Ramesh, S. G.; Re, S.; Hynes, J. T. *J. Phys. Chem. A* **2008**, *112*, 3391 – 3398.

[262] Ebner, C.; Sansone, R.; Probst, M. *Int. J. Quantum Chem.* **1998**, *70*, 877 – 886.

[263] Howell, J. M.; Sapse, A. M.; Singman, E.; Snyder, G. *J. Phys. Chem.* **1982**, *86*, 2345 – 2349.

[264] Bartlett, R. J.; Watts, J.; Kucharski, S.; Noga, J. *Chem. Phys. Lett.* **1990**, *165*, 513 – 522.

[265] Raghavachari, K.; Trucks, G. W.; Pople, J. A.; Head-Gordon, M. *Chem. Phys. Lett.* **1989**, *157*, 479 – 483.

[266] Kendall, R. A.; Dunning, T. H., Jr.; Harrison, R. J. *J. Chem. Phys.* **1992**, *96*, 6796 – 6806.

[267] Dunning, T. H., Jr. *J. Chem. Phys.* **1989**, *90*, 1007 – 1023.

[268] Harding, M. E.; Metzroth, T.; Gauss, J.; Auer, A. A. *J. Chem. Theor. Comp.* **2008**, *4*, 64 – 74.

[269] Adler, T. B.; Knizia, G.; Werner, H.-J. *J. Chem. Phys.* **2007**, *127*, 221106 – 4.

[270] Peterson, K. A.; Adler, T. B.; Werner, H.-J. *J. Chem. Phys.* **2008**, *128*, 084102 – 12.

[271] Werner, H.-J.; Knowles, P. J.; Knizia, G.; Manby, F. R.; Schütz, M.; Others; *MOLPRO, version 2009.1, a package of ab initio programs*; 2009; see http://www.molpro.net.

[272] Herzberg, G. *Molecular spectra and molecular structure*; Van Nostrand, 1966.

[273] Ayotte, P.; Kelley, J. A.; Nielsen, S. B.; Johnson, M. A. *Chemical Physics Letters* **2000**, *316*, 455 – 459.

[274] Pauly, M.; Sroka, M.; Reiss, J.; Rinke, G.; Albarghash, A.; Vogelgesang, R.; Hahne, H.; Kuster, B.; Sesterhenn, J.; Kern, K.; Rauschenbach, S. *Analyst* **2014**, *139*, 1856 – 1867.

[275] TURBOMOLE*, V6.1 2009, a development of University of Karlsruhe and Forschungszentrum Karlsruhe GmbH, 1989-2007,* TURBOMOLE *GmbH, since 2007; available from http://www.turbomole.com.*

[276] McQuarrie, D. *Statistical Mechanics*, 1st ed.; HarperCollins, s. E., Ed.; New York, N.Y., 1976.

[277] CP2K*, available from http://www.cp2k.org/.*

[278] Nose, S. *J. Chem. Phys.* **1984**, *81*, 511 – 519.

[279] Hoover, W. G. *Phys. Rev. A* **1985**, *31*, 1695 – 1697.

List of Publications

12. S.-T. Sun, L. Jiang, J.-W. Liu, N. Heine, T. I. Yacovitch, T. Wende, D. M. Neumark, K. R. Asmis, and Z.-F. Liu, "Interactions between a Dihydrogen Phosphate Ion and Water Molecules Probed by Infrared Multiphoton Dissociation Spectroscopy and First Principles Calculations ", in preparation.

11. N. Heine and K. R. Asmis, "Cryogenic Ion Trap Vibrational Spectroscopy of Hydrogen-Bonded Clusters Relevant in Atmospheric Chemistry", invited article in *Int. Rev. Phys. Chem.*, in preparation.

10. N. Heine, M. R. Fagiani, and K. R. Asmis, "IR/IR Double Resonance Spectroscopy of Protonated Water Clusters $H^+(H_2O)_n$ with n = 5,7-10: Disentangling the Contribution of Multiple Isomers", in preparation.

9. N. Heine, E. G. Kratz, R. Bergmann, D. Schofield, K. D. Jordan, K. R. Asmis, and A. B. McCoy, "Vibrational Spectroscopy of the Water-Nitrate Complex in the O-H Stretching Region", *J. Phys. Chem. A*, **118**, 8188 – 8197 (2014).

8. N. Heine, T. I. Yacovitch, F. Schubert, C. Brieger, K. R. Asmis, and D. M. Neumark, "Infrared Photodissociation Spectroscopy of Microhydrated Nitrate-Nitric Acid Clusters $NO_3^-(HNO_3)_m(H_2O)_n$", *J. Phys. Chem. A*, **118** 7613 – 7622 (2014).

7. L. Jiang, S.-T. Sun, N. Heine, J.-W. Liu, T. I. Yacovitch, T. Wende, Z.-F. Liu, D. M. Neumark, and K. R. Asmis, "Large Amplitude Motion in Cold Monohydrated Dihydrogen Phosphate Anion $H_2PO_4^-(H_2O)$: Infrared Photodissociation Spectroscopy combined with *Ab Initio* Molecular Dynamics Simulations", *Phys. Chem. Chem. Phys.* **16** 1314 – 1318 (2014).

6. T. I. Yacovitch, N. Heine, C. Brieger, T. Wende, C. Hock, D. M. Neumark, and K. R. Asmis, "Vibrational Spectroscopy of Bisul-

fate/Sulfuric Acid/Water Clusters: Structure, Stability and IRMPD Intensities", *J. Phys. Chem. A* **117** 7081 – 7090 (2013).

5. N. Heine, M. R. Fagiani, M. Rossi, T. Wende, G. Berden, Volker Blum and K. R. Asmis, "Isomer-Selective Detection of Hydrogen-Bond Vibrations in the Protonated Water Hexamer", *J. Am. Chem. Soc.* **135** 8266 – 8273 (2013).

4. T. I. Yacovitch, N. Heine, C. Brieger, T. Wende, C. Hock, D. M. Neumark, and K. R. Asmis, "Communication: Vibrational Spectroscopy of Atmospherically Relevant Acid Cluster Anions: Bisulfate versus Nitrate Core Structures", *J. Chem. Phys.* **136** 241102–(1–4) (2012).

3. T. I. Yacovitch, T. Wende, L. Jiang, N. Heine, G. Meijer, D. M. Neumark, and K. R. Asmis, "Infrared Spectroscopy of Hydrated Bisulfate Anion Clusters: $HSO_4^- \cdot (H_2O)_{1-16}$", *J. Phys. Chem. Lett.* **2** 2135 – 2140 (2011).

2. F. Buchner, A. Lübcke, N. Heine, and T. Schultz, "Time-Resolved Photoelectron Spectroscopy of Liquids", *Rev. Sci. Instrum.* **81** 113107 – 113112 (2010).

1. A. Lübcke, F. Buchner, N. Heine, I.V. Hertel, and T. Schultz, "Time-Resolved Photoelectron Spectroscopy of Solvated Electrons in Aqueous NaI Solution", *Phys. Chem. Chem. Phys.* **12** 14629 – 14634 (2010).

Lebenslauf

Der Lebenslauf ist in der Online-Version aus Gründen des Datenschutzes nicht enthalten.

For reasons of data protection, the curriculum vitae is not included in the online version.

Acknowledgements

Die letzten 4 Jahre waren eine außergewöhnliche Zeit, in der ich mit tollen Kollegen zusammenarbeiten durfte, von denen viele zu Freunden geworden sind. Zahlreiche Kleinigkeiten machten die Arbeit hier besonders, nicht nur die uneingeschränkte Hilfsbereitschaft aller, auch diverse social events, wie regelmässige Kickerturniere, Kaffee und Kuchen, BBQ + Bier auf der Terrasse, unzählige Wine Tastings, Defense-Ausflüge nach Nijmegen mit den dazugehörenden MP Blockbustern und natürlich der legendäre Wandertag nach Jessen. Für diese tolle Atmosphäre und schöne Zeit in der Abteilung, möchte ich mich bei euch allen herzlich bedanken!

Zuerst möchte ich Gerard Meijer danken, der mir die Möglichkeit gegeben hat in dieser einzigartigen Umgebung zu arbeiten und natürlich für die Unterstützung meiner wissenschaftlichen Arbeit.

Mein besonderer Dank gilt Knut Asmis, der nicht nur das Thema meiner Arbeit stellte, sondern diese auch in allen Phasen unterstützte. Mein Dank betrifft vor allem die zahlreichen und hilfreichen Diskussionen und Anregungen im Hinblick auf das Forschungsprojekt, so wie das entgegengebrachte Vertrauen, welches mir schon früh eine eigenverantwortliche und selbständige Vorgehensweise bei der Planung, Koordination und Durchführung meiner Arbeit ermöglicht hat. Besonders möchte ich mich auch für die vielen Möglichkeiten bedanken an zahlreichen nationalen und internationalen Konferenzen teilzunehmen.

Mein Dank geht auch an alle ehemaligen und aktuellen Mitglieder unserer Arbeitsgruppe, für die tolle Zusammenarbeit und gegenseitige Unterstützung: Torsten, Ling, Claudia, Matias, (Tofu-)Tim, Xiaowei und Harald Knorke.

Almost all projects presented in this thesis are the result of fruitful collaborations with scientists all over the world. I am very grateful for a productive and enjoyable time! For the FELIX campaigns I would like to thank Tara Yacovitch and Dan Neumark. For the many exceptional calculations I want to thank Eric Kratz, Ken Jordan, Anne McCoy, Mariana Rossi, Franziska Schubert and Volker Blum. I also like to thank Mark Johnson and Mike Duncan for always providing helpful advice and giving new perspectives on scientific questions!

Mein Dank geht auch an das gesamte FELIX Team, insbesondere an

Britta, Lex und Giel, die mit ihrer Unterstützung massgeblich zum Erfolg vieler Messprojekte beigetragen haben!

Ein grosser Dank geht an die Elektronikwerkstatt, insbesondere an Georg und Victor, die mir beim Aufbau der Elektronik fur die gesamte Apparatur zur Seite standen und mich auch jederzeit bei Problemen unterstützt haben. Und auch an Frank und Mariüs, Klaus, Hans und allen anderen die massgeblich zum Gelingen des Projektes beigegtragen haben.

Besonders wichtig für den Erfolg des Projektes waren natürlich die beiden Werkstätten, die am Bau der einzelnen Elemente mitgearbeitet haben. Vielen Dank an alle Mitarbeiter der FHI und FU Feinwerktechnik, die an Planung, Konstruktion und Anfertigung beteiligt waren und auch mal Fehler in meinen Zeichnungen korrigierten. Insbesondere an Herrn Schwäricke, Petrik, Detlef, Micha und Dirk.

Vielen Dank auch an alle Techniker und administrativen Mitarbeiter der Abteilung, die mich bei der Arbeit unterstützt haben. Allen voran Inga und Andrea, die immer da waren, wenn es etwas zu organisieren oder einfach nur zu Quatschen gab. Im Labor standen mir Georg, Andreas, Rolf und Petrik immer unterstützend zur Seite, besonders wenn mal wieder die Falle ausgebaut oder eine Pumpe angeschlossen werden musste. Hendrik und Wolfgang hatten immer ein offenes Ohr für meine Zeichnungen und hielten guten Tipps bereit.

Und schliesslich mochte ich noch allen Praktikanten, Doktoranden, Post-Docs und allen anderen für die schöne Zeit in der MP danken. Viele waren zwar nicht direkt an meinem Projekt beteiligt, haben dieses aber in anderer Hinsicht positiv beeinflusst. Besonders möchte ich Christian S. für den Pep Talk auf den letzten Metern danken. Isa, für eine lustige Zeit und viele Diskussionen in unserem girls' office und Alex und Christian, unter anderem für die tollen Winetastings. Aber auch allen anderen nicht genannten (Ex-)MPlern möchte ich nochmal ausdrücklich danken!!

Zuletzt möchte ich noch allen meinen Freunden und meiner Familie ganz herzlich danken, die mich während der ganzen langen Zeit des Studiums und der Doktorarbeit unterstützt haben, insbesondere To Ly.

Eidesstattliche Erklärung

(gemäß §7, Ziffer (4) der Promotionsordnung vom 20.08.2013 des Fachbereichs Physik an der Freien Universität Berlin)

Die Disseration habe ich selbstständig angefertigt. Alle Hilfsmittel und Hilfen habe ich angegeben, insbesondere habe ich die wörtlich oder dem Sinne nach anderen Veröffentlichungen entnommenen Stellen kenntlich gemacht.

Die Dissertation hat bisher weder in der gegenwärtigen noch in einer anderen Fassung weder dem Fachbereich Physik der Freien Universität Berlin noch einer anderen Fakultät oder Universität vorgelegen.

Ort, Datum	Unterschrift